ADVANCED STEEL CONSTRUCTION

An International Journal

Volume 16 Number 2

June 2020

CONTENTS

Technical Papers

Website: *http://www.hkisc.org*
ISSN 1816-112X
Science Citation Index Expanded, Materials Science Citation Index and ISI Alerting
Cover: Zhangjiang International Brain Imaging Centre, Shanghai, China
Designed by Tongji Architectural Design (Group) Co., Ltd
e-copy of IJASC is free to download at "www.ascjournal.com" in internet and mobile apps.

ADVANCED STEEL CONSTRUCTION

VOL.16, NO.2 (2020)

ADVANCED STEEL CONSTRUCTION

an International Journal

ISSN 1816-112X

Volume 16 Number 2 *June 2020*

ISSN 1816-112X

Science Citation Index Expanded, Materials Science Citation Index and ISI Alerting

Advanced Steel Construction
an international journal

Cover: Zhangjiang International Brain Imaging Centre, Shanghai, China
Designed by Tongji Architectural Design (Group) Co., Ltd
e-copy of IJASC is free to download at "www.ascjournal.com" in internet and mobile apps.

General Information
Advanced Steel Construction, an international journal

Aims and scope

The International Journal of Advanced Steel Construction provides a platform for the publication and rapid dissemination of original and up-to-date research and technological developments in steel construction, design and analysis. Scope of research papers published in this journal includes but is not limited to theoretical and experimental research on elements, assemblages, systems, material, design philosophy and codification, standards, fabrication, projects of innovative nature and computer techniques. The journal is specifically tailored to channel the exchange of technological know-how between researchers and practitioners. Contributions from all aspects related to the recent developments of advanced steel construction are welcome.

Subscription inquiries and change of address. Address all subscription inquiries and correspondence to Member Records, IJASC. Notify an address change as soon as possible. All communications should include both old and new addresses with zip codes and be accompanied by a mailing label from a recent issue. Allow six weeks for all changes to become effective.

The Hong Kong Institute of Steel Construction
HKISC
c/o Department of Civil and Environmental Engineering,
The Hong Kong Polytechnic University,
Hunghom, Kowloon, Hong Kong, China.
Tel: 852- 2766 6047 Fax: 852- 2334 6389
Email: *ceslchan@polyu.edu.hk* Website: *http://www.hkisc.org/*
ISSN 1816-112X
Science Citation Index Expanded, Materials Science Citation Index and ISI Alerting

ISSN 1816-112X

Science Citation Index Expanded, Materials Science Citation Index and ISI Alerting

Advanced Steel Construction
an international journal

VOLUME 16 NUMBER 2 June 2020

Technical Papers

Advanced Steel Construction – Vol. 16 No. 2 (2020) 94–98
DOI:10.18057/IJASC.2020.16.2.1

A REVIEW ON COMPOSITE ACTIONS OF PLATE-REINFORCED COMPOSITE COUPLING BEAMS

Z.W. Shan and R.K.L. Su *

Department of Civil Engineering, The University of Hong Kong, Pokfulam Road, Hong Kong, PRC
** (Corresponding author: E-mail: klsu@hku.hk)*

ABSTRACT

Reinforced concrete (RC) shear walls are widely utilized to resist lateral and gravity loads in modern building designs. The adjacent wall piers are usually connected to the coupling beams. Severe earthquake and wind loads challenge the seismic and shear resistance of conventional reinforced concrete (RC) coupling beams respectively. Their shear and chord rotational capacities may not be able to prevent excessive loading and deformation. Therefore, a plate-reinforced composite (PRC) coupling beam has been developed with the aim to provide a practical and effective alternative that resists extreme loads in building designs. The PRC coupling beam comprises a vertically embedded steel plate that is framed into the wall piers for anchorage and spans across the RC beam. Shear studs are used to increase the composite interaction between the RC components and the embedded steel plate. In this paper, the composite actions between the RC components and the embeded steel plate are discussed. The factors that affect the shear strength and inelastic response of the PRC beams are elaborated. The findings in this paper can be used to enhance the understanding of practitioners on the load-transfer process and capability of PRC coupling beams.

ARTICLE HISTORY

Received: 25 October 2019
Revised: 24 February 2020
Accepted: 25 February 2020

KEYWORDS

Coupling beams;
steel composite structures;
steel studs;
shear strength;
Inelastic response

1. Introduction

In contemporary highrise buildings, coupled shear walls are commonly employed to resist lateral loads caused by wind and earthquake loads. Typical coupling beams that connect two wall piers together usually have small cross-section dimensions, short span and a low span-to-depth ratio. They are used to reduce flexural moments in coupled shear wall piers, reduce the lateral deflection of a tall building, and dissipate energy during a severe earthquake. As one of the most critical members in reinforced concrete (RC) buildings, coupling beams need to have high shear capacity, deformability and energy dissipation capacity. However, conventional RC coupling beams (as shown in Fig. 1(a)) are prone to brittle failure under severe earthquake loading. Diagonal cracks may form when the beam is under-reinforced in shear. On the other hand, even when there is sufficient shear reinforcement, sliding failure could not be avioded at the beam-wall joints. Therefore, conventional RC coupling beams have limited deformability and shear capacity [1-4].

For existing buildings, seismic strengthening of RC coupling beams [5-7] may be required. For new construction, different types of coupling beams as shown in Fig. 1 that have good hysteretic performance yet are practical for construction purposes can be adopted, including diagonally RC coupling beams [8-11], encased steel composite coupling beams [12-13], and composite coupling beams that are reinforced with steel plates [14] (plate-reinforced composite (PRC) coupling beams).

Diagonally RC coupling beams [8-11] are well known to have excellent energy dissipation capacity and deformability. However, their applicability is limited by constructability issues such as a large width (> 350 mm) required to accommodate all reinforcements, the labour intensity of steel fixing and their ineffectiveness when the span-to-depth ratio is larger than two. Although the structural performance of the encased steel composite coupling beams developed by Harries et al. [13] is comparable to that of diagonally RC coupling beams, the wide flange steel members can interfere with the vertical and confinement reinforcement in the shear walls. Furthermore, the embedded steel members may block the sleeves that are required to run laterally through the beam as the service ducts.

Therefore, PRC coupling beams have been proposed to address the issues on the use of steel members and shear wall reinforcement; see Fig. 1(d). These beams comprise a steel plate which is embedded onto a conventional RC beam. Shear studs are provided to bond together the steel plate and the concrete. They are flexible in design, simple in construction and particularly suitable for slim floor systems with restrictive height limits. The embedment of a steel plate does not interrup the existing reinforcement details. Therefore, walls, slabs and coupling beam reinforcements can be seamlessly integrated together. The vertical arrangement of the steel plate allows concrete to be filled and compacted easily, so honeycomb defects can be avoided. In addition, the surrounding concrete can provide fire and lateral buckling resistance for the cast-in steel plate.

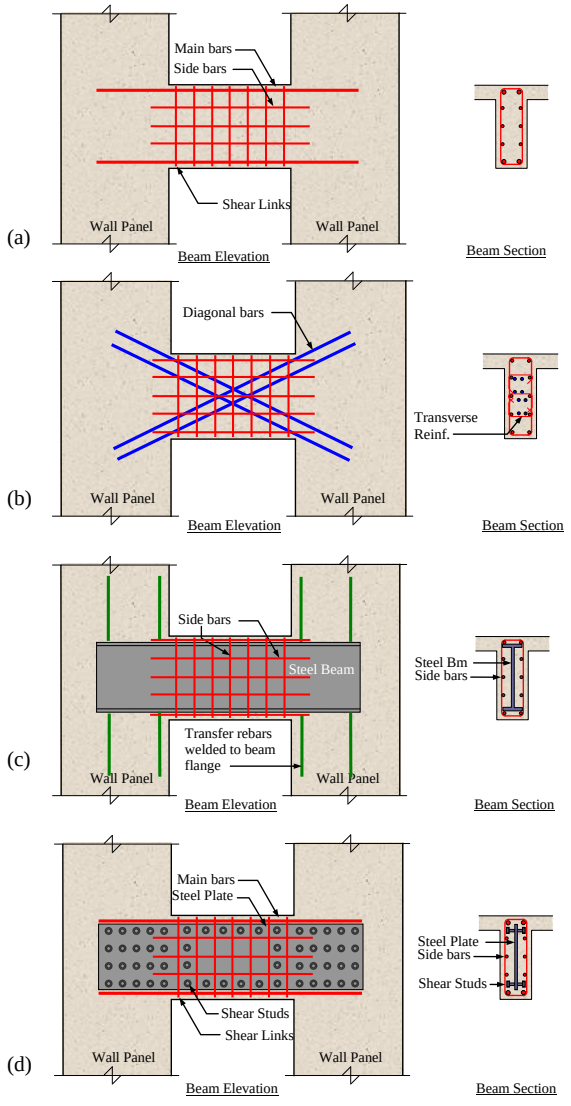

Fig. 1 Different types of coupling beams: (a) conventional RC, (b) diagonally RC, (c) encased steel composite, and (d) PRC coupling beams

A 2019 review of the structural performance and practical limitations of

various types of coupling beams by Liao and Pimento [15] recently found that the PRC coupling beam can provide an 80% higher shear capacity and a wider applicable range of span-to-depth ratios than the diagonally reinforced concrete coupling beam. The PRC coupling beam also has better constructability than: steel coupling beams, encased steel composite coupling beams and diagonally reinforced coupling beams. This novel method provides an easy and practical design solution for coupling beams used in tall buildings that are over 50 stories in height to resist strong wind and earthquake forces.

Many experimental studies [14, 16-19] have been done to (i) investigate the effectiveness of PRC coupling beams in shear strength enhancement, (ii) examine the inelastic bahavior of PRC coupling beams under reverse cyclic loads, (iii) explore the role of shear studs during the interaction between the steel plate and RC component, and (iv) study the load distribution in the RC beam and steel plate. Furthermore, comprehensive non-linear finite element analyses [20-21] have been carried out to quantify the forces of shear stud in beam span and to establish the design model of wall anchorage system which includes (i) determination of axial force induced in the wall anchor, (ii) evaluation of optimum plate anchorage length in wall region, and (iii) determination of the moment from the vertical and horizontal bearing forces. Based on those studies, Su and Lam [22] proposed design guidelines for PRC coupling beams in accordance with British standards. Since then, this new design method has been adopted worldwide in the design of tall and super tall buildings; for instance, the Trump International Hotel Waikiki in Hawaii [23], Pacifica Honolulu in Hawaii [24], Tsubaki Tower in Guam, and other high-rise buildings in Bangkok, Thailand; Dubai, United Arab Emirates; and Florida, USA.

In this paper, the composite action between the steel plate and RC components which have not been systematically discussed in previous studies will be elaborated. The influence of shear stud arrangements on the shear strength and inelastic response of PRC coupling beams will be presented. The intention of this study is to inform building designers of the load transfer process and behaviour between steel plates and PRC coupling beams.

2. Composite actions

When a building with coupled shear walls is subjected to wind or seismic loads, the building will deform due to the rotation of the wall piers as shown in Fig. 2. When PRC coupling beams are used instead and a steel plate is embedded onto the wall piers by using shear connectors, the steel plate and the RC component will sustain a similar rotation demand at the ends of the coupling beams. Shear studs placed on the different wall regions primarily contribute to the composite action between the steel plate and RC component. Furthermore, the shear connectors that are placed along the beam span also contribute to the composite action. These composite actions which can greatly affect the strength and deformability of beams will be discussed in the following sections.

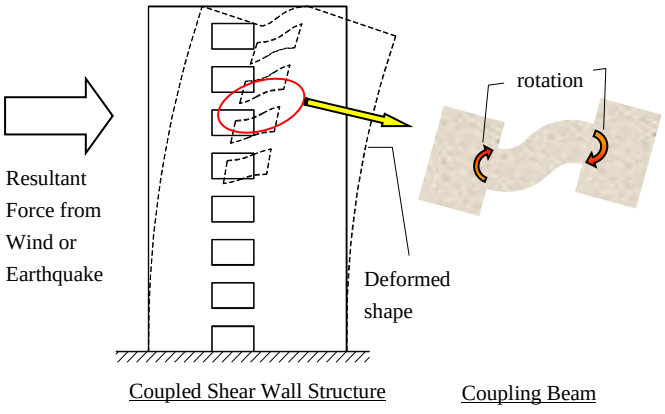

Fig. 2 Wind or earthquake induced deformations on coupling beams

2.1. Composite action along beam span

Assuming that the steel plate has been properly installed on the wall piers, the embedded steel plate and RC component will sustain the same rotation at the beam-wall interface when the beam is subjected to bending. If shear studs along the beam span have not been installed, the strain profile of the RC component and steel plate will not match. The neutral axis of the steel plate and that of RC components will separate as illustrated in Fig. 3(a). Conversely, if a sufficient number of shear studs have been installed along the beam span, the separation of the two neutral axes will be reduced and the two strain profiles will be more similar, see Fig. 3(b). The changes in the strain profile will cause axial tensile deformation in the steel plate and axial compressive deformation is produced in the RC component. Such axial force induced along the steel plate has been revealed from a reverse cyclic load test by Lam et al. [17]. They added shear studs to the wall regions and along the beam span. The differences in the internal axial forces of the embedded steel plate at different load levels from the first load cycle up to the peak load is shown in Fig. 4. It can be seen that the plate is always under axial tension. The maximum axial force is obtained near the beam-wall interface, which decreases from the beam-wall joints to a minimum value at mid-span. The induced axial force is comparable to the shear load that is acting on the beam. This type of interaction should be considered in the flexural design of RC sections and the steel plate as well as in the anchoring design of steel plates.

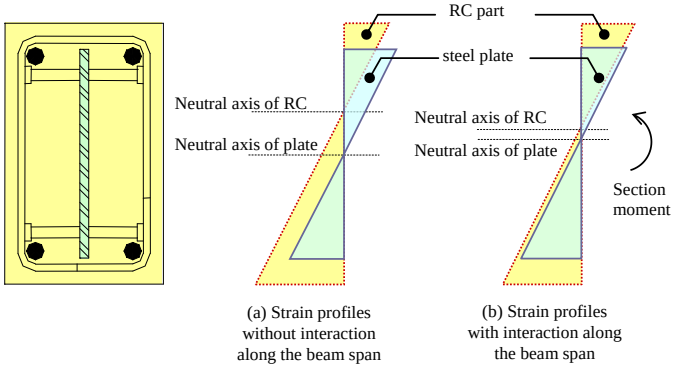

Fig. 3 Strain profiles of concrete and steel plates (a) without and (b) with interaction along the beam span

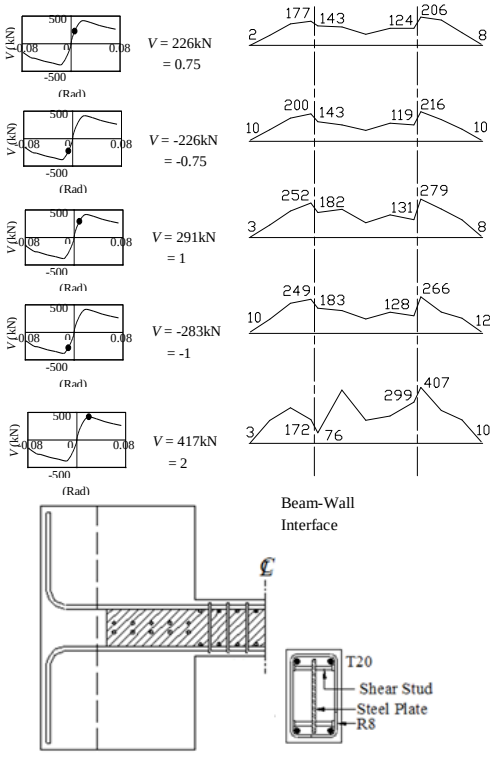

Fig. 4 Typical distribution of internal axial force on embedded steel plate [17]

Using a non-linear finite element method, Su et al. [20] determined the maximum axial force at beam-wall joints. Typical variations in the axial load in the ratio of the span-to-depth (l/h) of the coupling beam and the thickness of the plate to the beam width ratio (t_p/b) are shown in Fig. 5. In this figure, F is the induced axial force and V_u is the design ultimate shear load. The results indicate that the induced axial load increases with an increase in the span-to-depth ratio of the coupling beam.

According to their numerical analysis, four functions of shear studs that are installed on the beam span as illustrated in Fig. 6 are observed and described below.

(i) Forces in the vertical studs maintain the tension tie effect of the steel plate

Although shear is mainly developed on the steel plate on the wall anchors, approximately 15% to 30% of the design shear capacity of the PRC coupling beam is induced on the beam span near the beam-wall interface. Therefore, plate anchor should also be placed away from the beam-wall joint to transfer the plate shear force.

(ii) Vertical forces in the studs induce shear in the steel plate

The stud forces are meant to maintain tension tie action through the steel plate.. Tension tie action is similar to the strengthening provided by the shear stirrups.

(iii) Horizontal forces in the studs apply moments on the steel plate

The difference in curvature between the RC component and steel plate mobilise the shear connectors. Opposite horizontal forces are generated in the pairs of shear studs near the top and the bottom of steel plate, which induces bending moments on the steel plate and thus enhance the composite action between the plate and RC component.

(iv) Horizontal forces of studs that apply axial tension force on steel plate

These horizontal forces in shear studs are due to the shifting of the neutral axis of the RC component and embedded steel plate as described in the previous section.

In the light of the results from the comprehensive parametric study, design equations were proposed to predict the required shear connection forces associated with the aforementioned functions through a non-linear regression analysis [20].

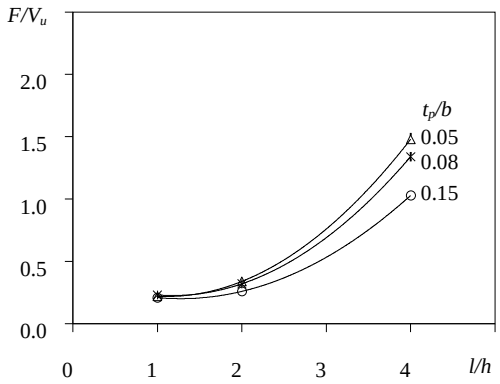

Fig. 5 Typical variations in the axial load of steel plate in the span-to-depth ratio of the coupling beam

2.2. Composite action along wall anchor

To ensure good composite interaction between the RC component and the embedded steel plate, the plate end should be fully fixed on the wall piers such that the plate and the wall pier sustain the same rotation at the beam-wall joint. To achieve this, the anchor of the plate resists all of the forces in the plate including the horizontal forces caused by the elongation of the RC component. The bearing force distributions at wall anchor of the embedded steel plate are shown in Fig. 7.

The bearing force distributions at the anchor of the plate actually depend on the anchorage load from the plate, arrangement of the shear studs, and embedment length of the plate L_a. The embedment model proposed in Mattock and Gaafar [25] which is widely used for the design of encased steel composite coupling beams is not applicable to the plate anchor design of PRC coupling beams as the horizontal anchorage force and the moment resistance from the horizontal bearing forces have not been considered in their model.

Su et al. [20] and Lam et al. [21] used a non-linear finite element analysis with a uniform distribution of the shear studs in both the vertical and horizontal directions to derive the minimum anchorage length of the embedded steel plate and the moment resistance associated with the bearing force distribution in the horizontal and vertical directions. Their studies found that the minimum anchorage length for a steel plate depends on the span-to-depth ratio of the coupling beam. The anchor length-to-beam span ratio (L_a/l) decreases with an increase in the span-to-depth ratio (l/h) of the beam. It has been indicated that when the l/h ratio is 1, 2, or 4, the corresponding L_a/l ratio is 0.76, 0.58 and 0.4, respectively. Furthermore, these two studies found that the contribution from the horizontal bearing force (M_1) to the moment resistance decreases with an increase in the L_a/h_p where h_p represents the emebeded steel plate depth. Conversely, the contribution of the vertical bearing force (M_2) to the moment resistance increases with that of L_a/h_p.

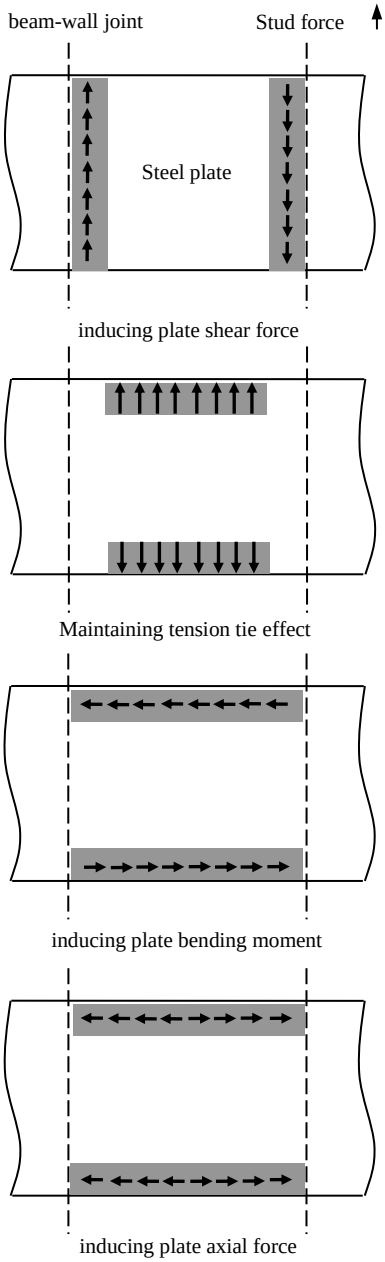

Fig. 6 Four basic functions of shear connectors in beam span

3. Shear strength of PRC coupling beams

Coupling beams with high shear capacity are often required when designing tall buildings with a coupled shear wall system to resist wind loading. The ultimate shear capacity of the PRC coupling beams is governed by the strength of the RC component, steel plate and wall piers for plate anchor together with the arrangements of shear connectors. An experimental study [18] on PRC coupling beams that comprise different arrangements of shear connectors in the wall and beam regions found that there should be sufficient shear connectors in the wall region to avoid anchorage bond slip of the plate. Poor anchorage of the plate to the wall region can inhibit the development of the full shear capacity of short PRC coupling beams. The shear studs that are installed on the beam span can only marginally improve the composite action between the emebeded steel plate and RC component and the shear strength of the PRC coupling beam.

When there is a large amount of composite action on the PRC coupling beam, a similar internal deformation of the steel plate and RC component is expected. To realise the full potential of the PRC coupling beam in resisting

shear, yielding of the steel plate and longitudinal reinforcement should occur at the same time. Thus the strength of the steel plate should be similar to that of the longitudinal reinforcement. If a high yield steel is used for the longitudinal bars, high strength steel plates should also be used on the PRC coupling beams.

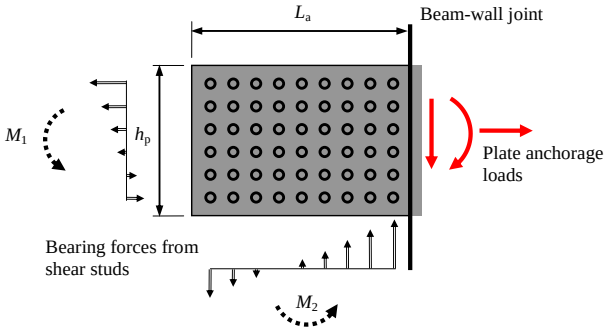

Fig. 7 Bearing force distributions at the plate anchor

An experimental study by Lam et al. [26] on PRC coupling beams demonstrated that the shear capacity of a PRC coupling beam (MPrc-2, with a plate area ratio of 4.4%) can double in comparison to conventional RC coupling beams (MRc), see Table 1. In addition, the shear resistance of PRC coupling beams (SPrc-1 and SPrc-2) is around 30% higher than that of the diagonally RC beam (SDRc) as shown in Table 1. It is possible to further increase the shear capacity of PRC coupling beams by adopting a thicker plate without the steel congestion problem faced by diagonally RC coupling beams. In the design guide of PRC coupling beams [22], the shear resistance from the steel plate is recommended to be limited to 45% of the total shear capacity.

As the shear loads sustained by the steel plate together with the RC component will eventually be transferred to the wall piers, the total shear capacity of the PRC coupling beam will also be limited by the load carrying capacity of the wall piers. Lam et al. [21] conducted a numerical parametric study, and recommended that the maximum shear stress (V_u/bd) of PRC coupling beams should not be more than 15 MPa. With a material safety factor of 1.25, the allowable design shear stress should be restricted to $v_u = V_u / bd \le 1.5\sqrt{f_{cu}} \le 12\,\text{MPa}$.

4. Inelastic performance of PRC coupling beams

In designing RC coupled shear wall systems with seismic resistance, practitioners are often concerned about the inelastic response of the coupling beams, such as the ultimate rotation, ductility, hysteretic response, damping ratio, etc.

Lam et al. [17] conducted an experimental study on PRC coupling beams which applied a span-to-depth ratio of 2.5 under reverse cyclic loading. They fiund that shear connectors are necessary to increase the composite action between RC component and the plate, in order to obtain a good inelastic performance under large imposed deformations. Fig. 8 compares the hysteretic loops of the coupling beams with and without shear studs in the wall regions. In Unit MPrc-N with a plain plate, severe pinching can be observed in the load-rotation hysteretic curve after reaching the peak load. Unit MPrc-W with shear studs welded on its plate in the wall regions can maintain load-resistance of the beam even after serious cracking of the beam-wall joints. By comparing the hysteretic loops of the PRC coupling beams with and without shear studs along the beam span, Lam et al. [17] found that studs along the beam span would only slightly improve the inelastic response of PRC coupling beams. They showed that shear studs in the wall regions rather than along the beam span can effectively mitigate pinching in the inelastic hysteretic loops and improve the deformability, ductility and energy dissipation capacity of PRC coupling beams. It should be noted that the embedded steel plate can maintain continuous shear transfer in the beam-wall joints even after concrete cracking and loss of aggregate interlock. The embeded steel plate is vital for achieving a desirable inelastic performance.

The structural performance of PRC coupling beams with the same total longitudinal reinforcement ratio but different bar diameters was investigated by Lam et al. [16]; see Fig. 9(a). Their study found that the patterns of the cracking of these two beams are similar before reaching the peak loads, where shear cracks and small flexural cracks are observed at the plastic hinges and along the longitudinal reinforcing bars respectively. However, after reaching the peak load, bond-slip cracks began to be pre-dominant in the beam with larger diameter longitudinal reinforcement which did not initiate cracking in the centre of the beam throughout the tests. Very little bond-slip occurs in beams with smaller diameter longitudinal reinforcement, while flexural shear cracks continue to develop and propagate towards the centre of the beam, see Fig. 9(b). Thus, to avoid bond-slip failure under large deformations and fully utilize the potential capacity, a longitudinal bar size over 1/10 of the smallest dimension of the beam is recommended.

In general, the rotation and ductility capacities of properly designed PRC coupling beams with a sufficient number of shear studs in the wall anchors could reach 0.04 rad and 4 respectively for beams. The equivalent elastic damping coefficient can be increased from around 5% to 12% for a ductility factor that has increased from 1.0 to 4.0.

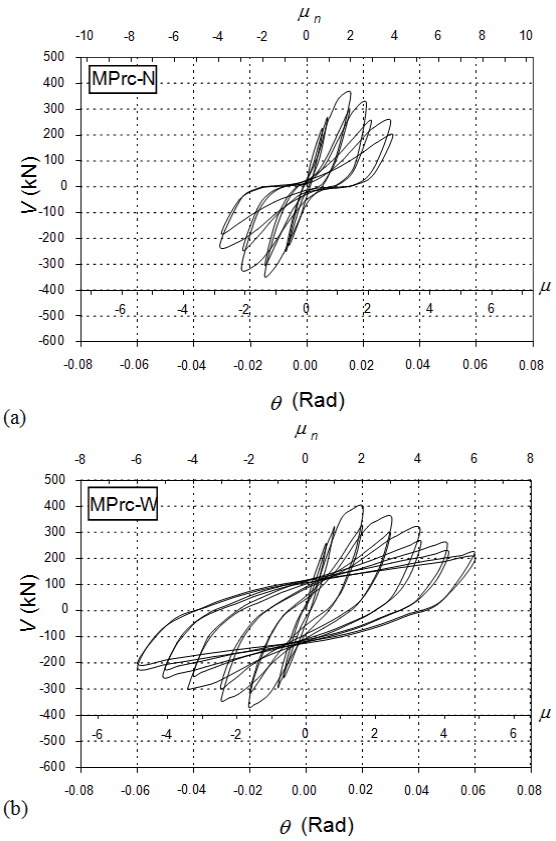

Fig. 8 Comparison of hysteretic loops (a) MPrc-N [17] and (b) MPrc-W [18]

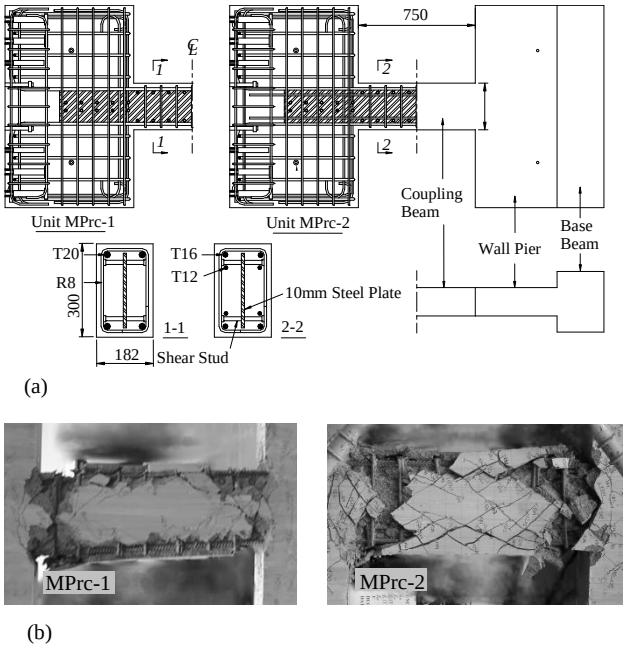

Fig. 9 PRC coupling beams (a) geometry and details of RC component and (b) failure modes [26]

Table 1
Summary of experimental results

Span-to-depth ratio	Reference	Unit	Failure Mode	V_{max} (kN)	θ_u (Rad)
2.5	[17]	MRc	Flexural shear / Bond-slip	213	0.029
	[17]	MPrc-N	Flexural shear / Bond-slip	360	0.031
	[18]	MPrc-B	Flexural shear / Bond-slip	408	0.048
	[17]	MPrc-W	Flexural shear / Bond-slip	397	0.050
	[16]	MPrc-1	Flexural shear / Bond-slip	417	0.080
	[16]	MPrc-2	Flexural shear	434	0.056
1.17	[19]	SDRc	Buckling of Bars	346	0.044
	[19]	SPrc-1	Shear-sliding	438	0.037
	[19]	SPrc-2	Shear - compression	474	0.041

10. Conclusions

Previous experimental and numerical results in the literature are used to discuss the interaction process of RC components and embedded steel plates and the functions of shear studs on PRC coupling beams. Two composite actions are found; one at the wall anchor and the other along the span region of the beam. It is found that the full strength potential of PRC coupling beams is not only affected by the strength of the steel plate and wall anchor but also the reinforcement ratio of the RC wall piers. The inelastic response of PRC coupling beams is significantly affected by the composite action at the wall anchor. The embedded steel plate can contribute to continuing shear transfer across the beam-wall joints after concrete cracking. Furthermore, the typical shear strength limit, ductility and rotation capacities and damping coefficient of properly designed PRC coupling beams are found to increase in PRC coupling beams with sufficient number of shear connectors in the wall anchors. The equivalent elastic damping coefficient can be increased from around 5% to 12% for a ductility factor that has increased from 1.0 to 4.0. The findings in this paper can be used to enhance the understanding of practitioners on the load-transfer process and capability of PRC coupling beams.

References

[1] Tassios T.P., Moretti M. and Bezas A., “On the behavior and ductility of reinforced concrete coupling beams of shear walls”, ACI Structural Journal, 93(6), 711-720, 1996.
[2] Galano L. and Vignoli A., “Seismic behavior of short coupling beams with different reinforcement layouts”, ACI Structural Journal, 97(6), 876-885, 2000.
[3] Breña S.F. and Ihtiyar O., “Performance of conventionally reinforced coupling beams subjected to cyclic loading”, Journal of Structural Engineering, 137(6), 665-676, 2011.
[4] Li X., Sun Y.S., Ding B.D. and Xia C.Z., “Cyclic Behavior of Deep RC Coupling Beams with Different Reinforcement Layouts”, Journal of Earthquake Engineering, 24(1), 155-174, 2020.
[5] Cheng B. and Su R.K.L., “Numerical studies of deep concrete coupling beams retrofitted with a laterally restrained steel plate”, Advances in Structural Engineering, 14(5), 903-915, 2011.
[6] Cheng B. and Su R.K.L., “Retrofit of deep concrete coupling beams by a laterally restrained side plate”, Journal of Structural Engineering, 137(4), 503-512, 2011.
[7] Cheng B., Su R.K.L., Shi C. and Yang C.T., "Laterally restrained steel plate with stiffeners for seismic retrofitting of concrete coupling beams", Advanced Steel Construction, 12(2), 194-210, 2016.
[8] Fortney P.J., Rassati G.A. and Shahrooz B.M., “Investigation on effect of transverse reinforcement on performance of diagonally reinforced coupling beams”, ACI Structural Journal, 105(6), 781, 2008.
[9] Harries K.A., Fortney P.J., Shahrooz B.M. and Brienen P.J., “Practical design of diagonally reinforced concrete coupling beams-critical review of ACI 318 requirements”, ACI Structural Journal, 102(6), 876-882, 2005.
[10] Chun Y.S. and Chang K.K., “Seismic performance of special reinforced concrete coupling beams with diagonal reinforcement and headed bars”, Magazine of Concrete Research, 68(6), 283-290, 2016.
[11] Paulay T. and Binney J.R., "Diagonally reinforced coupling beams of shear walls", ACI Special Publication, SP-42, 579-598, 1974.
[12] Li Y., Jiang H. and Yang T.Y., “Damage Deformation of Flexure-Yielding Steel-Reinforced Concrete Coupling Beams: Experimental and Numerical Investigation”, Advances in Civil Engineering, Article ID 7071243, 2019.
[13] Harries K.A., Gong B.N. and Shahrooz B.M., "Behavior and design of reinforced concrete, steel, and steel-concrete coupling beams", Earthquake Spectra, 16, 775-799, 2000.
[14] Lam W.Y., Su R.K.L. and Pam H.J., "Strength and ductility of embedded steel composite coupling beams". Advances in Structural Engineering, 6, 23-35, 2003.
[15] Liao S. and Pimentel B., "Coupling beam types", Structure Magazine, 1, 8-13, 2019.
[16] Lam W.Y., Su R.K.L. and Pam H.J., "Seismic performance of plate reinforced composite coupling beams", Proceedings of the 13th World Conference on Earthquake Engineering, Vancouver, BC Canada, paper no. 316, 1-11, 2004.
[17] Lam W.Y., Su R.K.L. and Pam H.J., "Experimental study on embedded steel plate composite coupling beams", Journal of Structural Engineering ASCE, 131, 1294-1302, 2005.
[18] Su R.K.L., Pam H.J. and Lam W.Y., "Effects of shear connectors on plate-reinforced composite coupling beams of short and medium-length spans", Journal of Constructional Steel Research, 62, 178-188, 2006.
[19] Su R.K.L., Lam W.Y. and Pam H.J., "Experimental study of plate-reinforced composite deep coupling beams", The Structural Design of Tall and Special Buildings, 18, 235-257, 2009.
[20] Su R.K.L., Lam W.Y. and Pam H.J., "Behaviour of embedded steel plate in composite coupling beams", Journal of Constructional Steel Research, 64, 1112-1128, 2008.
[21] Lam W.Y., Li L.Z., Su R.K.L. and Pam H.J., "Behavior of plate anchorage in plate-reinforced composite beams", The Scientific world Journal, Article ID 190430, 2013.
[22] Su R.K.L. and Lam W.Y., "A unified design approach for plate-reinforced composite coupling beams", Journal of Constructional Steel Research, 65, 675-686, 2009.
[23] Baldridge S.M., Popp D.R. and Mizue E., "Structural performance on Waikiki Beach", Structural Engineer, 3e, 30-33, 2009.
[24] Baldridge S.M., "400 feet, 53 stories: How a structural engineer was able to squeeze as many floors as possible under restrictive height", Structural Engineer, 7, 16-20, 2012.
[25] Mattock A.H. and Gaafar G.H., "Strength of embedded steel sections as brackets", ACI Journal, 79(9), 83-93, 1982.
[26] Lam W.Y. Plate-Reinforced Composite Coupling Beams-Experimental and Numerical Studies, PhD thesis, The University of Hong Kong, Hong Kong, 2006.

Advanced Steel Construction – Vol. 16 No. 2 (2020) 99–111
DOI:10.18057/IJASC.2020.16.2.2

EXPERIMENTAL STUDIES ON THE GLOBAL STABILITY OF CONCRETE SANDWICHED DOUBLE STEEL TUBULAR COLUMNS

Mashudha Sulthana U.[1,*] and Arul Jayachandran S.[2]

[1]*Post Doctoral Research Scholar, Department of Civil Engineering, Indian Institute of Technology Madras, Chennai-600036, India.*
[2] *Professor, Department of Civil Engineering, Indian Institute of Technology Madras, Chennai-600036, India.*
[*]*(Corresponding author: Email: mashudha@gmail.com)*

ABSTRACT

In improving the ductility and fire-resistance properties of framed structural systems, concrete sandwiched double steel tubular columns (CSDST) are found to be advantageous over concrete filled steel tubular columns (CFST), particularly when the columns are slender. However, a comprehensive understanding of the long column behaviour of CSDST is not fully developed. In this paper, experimental studies on the global stability aspects of CFDST columns is presented. Axial compression tests are carried out on twelve CSDST specimens with two CFST as benchmark specimens having non-dimensional member slenderness value around unity. Shape of the inner and outer steel tubes, hollowness ratio and concrete strength are selected as primary parameters for the experimental study. Comparing the experimental results of CSDST with CFST, it is found that the buckling capacity of CSDST is lesser than CFST. The degree of stability in CSDST is directly proportional to the hollowness ratio, irrespective of the cross-section shape and sandwiched concrete strength. The effective flexural rigidity of the specimens derived from the experimental results is reported here, which reiterates the inverse relation of hollowness ratio to the column instability. An average over-strength of around 12% for square and 20% for circular specimens is observed in the test axial capacities when compared to the code specifications (ANSI/AISC 360(16) and EN 1994-1-1 2004). Low initial global imperfection (≈ L/7000) in the specimens has led to the over-strength in test axial capacities. It is concluded that the code axial capacity equation for long column CFST (ANSI/AISC 360(16) and EN 1994-1-1 2004) can be adopted for CSDST long columns. However, these code equations are comparatively less conservative for CSDST with less than 50% hollowness.

ARTICLE HISTORY

Received: 1 August 2019
Revised: 8 March 2020
Accepted: 13 March 2020

KEYWORDS

Composite columns;
CFDST;
global stability;
confinement effect;
initial imperfection;
hollowness ratio

1. Introduction

In modern-day construction, concrete sandwiched double steel tubular column (CSDST) is preferred for enhancing the ductility and fire resistance properties in structural systems [3], [4], [5] in addition to the improved flexural rigidity. They also exhibit good structural performance under blast loads [6], [7]. Most of the research conducted towards the development of design framework for CSDST compares its behaviour with concrete filled steel tubes (CFST) considering the load transfer mechanism within the cross-section (Figure 1). Even though there is a visible similarity between these two cross-sections, apparent differences in the concrete confinement due to hollowness effect are confirmed through experiments [8], [9]. The existing literature has considerable experimental works on short column CSDST that lead to a reasonable quantification of the cross-section capacity [8]–[15]. However, experimental data available on long column CSDST are limited and inconclusive on its global stability aspects.

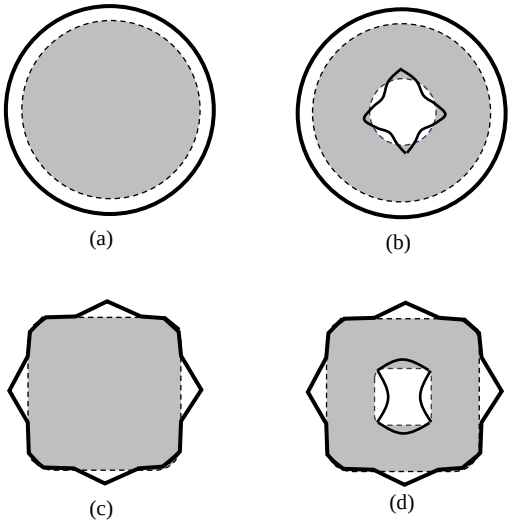

Fig. 1 Comparison of deformed CFST and CSDST cross-sections under axial compression. (a) CFST-circular; (b) CSDST-CC; (c) CFST-square; (d) CSDST-SS

Slender column CSDST specimens with inner and outer circular steel tubes (CSDST-CC) have been experimentally studied by Tao et al.[8], wherein only two numbers of specimens are axially loaded. The non-dimensional member slenderness (λ) of the specimens is around 0.66 and the concrete compressive strength is 46.3 N/mm^2. The code predictions (ANSI/AISC 360(16) and EN 1994-1-1 2004) are found to be marginally over-estimating the actual capacity of the specimens. Essopjee and Dundu [16] tested twenty two CSDST-CC columns in the slenderness range from 0.5 to 0.8, with concrete cube compressive strength around 30 N/mm^2. The test findings have shown EN 1994-1-1 (2004) (EC4) [1] curve *a* to be un-conservative for CSDST columns in inelastic buckling range and a modified column curve has been proposed [16] as shown in Figure 2. However, the proposed column strength curve is not applicable for slenderness region beyond the reported test data range. Romero et al. [4] conducted axial compressive tests on long column ($\lambda \approx 0.8$) CSDST-CC under ambient and elevated temperatures. The study finds the CSDST cross-section to be the most suitable choice for fire resistance, albeit the over estimation in the capacity prediction using EC4 under ambient conditions. The axial compressive tests have been conducted on CSDST with inner and outer square steel tubes (CSDST-SS) with hollowness and non-dimentional slenderness ratio around 0.35 and 0.75, respectively [17]. Unconservative axial capacity predictions have been observed on using ANSI/AISC 360(16) and EN 1994-1-1 (2004). The above experimental studies have reported the buckling strength of CSDST slender column as overpredicted by code provisions available for CFST. However, a comprehensive justification for the same is not found. Moreover, these studies have not evaluated the parameters that distincts CSDST from CFST like hollowness ratio etc. Further, these reported test data have not presented the initial imperfection condition of the specimens, which is an important factor for using the column curves in ANSI/AISC 360(16) and EN 1994-1-1 (2004), particularly for the inelastic region of column slenderness ($0.3 < \lambda < 1.4$) Galambos and Surovek [18].

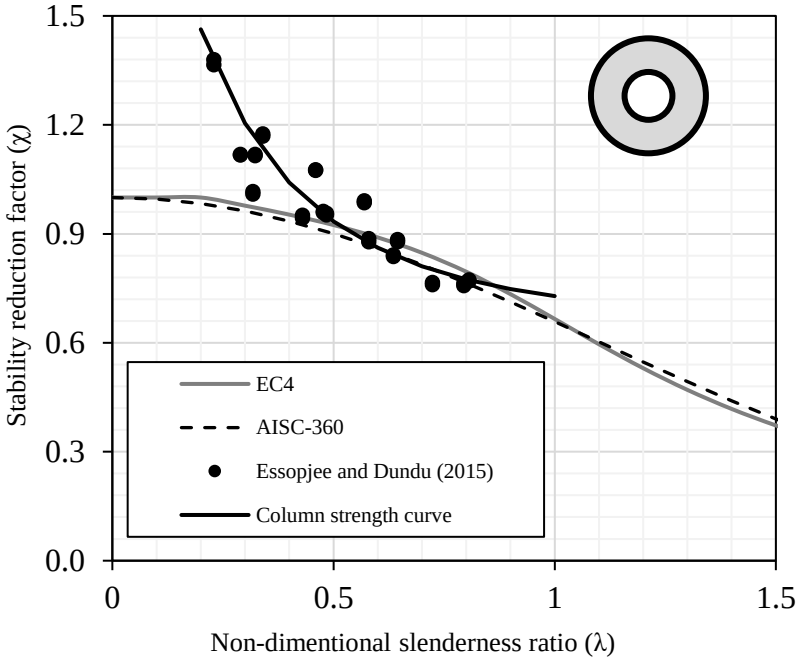

Fig 2 Comparison of long column CSDST test data from literature

The present research aims to expand the experimental database of CSDST slender columns in higher slenderness range (around unity), where the current literature is inadequate. Parameters that distincts CSDST from CFST cross-sections are selected for the study. In this paper, the axial compression test results of twelve CSDST and two CFST long columns with hollowness ratio as a primary parameter is presented. The shape of the steel tubes (square and circular) and concrete strength (normal and high strength) are selected as sub-set parameters in the experimental study. The test ultimate load is compared with the code equations (ANSI/AISC 360(16); EN 1994-1-1 2004) to examine the applicability of the current methods in the design of long column CSDST. The effective flexural rigidity (EI_{eff}) of the specimens that defines the member and system stability of the composite column is derived from the experimental results and presented here. The significance of inner steel tube in predicting the buckling capacity and effective flexural rigidity of CSDST long column is discussed through experimental findings.

2. Experimental program

2.1. Geometric and material properties of the specimens

The cross-section of fourteen specimens selected for the experimental study is widely divided based on the shape of the outer steel tube, as square and circular (Figure 3). They are in turn classified based on the hollowness ratio ($h_r = D_i/(D_o\text{-}2t_o)$) of the cross-sections, and the compressive strength of the infill concrete. The unique ID assigned for each specimen contains details about the parameters considered in the study, namely, the cross-section shape, hollowness ratio and concrete strength. The representation of the specimen ID is shown in Figure 3. Three types of hollowness ratios (h_r) are selected for CSDST specimens (0.2, 0.5 and 0.7). The maximum hollowness ratio is restricted to 0.7 due to practical difficulties in ensuring concrete flow through the annular space while concreting. The minimum value of 0.2 is selected based on the commercially available minimum dimension of the steel tube. The intermediate hollowness ratio of 0.5 is considered, as the effective axial stiffness of this cross-section is same as the corresponding CFST. Normal strength (40 N/mm^2) and high strength (80 N/mm^2) concrete are selected to understand the effect of concrete strength on the long column behaviour. Length of all test specimens is 3.6 m, and the cross-section dimensions are selected (Table 1) such that the non-dimensional member slenderness ratio (λ) will be around unity and specimens fail by global buckling. Compact cross-sections are selected, where $D/t < 0.15\,(E_s/f_y)$ for circular tubes, and $B/t < 2.26\sqrt{(E_s/f_y)}$ for square tubes, to avoid local and interaction buckling effects. The steel tubes have been manufactured by cold-rolling and cold-forming process and a finishing seam is developed by high frequency induction weld. As they are supplied in 6 m length, they are cut into the required length using an automated cutting blade, while ensuring a perpendicular plane of cut across the longitudinal axis of the steel tube. The actual dimensions measured from each steel tube is shown in Table 1.

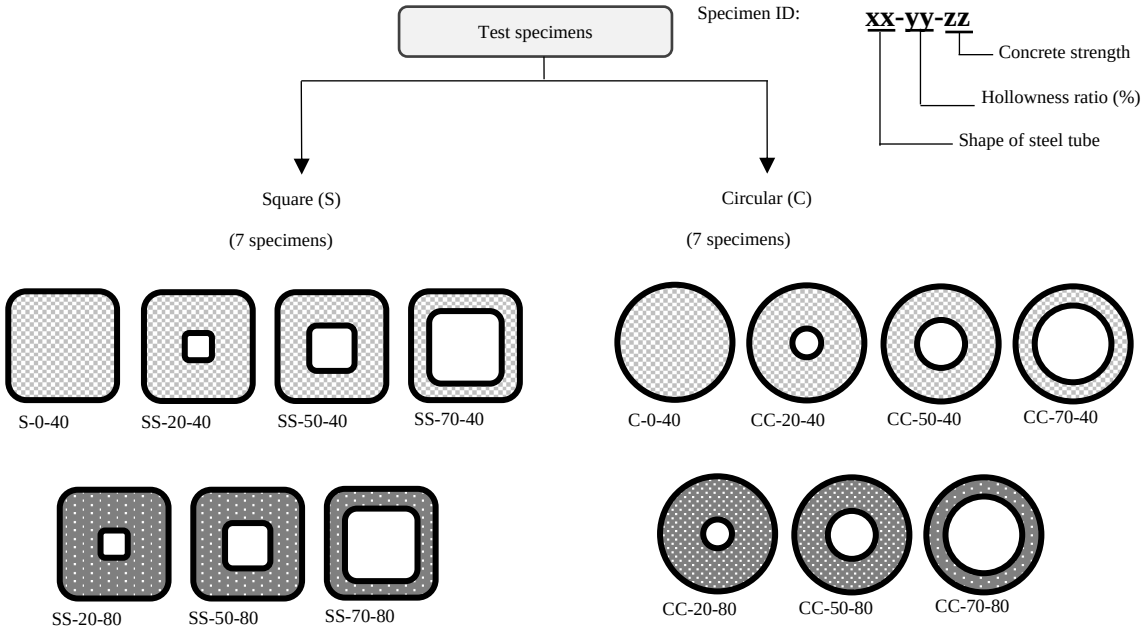

Fig 3 Classification of test specimens in the present study

Three numbers of tension coupons are prepared from each steel tube and tested as per ASTM-E8/E8M (2009) [19]. The yield strength of the steel tube, derieved from the coupon test, is well above the nominal strength of 310 N/mm^2, which is typical for cold-rolled and cold-formed steel. The tension coupon from circular steel tubes underwent a bending deformation along its length that is indicative of residual stress release, while cutting the steel tubes to make coupons. Since the total tensile load applied in the coupon test is inclusive of correcting this bending deformation, residual stresses are not measured separately. The average mechanical properties from the coupon test is presented in Table 2. The average modulus of elasticity and Poisson's ratio of the steel tubes is 2x10^5 MPa and 0.28, respectively.

Table 1
Geometric properties of steel tubes selected for the test

Sp. ID	Nominal size		Measured size				D_o/ t_o	D_i/ t_i
	Outer tube (mm)	Inner tube (mm)	D_o (mm)	t_o (mm)	D_i (mm)	t_i (mm)		
S-0-40	150x150x6	-	150	6.08	-	-	24.67	-
SS-20-40	150x150x6	32x32x2	150.65	6.16	32	2	24.46	16.00
SS-50-40	150x150x6	72x72x4	150.62	6.12	72.22	4	24.61	18.06
SS-70-40	150x150x6	100x100x4	149.88	6.08	100.3	4.06	24.65	24.71
SS-20-80	150x150x6	32x32x2	151.05	6.1	32	2	24.76	16.00
SS-50-80	150x150x6	72x72x4	150.35	6.14	72.52	3.96	24.49	18.31
SS-70-80	150x150x6	100x100x4	149.98	6.08	100.3	3.94	24.67	25.46
C-0-40	NB-150x5.4	-	166.06	5.18	-	-	32.06	-
CC-20-40	NB-150x5.4	NB-25x4	166.34	5.24	33.7	4	31.74	8.43
CC-50-40	NB-150x5.4	NB-65x3.6	166	5.04	76.66	3.58	32.94	21.41
CC-70-40	NB-150x5.4	NB-100x5.4	165.84	5.06	114.1	5.2	32.77	21.94
CC-20-80	NB-150x5.4	NB-25x4	166.36	5.22	33.7	4	31.87	8.43
CC-50-80	NB-150x5.4	NB-65x3.6	165.86	5.24	76.74	3.58	31.65	21.44
CC-70-80	NB-150x5.4	NB-100x5.4	166.32	5.24	114.2	5.22	31.74	21.88

Self-compacting concrete having a slump value of around 600 – 700 mm (from concrete flow test) is used for filling the steel tubes. Steel tubes are taken to a ready mix concrete plant for concreting due to logistical constraints. Normal and high strength concrete mix is designed for 40 N/mm^2 and 80 N/mm^2 respectively, and the mix design quantities of concrete ingredients is tabulated in Appendix-I. Separate batches of concrete is prepared for filling each specimen, and three sets of 150 mm concrete cubes are cast from each batch for material characterization. The compressive strength of the concrete cube is tested as per IS:516 (1959) [20] (Indian Standard that is in line with BSI and ASTM standards) on 28-day and on the day of testing, which are found to be almost the same. The mean compressive strength of concrete on the day of testing for the respective specimens is presented in Table 2. Typical nominal coarse aggregate size used for concreting is 12 mm, except for CSDST with 70% hollowness, where 6 mm is used to facilitate free flow while concreting.

Table 2
Mechanical properties of steel and concrete used in the test specimens

Sp. ID	f_{yo} (N/mm^2)	f_{yi} (N/mm^2)	f_{uo} (N/mm^2)	f_{ui} (N/mm^2)	f_{ck} N/mm^2
S-0-40	401	-	445	-	51.28
SS-20-40	400	400	445	450	51.28
SS-50-40	400	400	440	450	54.83
SS-70-40	405	400	430	450	57.5
SS-20-80	400	400	450	450	89.02
SS-50-80	390	400	430	450	84.95
SS-70-80	390	400	428	450	87.25
C-0-40	522	-	581	-	58.61
CC-20-40	523	519	570	561	57.94
CC-50-40	518	521	550	561	55.5
CC-70-40	521	520	560	561	60.61
CC-20-80	523	519	568	561	84.95
CC-50-80	519	520	560	561	85.47
CC-70-80	519	520	551	561	84.36

2.2. Preparation of test specimens

After the steel tubes are cut for the required length, one end of the outer steel tube (for each specimen) is welded (fillet type) to a 20 mm thick mild steel base plate, ensuring the perpendicularity between the tube and the base plate. The initial imperfection profile of the outer steel tube is measured by placing it on a lathe bed that has an accurate horizontal orientation. The imperfections are measured using a laser beam arrangement at an interval of 100 mm along the length of the specimen, and they are found to be mostly localized with a maximum offset of 2 mm. Since the problem at hand is sensitive for global imperfections, a moving average of the measured imperfections is presented in Figure 4 that represents the initial global profile of the outer steel tube. Typical global imperfection profile of a square and circular steel tube is given in Figure 4, with a maximum bow in the order of *L*/7000. The outer steel tube profile represents the initial overall profile of the test specimen.

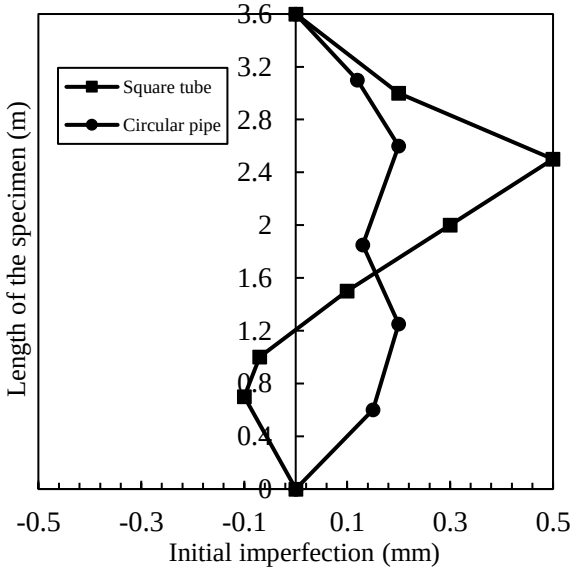

Fig. 4 Initial imperfection in the steel tubes

In CSDST specimen preparation, to ensure the concentricity between the inner and outer steel tubes during concreting, the inner steel tube is welded to steel spacer bars at both ends of the specimen (Figure 5). At the concreting end of the specimen, hollow space in the inner steel tube is covered to avoid accidental intrusion of concrete. Specimens are concreted from the top in upright position at the ready mix concrete plant (Figure 6). All specimens except SS-70-40 are successfully filled with concrete. The inner steel tube orientation in SS-70-40 is slightly disturbed while concreting, and the annular space became insufficient for a smooth concrete flow. The specimens are kept in the plant for two days, until complete hardening of concrete, and later shifted to Structural Engineering Laboratory, IIT Madras. The specimens are allowed to air cure for 28 days along with their respective concrete cubes. Towards the end of the curing period, the specimens are prepared for the testing process. The concreted end of the specimen is inspected for concrete shrinkage. The excess concrete at the tube edge is removed, and cement-sand mortar in the ratio of 1:1 is applied to even out the undulations. The specimen end prepared with mortar is fillet-welded to a 20 mm mild steel plate, similar to the other end. The surface of the outer steel tube is cleaned thoroughly before testing and strain gauges are pasted at locations specified in the instrumentation scheme (Figure 9).

Fig. 5 Inner steel tubes with spacer bars and dummied concreting end

Fig. 6 Concreting of the specimens

2.3. Test set-up, instrumentation and loading

Axial compression test is conducted in a 6000 kN self-equilibriating testing frame, and specimens are loaded using a 5000 kN hydraulic jack. Even though the set-up is load-controlled in nature, behaviour of the specimen beyond the ultimate load could be measured by manual control of the machine, for few points in the post-peak range. The schematic diagram of the test set-up is shown in Figure 7. The test specimens are fillet-welded to mild steel plates of size 250×300×20 mm on both the ends, to ensure uniform distribution of axial load across the cross-section. Pin-pin boundary condition is designed for the test set-up by fabricating roller bar and tapered plates arrangement as shown in the schematic diagram (Figure 7). Buckling of the specimen is constrained to single axis of cross-section by providing a roller bar as hinge supports. Before mounting the specimen, roller bars are applied with grease to avoid load losses due to friction (Figure 8). Sufficiently thick steel end plates (60 mm) with higher grade (EN8) is chosen to reduce end plate deformation upon load transfer.

Linear variable displacement transducers (LVDTs) and linear strain gauges are used for measuring the specimen deformation under loaded condition. Since the specimen buckling is constrained to single axis, instrumentation is located in the allowable buckling plane alone. Two numbers of LVDTs to measure axial deformation and three numbers of LVDTs for measuring lateral displacement are placed at the locations as indicated in Figure 9(a). Strain gauges are pasted on either faces of the specimen across the buckling axis at the mid-height to measure longitudinal as well as circumferencial strains (Figure 9b). Linear strain gauges are also pasted in the longitudinal axis of inner steel tube, to study a probable non-composite action between the steel tubes in CSDST. A 5000 kN load cell is placed as shown in the test set-up, and it is synced with LVDT and strain gauge readings. The instrumentation is connected to a data logger for continuous recording of measurements. The specimens are axially compressed by the hydraulic jack till they undergo a complete buckling failure. A typical failure mode of the test specimens is presented in the photograph of a representative specimen (Figure 10). Specimens are failed by global buckling under axial compression, as expected in the pre-processing of this experimental study. The failure mode of the specimen is compared with its corresponding initial configuration before loading (Figure 10a). The deformed configuration of the specimen shows smooth rotation at the pin ends (i.e. no frictional load losses at the pin supports).

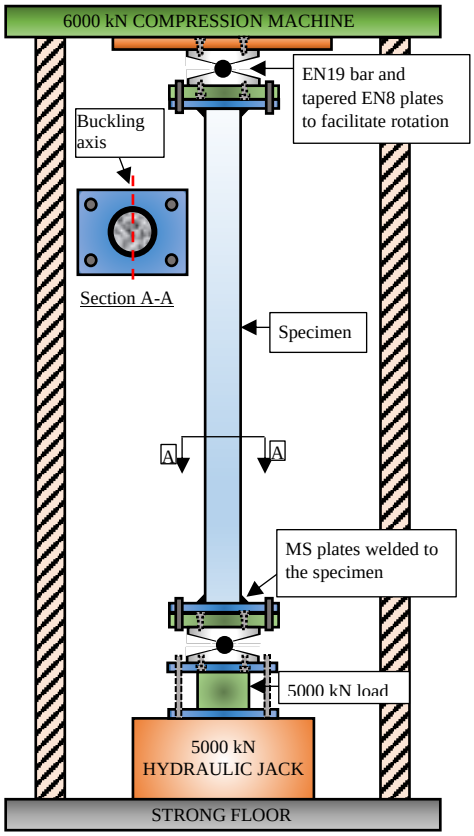

Fig 7 Schematic diagram of the test set-up

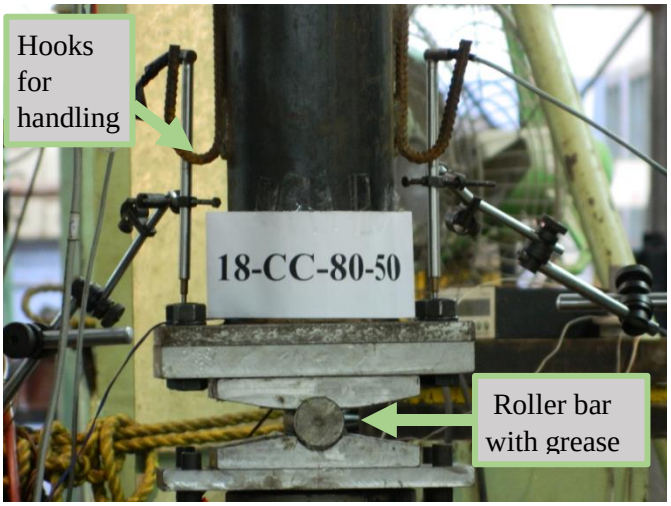

Fig 8 Arrangement of pinned boundary condition

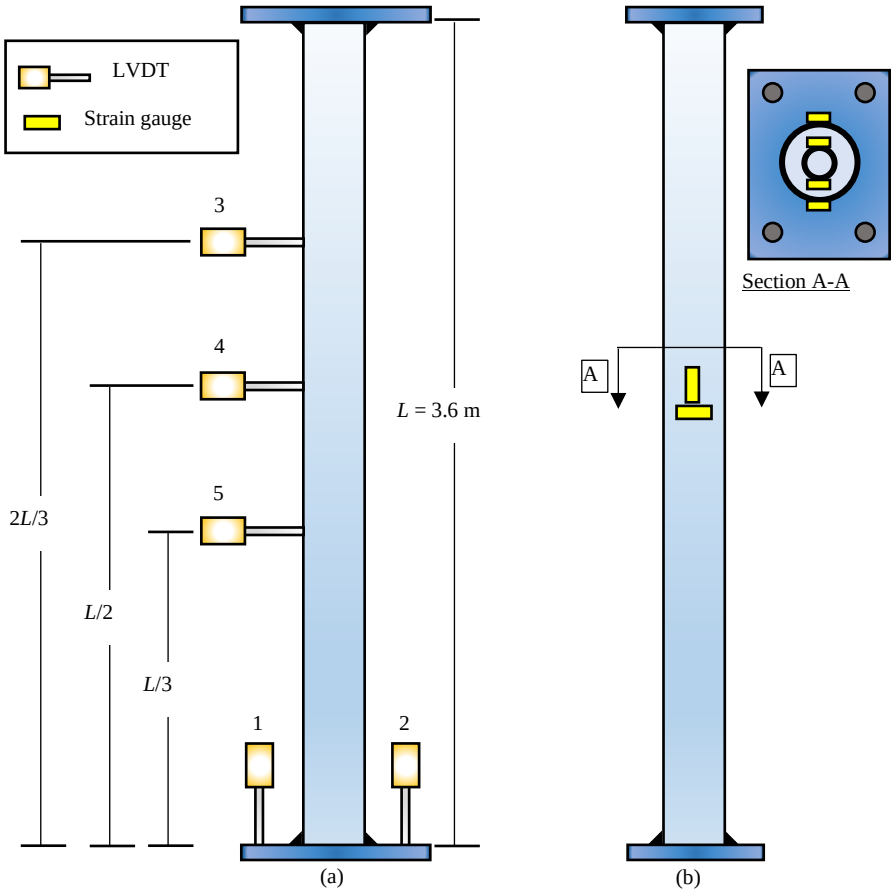

Fig 9 Location of LVDTs and strain gauges. (a) Elevation (b) Side view

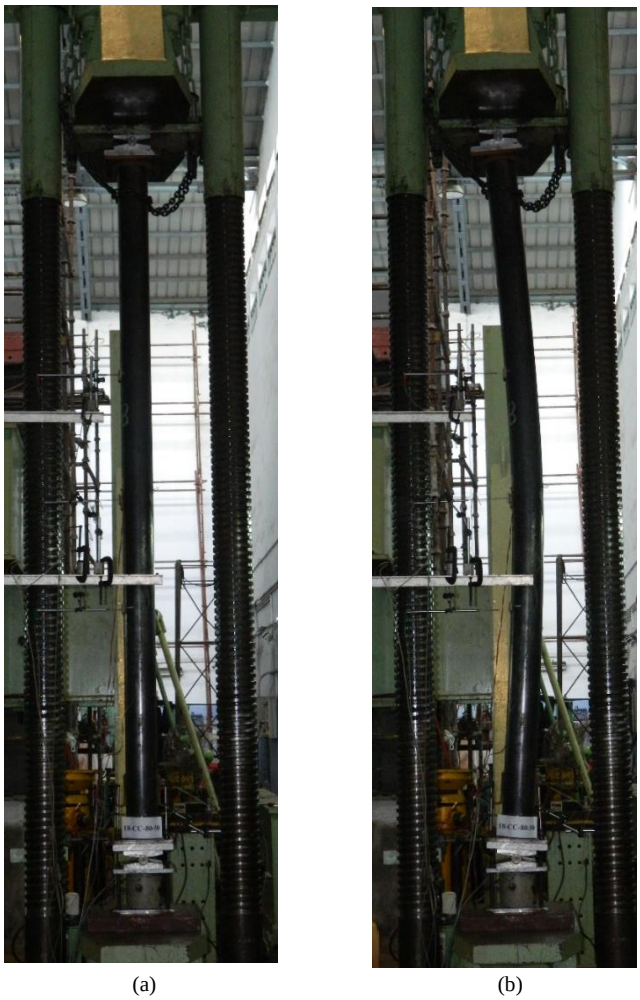

Fig. 10 Typical failure mode in the test specimen. (a) Initial configuration (b) Deformed configuration

3. Test results and discussions

3.1. Axial compressive strength

The maximum axial compressive strength of the test specimens found from the experiment (P_{test}) is shown in Table 3. It is lesser than their corresponding superposed strength (P_{sum}) due to instability in the member at failure. The stability reduction factor that are specified for CFST design as per EN 1994-1-1 (2004) and ANSI/AISC 360(16) is modified for CSDST cross-sections in Eqs. (3 – 7) and Eqs. (8 – 10), respectively. In Table 3, the instability effect from the test (χ_{test}) is compared with code-based predictions, namely χ_{EC4} and $\chi_{AISC\text{-}360}$. The actual instability in the test is lesser than the code predictions. Consequentially, the test axial capacities are higher than code-based capacity predictions as shown in Table 3. This comparison is also presented in Figure 11, along with the literature test data for CSDST [4], [8], [16]. The present experimental data extends the available test database for CSDST in the higher slenderness range, which is useful in the study of column instability.

Table 3
Test axial strength compared with AISC-360(16) and EC4 capacity predictions

Sp. ID	P_{test} (kN)	P_{sum} (kN)	P_{EC4} (kN)	P_{AISC} (kN)	P_{EC4}/P_{test}	P_{AISC}/P_{test}	χ_{test}	χ_{EC4}	χ_{AISC}
S-0-40	1801	2183	1494	1420	0.83	0.79	0.83	0.68	0.69
SS-20-40	1694	2263	1540	1470	0.91	0.87	0.75	0.68	0.68
SS-50-40	1750	2463	1635	1582	0.93	0.90	0.71	0.98	0.67
SS-70-40	1568	2291	1594	1546	1.02	0.99	0.68	0.69	0.70
SS-20-80	1901	2811	1733	1675	0.91	0.88	0.68	0.62	0.64
SS-50-80	1998	2754	1739	1689	0.87	0.85	0.73	0.63	0.65
SS-70-80	1959	2596	1726	1670	0.88	0.85	0.75	0.66	0.67
C-0-40	1726	2259	1292	1305	0.75	0.76	0.76	0.57	0.60
CC-20-40	1557	2424	1335	1360	0.86	0.87	0.64	0.55	0.58
CC-50-40	1771	2392	1326	1351	0.75	0.76	0.74	0.55	0.58
CC-70-40	1803	2684	1491	1522	0.83	0.84	0.67	0.56	0.58
CC-20-80	1496	2813	1422	1467	0.95	0.98	0.53	0.51	0.55
CC-50-80	1705	2781	1438	1481	0.84	0.87	0.61	0.52	0.55
CC-70-80	1899	2900	1574	1612	0.83	0.85	0.65	0.54	0.57

$$P_u = \chi P_{sum} \tag{1}$$

$$P_{sum} = A_{so} f_{yo} + A_{si} f_{yi} + A_c \left(0.8 f_{cm}\right) \tag{2}$$

3.1.1. EN 1994-1-1 (2004) based instability factor

$$\chi_{EC4} = \frac{1}{\phi + \sqrt{\phi^2 - \lambda^2}} \tag{3}$$

where, $\phi = 0.5\left[1 + \alpha\left(\lambda - 0.2\right) + \lambda^2\right]$ (4)

$$\lambda_{EC4} = \sqrt{\frac{P_{sum}}{P_{cr,EC4}}} \tag{5}$$

$$P_{cr,EC4} = \frac{\pi^2 EI_{eff,EC4}}{L_{eff}^2} \tag{6}$$

$$EI_{eff,EC4} = E_{so} I_{so} + E_{si} I_{si} + 0.6 E_c I_c \tag{7}$$

3.1.2. ANSI/AISC 360(16) based instability factor

$$\chi_{AISC-360} = \left(0.658\right)^{\lambda_{AISC}^2} \quad \text{for, } \lambda_{AISC} \le 1.5 \tag{8}$$

$$\lambda_{AISC} = \sqrt{\frac{P_{sum}}{P_{cr,AISC}}} \tag{9}$$

$$P_{cr,AISC} = \frac{\pi^2 EI_{eff,AISC}}{L_{eff}^2} \tag{10}$$

$$EI_{eff,AISC} = E_{so} I_{so} + E_{si} I_{si} + C_3 E_c I_c \tag{11}$$

$$C_3 = 0.45 + 3\left(\frac{A_{so} + A_{si}}{A_g}\right) \le 0.9 \tag{12}$$

$$\chi_{test} = \frac{P_{test}}{P_{sum}} \tag{13}$$

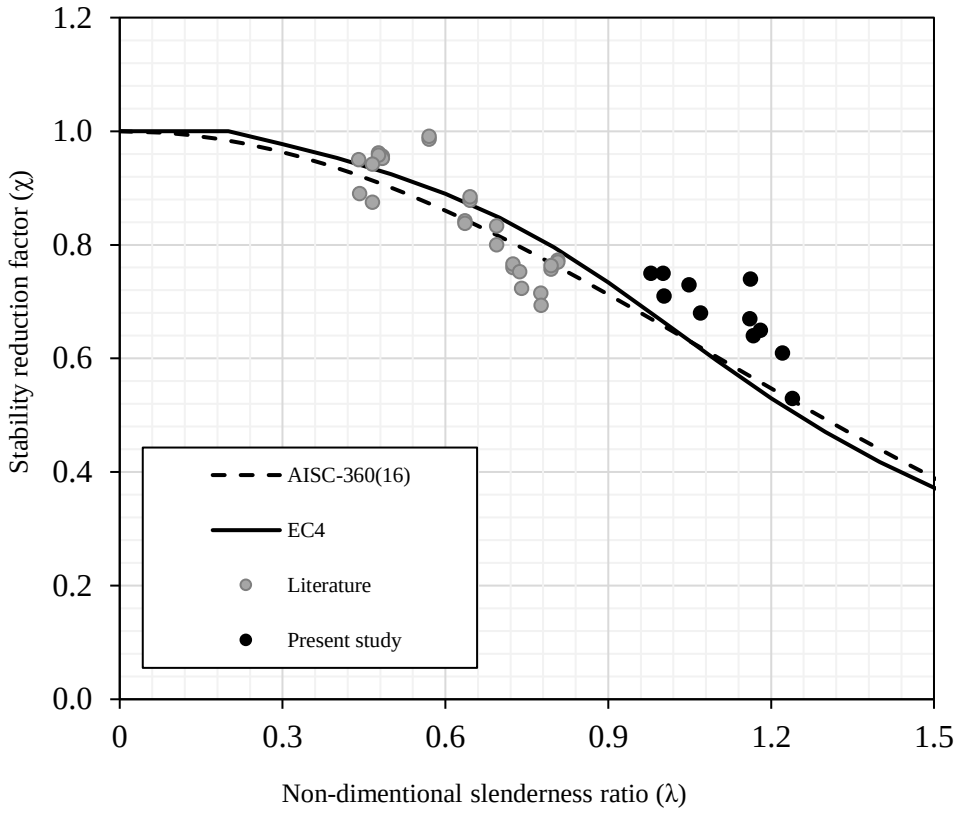

Fig. 11 Comparison of test capacities and code predictions

Over-strength is observed in the test axial capacity (P_{test}) of the specimens when compared to code based equations. Square specimens have an average over-strength of 12% except SS-70-40 that had concreting issues. Circular specimens have an average over strength of 25 % for normal strength, and 15% for high strength concrete. Over-strength in the buckling capacity of CFST has also been observed in few other test data reported in literature, like Han [21], Perea [22] and Xiong et al. [23]. Han [21] has regarded the axial capacity prediction by code recommendations as conservative, and thereby higher reliability is marked for these predictions An et al. [24]. Perea et al. [22], [25] and Xiong et al. [23] have reported frictional resistance at the supports as the reason for over-strength in test capacities, and corrections are made in the raw data. Perceiving these reports, the friction resistance at the supports are minimized in the present experiment by applying grease in the roller bar. In spite of it, the over-strength is found in the tests. The magnitude of initial imperfection in the test specimens is $L/7000$, and it is very low compared to the initial imperfections ($L/1000$ or $L/1500$) assumed in the development of code equations [1], [2]. This disparity makes the code-based capacity predictions significantly conservative. The magnitude and shape of the initial imperfection profile is crucial in undertanding the long column behaviour of concrete filled steel tubes, unlike slender hollow steel tubes whose failure load is always less than the critical buckling load Galambos and Surovek [18]. The associated concrete confinement effect is one of the factors for the increase in the axial capacity of test specimens. This effect is discussed in following sections using the axial and circumferential strains measured during the test.

3.2. Experimental behaviour curves

3.2.1. Axial compressive load – axial deformation curves

A typical axial load versus axial shortening curve of the test specimens is shown in Figure 12. The axial deformations measured from LVDT-1 and LVDT-2 are the same untill the specimen undergoes buckling. At the ultimate point, the plots diverge due to rotation of the end plate. The compression side shows larger shortening and the tension side shows unloading. The actual axial shortening in the specimen is the average of these two values, which has negligible rate of increase beyond the ultimate load. Even though, the compression testing machine is load-controlled, few points beyond ultimate is recorded through manual operation as mentioned before. This is the reason why the axial deformation in the specimen remains constant beyond ultimate load point. Axial shortening (Δ) of the test specimens at the ultimate load point is reported in Table 4.

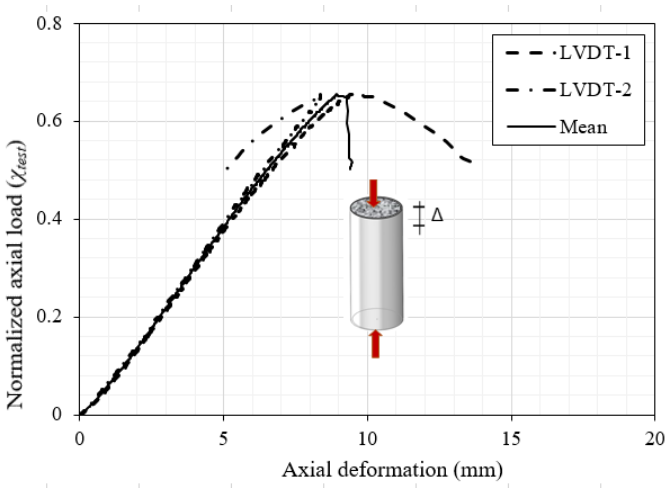

Fig 12 Typical axial deformation behaviour of test specimens

3.2.2. Axial compressive load – lateral deflection curves

The axial load versus lateral displacements measured at the mid-height of the specimens is presented in Figures 13 (a – b). The axial loading (y-axis) is normalized with respect to the corresponding cross-section strength (P_{sum}) of the specimens. Since the concrete strength in these specimens are not exactly the same, absolute load plot does not make a meaningful comparison, so therefore, the values are normalized. The normalized axial load in the plots is in fact the stability reduction factor from the tests (χ_{test}). This factor is higher compared to the corresponding code provisions ($\chi_{AISC\text{-}360}$, χ_{EC4}) (Table 3), indicating over-strength in the test results. The χ_{test} value for high strength concrete is lesser compared to normal strength concrete in both square and circular specimens. It is obvious as the instability of the specimen increases with high strength concrete filling, and this effect could be captured in the present strength equations used for long column design [1], [2]. Hollowness ratio is a major parameter that has significant effect in the buckling of CSDST, especially in circular cross-section. The χ_{test} value in CSDST is lesser compared to CFST both in square as well as circular cross-sections. Further,

the instability is observed to be the least for CSDST specimens with 20% hollowness. The reasons for higher instability in CSDST are inferred as, (i) increase in the non-dimensional slenderness ratio (λ), (ii) increase in the unavoidable initial imperfections compared to an equivalent CFST (due to practical difficulties in developing perfect concentricity between the inner and outer steel tubes). (iii) The inner steel tube is located in low stress zone of the cross-section and therefore it is contributing less in buckling resistance. Therefore, eventhough the present design methods [1], [2] have predicted the axial capacity of test specimens conservatively, their effective flexural rigidity has to be studied to understand the significance of inner steel tube in global buckling resistance.

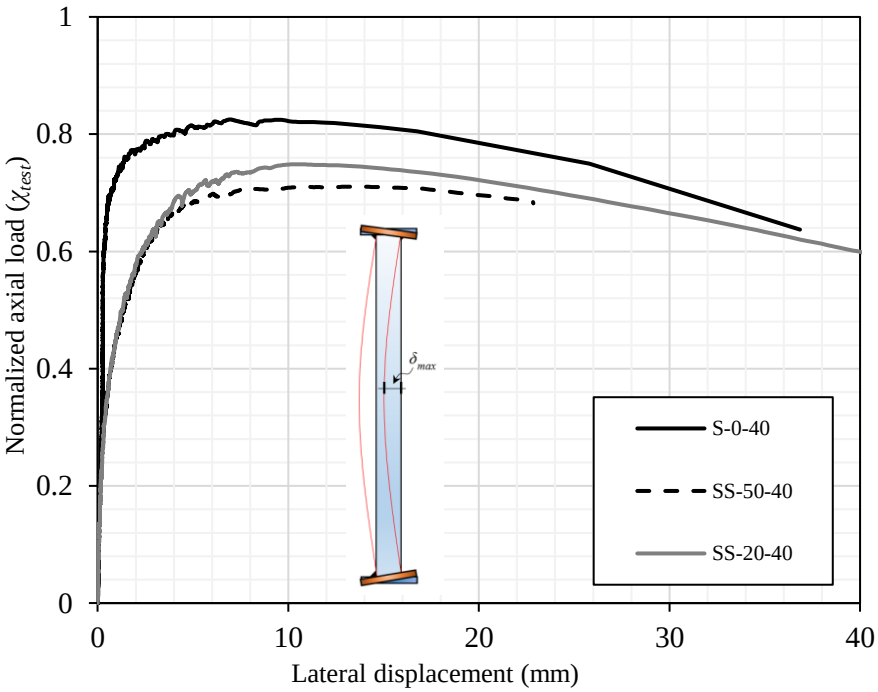

(a) Square specimens with normal strength concrete

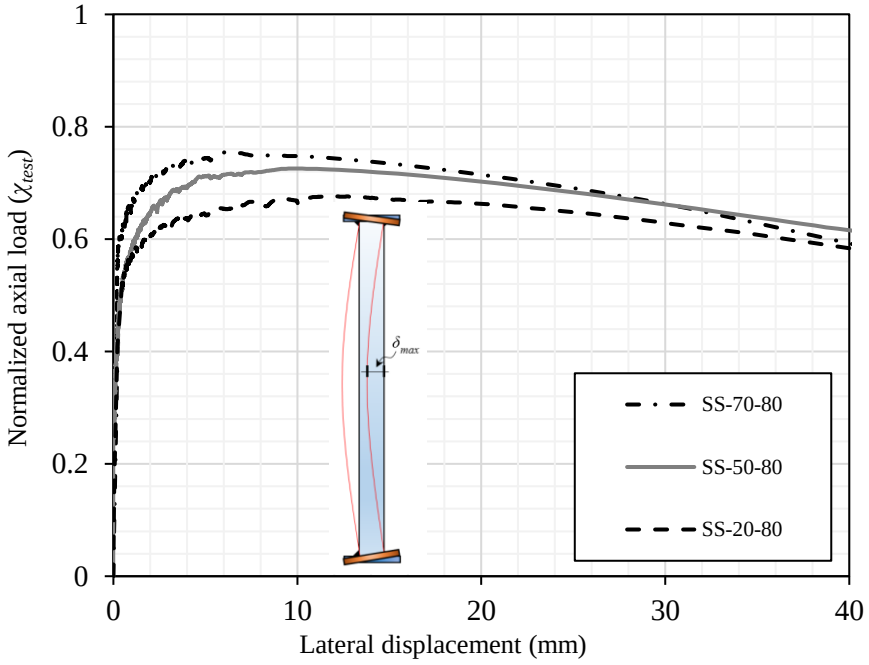

(b) Square specimens with high strength concrete

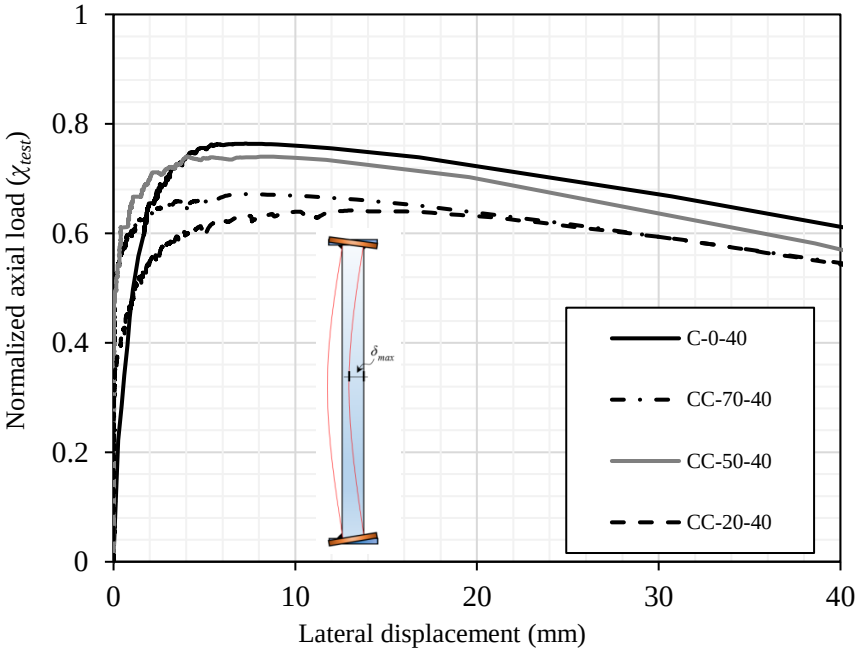

(c) Circular specimens with normal strength concrete

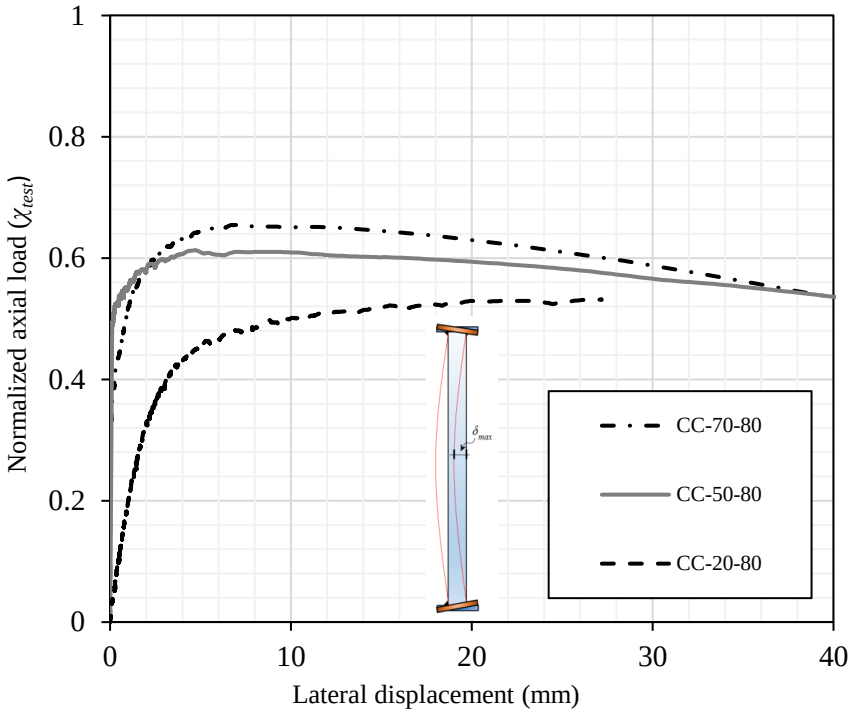

(d) Circular specimens with high strength concrete

Fig.13 Axial compressive loading versus mid-height lateral deflection

3.2.3. Axial compressive load – axial and circumferential strain curves

The plots of axial load versus longitudinal (l) and circumferential (c) strains in the test specimens is presented in Figures 14 (a – d). The behaviour of the test specimens is linear upto 80% of the peak load. Development of non-linearlity in the behaviour is found for longitudinal strain values beyond the non-proportional limit of steel material. The maximum strain in the specimens at the ultimate load point is greater than 2000 μ (Table 4), whereas, the maximum strain at proportional limit in the material characterization of steel is found to be around 1700 μ. This indicates an inelastic buckling failure, and it is the expected mode of failure for steel columns with non-dimensional slenderness (λ) between 0.3 and 1.4 [18]. The load drops suddenly after reaching the peak load and it indicates the buckling mode of failure in the test specimens. The longitudinal ($\varepsilon_{o,h}$) and circumferential strains ($\varepsilon_{o,l}$) measured from the most compressed fiber of the specimen at the ultimate load is reported in Table 4. The longitudinal strains measured in the inner steel tubes is also shown in Table 4. The $\varepsilon_{i,long}$ values are lesser than their corresponding outer steel tubes, which confirms the composite action within the cross-section, and simultaneous buckling failure of the inner and outer steel tubes. The ratio of hoop strain to longitudinal strain in the outer steel tube (v_o) at the ultimate load (Table 4) is consistently higher than the average Poisson's ratio of 0.28 measured in the tension coupon test. A substantial lateral pressure due to interaction between the infilled concrete and the outer steel tubes (i.e. concrete confinement) is considered as the reason for increased strain ratios, which has incurred over-strength in the test specimens. This signifies the effect of column initial imperfections on the buckling capacity of concrete filled steel tubes, and the presence of concrete confinement in slender columns with very low initial imperfections.

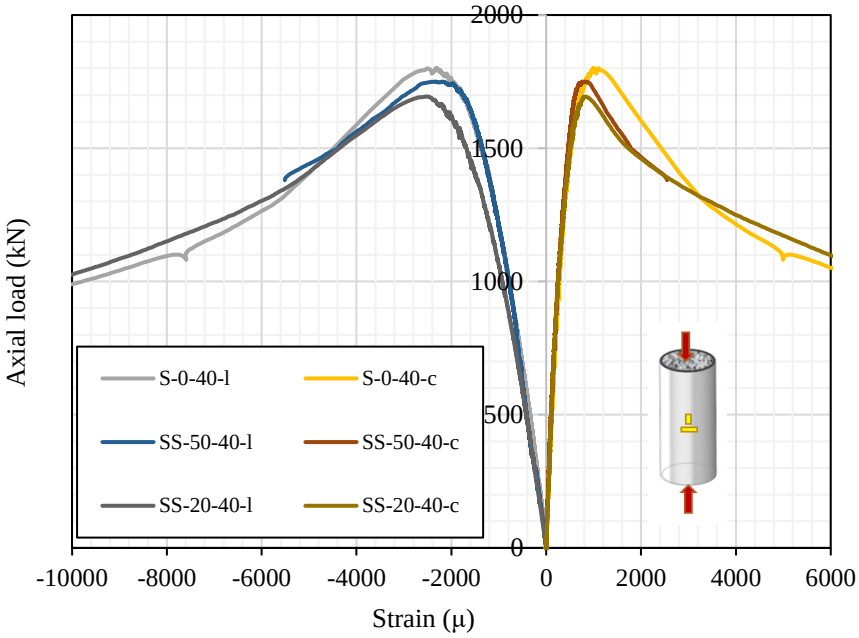

(a) Square specimens with normal strength concrete

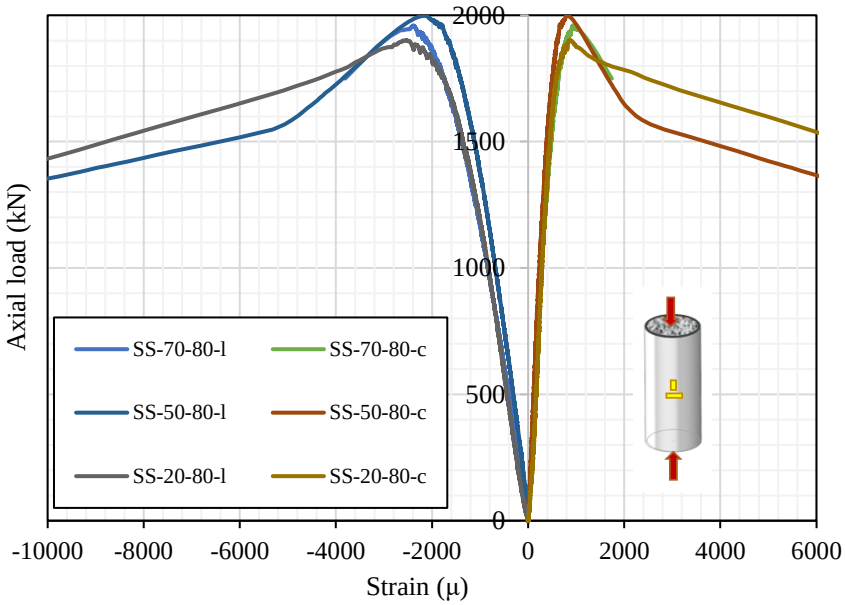

(b) Square specimens with high strength concrete

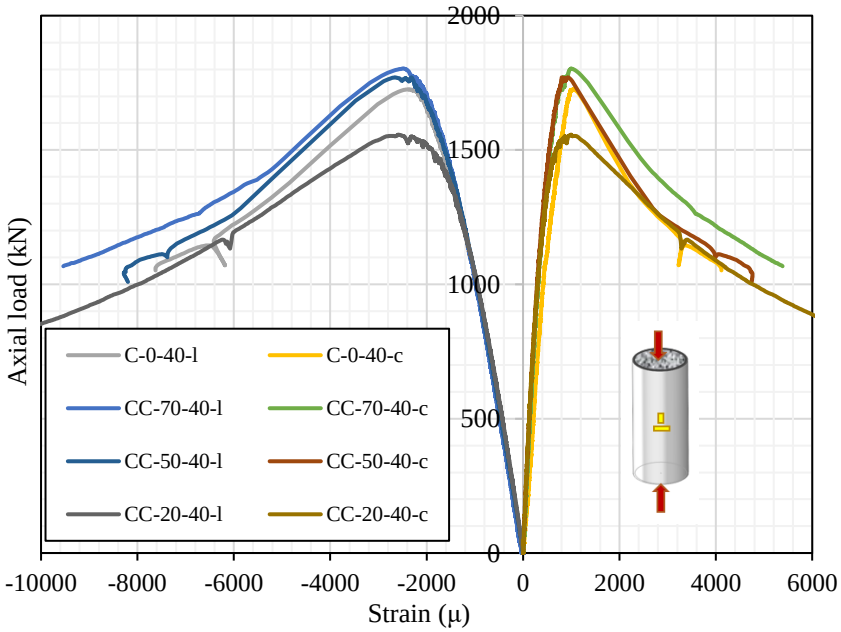

(c) Circular specimens with normal strength concrete

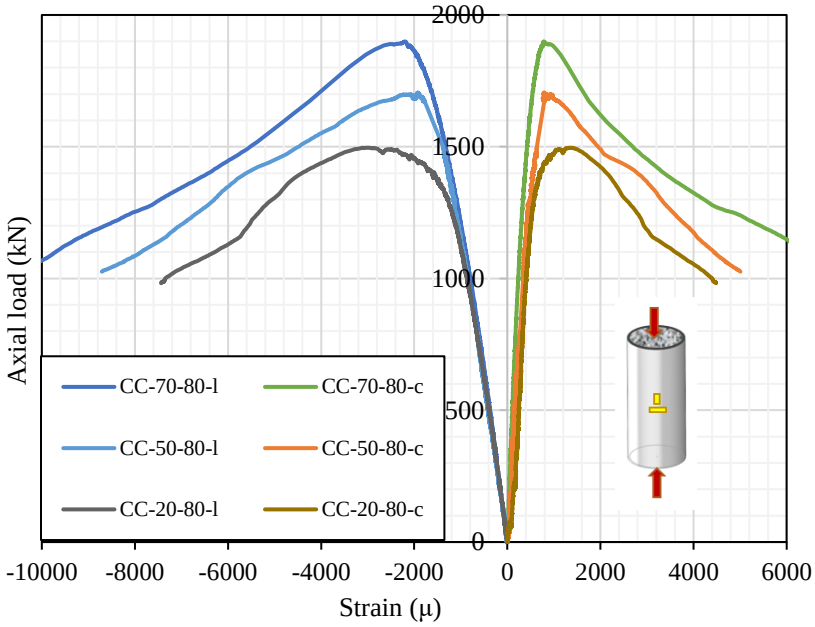

(d) Circular specimens with high strength concrete

Fig. 14 Axial load versus strain curves

Table 4
Maximum strain, axial shortening and lateral deflection at the ultimate load

Sp. ID	P_{test} (kN)	$\varepsilon_{o,long}$ (μ)	$\varepsilon_{i,long}$ (μ)	$\varepsilon_{o,circum}$ (μ)	ν_o	Δ_{ax} (mm)	δ_{lat} (mm)
S-0-40	1801	2315	NA	1003	0.4	9.2	7.0
SS-20-40	1694	2506	1768	807	0.32	7.22	10.36
SS-50-40	1750	2189	1821	764	0.35	8.00	11.01
SS-70-40	1568	2261	2164	855	0.38	6.47	12.05
SS-20-80	1901	2522	2049	867	0.34	8.65	11.87
SS-50-80	1998	2161	1881	818	0.38	8.51	10.59
SS-70-80	1959	2379	2372	925	0.39	8.79	6.09
C-0-40	1726	2370	-	1044	0.44	9.15	7.54
CC-20-40	1557	2590	1337	994	0.38	7.10	13.44
CC-50-40	1771	2244	2046	805	0.36	9.43	4.59
CC-70-40	1803	2490	2330	1003	0.40	8.72	7.46
CC-20-80	1496	3008	-	1351	0.4	7.1	27.2
CC-50-80	1705	1932	1795	787	0.41	7.47	4.71
CC-70-80	1899	2211	1899	788	0.36	8.92	7.18

3.3. Effective flexural rigidity (EI_{eff})

The effective flexural rigidity of the test specimens is derived from the experimental results using Euler-Bernoulli beam theory. This theory is applicable till the ultimate load point, where $\delta_{lat} < 0.01L$ (i.e. small deflection,), beyond which the lateral deflections are large. The bending moment at the mid-height of the specimen due to lateral deflection ($M = P\delta$) and the curvature developed (φ) is plotted to find EI_{eff}. A representative plot (for circular specimens with normal strength concrete) is presented in Figure 15. In the previous section, the suitability of adopting the existing design principles specified for CFST long columns [1], [2] to CSDST is checked by comparing the axial capacities from the test. The predictions are found to be conservative for the selected cross-sections. However, the degree of conservativeness is lesser for specimens with low hollowness ratio. This phenomenon is further clarified by comparing the effective flexural rigidity of the specimens from test and code-based predictions, as shown in Table 5. The EI_{eff} from the tests is lesser compared to the code equations since the specimens have failed by inelastic buckling, and reduced stiffness modulus is obtained from the M-φ plots. The mean and standard deviation of EI_{eff} ratio using EC4 is 0.77 and 0.1, whereas, AISC-360 gives 0.69 and 0.08 for square cross-section. In circular specimens, the mean and standard deviation of EI_{eff} ratio is 0.93 and 0.1 using EC4, and AISC-360 gives 0.81 and 0.09. This level of accuracy in EI_{eff} prediction is considered to be acceptable as per design standards [25]. However, the EI_{eff} of CSDST with 20% hollowness is consistently below average, and therefore, the reliability of code-based design equations will be less for CSDST with low hollowness ratio. The normalized EI_{eff} of CSDST specimens with respect to the values of CFST is given in Table 5. It shows that the flexural rigidity and buckling resistance of CSDST columns with smaller hollowness (less than 50%) is relatively low.

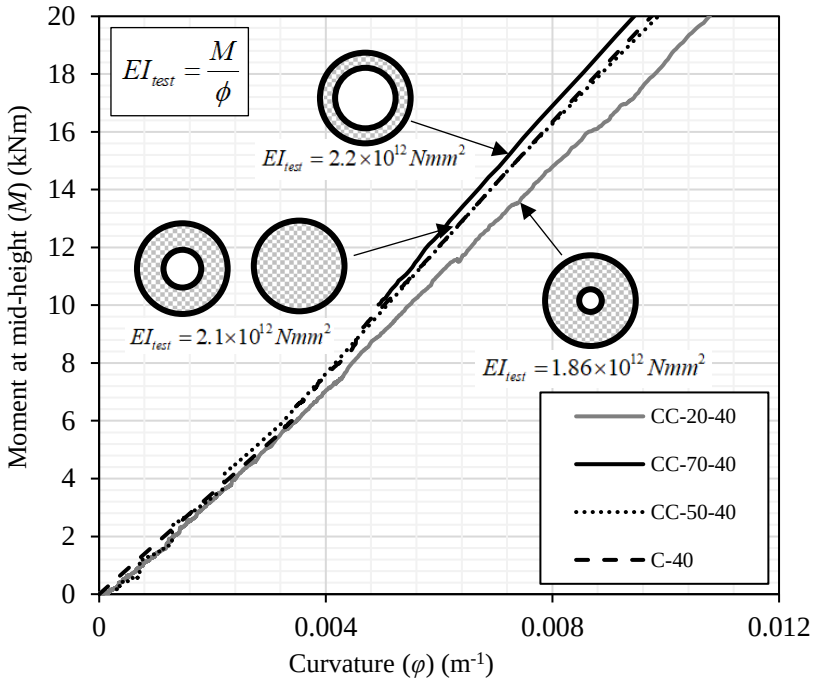

Fig. 15 Moment versus curvature plots

Table 5
Comparison of effective flexural rigidity from test and code equations

Sp. ID	EI_{test} (10^{12} N mm^2)	EI_{EC4} (10^{12} N mm^2)	EI_{AISC} (10^{12} N mm^2)	EI_{test}/EI_{EC4}	EI_{test}/EI_{AISC}	Normalized EI_{test}
S-0-40	2.22	3.03	3.35	0.73	0.66	1.00
SS-20-40	1.90	3.10	3.43	0.61	0.55	**0.86**
SS-50-40	2.63	3.22	3.54	0.82	0.74	1.18
SS-70-40	-	3.29	3.45	-	-	-
SS-20-80	2.50	3.22	3.75	0.78	0.67	**0.94**
SS-50-80	3.00	3.29	3.75	0.91	0.80	1.13
SS-70-80	2.65	3.40	3.76	0.78	0.70	1.00
			Mean	0.77	0.69	
			Std dev	0.10	0.08	
C-0-40	2.10	2.30	2.56	0.91	0.82	1.00
CC-20-40	1.86	2.34	2.66	0.80	0.70	**0.89**
CC-50-40	2.10	2.33	2.64	0.90	0.79	1.00
CC-70-40	2.20	2.62	2.87	0.84	0.77	1.05
CC-20-80	2.22	2.40	2.85	0.92	0.78	**0.74**
CC-50-80	2.50	2.45	2.89	1.02	0.86	0.83
CC-70-80	3.00	2.74	3.07	1.10	0.98	1.00
			Mean	0.93	0.81	
			Std dev	0.10	0.09	

4. Summary and conclusions

The global stability of concrete sandwiched double steel tubular columns (CSDST) is investigated by conducting axial compression tests. Twelve CSDST and two CFST long column specimens ($\lambda \approx 1$) are tested with hollowness ratio as the primary parameter. Shape of steel tubes and concrete strength are secondary parameters for the experimental study. Three types of hollowness are selected for CSDST specimens, namely, 20%, 50% and 70%. Square and circular shapes are considered for the outer and inner steel tubes. Normal and high strength concrete of 40 N/mm^2 and 80 N/mm^2 respectively are selected as the in-fill. The behaviour of CSDST specimens are comparatively studied with CFST. The applicability of design equations specified for long column CFST in ANSI/AISC 360(16) and EN 1994-1-1 (2004) to CSDST column design is quantified and reported. The salient conclusions from the study are enumerated as below.

- The buckling capacity of CSDST is found to be lesser than an equivalent CFST long column specimen. The reasons are; (i) non-dimensional slenderness ratio (λ) of CSDST is higher than CFST for the same *L*/*D*, (ii) the degree of initial imperfections in CSDST is larger than CFST due to unavoidable error in the concentricity of inner and outer steel tubes, and (iii) the contribution of flexural rigidity provided by the inner steel tube is lesser than the theoretical predictions.
- The global instability of CSDST columns is inversely related to the hollowness ratio of the cross-section. This phenomenon is observed in both square as well as circular cross-sections irrespective of the sandwiched concrete strength.
- The test axial capacity of the specimens is greater than the ANSI/AISC 360(16) and EN 1994-1-1 (2004) based strength predictions. The average degree of conservativeness in the code predictions is 12% and 20% for square and circular specimens, respectively. Low initial imperfection in the steel tubes and concrete confinement have increased the test specimen capacity.
- Effective flexural rigidity (EI_{eff}) derived from the experimental results is in good agreement with the code-based predictions except for CSDST with 20% hollowness. It enunciates the inverse relation of column instability and hollowness ratio in CSDST.
- The long column axial capacity equations for CFST in ANSI/AISC 360(16) and EN 1994-1-1 (2004) can be adopted for CSDST. However, the equations are less conservative for cross-sections with less than 50% hollowness.

Appendix-I

The concrete mix proportion is prepared with reference to the Indian Standards IS:456-2000 and IS:10262-2009. The quantities of concrete ingredients used for preparing the normal (40 N/mm^2) and high strength concrete (80 N/mm^2) are given in Tables A.I-1 and A.I-2, respectively.

Table A.I.1
Quantity of ingredients in normal strength concrete (40 N/mm^2)

Raw materials	Quantity (kg/m^3)
Water	180
Cement (OPC53)	400
Flyash	100
Coarse aggregate (12.5 mm/6 mm)	836
Sand (M)	896
Chemical admixture (BASF ACE 30 IT)	3

Table A.I.2
Quantity of ingredients in high strength concrete (80 N/mm^2)

Raw materials	Quantity (kg/m^3)
Water	185
Cement (OPC53)	550
Flyash	200
Micro-silica	50
Coarse aggregate (12.5 mm/6 mm)	727
Sand (M)	691
Chemical admixture (BASF ACE 30 IT)	5.25

Acknowledgements

The authors wish to extend their thanks to TATAstructura for supplying the steel tubes for this experimental work. They are also very thankful for the lab staff at Structural engineering lab, IIT Madras for their help during the experimental process.

NOTATIONS

A_c, A_{so}, A_{si}, A_g – Area of concrete, outer steel tube, inner steel tube, and gross cross-section, respectively
B – Width of general tubular cross-section
D, D_o, D_i – Diameter or width of general steel tube, outer steel tube, and inner steel tube, respectively
E_c, E_s, E_{so}, E_{si} – Young's modulus of concrete, general steel, outer steel tube, and inner steel tube, respectively
I_c, I_s, I_{so}, I_{si} – Moment of inertia of concrete, general steel, outer steel tube, and inner steel tube, respectively
L, L_{eff} – Length of the test specimen and effective length, respectively
$P_{cr,EC4}$ – Elastic *c*ritical buckling load as per EC4
$P_{cr,AISC}$ – Elastic *c*ritical buckling load as per AISC-360(16)
P_{EC4} – Axial capacity predicted using EC4 provisions
P_{AISC} – Axial capacity predicted using AISC-360(16) provisions
P_{sum} – Superimposed axial strength of steel and concrete ($P_{sum} = A_{so}f_{yo} + A_{si}f_{yi} + 0.8A_cf_{cm}$)
P_{test} – Ultimate strength of the specimens from test
P_u – Ultimate axial capacity
f_{cc} – Confined compressive strength of concrete
f_{cm} – Mean compressive strength of concrete cube
f_y, f_{yo}, f_{yi} – Yield strength of general steel, outer and inner steel tubes, respectively
f_{uo}, f_{ui} – Ultimate strength of outer and inner steel tubes, respectively
h_r – Hollowness ratio ($h_r = D_i / (D_o - 2\ t_o)$)
k – Factor to account for concrete strength enhancement due to lateral confinement
r_o, r_i – Outer and Inner radius of sandwiched concrete
t, t_o, t_i – Thickness of a general steel tube, outer steel tube and inner steel tube, respectively
γ – Initial eccentricity factor
Δ – Axial deformation
δ_c – Imperfection due to curvature effect
δ_{max} – Maximum lateral displacement
δ_o – Initial lateral displacement
ε_c, ε_{cc} – Axial strain in unconfined and confined concrete at the ultimate load point
ε_{ol}, ε_{oh} – Longitudinal and circumferential strain in the outer steel tube
ε_{il} – Longitudinal strain in the inner steel tube
λ_{EC4} – Non-dimensional slenderness ratio of a member as per EC4
λ_{AISC} – Non-dimensional slenderness ratio of a member as per AISC-360(16)
v_o – Strain ratio in a concrete filled steel tube

References

[1] EN 1994-1-1, "Eurocode 4 : Design of composite steel and concrete structures Part 1-1 : General rules and rules for buildings," 2004.
[2] ANSI/AISC, "Specification for Structural Steel Buildings," 2016.
[3] P. Hsiao, K. K. Hayashi, R. Nishi, X. Lin, and M. Nakashima, "Investigation of Concrete-Filled Double-Skin Steel Tubular Columns with Ultrahigh-Strength Steel," Journal of Structural Engineering, ASCE, 2014, pp. 1–8.
[4] M. L. Romero, A. Espinos, J. M. Portolés, A. Hospitaler, and C. Ibañez, "Slender double-tube ultra-high strength concrete-filled tubular columns under ambient temperature and fire," Engineering Structures, 2015, vol. 99, pp. 536–545.
[5] H. Lu, X.-L. Zhao, and L.-H. Han, "FE modelling and fire resistance design of concrete filled double skin tubular columns," Journal of Constructional Steel Research, 2011, vol. 67, no. 11, pp. 1733–1748.
[6] F. Zhang, C. Wu, X. Zhao, Z. Li, A. Heidarpour, and H. Wang, "Numerical Modeling of Concrete-Filled Double-Skin Steel Square Tubular Columns under Blast Loading," Journal of performance of constructed facilities (ASCE), 2015, vol. 29, no. 5, pp. 1–12.
[7] C. B. Ritchie, J. A. Packer, M. V Seica, and X. Zhao, "Behaviour and analysis of concrete-filled rectangular hollow sections subject to blast loading," Journal of Constructional Steel Research, 2018, vol. 147, pp. 340–359.
[8] Z. Tao, L.-H. Han, and X.-L. Zhao, "Behaviour of concrete-filled double skin (CHS inner and CHS outer) steel tubular stub columns and beam-columns," Journal of Constructional Steel Research, 2004, vol. 60, no. 8, pp. 1129–1158.
[9] K. Uenaka, H. Kitoh, and K. Sonoda, "Concrete filled double skin circular stub columns under compression," Thin-Walled Structures, 2010, vol. 48, no. 1, pp. 19–24.
[10] X.-L. Zhao and R. Grzebieta, "Strength and ductility of concrete filled double skin (SHS inner and SHS outer) tubes," Thin-Walled Structures, 2002, vol. 40, no. 2, pp. 199–213.
[11] L.-H. Han, Z. Tao, H. Huang, and X.-L. Zhao, "Concrete-filled double skin (SHS outer and CHS inner) steel tubular beam-columns," Thin-Walled Structures, 2004, vol. 42, no. 9, pp. 1329–1355.
[12] M. Elchalakani, X.-L. Zhao, and R. Grzebieta, "Tests on concrete filled double-skin (CHS outer and SHS inner) composite short columns under axial compression," Thin-Walled Structures, 2002, vol. 40, no. 5, pp. 415–441.
[13] K. Uenaka, "CFDST stub columns having outer circular and inner square sections under compression," Journal of Constructional Steel Research, 2016, vol. 120, pp. 1–7.
[14] M. F. Hassanein, O. F. Kharoob, and Q. Q. Liang, "Thin-Walled Structures Circular concrete- filled double skin tubular short columns with external stainless steel tubes under axial compression," Thin Walled Structures, 2013, vol. 73, pp. 252–263.
[15] M. F. Hassanein and O. F. Kharoob, "Compressive strength of circular concrete-filled double skin tubular short columns," Thin-Walled Structures, 2014, vol. 77, pp. 165–173.
[16] Y. Essopjee and M. Dundu, "Performance of concrete-filled double-skin circular tubes in compression," Composite Structures, 2015, vol. 133, pp. 1276–1283.
[17] U. M. Sulthana and S. A. Jayachandran, "Axial Compression Behaviour of Long Concrete Filled Double Skinned Steel Tubular Columns," Structures, 2017, vol. 9, pp. 157–164.
[18] T. V. Galambos and A. E. Surovek, *Structural Stability of Steel: Concepts and applications for structural engineers*. 2008.
[19] ASTM-E8/E8M, "Standard Test Methods for Tension Testing of Metallic Materials," 2009.
[20] IS:516, "Indian Standard methods of tests for strength of concrete," 1959.
[21] L.-H. Han, "Tests on Concrete Filled Steel Tubular Columns with High Slenderness Ratio," Advances in Structural Engineering, 2000, vol. 3, no. 4, pp. 337–344.
[22] T. Perea, "Analytical and Experimental Study on Slender Concrete-Filled Steel Tube Columns and Beam-Columns (PhD Thesis)," Georgia Institute of Technology, 2010.
[23] M. Xiong, D. Xiong, and J. Y. R. Liew, "Behaviour of steel tubular members in fi lled with ultra high strength concrete," Journal of Constructional Steel Research, 2017, vol. 138, pp. 168–183.
[24] Y.-F. An, L.-H. Han, and X.-L. Zhao, "Behaviour and design calculations on very slender thin-walled CFST columns," Thin-Walled Structures, 2012, vol. 53, pp. 161–175.
[25] T. Perea, R. T. Leon, J. F. Hajjar, and M. D. Denavit, "Full-scale tests of slender concrete-filled tubes: Interaction behavior," Journal of Structural Engineering, 2013, vol. 139, no. 7, pp. 1249–1262.

.

Advanced Steel Construction – Vol. 16 No. 2 (2020) 112–123
DOI:10.18057/IJASC.2020.16.2.3

SEISMIC PERFORMANCE OF HIGH STRENGTH CONCRETE FILLED HIGH STRENGTH SQUARE STEEL TUBES UNDER CYCLIC PURE BENDING

Guochang Li [1], Zengmei Qiu [1, *], Zhijian Yang [1], Bowen Chen [1] and Yihe Feng [2]

[1] *School of Civil Engineering, Shenyang Jianzhu University, Shenyang 110168, China*
[2] *Liaoning Province Shiyan High School, Shenyang 110841, China*
** (Corresponding author: E-mail: qzmfighting@126.com)*

ABSTRACT

To investigate the flexural behavior of high-strength concrete filled high-strength square steel tubes (HCFHSTs) under low-frequency cyclic loading, a test study was conducted on six HCFHSTs adopting different steel ratio. The objective of these tests was to analyze the failure modes, hysteresis curves, envelope curves, strength degradation, stiffness degradation, energy dissipation, and ductility of HCFHSTs. The results indicated that the HCFHST members had great performance, with highly saturated hysteresis curves, excellent energy dissipation capacity, and good ductility. Additionally, more models with different parameters were analyzed using the numerical analysis software ABAQUS, to determine the effects of the parameters on the flexural capacity and seismic performance of the HCFHST members with different steel yield strength (460–960 MPa), concrete compressive strength (60–110 MPa), and steel ratio. The ultimate flexural capacity, initial flexural stiffness, and serviceability-level flexural stiffness of the HCFHST members were calculated using the engineering design codes of several countries. The estimated results of the design codes were compared with the values obtained via the tests and numerical simulations to confirm the feasibility of various engineering design codes for calculating the flexural stiffness and ultimate flexural capacity of HCFHST members. This work will serve as a reference for future engineering design and broaden the applicability of engineering design codes.

ARTICLE HISTORY

Received: 15 November 2019
Revised: 11 March 2020
Accepted: 13 March 2020

KEYWORDS

high strength;
pure bending;
steel ratio;
hysteretic behavior;
flexural stiffness

1. Introduction

All over the world, concrete filled steel tubes (CFSTs) are generally utilized in practical engineering applications owing to excellent load-bearing capacity, ductility, and fire resistance, along with their ease of use in construction. The rapid development of the construction industry has increased the seismic performance requirements of CFST members. To improve the utility of CFSTs in engineering, many researchers have investigated the mechanical behaviors of CFSTs worldwide. Furthermore, owing to the recent development and application of materials with high performance, researchers have studied the potential of high-strength steel (HSS) and high-strength concrete (HSC) for replacing conventional concrete and steel materials in CFST members. The use of high-performance materials in CFSTs can improve their load-bearing capacity and reduce their cross-sectional size, thus reducing the structural self-weight and the amplitude of the seismic response of the structural members. Therefore, the application of high-performance materials in CFSTs has considerable promise.

Thus far, numerous experimental studies and numerical simulations have been conducted on the axial and eccentric compression performance of CFSTs. For example, Uy *et al*. [1] performed numerous experimental analyses, where eight short composite HSS (f_y = 761 MPa)-concrete columns and eight slender columns were tested. Li *et al*. [2-4] investigated the mechanism of HSC-filled square steel tube columns under axial and bi-axial eccentric loadings. Portolés *et al*. [5] carried out a test investigation of HSC-filled circular steel tubes under eccentric loading. Abramski [6] performed axial-compression experiments on 30 CFST columns with steel ratios between 4% and 6%. Using a numerical analysis software, Ouyang *et al*. [7] studied the axial-compression performance of 92 square CFSTs, whose steel strength, concrete strength, and steel tube depth-to-thickness ratios were in the ranges of 24–110 MPa, 262–835 MPa, and 18–102, respectively. It was concluded that increasing the corner radius enhanced the post-peak behavior of the CFST columns.

The flexural behaviors of CFSTs have also been studied by numerous scholars. Elchalakani *et al*. [8,9] investigated the flexural behaviors of circular CFST members; it was observed that the filling of steel tubes within $D/t \leq 40$ with concrete delays local buckling failures. Lu *et al*. [10] performed pure bending tests and finite-element analysis on three rectangular CFSTs. The experimental data and finite-element analyses indicated that the flexural capacity of the rectangular CFSTs could be enhanced by 5% when the steel plate thickness ratio (t_2/t_1) of the rectangular section ranged from 1.5 to 2.0. Chitawadagi *et al*. [11] investigated the strength deformation behavior of CFST specimens. According to the testing of 99 specimens with various in-fill concrete strength and D/t ratios, an interaction model that relates the curvature of the CFST specimens to the applied bending moment was developed. Moon *et al*. [12] researched the mechanical behavior of CFST members via numerical analysis and compared the analysis results with design specification formulas. To calculate the moment versus drift curve of CFSTs subjected to pure bending, a simplified model was established. Zha *et al*. [13] derived the theoretical models for calculating the ultimate flexural capacity of concrete filled elliptical steel tube members. Wang *et al*. [14] performed pure bending experiments on CFSTs with different sections. It was observed that stress redistributions caused by the interactions between the steel tube and the concrete could enhance the load-bearing capacity of the CFST members. Montuori *et al*. [15] carried out a pure bending test investigation of CFSTs using HSS and constructed a corresponding finite-element model. Fu *et al*. [16] and Wang *et al*. [17] researched the bending resistance ability of circular concrete filled CFRP-steel tubes and lightweight aggregate CFSTs, respectively. Xu *et al*. [18] conducted axial compression and bending tests on hexagonal CFST members constructed using an HSC in-fill and different steel ratio. The behaviors of these CFSTs were then compared with those of hollow tubular members. On this basis, simplified models of the ultimate compression-bending capacity were proposed. Additionally, the plastic stress distribution method and the fiber model method can be adopted to predict the ultimate flexural capacity of CFSTs with hexagonal sections. Li *et al*. [19] analyzed the flexural behaviors of high strength concrete filled high strength square steel tubes (HCFHSTs) via experiments and numerical analysis, and compared the ultimate flexural capacity derived from the experimental research and numerical simulation method with the estimations of various design codes. The calculations of the EC4 specification were the most similar to the experimental/modeled values. Xiong *et al*. [20] conducted pure bending tests on eight CFSTs that used HSS with a yield stress of 780 MPa and HSC with a compressive strength of 180 MPa. The maximum moment resistances obtained in these tests were compared with calculations based on the EC4 specification. According to their findings, they presented design proposals suitable for HCFHST members. Xie *et al*. [21] conducted bending and corrosion tests on 14 circular and square-shaped CFSTs filled with ordinary and recycled concrete. Pure bending experiments were performed by Chen *et al*. [22,23] on 28 circular CFAT members. As the thickness of the aluminum tube enhanced, the ductility and load-bearing capacity of CFATs improved. In contrast, the concrete strength had insignificant influence on the flexural behaviors or ductility of the CFATs.

Furthermore, the seismic performance of CFSTs has been investigated via experimental and finite element modeling approaches, on the basis of previous studies on the basic mechanical properties of CFSTs. Han *et al*. [24–27] performed a test study on the hysteretic behaviors of eight CFST specimens

under cyclically increasing flexural loading with constant axial loads. On the basis of theoretical calculations, a simplified model was given to obtain the moment–curvature relationship, and a formula for calculating the ductility coefficient of CFST specimens was developed. Additionally, Han et al. analyzed the mechanical performance of 28 concrete-filled double skin steel tubes with different hollow sections and 18 HSC filled CFSTs with circular and square sections subjected to cyclically increasing flexural loading with constant axial loads. Elchalakani *et al*. [28] studied the hysteresis behavior of circular CFSTs and then compared the peak moments calculated from the test results with those predicted by various specifications. Thus, the new section slenderness was determined to limit the construction of earthquake-resistant structural systems. Liao *et al*. [29] had made suggestions for the design of the concrete-filled stainless steel tubular (CFSST) columns via testing 10 CFSST columns, according to the ultimate bearing capacity and flexural stiffness predicted using several design codes for CFSST specimens. Serras *et al*. [30] put forward a simple yet efficient model aiming to analyze the hysteretic behavior and load-bearing capacity of CFSTs and tested circular CFST specimens subjected to cyclically increasing flexural loading with constant axial loads. In numerous studies on CFST specimens with varying steel yield strength, concrete compressive strength and D/t ratio, the results indicated that the model reliably described the mechanical behaviors of the circular CFST specimens under cyclic loading. Chen *et al*. [31] studied the behavior of partially encased composite beams, concluding that the specimens under cyclic loads exhibited the excellent energy dissipation capacity, with equivalent viscous damping up to 49%. A numerical analysis model was proposed by Ma *et al*. [32] to study the performance of hexagonal CFST members under cyclically increasing bending loads with a constant axial load. According to numerous parametric tests, a practical calculation method was developed for predicting the flexural capacity of hexagonal CFSTs.

As described previously, there are considerable research results regarding the static behavior of axially and eccentrically loaded CFSTs and the flexural behavior of CFSTs, and a few scholars have studied the hysteretic behavior of CFSTs subjected to cyclically increasing flexural loading with constant axial loads. However, there are very few reports on the hysteretic behavior of CFSTs under pure bending, particularly HCFHST members. Although CFSTs are rarely used as pure bending members in practical structures, the analysis of the seismic performance of CFSTs subjected to pure bending will provide useful insights to further study the functional mechanisms of CFST members under cyclically increasing flexural loading with a constant axial load. Moreover, all CFST related design codes around the world have specified limits for the scope of application of HSS tubes and HSC. In view of the foregoing, the hysteretic behavior of HCFHST members was investigated, and a parametric analysis was carried out adopting the simulation method. The ultimate flexural capacity, initial flexural stiffness, and serviceability-level flexural stiffness of HCFHST members obtained via experiments and numerical analysis were compared with the values calculated via the design codes of different countries, to determine whether these design codes are feasible for calculating the ultimate flexural capacity and flexural stiffness of HCFHST members. The findings of this study provide a reference for future engineering designs and broaden the applicability of engineering design codes.

2. Experimental program

2.1. Test design

Hysteresis tests were performed on six HCFHST members, which were divided into three sets. All the specimens had a length of 1500 mm and a cross-sectional area of 150 mm × 150 mm. The wall thicknesses of the steel tubes were 4, 5, and 6 mm, and changes in the wall thicknesses were used to vary the steel ratio (α) of the specimens. The HSS square tubes were cold-formed steel tubes. The strength and elastic modulus of the steel materials were confirmed using the tensile tests specified in the GB/T228-2010 standard [33]. C100 HSC was used as the HSC in-fill of the HCFHST specimens. Standard concrete test cubes with dimensions of 150 mm × 150 mm × 150 mm were prepared for compressive-strength tests. According to the tests specified by the GB/T50081-2002 standard [34], the mean value of the compression strength of the cube specimens was 95 MPa. Steel plates with a thickness of 20 mm and a cross-section of 300 mm × 300 mm were welded onto both ends of each HCFHST specimen. Details regarding the tested members are presented in Table 1.

Table 1
Parameters of the specimens

Specimen	$B \times t \times L$ (mm)	α	f_{cu} (MPa)	f_y (MPa)	f_u (MPa)	E_s (GPa)
SPB1-1	150 × 4 × 1500	0.116	95	434.56	546.2	206
SPB1-2	150 × 4 × 1500	0.116	95	430.00	547.0	206
SPB2-1	150 × 5 × 1500	0.148	95	416.31	513.7	206
SPB2-2	150 × 5 × 1500	0.148	95	420.00	516.0	206
SPB3-1	150 × 6 × 1500	0.182	95	430.00	545.0	206
SPB3-2	150 × 6 × 1500	0.182	95	436.91	550.4	206

Note: B is the cross-sectional width. t is the wall thickness of the steel tube. L is the length of the member. α is the steel ratio. f_{cu} is the compressive strength of the cube concrete. f_y and f_u are the steel yield strength and ultimate strength, respectively. E_s is the Young's modulus of steel.

2.2. Loading device

An MTS hydraulic servo loading system was adopted to test the specimens. The cyclic loading was applied by a vertically set 100 t MTS actuator situated at the mid-span position of the member, and then the MTS actuator was linked with a distribution beam via a set of rigid fixtures with the purpose of achieving pure bending loads. The specimens were horizontally placed in the middle of the loading system, and the boundary conditions on either side of the specimens were hinged connections. Because of the complex test equipment, a set of lateral supports was installed to prevent instability failure due to misalignment between the MTS actuator and the specimen axis. To allow the specimen to move freely in the vertical direction within the plane of the test equipment during the whole loading process, roller boards were welded onto the lateral supports. Two supports were tightly affixed to either side of the MTS actuator using screws. The bottom part of the supports was connected to an anchor via a beam, which limited lateral displacements of the member. The loading device is illustrated in Fig. 1.

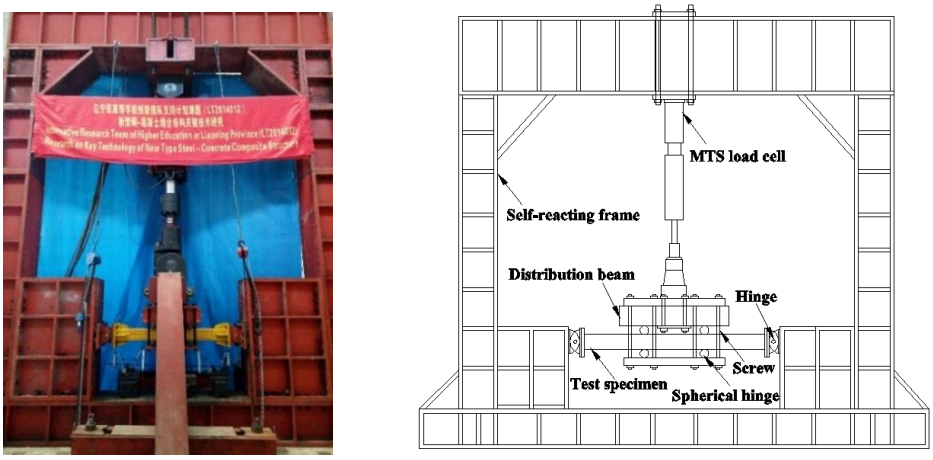

Fig. 1 Loading device.

2.3. Measurement scheme

Five displacement transducers were arranged in the mid-span, quarter-span, and endpoints of the HCFHST member to measure the deformation. Strain gauges were arranged on the top and bottom sides of the mid-span of the specimen to measure the strain on the surfaces of the steel tube, to study the constraining effects of the steel tube on the concrete. Strain gauges were also installed along the height of the specimen to study the change of the specimen's neutral axis. Fig. 2 shows the arrangement of the measuring devices.

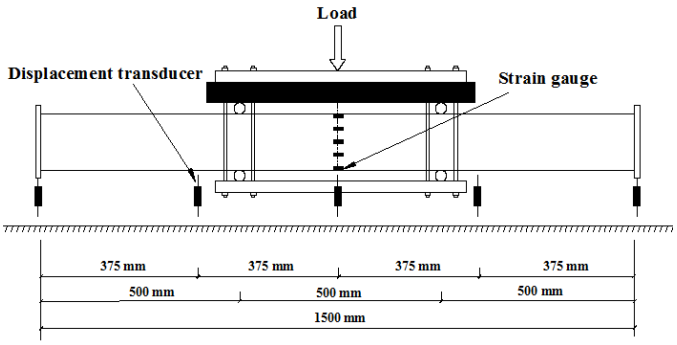

Fig. 2 Arrangement of measuring devices

2.4. Loading procedure

During the experiments, pre-loading was first performed to ensure that the test equipment and measuring instruments functioned properly. Fig. 3 presents the loading procedure of the HCFHST members, which comprised a load-control stage and a displacement-control stage. Prior to specimen yielding, force-controlled loading was used to load the specimen incrementally; the load was increased by approximately 20 kN in each step, and each load level was cycled twice. Displacement-controlled loading was used after the specimen yielded. During this mode of loading, the loads were incremented stage-wise by 0.5Δy or 1.0Δy (Δy represents the yield displacement of the specimen). The specimen was cycled three times at the first three load levels and then cycled twice at all other load levels. The test terminated when the specimen could not bear additional loads or after the applied load decreased to 85% of the peak load.

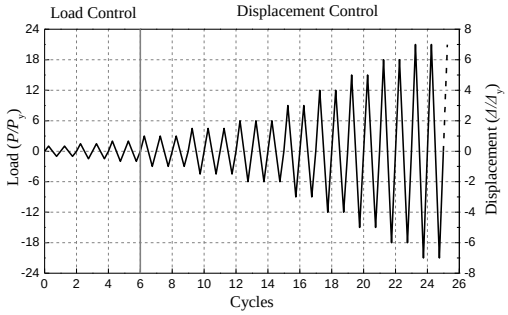

Fig. 3 Loading procedure

3. Experimental results and specimen behavior

3.1. Loading process and failure mode

The experimental loading procedure is described using specimen SPB1-2 as a typical specimen. Load control was used during the early stage of the experiment, where the member was still in elastic stage and did not exhibit significant bending deformation. As the applied load enhanced to 160 kN and the displacement reached 11 mm, the specimen began to yield. Displacement control was used beyond this point, and the load was 60% of the peak load at this point. When the load reached 2Δy, small concrete-cracking sounds were heard from inside the steel tube, and the increase in the load began to slow. When the load was 3Δy, clear and continuous concrete-cracking sounds were heard, and the inner side of the spherical hinge buckled slightly. When the load increased to 4Δy, the concrete-cracking noises became very loud, and the peak load was reached at this point. When the load was 5Δy, buckling deformation slowly spread around the outer side of the spherical hinge in a half-waved shape; slight buckling was appeared in the mid-span of the specimen. When the load increased to 6Δy, the area affected by buckling deformation near the spherical hinge gradually expanded, and the buckling deformations around the spherical hinge spread rapidly in the circumferential direction. When the load reached 7Δy, buckling deformations covered the entirety of the circumference near the spherical hinge, resulting in a lantern-shaped appearance. The continuation of the loading process caused the tension face (steel tube) near the spherical hinge to crack, which was accompanied by bits of crushed concrete falling out of the specimen. The experiment was terminated at this point. In particular, loading of specimen SPB1-1 was performed using a knife hinge on one end and a spherical hinge on the other end; the test of this specimen was terminated at 4.5Δy, as the stress-concentrating effects of the knife hinge caused the specimen to crack prematurely. The failure modes of the other five specimens were similar. Similar to specimen SPB1-2 (whose failure mode is shown in Fig. 4), the other five specimens exhibited severe buckling near the spherical hinges, which caused the steel tube to crack.

After the loading tests, the outer steel tube of the HCFHST was separated from the specimens, for examining the damage of the concrete. Fig. 5 shows that concrete was crushed near the spherical hinges in specimen SPB1-2. This was caused by the concentration of stress near the spherical hinges. In the mid-span area, numerous transverse cracks appeared in the concrete. The concrete was crushed where buckling occurred in the steel tube.

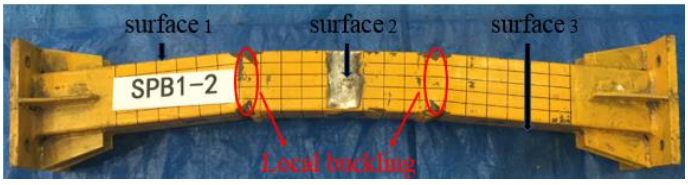

Fig. 4 Failure mode of the typical specimen

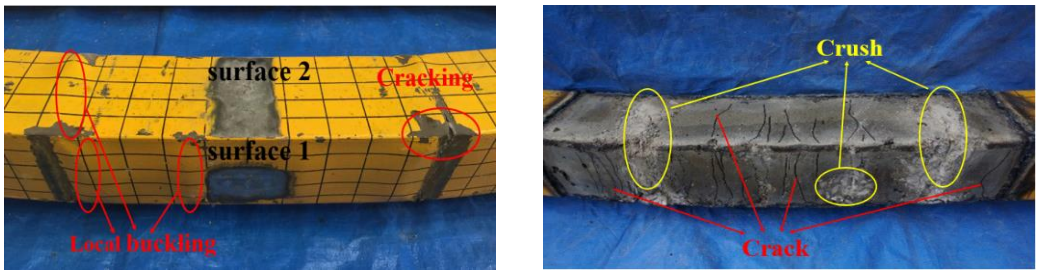

(a) Corners of the specimen

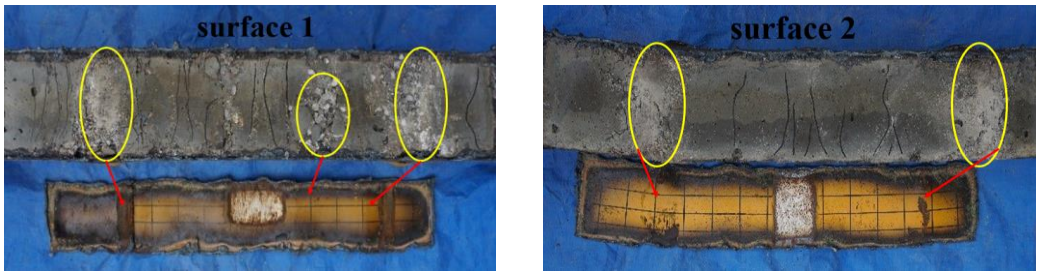

(b) Surfaces of the specimen

Fig. 5 Internal failure mode of the specimen

3.2. Distribution of the deflection curves

Fig. 6 illustrates the deflection of the HCFHST members at each level of pure bending load, along the length of each specimen. The dotted lines are standard sinusoid curves. The horizontal and vertical axes represent the length of the specimen (L) and the deflection along the length (ω), respectively. The deformations of the HCFHST specimens generally conformed to the half-sine wave.

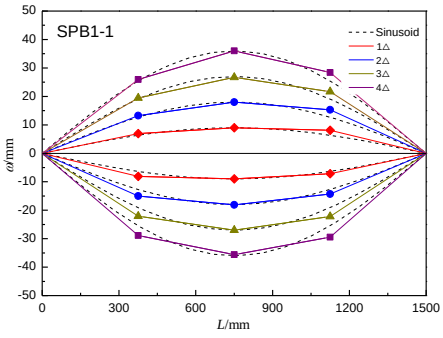

(a) SPB1-1

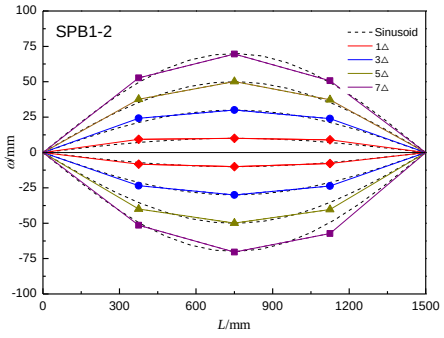

(b) SPB1-2

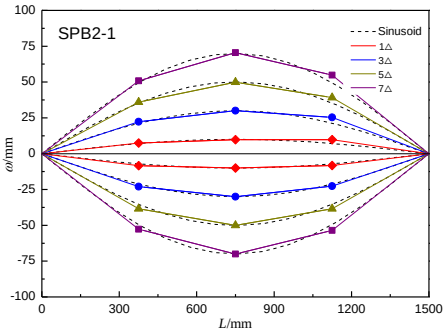

(c) SPB2-1

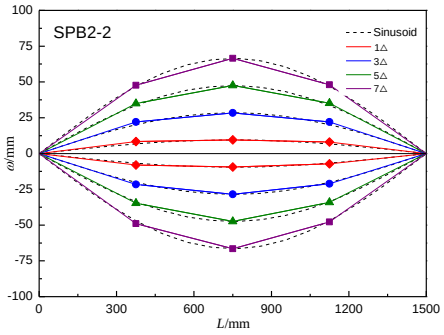

(d) SPB2-2

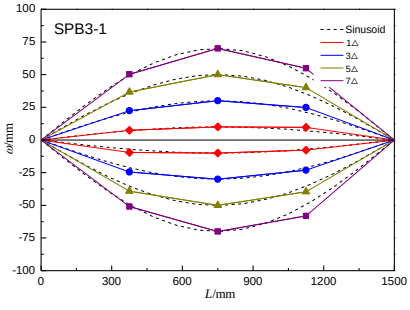

(e) SPB3-1

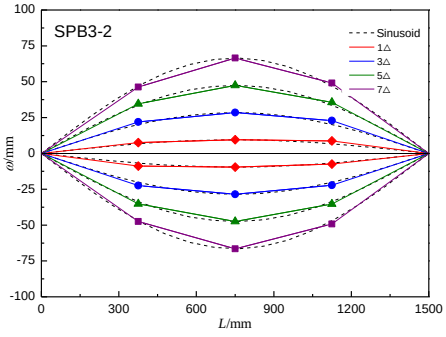

(f) SPB3-2

Fig. 6 Distribution of the deflection curves

3.3. Load versus displacement hysteretic curves

The load versus displacement hysteretic curves of the HCFHST members under pure bending are shown in Fig. 7.

Before the specimen yielded, the displacement of the specimen changed linearly with respect to the load, as the member was still in elastic stage. Therefore, the area of the hysteresis loop formed by a single load cycle was relatively small, and the stiffness of the specimen did not change significantly during loading and unloading. The specimen entered the plastic stage after the yield point, which caused its stiffness to decrease slightly during the loading and unloading. With increasing load cycles, the stiffness decreased, but the area of the hysteresis loop enhanced.

The load versus displacement hysteresis loops of the HCFHSTs were highly full, as given in Fig. 7. Furthermore, the area of the hysteresis loops enhanced with the steel ratio, indicating an increase in the energy dissipation capacity. The bearing capacity of the specimens did not decrease significantly after reaching the peak load. Hence, the HCFHST specimens showed excellent seismic performance.

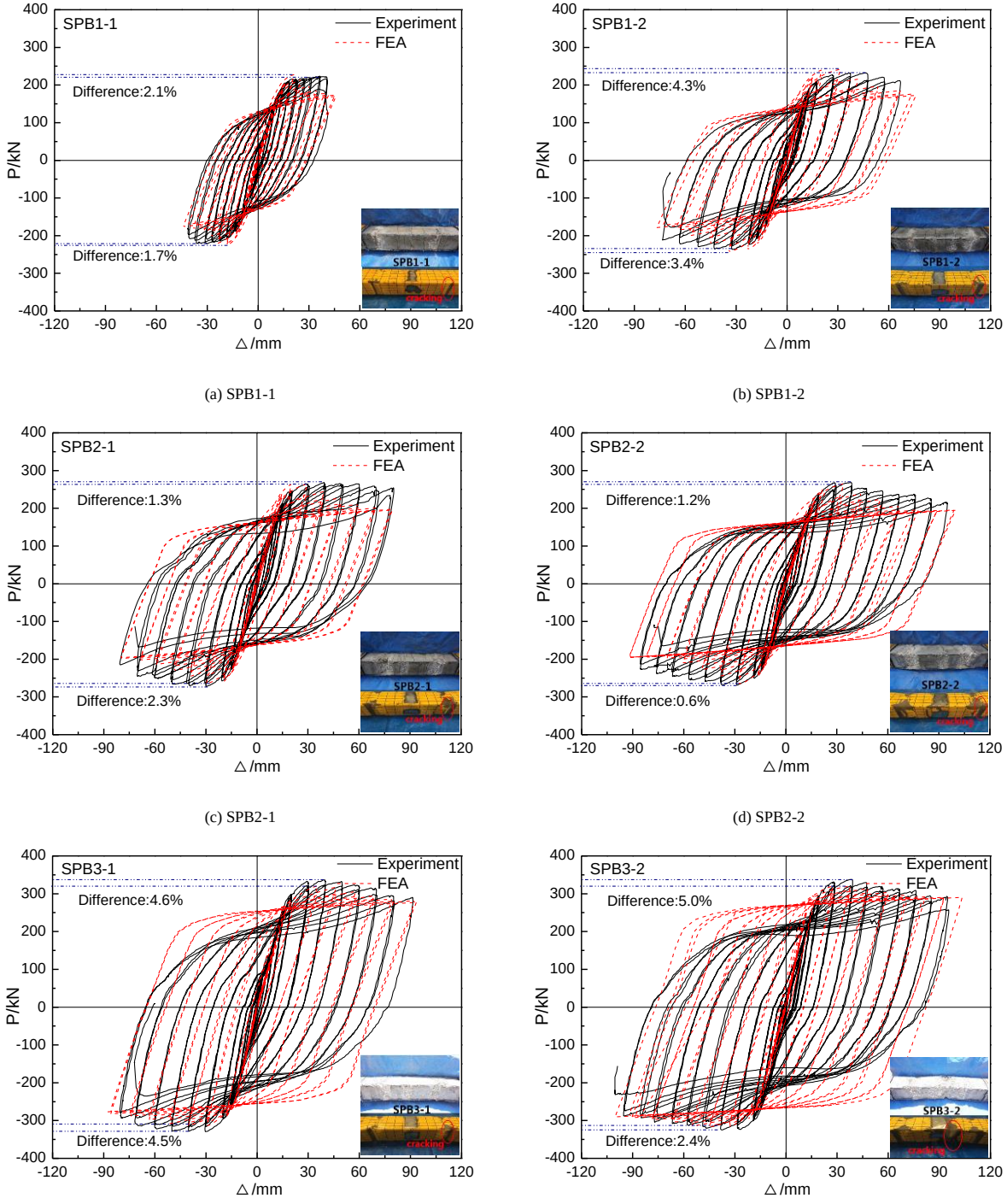

(a) SPB1-1 (b) SPB1-2

(c) SPB2-1 (d) SPB2-2

(e) SPB3-1 (f) SPB3-2

Fig. 7 Load versus displacement hysteretic curves

3.4. Load versus displacement envelope curves

As the load versus displacement envelope curve of the HCFHST member under pure bending did not exhibit a distinct yield point, the envelope curve can be simplified into a trilinear model, as given in Fig. 8. The yield displacement (Δy) was calculated using the displacement corresponding to the intersection between the extrapolation of the elastic segment and the tangent line at the peak of the envelope curve. The ultimate displacement (Δu) was calculated using the displacement of the point where the applied load decreased to 85% of the peak load or the displacement where specimen failure

occurred.

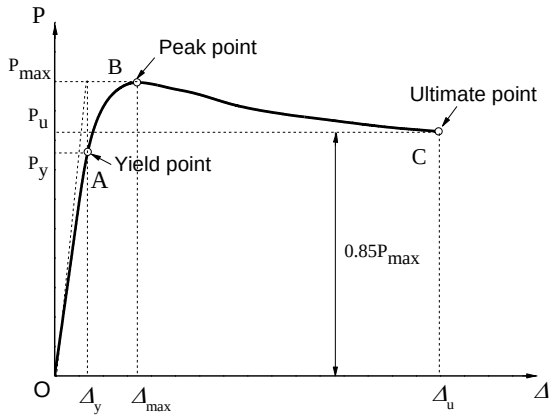

Fig. 8 Model of the trilinear envelope curve

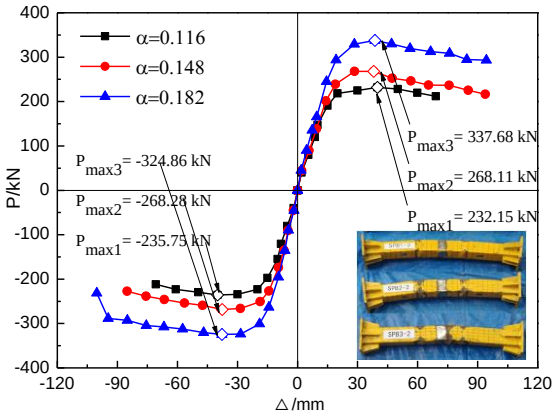

Fig. 9 Influence of P–Δ envelope curves with different steel ratio

Fig. 9 shows the P–Δ envelope curves of the HCFHST members, which can be divided into the following three stages.

1) Elastic stage: The bearing capacity increased linearly with respect to the displacement, and the envelope curve was linear, as the specimen was still elastic.

2) Elastic–plastic stage: The bearing capacity declined with an enhancement in displacement, and the envelope curve began to deviate from linearity. The bearing capacity increased slowly until the peak load was reached.

3) Post-yield stage: The bearing capacity decreased with an increase in the displacement, and the deformations of the specimen were large, resulting in stiffness degradation.

Table 2 presents the characteristic values of the envelope curve for each specimen. The envelope curves indicate that the HCFHST members had excellent ductility under pure bending, as throughout the loading process, significant degradations in the bearing capacity were not observed. The peak loads of these specimens significantly enhanced with the steel ratio: an enhancement in steel ratio from 0.116 to 0.148 increased the peak load of the HCFHSTs by approximately 17%. When the steel ratio increased from 0.148 to 0.182, the peak load of the HCFHST members increased by approximately 25%. The peak load increased by approximately 45% when the steel ratio of the HCFHST members increased from 0.116 to 0.182.

Table 2

Characteristic values of the specimens

Specimen	Loading stage	Yield point		Peak point		Ultimate point		Ductility factor
		Δ_y (mm)	P_y (kN)	Δ_{max} (mm)	P_{max} (kN)	Δ_u (mm)	P_u (kN)	μ
SPB1-1	Positive	11.88	172.70	36.18	223.64	40.50	220.18	3.41
	Negative	9.22	151.24	30.96	221.59	40.59	206.46	4.40
SPB1-2	Positive	11.87	163.33	39.96	232.15	69.12	211.92	5.82
	Negative	11.04	164.62	39.90	235.75	70.78	211.62	6.41
SPB2-1	Positive	12.63	180.34	39.48	268.66	80.24	254.28	6.35
	Negative	10.96	183.09	39.70	272.26	74.58	231.42	6.80
SPB2-2	Positive	12.24	174.30	38.07	268.11	83.10	227.89	6.79
	Negative	12.15	203.59	37.68	268.28	84.33	228.04	6.94
SPB3-1	Positive	11.22	197.88	39.60	336.80	91.04	290.51	8.11
	Negative	11.46	202.97	40.02	329.39	79.13	293.10	6.91
SPB3-2	Positive	13.61	232.15	38.66	337.68	94.35	293.26	6.93
	Negative	11.80	227.10	37.77	324.86	94.57	288.38	8.01

Note: P_y and Δ_y are the yield load and yield displacement, respectively. P_{max} and Δ_{max} are the peak load and peak displacement, respectively. P_u and Δ_u are the ultimate load and ultimate displacement, respectively. μ is the ductility factor.

3.5. Strength degradation

The strength degradation curve reflects the strength and deformation performance of a specimen under cyclic loading. Hence, it can be used to assess the overall strength degradation trends of a specimen and the degradation in the specimen strength at each load level. The overall strength degradation coefficient of a specimen (η) is given by Eq. (1), and the strength degradation coefficient for each load level (β) is given by Eq. (2).

$$\eta_{i=} P_i/P_{max} \quad (1)$$

Where, η_i is the overall strength degradation coefficient at the i^{th} load level,

P_i is the maximum load of the i^{th} load level, and P_{max} is the maximum value of the loading process.

$$\beta_{i=} P_i^j / P_i^l \quad (2)$$

Where, β_i is the strength degradation coefficient of the i^{th} load level, P_i^j is the maximum load of the j^{th} cycle of the i^{th} load level, P_i^l is the maximum load of the l^{th} cycle at the i^{th} load level, and j and l are the second and first cycles of each load level, respectively.

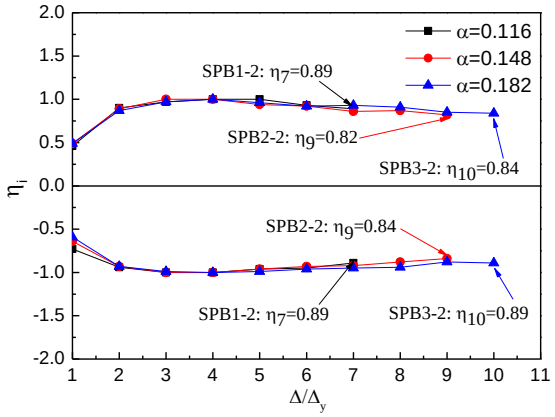

Fig. 10 Overall strength degradation curves

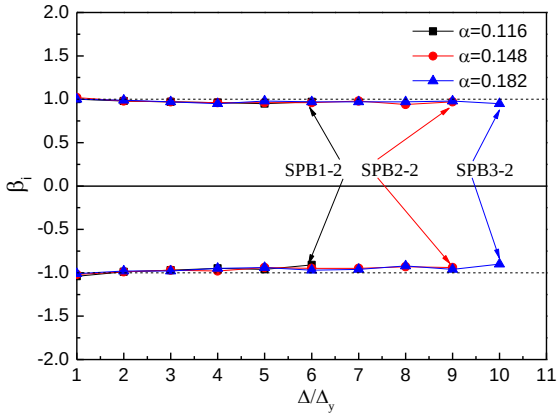

Fig. 11 Equivalent strength degradation curves

The overall strength degradation curves of members with several steel ratios are given in Fig. 10. The overall strength of each specimen increased with the load during the early stages of the loading. The strength degradation curve of each specimen trends downward in a linear fashion after the peak load, but the decrease in the strength appears to be insignificant. At the termination of the experiment, the overall strength degradation coefficients of the specimens ranged between 0.82 and 0.89. This illustrates that the overall strength degradation of the members during the loading was not significant. The confinement effect of the steel tube prevented the concrete from splitting apart, which delayed the strength degradation and improved the seismic performance of the HCFHST members. Fig. 11 indicates that the strength degradation coefficient at each load level was close to 1.0 for the specimens. Hence, the bearing capacity of the specimens was relatively stable, and no specimen exhibited significant strength degradation at the same load level.

3.6. Stiffness degradation

Reductions in the bearing capacity of a specimen under cyclic loading are mainly caused by degradations in the specimen stiffness. Therefore, it is necessary to study the stiffness degradation curves of the members. In this paper, the stiffness (EI) of a member subjected to a pure bending load can be determined as follows:

$$EI = \frac{M}{\varphi} \quad (3)$$

Where, M is the moment, and φ is the curvature.

The stiffness-degradation trends of the HCFHST members under pure bending are illustrated in Fig. 12. The Y-axis of this figure indicates the dimensionless $EI/(EI)_{first}$ ratio, where $(EI)_{first}$ represents the stiffness of the member at the first loading level. The stiffness of the members continuously decreased with increasing in the displacement and cycle number, owing to the accumulation of damage. The degradation in the specimen stiffness was also due to continuous reductions in the elastic modulus of the concrete and steel materials. The stiffness degradation slowed after reaching the peak load, because the HSS steel tube confined the concrete and slowed its splitting, reducing the velocity of specimen stiffness degradation. Thus, the HCFHST members had excellent seismic performance. Fig. 12 also illustrates that the steel ratio had little effect on the stiffness degradation curves of members. Specimen failure generally occurred when the stiffness of the specimen decreased to approximately 11%–15% of the initial value.

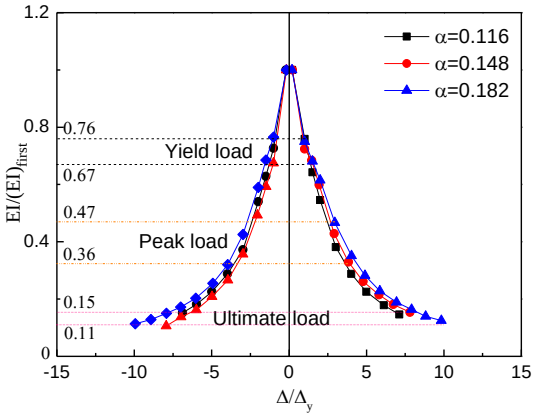

Fig. 12 Influence of stiffness-degradation curves with different steel ratio

3.7. Energy dissipation capacity

The energy dissipation capacity of members is usually determined via the equivalent viscous damping coefficient (h_e). The larger value of h_e indicates the better energy dissipation capacity of specimens. In this paper, h_e was calculated using the last P–Δ hysteresis loop prior to specimen failure, as indicated by Eq. (4). Fig. 13 shows the typical P–Δ hysteresis loop of a member subjected to cyclic loading.

$$h_e = \frac{E}{2\pi}, \quad E = \frac{S_{ABCDA}}{S_{OBE} + S_{ODF}} \quad (4)$$

Where, E is the energy dissipation coefficient, S_{ABCDA} is the area of the hysteresis loop in Fig. 13, and S_{OBE} and S_{ODF} are the area of the triangle in Fig. 13.

The area covered by S_{ABCDA} represents the energy absorbed by the member in a single cycle, whereas $S_{OBE} + S_{ODF}$ represents the energy released by the member during the unloading process.

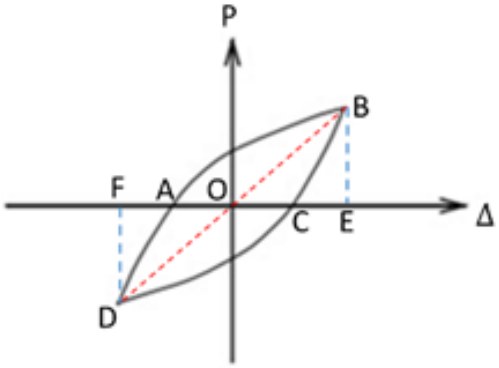

Fig. 13 Hysteresis loop of the load versus displacement curve

Table 3
Energy dissipation

Specimen	S_{ABCDA}	S_{OBE}	S_{ODF}	E	h_e
SPB1-1	16402.22	4435.45	4188.78	1.9019	0.3027
SPB1-2	29512.30	7323.96	7489.23	1.9923	0.3171
SPB2-1	39007.82	10042.71	8640.12	2.0879	0.3323
SPB2-2	43068.15	9485.04	9665.94	2.2489	0.3579
SPB3-1	53200.00	11694.38	11596.50	2.2842	0.3635
SPB3-2	62818.00	13834.54	13636.05	2.2867	0.3639

In an HCFHST member subjected to pure bending loads, energy dissipation mainly occurs via crack propagation in the concrete, the development of plasticity in the steel tube, and contact between the concrete and steel tube. Table 3 presents the cumulative energy dissipation of each specimen. As shown, h_e varied between 0.3027 and 0.3639, and the energy dissipation capacity of the specimens increased with the steel ratio.

The h_e versus Δ/Δ_y plot of each specimen is presented in Fig. 14. As shown, h_e increased with the displacement, indicating that the energy dissipation capacity of the members enhanced with the displacement. The growth of the h_e versus Δ/Δ_y curve began to slow after the peak load was reached, with h_e decreasing slightly near specimen failure. This is because the energy dissipation capacity of members decreased when severe crushing and buckling occurred in the concrete and steel tube. During the early stage of loading, an enhancement in the steel ratio had no significant influence on the energy dissipation capacity of the specimens. However, after the peak load was reached, the energy-dissipation capacity increased by 11.4% (17.4%) when the steel ratio was increased from 0.116 to 0.148 (0.182). This is because the confinement of the concrete by the HSS tube increased with an increase in the steel ratio, which enhanced the deformation capacity of the concrete and thus improved the energy dissipation capacity of specimens.

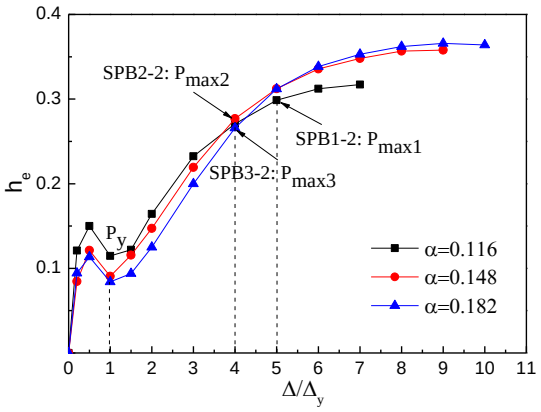

Fig. 14 Influence of energy-dissipation curves with different steel ratio

3.8. Ductility

The ductility of the HCFHST members was investigated according to the displacement ductility factor (μ), which was calculated as follows:

$$\mu = \frac{\Delta_u}{\Delta_y} \tag{5}$$

The μ values of the test specimens are presented in Table 2. An analysis of these data reveals that the specimens generally exhibited excellent ductility. Furthermore, the ductility performance of the HCFHST members improved with the steel ratio.

4. Finite element analysis and discussions

4.1. Material

4.1.1. Steel

The stress–strain curve of steel comprised two stages: an elastic stage and a hardening stage. The initial elastic modulus (E_S) was defined as the loading and unloading stiffness of the elastic stage, whereas the hardening modulus was defined as $0.01E_S$. To consider the influence of the Bauschinger effect on the loading and unloading processes of the HCFHST members, the bilinear kinematic hardening model was adopted to simulate the constitutive model of steel.

4.1.2. Concrete

The concrete model suggested by Han [35] was adopted to simulate the in-fill concrete. The equations are as follows:

$$y = \begin{cases} 2x - x^2 & (x \le 1) \\ \dfrac{x}{\beta_0 (x-1)^{\eta} + x} & (x > 1) \end{cases} \tag{6}$$

In which

$$x = \frac{\varepsilon_c}{\varepsilon_{c0}} \ , \ y = \frac{\delta_c}{\delta_{c0}} \ , \ \delta_{c0} = f_c^{'}(\mathrm{N/mm^2})$$

$$\varepsilon_{c0} = \varepsilon_{cc} + 800\xi^{0.2} \cdot 10^{-6}$$

$$\varepsilon_{cc} = (1300 + 12.5 f_c^{'}) \cdot 10^{-6}$$

$$\eta = 1.6 + 1.5/x$$

$$\beta_0 = \frac{f_c^{'0.1}}{1.2\sqrt{1+\xi}} \ , \ \xi = \frac{A_s f_y}{A_c f_{ck}} = \alpha \cdot \frac{f_y}{f_{ck}}$$

Where, f_c is the cylinder concrete strength, and f_{ck} is the characteristic concrete strength.

To account for degradations in the concrete stiffness that occur gradually during cyclic loading (resulting from the damage sustained by the concrete during cyclic loading), the concrete plastic damage model given by ABAQUS was used to simulate the mechanical behaviors of the concrete. The main parameters (the dilation angle (ψ), the flow potential eccentricity (e_f), etc.) in the elastic damage model were obtained according to the work of Li [36]. The stiffness degradations induced by compressive and tensile damage were denoted as d_c and d_t, which were calculated using Eqs. (7) and (8), respectively.

$$d_c = 1 - \frac{(\sigma_c + 0.5\sigma_{c0})}{E_c(0.5\sigma_{c0}/E_c + \varepsilon_c)} \qquad (d_c \ge 0) \tag{7}$$

$$d_t = 1 - \frac{(\sigma_t + 0.5\sigma_{t0})}{E_c(0.5\sigma_{t0}/E_c + \varepsilon_t)} \qquad (d_t \ge 0) \tag{8}$$

In these equations, δ_c, ε_c, and δ_{c0} are the compressive stress, compressive strain, and uniaxial compressive peak stress of the concrete, respectively; δ_t, ε_t, and δ_{t0} are the tensile stress, tensile strain, and uniaxial tensile peak stress of the concrete, respectively.

4.2. Details of Finite Element Model

The solid element C3D8R was employed to model the steel tube, the concrete, and the end plates of HCFHSTs. "Tie" constraint was used to simulate the contact between the end plates and steel tube. The relationship between the end plates and concrete in the normal direction was subjected to the hard contact. Between the steel tube and concrete, surface-to-surface contact was applied to model the interaction. The contacts in the normal direction were modeled as hard contact, whereas the tangential contacts were simulated adopting a Coulomb friction model with a friction factor of 0.6 [35].

During the simulation analysis of the HCFHST model, cyclic displacement loading was performed by defining the one-third points of the specimen as reference points. Additionally, kinematic constraints were imposed on the end plates of the HCFHST model to simulate the boundary conditions imposed by the hinge connections. The details of the numerical model are shown in Fig. 15.

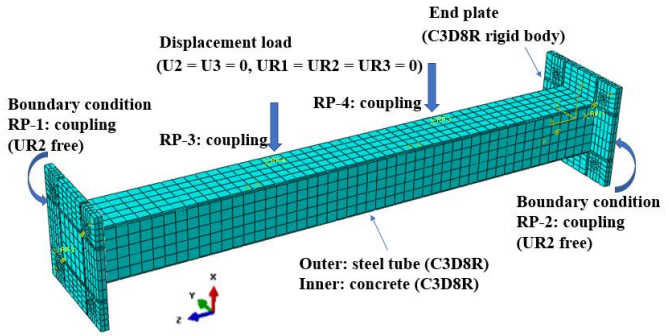

Fig. 15 Finite element model

4.3. Model verification

Fig. 7 illustrates the load versus displacement hysteretic curves of the HCFHST members obtained via simulations, which were compared with the experiment results. The results obtained via the numerical model agreed well with the experimental results, with errors of <5%.

4.4. Parameters analysis

The numerical analysis models were adopted to research the influences of various parameters (thickness of the steel tube, 4–6 mm; steel yield strength, 460–960 MPa; concrete compressive strength, 60–110 MPa) on the hysteretic behaviors of the HCFHST members under pure bending. The moment versus curvature (M–φ) envelope curves of the models are shown in Fig. 16.

4.4.1. Steel strength

As shown in Fig. 16(a), the steel strength did not significantly affect the elastic stiffness. This is because the elastic modulus of steel does not influence its strength. However, the yield moment and ultimate moment of the members increased with the steel strength.

4.4.2. Concrete compressive strength

The M–φ curves of HCFHST members with several concrete compressive strengths under pure bending are given in Fig. 16(b). The results illustrate that the concrete strength did not affect the elastic stiffness or the yield moment. However, an enhancement in the concrete strength caused the downward trend in the bearing capacity after the peak load was reached to become more pronounced. This is due to the increases in the concrete strength are accompanied by increases in the specimen brittleness and reductions in the ductility.

4.4.3. Steel ratio

Fig. 16(c) illustrates the effects of the steel ratio on the M–φ curves of the HCFHST members. The elastic stiffness, yield moment, and bearing capacity of the model enhanced with the steel ratio. This is because the confinement of the concrete by the steel tube was improved by increasing the steel ratio, which improved the deformation capacity of the HCFHST member and thus increased its bearing capacity and ductility.

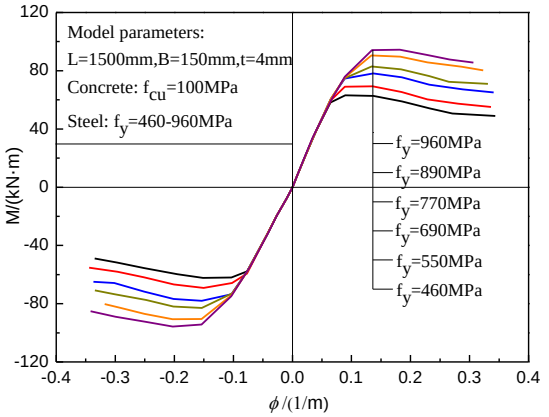

(a) Steel strength

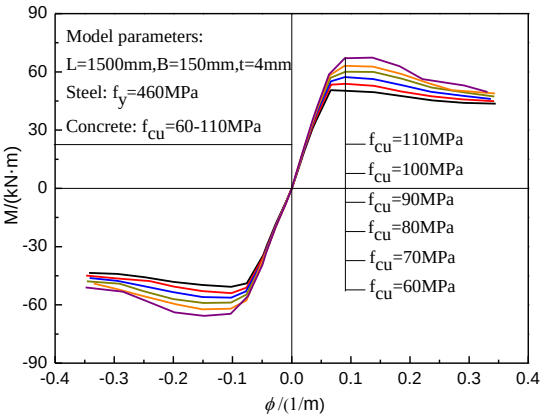

(b) Concrete compressive strength

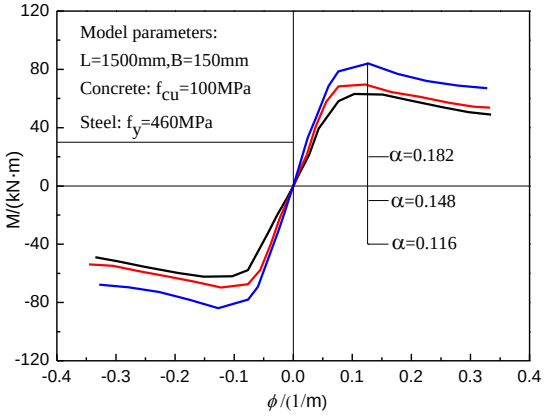

(c) Steel ratio

Fig. 26 Effects of M–φ envelope curves with different parameters

5. Code comparison

5.1. Ultimate flexural capacity

The AISC-LRFD (2010) [37], AIJ (1997) [38], EC4 (2004) [39], GB50936 (2014) [40], and DBJ (2010) [41] design codes were adopted to calculate the theoretical ultimate flexural capacity of the HCFHST specimen, and the suitability of these design codes was analyzed. Table 4 presents the calculated experimental and simulated values. M_{ue} represents the ultimate flexural capacity of the finite element analysis, and M_{uc} represents the

theoretical ultimate flexural capacity calculated using a design code.

Table 4 indicates that the results for the ultimate flexural capacity calculated using the EC4 (2004) and DBJ (2010) design codes were higher than the experimental/simulated values by 16.7% and 18%, respectively. The values of the ultimate flexural capacity calculated using the GB50936 (2014) design code were higher than the experimental/simulated values by slightly more than 20%. Consequently, the calculations of the AISC (2010) and AIJ (1997) design codes were only 3.4% higher than the experimental/simulated values. Thus, the AISC (2010) and AIJ (1997) design codes were the most suitable for calculating the ultimate flexural capacity of the HCFHST members under pure bending.

5.2. Flexural stiffness

The initial flexural stiffness of CFSTs under pure bending is usually confirmed as the stiffness at M = 0.2M_{ue}. At this moment, the deformations of the CFST are completely linear elastic, because the concrete has yet to crack or is just beginning to crack in the tensile zones. The serviceability-level flexural stiffness of the CFST is confirmed as its stiffness at M = 0.6M_{ue}; according to the M–φ curve, the member was still in the elastic stage at this load level.

The flexural stiffness of an HCFHST member is evaluated via its initial and serviceability-level flexural stiffness. The design codes of different countries for calculating the flexural stiffness are different, in which, the concrete and the steel tube of CFST members are generally assumed to contribute independently to the overall stiffness of the members. Hence, the basic equation for calculating the stiffness of an HCFHST member is

$$K_e = mE_sI_s + nE_cI_c \tag{9}$$

Where, E_s and E_c are the elastic moduli of the steel tube and concrete, respectively; I_s and I_c are the second moment of area for the steel tube and the gross concrete section, respectively; and m and n are the contribution coefficients of the flexural stiffness.

The AIJ (1997), EC4 (2004) ,and AISC-LRFD (2010) design codes have the same values of m but different values of n, whereas the BS5400 (2005) [42] design code simultaneously accounts for the effects of the steel material and concrete on the flexural stiffness of CFSTs. The flexural stiffness calculations of each design code are given as follows.

1）AISC-LRFD (2010)

$$K_e = E_sI_s + 0.8E_cI_c \tag{10}$$

Where $E_s = 210000(\text{MPa})$ and $E_c = 4700\sqrt{f_c'}(\text{MPa})$.

2）AIJ (1997)

$$K_e = E_sI_s + 0.2E_cI_c \tag{11}$$

Where $E_s = 205800(\text{MPa})$ and $E_c = 21000\sqrt{f_c'/19.6}(\text{MPa})$.

3）EC4 (2004)

$$K_e = E_sI_s + 0.6E_cI_c \tag{12}$$

Where $E_s = 210000(\text{MPa})$ and $E_c = 22000\cdot\left(f_c'/10\right)^{0.3}(\text{MPa})$.

Table 4

Comparisons between the experimental/simulated values and the design code values

Type	specimen	α	f_{cu} (MPa)	f_y (MPa)	M_{ue} (kN·m)	AISC/ AIJ		EC4		GB50936		DBJ	
						M_{uc} (kN·m)	M_{uc}/M_{ue}	M_{uc} (kN·m)	M_{uc}/M_{ue}	M_{uc} (kN·m)	M_{uc}/M_{ue}	M_{uc} (kN·m)	M_{uc}/M_{ue}
Test	SPB1-1	0.116	95	434.56	55.65	54.73	0.98	63.19	1.14	72.95	1.31	65.09	1.17
	SPB1-2	0.116	95	434.56	58.49	54.73	0.94	63.19	1.08	72.95	1.25	65.09	1.11
	SPB2-1	0.148	95	416.31	67.62	65.09	0.96	73.56	1.09	81.52	1.21	76.62	1.13
	SPB2-2	0.148	95	416.31	67.05	65.09	0.97	73.56	1.10	81.52	1.22	76.62	1.14
	SPB3-1	0.182	95	436.91	83.27	81.41	0.98	89.83	1.08	93.73	1.13	94.60	1.14
	SPB3-2	0.182	95	436.91	82.82	81.41	0.98	89.83	1.08	93.73	1.13	94.60	1.14
FEA	ASPB-1	0.116	100	460	62.72	57.94	0.92	66.88	1.07	77.24	1.23	68.89	1.10
	ASPB-2	0.116	100	550	69.22	69.27	1.00	79.01	1.14	87.98	1.27	79.57	1.14
	ASPB-3	0.116	100	690	78.08	86.91	1.11	97.66	1.25	104.68	1.34	96.06	1.23
	ASPB-4	0.116	100	770	82.96	96.98	1.17	108.24	1.30	114.27	1.38	105.48	1.27
	ASPB-5	0.116	100	890	90.48	112.10	1.24	124.02	1.37	128.73	1.42	119.65	1.32
	ASPB-6	0.116	100	960	95.07	120.91	1.27	133.19	1.40	137.23	1.44	127.96	1.35
	ASPB-7	0.116	60	460	50.47	57.94	1.15	64.44	1.28	66.82	1.32	62.54	1.24
	ASPB-8	0.116	70	460	53.86	57.94	1.08	65.15	1.21	69.50	1.29	64.15	1.19
	ASPB-9	0.116	80	460	56.82	57.94	1.02	65.79	1.16	72.13	1.27	65.76	1.16
	ASPB-10	0.116	90	460	59.46	57.94	0.97	66.37	1.12	74.71	1.26	67.35	1.13
	ASPB-11	0.116	110	460	66.50	57.94	0.87	67.36	1.01	79.71	1.20	70.38	1.06
	ASPB-12	0.148	100	460	69.64	71.93	1.03	81.04	1.16	88.74	1.27	84.00	1.21
	ASPB-13	0.182	100	460	83.98	85.72	1.02	94.60	1.13	98.42	1.17	99.67	1.19
	Mean value					1.034		1.167		1.269		1.180	
	Standard Deviation (COV)					0.108		0.107		0.087		0.075	

4）BS5400 (2005)

$$K_e = 0.95E_sI_s + 0.45E_cI_c \quad (13)$$

Where $E_s = 206000(\text{MPa})$ and $E_c = 450f_{cu}(\text{MPa})$.

The initial and serviceability-level flexural stiffness of the test are compared with the results obtained using the design codes in Tables 5 and 6, respectively.

As shown in Table 5, the initial flexural stiffness values calculated using the various design codes were larger than the experimental results, except for the values obtained from AIJ (1997) design code, which were a little lower than the experimental results. The flexural stiffness values calculated using BS5400 (2005) design code were the closest to the experimental results, as the mean and standard deviation of the K_{ic}/K_{ie} ratios were 1.038 and 0.089, respectively. The flexural stiffness values calculated using the AIJ (1997) design code were the second-closest; on average, they were only 5.7% lower than the experimental values. The flexural stiffness values calculated using the AISC (2010) and EC4 (2004) design codes were 29.8% and 16.8% higher than the experimental values, respectively.

Table 6 indicates that the serviceability-level flexural stiffness calculated using AIJ (1997) and BS5400 (2005) design codes were in better accordance with the experimental values than the values calculated by the other codes, as the results for AIJ (1997) and BS5400 (2005) were 26% and 38.3% higher than the experimental values, respectively. The serviceability-level flexural stiffness values calculated using the AISC (2010) and EC4 (2004) design codes differed significantly from the experimental values; they were 73% and 55% higher than the experimental values, respectively.

According to the foregoing results, the BS5400 (2005) and AIJ (1997) design codes can be used to satisfy design requirements for the initial and serviceability-level flexural stiffness of HCFHST members, whereas the AISC (2010) and EC4 (2004) design codes are not suitable for estimating the serviceability-level flexural stiffness of HCFHST members.

Table 5
Comparisons between the experiment results and predicted values for the initial flexural stiffness

specimen	K_{ie}	AISC		AIJ		EC4		BS5400	
		K_{ic}	K_{ic}/K_{ie}	K_{ic}	K_{ic}/K_{ie}	K_{ic}	K_{ic}/K_{ie}	K_{ic}	K_{ic}/K_{ie}
SPB1-1	2396	2932	1.22	2009	0.84	2560	1.07	2277	0.95
SPB1-2	2416	2932	1.21	2009	0.83	2560	1.06	2277	0.94
SPB2-1	2615	3259	1.25	2377	0.91	2945	1.13	2607	1.00
SPB2-2	2439	3259	1.34	2377	0.97	2945	1.21	2607	1.07
SPB3-1	2644	3573	1.35	2730	1.03	3276	1.24	2923	1.11
SPB3-2	2520	3573	1.42	2730	1.08	3276	1.30	2923	1.16
Mean value			1.298		0.943		1.168		1.038
Standard Deviation (COV)			0.084		0.102		0.097		0.089

Note: K_{ie} and K_{se} are the values of the initial and serviceability-level flexural stiffness, respectively, obtained from the experiments. K_{ic} and K_{sc} are the values of the initial and serviceability-level flexural stiffness, respectively, calculated using a design code.

Table 6
Comparisons between the experiment results and predicted values for the serviceability-level flexural stiffness

specimen	K_{se}	AISC		AIJ		EC4		BS5400	
		K_{sc}	K_{sc}/K_{se}	K_{sc}	K_{sc}/K_{se}	K_{sc}	K_{sc}/K_{se}	K_{sc}	K_{sc}/K_{se}
SPB1-1	1721	2932	1.70	2009	1.17	2560	1.49	2277	1.32
SPB1-2	1800	2932	1.63	2009	1.12	2560	1.42	2277	1.27
SPB2-1	1866	3259	1.75	2377	1.27	2945	1.58	2607	1.40
SPB2-2	1820	2010	1.79	2377	1.31	2945	1.62	2607	1.43
SPB3-1	1969	3573	1.81	2730	1.39	3276	1.66	2923	1.48
SPB3-2	2094	3573	1.71	2730	1.30	3276	1.56	2923	1.40
Mean value			1.732		1.260		1.555		1.383
Standard Deviation (COV)			0.066		0.099		0.088		0.076

6. Conclusions

This paper has mainly studied the seismic performance of HCFHST members subjected to cyclic pure bending. Six specimens were tested and thirteen finite-element models were developed to analyze the effect of different parameters on the bearing capacity and flexural stiffness of HCFHSTs. Based on the comparison with different codes, suggestions for the design of the initial and serviceability-level flexural stiffness were proposed. The following conclusions were obtained from this study.

1) HCFHST members subjected to cyclic pure bending loads exhibit excellent seismic performance. The hysteretic curves of HCFHST members are plump in shape and have no obvious pinch phenomenon. Furthermore, the load versus displacement curves do not decrease significantly after the applied load reaches the peak load, indicating that these members have excellent ductility performance. Additionally, throughout the loading process, HCFHST specimens do not exhibit significant strength degradation.

2) Increases in the steel ratio of HCFHST specimens lead to significant increases in the bearing capacity and energy dissipation capacity. When the

steel ratio was increased from 0.116 to 0.182, the peak load and energy dissipation capacity of HCFHST members increased by 45% and 17.4%, respectively. However, the stiffness degradations of the specimens were not significantly affected by changes in the steel ratio.

3) Numerical analyses indicated that increases in the steel yield strength significantly improved the bearing capacity, yield moment, and ultimate moment of HCFHST members but hardly affected the stiffness in the elastic stage. Changes in the compressive strength of the concrete only slightly affected the elastic stiffness and yield moment of the HCFHST members. However, increases in the concrete strength increased the brittleness of the specimens, which reduced the ductility. Changes in the steel ratio of the members significantly affected the elastic stiffness and yield moment.

4) Comparison between design codes: Regarding the ultimate flexural capacity, the AISC (2010) and AIJ (1997) design codes were the most suitable codes for calculating the ultimate flexural capacity of HCFHSTs, as the estimates of these design codes were only 3.4% higher than the values of ultimate flexural capacity obtained from tests and simulations. Regarding the flexural stiffness, the BS5400 (2005) and AIJ (1997) design codes can be used to satisfy the design requirements for the initial flexural stiffness and serviceability-level flexural stiffness of HCFHST members, whereas the AISC (2010) and EC4 (2004) design codes are not suitable for estimating the serviceability-level flexural stiffness of HCFHST members.

Acknowledgements

This project was supported by National Key R&D Program of China (2018YFC0705704), Fundamental Research Project of Higher Education in Liaoning Province (LJZ2017004) and Liaoning Climbing Scholar Support Program (2018-0101).

References

[1] Mursi, M. and Uy, B., “Strength of slender concrete filled high strength steel box columns”, Journal of Constructional Steel Research, 2004, 60(12), pp. 1825-1848.
[2] Li, G. C., Yang, Z. J., and Lang Y. “Experimental behavior of high strength concrete-filled square steel tube under bi-axial eccentric loading”, Advanced Steel Construction, 2010, 6(4), pp. 963-975.
[3] Li, G. C., Di, C. Y., Tian, L. and Fang, C., “Nonlinear finite element analysis on long columns of high-strength concrete-filled square steel tube with inner CFRP circular tube under axial load”, Advanced Steel Construction, 2013, 9(2), pp. 124-138.
[4] Li, G. C., Yang, Z. J., Lang, Y. and Fang, C., “Behaviour of high strength concrete filled square steel tubular columns with inner CFRP circular tube under bi-axial eccentric loading”, Advanced Steel Construction, 2013, 9, pp. 231-246.
[5] Portolés, J. M., Romero, M. L., Filippou, F. C. and Bonet, J. L., “Simulation and design recommendations of eccentrically loaded slender concrete-filled tubular columns”, Engineering Structures, 2011, 33(5), pp. 1576-1593.
[6] Abramski, M., “Load-carrying capacity of axially loaded concrete-filled steel tubular columns made of thin tubes”, Archives of Civil and Mechanical Engineering, 2018, 18(3), pp. 902-913.
[7] Ouyang, Y. and Kwan, A. K. H., “Finite element analysis of square concrete-filled steel tube (CFST) columns under axial compressive load”, Engineering Structures, 2018, 156, pp. 443-459.
[8] Elchalakani, M., Zhao, X. L. and Grzebieta, R. H., “Concrete-filled circular steel tubes subjected to pure bending”, Journal of constructional steel research, 2001, 57(11), pp. 1141-1168.
[9] Elchalakani, M., Karrech, A., Hassanein, M. F. and Yang, B., “Plastic and yield slenderness limits for circular concrete filled tubes subjected to static pure bending”, Thin-Walled Structures, 2016, 109, pp. 50-64.
[10] Lu, F. W., Li, S. P., Li, D. W. and Sun, G. J., “Flexural behavior of concrete filled non-uni-thickness walled rectangular steel tube”, Journal of Constructional Steel Research, 2007, 63(8), pp. 1051-1057.
[11] Chitawadagi, M. V. and Narasimhan, M. C., “Strength deformation behaviour of circular concrete filled steel tubes subjected to pure bending”, Journal of Constructional Steel Research, 2009, 65(8-9), pp. 1836-1845.
[12] Moon, J., Roeder, C. W., Lehman, D. E. and Lee, H. E., “Analytical modeling of bending of circular concrete-filled steel tubes”, Engineering Structures, 2012, 42, pp. 349-361.
[13] Zha, X. X., Gong, G. B. and Liu, X. C., “Study on behavior of concrete filled elliptical steel tube members part II: under bending and eccentric compression”, Advanced Steel Construction, 2013, 9(2) pp. 108-123.
[14] Wang, R., Han, L. H., Nie, J. G. and Zhao, X. L., “Flexural performance of rectangular CFST members”, Thin-Walled Structures, 2014, 79, pp. 154-165.
[15] Montuori, R. and Piluso, V., “Analysis and modelling of CFT members: moment curvature analysis”, Thin-Walled Structures, 2015, 86, pp. 157-166.
[16] Wang, Q. L. and Shao, Y. B., “Flexural performance of circular concrete filled CFRP-steel tubes”, Advanced Steel Construction, 2015, 11(2), pp. 127-149.
[17] Fu, Z. Q., Ji, B. H., Maeno, H., Eizien, A. and Chen, J. S., “Flexural behavior of lightweight aggregate concrete filled steel tube”, Advanced Steel Construction, 2014, 10(4), pp. 385-403.
[18] Xu, W., Han, L. H. and Li, W., “Performance of hexagonal CFST members under axial compression and bending”, Journal of Constructional Steel Research, 2016, 123, pp. 162-175.
[19] Li, G. C., Liu, D., Yang, Z. J. and Zhang, C. Y., “Flexural behavior of high strength concrete filled high strength square steel tube”, Journal of Constructional Steel Research, 2017, 128, pp. 732-744.
[20] Xiong, M. X., Xiong, D. X. and Liew, J. Y. R., “Flexural performance of concrete filled tubes with high tensile steel and ultra-high strength concrete”, Journal of Constructional Steel Research, 2017, 132, pp. 191-202.
[21] Xie, L., Chen, M. C., Sun, W. and Yuan, F., “Behaviour of concrete-filled steel tubular members under pure bending and acid rain attack: Test simulation”, Advances in Structural Engineering, 2019, 22(1), pp. 240-253.
[22] Chen, Y., Feng, R. and Wang, L. P., “Flexural behaviour of concrete-filled stainless steel SHS and RHS tubes”, Engineering Structures, 2017, 134, pp. 159-171.
[23] Chen, Y., Feng, R. and Gong, W. Z., “Flexural behavior of concrete-filled aluminum alloy circular hollow section tubes”, Construction and Building Materials, 2018, 165, pp. 173-186.
[24] Han, L. H., You, J. T. and Lin, X. K., “Experimental behaviour of self-consolidating concrete (SCC) filled hollow structural steel (HSS) columns subjected to cyclic loadings”, Advances in Structural Engineering, 2005, 8(5), pp. 497-512.
[25] Han, L. H. and Yang, Y. F., “Cyclic performance of concrete-filled steel CHS columns under flexural loading”, Journal of Constructional Steel Research, 2005, 61(4), pp. 423-452.
[26] Han, L. H., Huang, H., Tao, Z. and .Zhao, X. L., “Concrete-filled double skin steel tubular (CFDST) beam–columns subjected to cyclic bending”, Engineering Structures, 2006, 28(12), pp. 1698-1714.
[27] Han, L. H., Huang, H. and Zhao, X. L., “Analytical behaviour of concrete-filled double skin steel tubular (CFDST) beam-columns under cyclic loading”, Thin-walled structures, 2009, 47(6-7), pp. 668-680.
[28] Elchalakani, M. and Zhao, X. L., “Concrete-filled cold-formed circular steel tubes subjected to variable amplitude cyclic pure bending”, Engineering Structures, 2008, 30(2), pp. 287-299.
[29] Liao, F. Y., Han, L. H., Tao, Z. and ASCE, M., “Experimental behavior of concrete-filled stainless steel tubular columns under cyclic lateral loading”, Journal of Structural Engineering, 2016, 143(4), pp. 04016219.
[30] Serras, D. N., Skalomenos, K. A., Hatzigeorgiou, G. D. and Beskos, D. E., “Modeling of circular concrete-filled steel tubes subjected to cyclic lateral loading”, Structures, 2016, 8, pp. 75-93.
[31] Chen, Y. Y., Li, W. and Fang, C., “Performance of partially encased composite beams under static and cyclic bending”, Structures, 2017, 9, pp. 29-40.
[32] Ma, D. Y., Han, L. H., Ji, X. D. and Yang, W. B., “Behaviour of hexagonal concrete-encased CFST columns subjected to cyclic bending”, Journal of Constructional Steel Research, 2018, 144, pp. 283-294.
[33] GB/T228-2010. Metallic Materials - Tensile Testing at Ambient Temperature, Beijing, China, 2010.
[34] GB/T50081-2002. Standard for test method of mechanical properties on ordinary concrete, Beijing, China, 2002.
[35] Han, L. H., Yao, G. H. and Tao, Z., “Performance of concrete-filled thin-walled steel tubes under pure torsion”, Thin-walled structures, 2007, 45(1), pp. 24–36.
[36] Li, W., Han, L. H. and Chan, T. M., “Numerical investigation on the performance of concrete-filled double-skin steel tubular members under tension”, Thin-walled structures, 2014, 79, pp. 108-118.
[37] ANSI/AISC 360-10, Specification for Structural Steel Buildings, American Institute of Steel Construction, Chicago-Illinois, 2010.
[38] AIJ, Recommendations for design and construction of concrete filled steel tubular structures, Architectural Institute of Japan, Tokyo, Japan, 1997.
[39] Eurocode 4, Design of Composite Steel and Concrete Structures-Part 1-1: General Rules and Rules for Buildings, European Committee for Standardization, Brussels, 2004.
[40] GB50936-2014, Technical Code for Concrete filled Steel Tubular Structures, Ministry of Housing and Urban-Rural Development of the People’s Republic of China, China Architecture & Building Press, Beijing, China, 2014.
[41] DBJ13-51-2010. Technical code of concrete-filled steel tubular structures, Fuzhou, Fujian; China, 2010.
[42] BS5400, Steel, Concrete and Composite Bridges – Part 5: Code of Practice for Design of Composite Bridges, British Standards Institution, London, 2005.

Advanced Steel Construction – Vol. 16 No. 2 (2020) 124–136
DOI:10.18057/IJASC.2020.16.2.4

A REFINED PRECISE INTEGRATION METHOD FOR NONLINEAR DYNAMIC ANALYSIS OF STRUCTURES

Zhi-xia Ding [1], Zuo-lei Du [1], Wei Su [2, *] and Yao-peng Liu [1, 3]

[1] *Department of Civil and Environmental Engineering, The Hong Kong Polytechnic University, Hung Hom, Kowloon, Hong Kong, China*
[2] *School of Aeronautics and Astronautics, Sun Yat-sen University, Guangzhou, 510275, China*
[3] *Nida Technology Co. Ltd., Hong Kong Science Park, Shatin, N.T., Hong Kong, China*
** (Corresponding author: E-mail: suwei@mail.sysu.edu.cn)*

ABSTRACT

In this paper, a refined precise integration method (RPIM) is proposed for nonlinear dynamic analysis of structures. It extends the conventional precise integration method (PIM) from linear analysis to nonlinear analysis through a novel algorithm to improve the conventional Duhamel integration method for nonhomogeneous parts in nonlinear equations. In the RPIM, the stiffness matrix of the motion equation can be updated during the analysis, leading to the proposed method applicable to nonlinear structural problems. With the introduction of a new velocity vector, the original exponential matrix in PIM is reduced to a 2×2 matrix and the efficiency of RPIM is highly improved for both computation time and storage space. The analysis of stability and accuracy shows that the RPIM is unconditionally stable with highly precision. Four examples, including linear analysis of free and forced vibration and nonlinear analysis of two structures, i.e. truss and membrane, are analyzed to verify the efficiency and accuracy of the proposed RPIM.

ARTICLE HISTORY

Received: 13 April 2019
Revised: 17 November 2019
Accepted: 3 December 2019

KEYWORDS

Refined precise integration method;
Nonlinear dynamic analysis;
Stiffness matrix;
Efficiency and accuracy

1. Introduction

Dynamic analysis plays a critical role in the wind-induced response [1] and wave-induced response [2] in the design process of offshore steel structures, in which time is an important effect. In dynamic structural analysis, both implicit and explicit procedures are developed and adopted to deal with the equation of motion. Implicit procedures such as Newmark method [3], trapezoidal rule [4] and Wilson θ-method [5], are unconditionally stable in the linear analysis but can become unstable in nonlinear analysis. Thus, equilibrium iteration is of great importance in each step [6], which involves the inverse of matrices. The explicit procedure is popular among software packages [7-8] and researchers [9-10] with the advantage of no demand on either iteration or forming tangent stiffness matrix, which is not only time consuming but also storage space consuming. Central difference method (CDM) is one such an explicit method generally adopted in many software packages, for example, the analysis software package ABAQUS [7] and OpenSees [8]. However, the CDM is conditionally stable and requires a small time increment to achieve accurate results. To avoid instability and save computation time, a new method is required to solve the differential equation for structures with amount of degrees of freedom.

The precise integration method (PIM) was firstly proposed by Zhong and Williams in 1994 [11-12] and then investigated and improved by many researchers. PIM adopts two strategies to achieve high accuracy. Firstly, PIM introduces a vector to convert the two-order differential equation to a one-order equation so that accurate results can be achieved. The vector introduced by Zhong [11-13] has been adopted by many scholars [14-15]. Gao et al. [16] also introduced a vector representing the monument of the system with specific physical meaning, so that the properties of a sparse matrix can be used to reduce the computation time and memory size. This vector was also adopted by some researchers [17]. Secondly, the exponential matrix is precisely calculated with an additional theorem [13], which is based on Taylor series introduced by Zhong [12]. It is also called the 2N algorithm [13] as the time increment is further divided into 2N small time domains. The value of N is recommended as 20 which is adequate to reach the accuracy of the computer. Another method to calculate the exponential matrix was proposed by Liu and Shen [18] based on Padé function, exhibiting better accuracy. However, the method proposed by Zhong [12] is still adopted by researchers due to its simplicity. More recently, Yue et al. [19] developed a method based on Magnus expansion to deal with exponential matrix and the high validity was approved.

One approximation in PIM is the dealing with inhomogeneous terms. Inhomogeneous terms with polynomials, exponential functions, trigonometric functions or products of these functions can be linearly interpolated with a rough approximation according to Zhong [13]. However, this method involves inverse of doubled matrix H, formed after introducing p vector, which will be discussed in section 3. To avoid the disadvantage of inverse calculation of matrices, dimensional expanding method, introducing one more vector to convert nonhomogeneous terms into homogeneous ones, was proposed by Gu et al. [20]. However, this method triples the matrix which further increases computation time and memory size. Thus, the direct integration method is studied by many researchers. Lin et al. [14] decomposed the nonlinear load with Fourier expansion based on the PIM and demonstrated the accuracy of this method. Rung-Kutta method was incorporated by Zhang et al. [21] to deal with nonlinear inhomogeneous terms and the accuracy and stability of PIM were improved. Wang and Au improved the accuracy of the PIM based on Gauss quadrature method [15] and Lagrange piecewise interpolation polynomials [22]. The Simpson, Romberg and Cotes integration methods were also adopted by researchers to improve the accuracy of the PIM [23]. Tan et al. [18] proposed a method to precisely calculate the Duhamel terms based on the additional theorem, in which the nonlinear part of inhomogeneous terms is approximated by polynomials, and the linear part can then be calculated accurately. The direct integration avoids the inverse of matrix. Nevertheless, additional exponential matrices need to be calculated at integration points.

Due to the introduction of another vector to reduce the order of differential equation, the matrices in the differential equations are doubled in the PIM, leading to more computational time for the calculation of the exponential matrix. To solve this problem, amount of efforts has been made on reducing the size of matrix. Zhong et al. [24] proposed a subdomain precise time integration method so that only a small size exponential matrix is calculated each time. Wu et al. [25] also proposed a subdomain precise integration method based on the PIM for periodic structures. The whole structure is considered as a combination of several super elements and such that the computational efforts and memory size are reduced with the same accuracy. Similarly, Gao and his team [26-29] proposed subdomain PIM for periodic structures based on the parametric variational principle (PVP). With the periodic structure, only one exponential matrix is required for calculation, the efficiency is highly improved compared with calculating all the exponential matrices. Fung and Chen [30] improved computational efficiency of the PIM with Krylov subspace method and Padé approximations. Su et al. [31] computed exponential matrix with the Suzuki's decomposition based technique of the fourth order. Some efforts, different from the subdomain, to improve the efficiency of the PIM were also made by researchers. Shen et al. [19] proposed a parallel algorithm with mixed fine and coarse grain strategy to improve the efficiency of the PIM. Gao et al. [21] introduced a fast precise integration method (FPIM) considering the sparse natural of the system matrices, and the accuracy, as well as efficiency, are addressed.

Up to now, the PIM method has been investigated and developed by researchers to achieve high accuracy and increase efficiency for dynamic problems. However, there are few studies focusing on the nonlinear structural

problems with varied stiffness matrix. In this paper, a refined precise integration method (RPIM) is proposed to deal with nonlinear dynamic problems of structures and to improve the efficiency of traditional PIM. A new vector, velocity, is introduced to simplify the calculation of the exponential matrix based on the PIM by Zhong [11] and the additional theorem of Duhamel integration by Tan [18]. After the introduction of this vector, only a 2×2 matrix is required for the calculation of the exponential matrix, with much computational time and memory size saved. In the equation of motion, the internal force, the product of varied stiffness matrix and displacement vector, are considered as an unknown variable which could be updated during the process of nonlinear analysis. Theoretically, the stability and accuracy analysis will be conducted to illustrate the stability and accuracy of the proposed method. The instability and high accuracy of the RPIM are also verified with four cases involving both linear and nonlinear dynamic analysis. Linear analysis with free vibration and forced vibration and nonlinear analysis with truss elements and membrane elements are adopted for verification of the RPIM. The accuracy of the RPIM is demonstrated by comparing with that of the CDM, and the efficiency is certified by comparison with the methods combining vectors introduced by Zhong [11] and Gao [16].

2. Conventional central difference method

In dynamic structural problems, the equation of motion is defined as

$$\mathbf{M}\ddot{\boldsymbol{x}} + \mathbf{C}\dot{\boldsymbol{x}} + \mathbf{K}\boldsymbol{x} = \mathbf{f}(\boldsymbol{x}, \mathrm{t}) \tag{1}$$

in which M, C, and K are the mass, damping and stiffness matrices of the structural system respectively; $\mathbf{f}(\boldsymbol{x}, \mathrm{t})$ is the external force vector related to time and the displacements of the degrees of freedom (DOF) in each node. $\boldsymbol{x}$, $\dot{\boldsymbol{x}}$ and $\ddot{\boldsymbol{x}}$ are the vectors regard to displacements, velocities and accelerations of each DOF.

The velocity, assumed linearly distributed from time t to $t + \Delta t$, and the accelerated velocity, assumed as the first-order derivative of velocity during time domain $[t - \Delta t/2, t + \Delta t/2]$, are respectively described as,

$$\dot{\boldsymbol{x}}_{t+\Delta t/2} = (\boldsymbol{x}_{t+\Delta t} - \boldsymbol{x}_t)/\Delta t \tag{2}$$

$$\ddot{\boldsymbol{x}}_t = \left(\dot{\boldsymbol{x}}_{t+\Delta t/2} - \dot{\boldsymbol{x}}_{t-\Delta t/2}\right)/\Delta t \tag{3}$$

where $\boldsymbol{x}$ is a DOF (displacement or rotation) with current time step and time increment denoted by subscript t and Δt respectively.

The central-difference integration operator is explicit in the sense that the kinematic state uses known values of $\boldsymbol{x}_t$ and $\ddot{\boldsymbol{x}}_t$ from the previous increment. The CDM is a self-starting method with the initial values of $\dot{\boldsymbol{x}}_{\Delta t/2}$ and $\dot{\boldsymbol{x}}_{-\Delta t/2}$ calculated with Eq.(4) and Eq.(5).

$$\dot{\boldsymbol{x}}_{\Delta t/2} = \dot{\boldsymbol{x}}_0 + \ddot{\boldsymbol{x}}_0 \Delta t/2 \tag{4}$$

$$\dot{\boldsymbol{x}}_{-\Delta t/2} = \dot{\boldsymbol{x}}_0 - \ddot{\boldsymbol{x}}_0 \Delta t/2 \tag{5}$$

During the recursion of the CDM, the inverse of matrix $\mathbf{M} + \Delta t/2\mathbf{C}$ is involved which might be time-consuming, especially for the case of consistent mass matrix.

3. RPIM for dynamic structural problems

In order to deal with nonlinear dynamic analysis, traditional PIM [11] is refined based on the additional theorem of Duhamel integration derived by Tan [32]. The essence of PIM is converting the original two-order equation of motion into a one-order differential equation by introducing a new vector. The vectors $\boldsymbol{p}$ introduced by Zhong [11] and Gao [16] are described with Eq.(6) and Eq.(7) respectively.

$$\boldsymbol{p} = \mathbf{M}\dot{\boldsymbol{x}} + \mathbf{C}\boldsymbol{x}/2, \qquad \boldsymbol{u} = \begin{bmatrix} \boldsymbol{x} \\ \mathbf{M}\dot{\boldsymbol{x}} + \mathbf{C}\boldsymbol{x}/2 \end{bmatrix} \tag{6}$$

$$\boldsymbol{p} = \mathbf{M}\dot{\boldsymbol{x}}, \qquad \boldsymbol{u} = \begin{bmatrix} \boldsymbol{x} \\ \mathbf{M}\dot{\boldsymbol{x}} \end{bmatrix} \tag{7}$$

So, the motion equation can be derived as Eq.(8) and Eq.(9) respectively.

$$\mathbf{H} = \begin{bmatrix} -\mathbf{M}^{-1}\mathbf{C} & \mathbf{M}^{-1} \\ \mathbf{M}^{-1}\mathbf{C}\mathbf{M}/4 - \mathbf{K} & -\mathbf{C}\mathbf{M}^{-1}/2 \end{bmatrix}, \qquad \dot{\boldsymbol{u}} = \mathbf{H}\boldsymbol{u} + \begin{bmatrix} \mathbf{0} \\ \mathbf{f}(\boldsymbol{x}, \mathrm{t}) \end{bmatrix} \tag{8}$$

$$\mathbf{H} = \begin{bmatrix} \mathbf{0} & \mathbf{M}^{-1} \\ -\mathbf{K} & -\mathbf{C}\mathbf{M}^{-1} \end{bmatrix}, \qquad \dot{\boldsymbol{u}} = \mathbf{H}\boldsymbol{u} + \begin{bmatrix} \mathbf{0} \\ \mathbf{f}(\boldsymbol{x}, \mathrm{t}) \end{bmatrix} \tag{9}$$

Obviously, the matrix formed in Eq. (9) is much simpler than that in Eq. (8). The solution to these equations written by Duhamel integration as,

$$\boldsymbol{u}(\mathrm{t}) = \exp(\mathbf{H}t)\,\boldsymbol{x}(0) + \int_0^t \exp\left(\mathbf{H}(t-\tau)\right) \begin{bmatrix} \mathbf{0} \\ \mathbf{f}(\boldsymbol{x}, \mathrm{t}) \end{bmatrix} d\tau \tag{10}$$

Despite the accuracy of the PIM, the disadvantages of this method are obvious. The size of matrices is doubled after transformation with the introduced vector, and such that more computational efforts are demanded. Another disadvantage is that the PIM is only applicable to linear dynamic analysis since the H matrix should be revised and the exponential matrix is recalculated in each step if nonlinear problem is involved.

3.1. Transformation of equation of motion

The stiffness matrix K is consistent in the elastic range of structures but varies with time during the elastic-plastic range, and thus, the K matrix needs to be updated in the process of nonlinear analysis. In this paper, the third item Kx in equation of motion Eq.(1) is considered as an unknown variable, and a new $\mathbf{F}(\boldsymbol{x}, t)$ combining the external force vector $\mathbf{f}(\boldsymbol{x}, t)$ and internal force vector Kx is formed. Then, the equation of motion is rewritten as,

$$\mathbf{M}\ddot{\boldsymbol{x}} + \mathbf{C}\dot{\boldsymbol{x}} = \mathbf{f}(\boldsymbol{x}, t) - \mathbf{K}\boldsymbol{x} = \mathbf{F}(\boldsymbol{x}, t) \tag{11}$$

To obtain a coarser matrix with the left half being a null matrix, a new vector p representing the velocity is introduced.

$$\boldsymbol{p} = \dot{\boldsymbol{x}} \tag{12}$$

Writing Eq.(11) and Eq.(12) in matrix form, we have,

$$\boldsymbol{u} = \begin{bmatrix} \boldsymbol{x} \\ \dot{\boldsymbol{x}} \end{bmatrix}, \qquad \boldsymbol{u} = \mathbf{H}\dot{\boldsymbol{u}} + \mathbf{F} \tag{13}$$

in which,

$$\mathbf{H} = \begin{bmatrix} \mathbf{0} & \boldsymbol{I} \\ \mathbf{0} & -\mathbf{M}^{-1}\mathbf{C} \end{bmatrix} \tag{14}$$

$$\mathbf{F} = \begin{bmatrix} \mathbf{0} \\ \mathbf{F}(\boldsymbol{x}, t) \end{bmatrix} = \begin{bmatrix} \mathbf{0} \\ \mathbf{M}^{-1}\mathbf{f}(\boldsymbol{x}, t) - \mathbf{M}^{-1}\mathbf{K}\boldsymbol{x} \end{bmatrix} \tag{15}$$

With a simpler transfer matrix H, the equation of motion is converted to a differential equation of one order. The absolute solution of Eq.(13) with Duhamel integral is given mathematically as Eq.(16).

$$\boldsymbol{u}(\mathrm{t}) = \exp(\mathbf{H}t)\,\boldsymbol{x}(0) + \int_0^t \exp\left(\mathbf{H}(t-\tau)\right) \mathbf{F}(x, \tau) d\tau \tag{16}$$

For elastic problem with constant stiffness matrix, an exact solution can be achieved with a different H matrix and external force $\mathbf{F}(\boldsymbol{x}, t)$ represented by Eq.(17) and Eq.(18) respectively.

$$\mathbf{H} = \begin{bmatrix} \mathbf{0} & \boldsymbol{I} \\ -\mathbf{M}^{-1}\mathbf{K} & -\mathbf{M}^{-1}\mathbf{C} \end{bmatrix} \tag{17}$$

$$\mathbf{F}(\boldsymbol{x}, t) = \begin{bmatrix} \mathbf{0} \\ \mathbf{M}^{-1}\mathbf{f}(t) \end{bmatrix} \tag{18}$$

3.2. Solution of differential equation

For easier numerical integration, the total time is divided into a series of step time η with time points given as,

$$t_0 = 0,\ t_1 = \eta,\ t_2 = 2\eta, \ldots,\ t_k = k\eta,\ t_{k+1} = (k+1)\eta, \ldots \tag{19}$$

The integration equation of Eq.(16) can be given as Eq.(20) with step time denoted by subscript k.

$$\boldsymbol{u}_{k+1} = \boldsymbol{\Phi}\boldsymbol{u}_k + \int_0^t \exp\big(\mathbf{H}(t_k-\tau)\big)\,\mathbf{F}(\boldsymbol{x}_k,\tau)\,d\tau \tag{20}$$

in which,

$$\boldsymbol{\Phi} = \exp(\mathbf{H}\eta) \tag{21}$$

Writing the formed 'external force' $\mathbf{F}(\boldsymbol{x},t)$ in Polynomial form for easy integration,

$$\mathbf{F}(\boldsymbol{x}_k,t_k+\tau) = \boldsymbol{f}_{0,k} + \tau\boldsymbol{f}_{1,k} + \cdots + \tau^m\boldsymbol{f}_{m,k} \quad \tau\in[0,\eta] \tag{22}$$

Substituting Eq.(22) into the general solution Eq.(20), the recursion formula can be derived as,

$$\boldsymbol{v}_{k+1} = \boldsymbol{\Phi}\boldsymbol{v}_k + \eta\boldsymbol{\Phi}_0\boldsymbol{f}_{0,k} + \cdots + \eta^{m+1}\boldsymbol{\Phi}_m\boldsymbol{f}_{m,k} \tag{23}$$

in which,

$$\boldsymbol{\Phi}_m = \frac{1}{\eta^{m+1}}\int_0^\eta \exp\big(\mathbf{H}(\eta-\tau)\big)\,\tau^m\,d\tau \tag{24}$$

Dividing the step time η into smaller time intervals τ with the following equation,

$$\tau = \eta/2^N \tag{25}$$

N is an integer ideally to be large enough so that the exponential of the matrix in Eq. (21) can be calculated with Taylor series. The value of N was recommended as 20 by Zhong [11], which is adequate to achieve a precise value of coefficient $\boldsymbol{\Phi}$, and this value for N can also be adopted to calculate $\boldsymbol{\Phi}_m$ as described below.

To reduce the error in storing the elements in $\boldsymbol{\Phi}$ and $\boldsymbol{\Phi}_m$, expanding Eq.(21) and Eq.(24) with Taylor series and extracting the parts with higher orders,

$$\boldsymbol{\Phi}(\tau) = \mathbf{I} + \mathbf{H}\tau + \frac{(\mathbf{H}\tau)^2}{2!} + \cdots + \frac{(\mathbf{H}\tau)^l}{l!} = \mathbf{I} + \boldsymbol{\Phi}_a \tag{26}$$

$$\begin{aligned}\boldsymbol{\Phi}_m(\tau) &= \frac{1}{m+1}\mathbf{I} + \frac{1}{\eta^{m+1}}\sum_{j=1}^{\infty}\frac{(\mathbf{H}\tau)^j}{j!}\int_0^\eta \tau^j(\eta-\tau)^m\,d\tau \\ &= \frac{1}{m+1}\mathbf{I} + \boldsymbol{\Phi}_{b,m}\end{aligned} \tag{27}$$

The coefficients $\boldsymbol{\Phi}_a$ and $\boldsymbol{\Phi}_b$ can be obtained by several times (20 times if N=20) of iteration according to the addition theorem given by Zhong [11] and Tan [32], and the iteration equations are derived as

$$\boldsymbol{\Phi}_a = \boldsymbol{\Phi}_a(2\mathbf{I} + \boldsymbol{\Phi}_a) \tag{28}$$

$$\begin{aligned}\boldsymbol{\Phi}_b = \frac{1}{2^{m+1}}\Big[\boldsymbol{\Phi}_a\Big(\frac{1}{m+1}\mathbf{I} + \boldsymbol{\Phi}_{b,m}\Big) + 2\boldsymbol{\Phi}_{b,m} + \mathrm{C}_m^1\boldsymbol{\Phi}_{b,m-1} \\ + \mathrm{C}_m^2\boldsymbol{\Phi}_{b,m-2} + \cdots\Big]\end{aligned} \tag{29}$$

3.3. Refined solution of inhomogeneous term

The coefficients in the recursion formula Eq. (23) can be achieved from the above procedures and only the $\boldsymbol{f}_{m,k}$ expanded from 'external force' $\mathbf{F}(\boldsymbol{x},t)$ is unsolved. Taylor series expansion can be used as described by Tan [32], but derivatives are required for relatively more accurate results which is quite difficult to obtain. The explicit method with Lagrange interpolation function is also provided in [32].

The Lagrange polynomials 'external force' $\mathbf{F}(\boldsymbol{x},t)$ within the time period $[t_k,t_{k+1}]$ is given as Eq.(30), in which $\tau\in[0,\eta]$.

$$\begin{aligned}\tilde{\mathbf{F}}(\boldsymbol{x}_k,t_k+\tau) = \boldsymbol{f}_k + \frac{11\boldsymbol{f}_k/6 - 3\boldsymbol{f}_{k1} + 3\boldsymbol{f}_{k2}/2 - \boldsymbol{f}_{k3}/3}{\eta}\tau \\ + \frac{\boldsymbol{f}_k - 5\boldsymbol{f}_{k1}/2 + 2\boldsymbol{f}_{k2} - \boldsymbol{f}_{k3}/2}{\eta^2}\tau^2 \\ + \frac{\boldsymbol{f}_k/6 - \boldsymbol{f}_{k1}/2 + \boldsymbol{f}_{k2}/2 - \boldsymbol{f}_{k3}/6}{\eta^3}\tau^3\end{aligned} \tag{30}$$

Comparing Eq.(30) with Eq.(22) leading to,

$$\begin{aligned}\boldsymbol{f}_{0,k} &= \boldsymbol{f}_k,\ \boldsymbol{f}_{1,k} = \frac{11\boldsymbol{f}_k/6 - 3\boldsymbol{f}_{k1} + 3\boldsymbol{f}_{k2}/2 - \boldsymbol{f}_{k3}/3}{\eta} \\ \boldsymbol{f}_{2,k} &= \frac{\boldsymbol{f}_k - 5\boldsymbol{f}_{k1}/2 + 2\boldsymbol{f}_{k2} - \boldsymbol{f}_{k3}/2}{\eta^2} \\ \boldsymbol{f}_{3,k} &= \frac{\boldsymbol{f}_k/6 - \boldsymbol{f}_{k1}/2 + \boldsymbol{f}_{k2}/2 - \boldsymbol{f}_{k3}/6}{\eta^3}\end{aligned} \tag{31}$$

Substituting Eq.(31) into Eq.(22), the recursion formula is then established as,

$$\boldsymbol{u}_{k+1} = \boldsymbol{\Phi}\boldsymbol{u}_k + \eta(\bar{\boldsymbol{\Phi}}_0\boldsymbol{f}_k + \bar{\boldsymbol{\Phi}}_1\boldsymbol{f}_{k-1} + \bar{\boldsymbol{\Phi}}_2\boldsymbol{f}_{k-2} + \bar{\boldsymbol{\Phi}}_3\boldsymbol{f}_{k-3}) \tag{32}$$

in which,

$$\begin{aligned}\bar{\boldsymbol{\Phi}}_0 &= \boldsymbol{\Phi}_0 + 11\boldsymbol{\Phi}_1/6 + \boldsymbol{\Phi}_2 + \boldsymbol{\Phi}_3/6 \\ \bar{\boldsymbol{\Phi}}_1 &= -3\boldsymbol{\Phi}_1 - 5\boldsymbol{\Phi}_2/2 - \boldsymbol{\Phi}_3/2 \\ \bar{\boldsymbol{\Phi}}_2 &= 3\boldsymbol{\Phi}_1/2 + 2\boldsymbol{\Phi}_2 + \boldsymbol{\Phi}_3/2 \\ \bar{\boldsymbol{\Phi}}_3 &= -\boldsymbol{\Phi}_1/3 - \boldsymbol{\Phi}_2/2 - \boldsymbol{\Phi}_3/6\end{aligned} \tag{33}$$

In structural engineering, the external forces are known and linearly distributed during each time increment. In commercial software package like ABAQUS [7], the amplitudes of external forces during analysis are given by tubular, periodic or other curves with specific functions. To solve structural problems, the external force can be written as a linear function in the time domain $[t_k,t_{k+1}]$ as,

$$\mathbf{f}(t_k+\tau) = \mathbf{f}_k + \tau(\mathbf{f}_{k+1} - \mathbf{f}_k)/\eta \tag{34}$$

For this external part, the exact result can be provided with Duhamel integration at $[t_k,t_{k+1}]$.

3.4. Simplification of coefficient matrices

Sparse matrices are obtained for $\boldsymbol{\Phi}$ and $\boldsymbol{\Phi}_m$ by introducing velocity vector, differing from the expression shown in Eq. (6) and Eq.(7), written as,

$$\boldsymbol{\Phi} = \begin{bmatrix}\mathbf{I} & \mathbf{T}_{12}\\ \mathbf{0} & \mathbf{T}_{22}\end{bmatrix} \tag{35}$$

$$\boldsymbol{\Phi}_m = \begin{bmatrix}\mathbf{I} & \boldsymbol{\Phi}_{m1}\\ \mathbf{0} & \boldsymbol{\Phi}_{m2}\end{bmatrix} \tag{36}$$

The upper-left part of the matrices $\boldsymbol{\Phi}$ and $\boldsymbol{\Phi}_m$ is an identity matrix and the bottom-left part is a null matrix, leading to much simpler calculation. In structural engineering, the Rayleigh damping [33] is often adopted which is proportional to the mass matrix $\mathbf{M}$ and stiffness matrix $\mathbf{K}$, defined as,

$$\mathbf{C} = \alpha\mathbf{M} + \beta\mathbf{K} \tag{37}$$

The coefficient β is often ignored in structural analysis and such that the matrix in Eq. (14) becomes,

$$\mathbf{H} = \begin{bmatrix} \mathbf{0} & \mathbf{I} \\ \mathbf{0} & -\mathbf{M}^{-1}\mathbf{C} \end{bmatrix} = \begin{bmatrix} \mathbf{0} & \mathbf{I} \\ \mathbf{0} & -\alpha\mathbf{I} \end{bmatrix} \tag{38}$$

In this case, the $\mathbf{H}$ matrix is simplified as a 2×2 matrix $\mathbf{H}'$ adopted directly in the iteration to calculate the coefficient matrix $\boldsymbol{\Phi}$,

$$\mathbf{H}' = \begin{bmatrix} 0 & 1 \\ 0 & -\alpha \end{bmatrix} \tag{39}$$

Then, the coefficient matrix $\boldsymbol{\Phi}$ becomes a matrix with two different constant coefficients as described as $\boldsymbol{\Phi}'$,

$$\boldsymbol{\Phi}' = \begin{bmatrix} 1 & c_1 \\ 0 & c_2 \end{bmatrix} \tag{40}$$

Thus, a large amount of computation time and memory storage could be saved with respect to both the calculation of coefficients and the recursion formula to obtain the displacements and velocities, regardless of the form of mass matrix (consistent mass matrix, or lumped mass matrix). In software packages like ABAQUS [7] and OpenSees [8], the lumped mass matrix can be adopted for explicit dynamic analysis for the benefit of simplicity when calculating the inverse of mass matrix. The advantage of the reduced matrix also applies to the calculation of coefficients $\boldsymbol{\Phi}_0$, $\boldsymbol{\Phi}_1$, $\boldsymbol{\Phi}_2$ and $\boldsymbol{\Phi}_3$. After the linear operation of $\boldsymbol{\Phi}_m$, similar 2×2 matrix with constant values can be established as,

$$\begin{aligned} \bar{\boldsymbol{\Phi}}_0 = \begin{bmatrix} \bar{\Phi}_{01} \\ \bar{\Phi}_{02} \end{bmatrix}, \bar{\boldsymbol{\Phi}}_1 = \begin{bmatrix} \bar{\Phi}_{11} \\ \bar{\Phi}_{12} \end{bmatrix}, \bar{\boldsymbol{\Phi}}_2 = \begin{bmatrix} \bar{\Phi}_{21} \\ \bar{\Phi}_{22} \end{bmatrix}, \bar{\boldsymbol{\Phi}}_3 \\ = \begin{bmatrix} \bar{\Phi}_{31} \\ \bar{\Phi}_{32} \end{bmatrix} \end{aligned} \tag{41}$$

It should be noted that matrix F in Eq. (15) is a vector with zero elements in the upper half, and such that the left half coefficients of matrices in Eq. (41) have no impact on the recursion results. Up to this step, all the coefficients required in the recursion formulation Eq. (41) have been converted to simple constant values, and the multiplication between matrices and vectors becomes much simpler multiplication between constant values and vectors, which greatly simplifies the calculation and saves a large amount of computation time and memory storage.

4. The algorithm of RPIM

For linear analysis, the stiffness matrix K is constant, and exact results can be derived with a different H matrix given in Eq. (17). This accurate method for linear analysis is defined as the accurate precise integration method (APIM) in this paper.

$$\begin{aligned} \boldsymbol{x}_{k+1} &= \boldsymbol{T}_{11}\boldsymbol{x}_k + \boldsymbol{T}_{12}\boldsymbol{v}_k + \eta\mathbf{M}^{-1}[\boldsymbol{\Phi}_{01}\boldsymbol{f}_k + \boldsymbol{\Phi}_{11}(\boldsymbol{f}_{k+1} - \boldsymbol{f}_k)] \\ \boldsymbol{v}_{k+1} &= \boldsymbol{T}_{21}\boldsymbol{x}_k + \boldsymbol{T}_{22}\boldsymbol{v}_k + \eta\mathbf{M}^{-1}[\boldsymbol{\Phi}_{02}\boldsymbol{f}_k + \boldsymbol{\Phi}_{12}(\boldsymbol{f}_{k+1} - \boldsymbol{f}_k)] \end{aligned} \tag{42}$$

For nonlinear analysis with variable stiffness matrix K, a refined explicit method, with the introduction of the velocity vector Eq. (12) and consideration of K as an unknown variable, is given in Eq. (43) based on the PIM and Duhamel integration. This method is defined as refined precise integration method (RPIM).

$$\begin{aligned} \boldsymbol{x}_{k+1} &= \boldsymbol{x}_k + \boldsymbol{T}_{12}\boldsymbol{v}_k + \eta\mathbf{M}^{-1}[\Phi_{01}\boldsymbol{f}_k + \Phi_{11}(\boldsymbol{f}_{k+1} - \boldsymbol{f}_k)] \\ &\quad + \eta\mathbf{M}^{-1}(\bar{\Phi}_{01}\mathbf{K}_k\boldsymbol{x}_k + \bar{\Phi}_{11}\mathbf{K}_{k-1}\boldsymbol{x}_{k-1} \\ &\quad + \bar{\Phi}_{21}\mathbf{K}_{k-2}\boldsymbol{x}_{k-2} + \bar{\Phi}_{31}\mathbf{K}_{k-3}\boldsymbol{x}_{k-3}) \\ \boldsymbol{v}_{k+1} &= \boldsymbol{T}_{22}\boldsymbol{v}_k + \eta\mathbf{M}^{-1}[\Phi_{02}\boldsymbol{f}_k + \Phi_{12}(\boldsymbol{f}_{k+1} - \boldsymbol{f}_k)] \\ &\quad + \eta\mathbf{M}^{-1}(\bar{\Phi}_{02}\mathbf{K}_k\boldsymbol{x}_k + \bar{\Phi}_{12}\mathbf{K}_{k-1}\boldsymbol{x}_{k-1} \\ &\quad + \bar{\Phi}_{22}\mathbf{K}_{k-2}\boldsymbol{x}_{k-2} + \bar{\Phi}_{32}\mathbf{K}_{k-3}\boldsymbol{x}_{k-3}) \end{aligned} \tag{43}$$

It should be noted that the RPIM is also applicable to linear dynamic analysis with constant K matrix. To evaluated the efficiency of the proposed RPIM, two methods, derived from the vectors given in Eq.(6) and Eq.(7), are used as references. They are named as p-vector precise integration method (PPIM) and monument precise integration method (MPIM) respectively. The stiffness matrices K in both the PPIM and MPIM are treated as an unknown variable for better comparison with the RPIM.

To incorporate the APIM, RPIM, PPIM, and MPIM into the program for the dynamic analysis, the first step is to form H matrix and calculate the coefficients required in each method. Then the displacements and velocities at the next time step could be achieved with the recursion formulas in Eq. (42) or Eq. (43). It should be noted that only the APIM is self-starting while the displacements and velocities in the first three steps are required in the other three methods (e.g., RPIM, PPIM, and MPIM). In this paper, the CDM is adopted to calculate the required parameters for both linear and nonlinear problems. The algorithm flowchart of the RPIM, PPIM, and MPIM for nonlinear dynamic analysis is detailed in Fig. 1. The APIM for linear analysis is omitted in flowchart since the only difference is no requirement on the first three steps with the CDM as well as updating stiffness matrix K. For linear analysis with RPIM, PPIM, and MPIM, the step of updating K should be neglected and replaced with constant K.

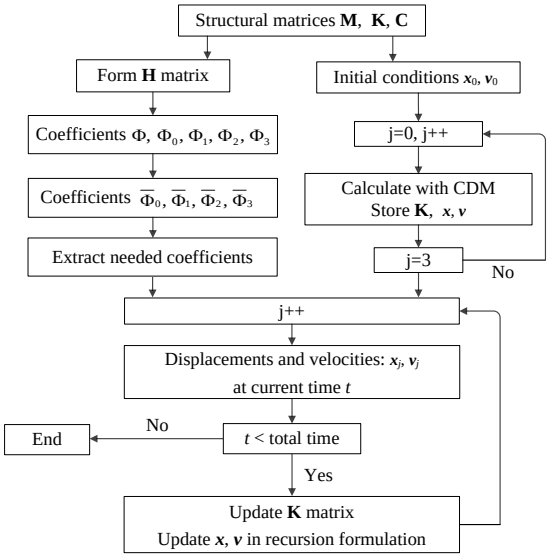

Fig. 1 Algorithm flowchart of the RPIM, PPIM, and MPIM for nonlinear dynamic analysis

5. Stability and precision analysis

The stability and precision are the two most important characteristics of an algorithm [34], and the performance of the RPIM will be evaluated in this section.

5.1. Stability analysis

The stability of a recursion formula is defined as whether the solution from recursion formula at any step time will increase infinitely with the initial conditions and rounding error in recursion. The recursion formula is unconditionally stable if the solution will not magnify without limits at any step time. To achieve unconditional stability, the coefficient $\boldsymbol{\Phi}$ must have a boundary, which means the spectral radius of $\boldsymbol{\Phi}$ cannot be greater than 1, as expressed in Eq. (44),

$$\rho(\boldsymbol{\Phi}) = \max|\lambda_i| \leq 1 \tag{44}$$

in which, λ_i is the eigenvalue of $\boldsymbol{\Phi}$.

Stability analysis of the typical equation of motion with one DOF system is commonly used to verify the stability of the algorithms [35] due to the satisfaction of the mode superposition technique. The equation of motion of a structure with one DOF is defined as,

$$\ddot{x} + 2\xi\dot{x} + \omega^2 x = f(t) \tag{45}$$

in which, ξ is the damping ratio and ω is the circular frequency of the structure, with the relation presented as,

$$\xi = \frac{c}{2m\omega} \tag{46}$$

where m is the mass, and c is the damping of the structure.

The matrix H in Eq. (14) is then established as,

$$\mathbf{H}=\begin{bmatrix}0 & 1\\ 0 & -\dfrac{c}{m}\end{bmatrix}=\begin{bmatrix}0 & 1\\ 0 & -2\xi\omega\end{bmatrix} \tag{47}$$

As derived in Eq. (21), matrix $\boldsymbol{\Phi}$ can be obtained by substituting Eq. (28) into Eq. (26) as,

$$\boldsymbol{\Phi}=\begin{bmatrix}1 & -\dfrac{f-1}{2\xi\omega\tau}\\ 0 & f\end{bmatrix} \tag{48}$$

in which,

$$f=1+(-2\xi\omega\tau)+\frac{(-2\xi\omega\tau)^2}{2!}+\frac{(-2\xi\omega\tau)^3}{3!}+\cdots+\frac{(-2\xi\omega\tau)^n}{n!} \tag{49}$$

The two eigenvalues of matrix $\boldsymbol{\Phi}$ are $\lambda_1=1$ and $\lambda_2=f$ respectively. Thus, the spectral radius of $\boldsymbol{\Phi}$ is obtained as

$$\rho(\boldsymbol{\Phi})=\max(\lambda_1,\lambda_2)=\max(1,|f|) \tag{50}$$

As seen from Eq. (50), the spectral radius of $\boldsymbol{\Phi}$ depends on $|f|$. When the number of calculation term n tends to infinity, the following relation is obtained,

$$|f|=e^{-2\xi\omega\tau}<1,\qquad n\to\infty \tag{51}$$

When the period τ tends to be zero, the spectral radius of $\boldsymbol{\Phi}$ equals to 1, and thus the RPIM is unconditionally stable.

$$\rho(\boldsymbol{\Phi})=\max(1,|f|)=\max(1,1)=1,\qquad \tau\to 0 \tag{52}$$

In practice, only limited number of terms in f are calculated with Eq. (49). Therefore, it is necessary to evaluate the stability with only several terms calculated in f. The curves of the ratio of calculation time period to basic period of structure τ/T and value of $|f|$ with different numbers of expanding terms n are illustrated in Fig. 2.

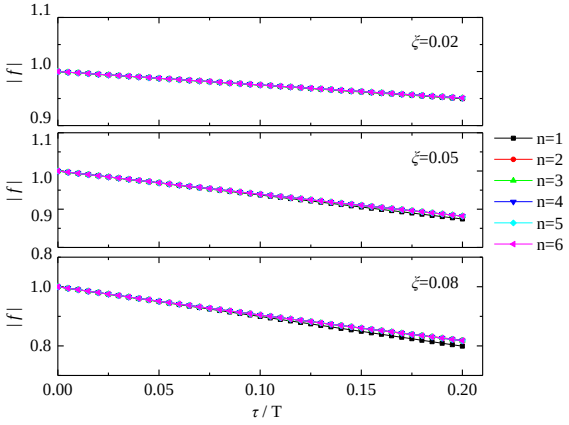

Fig. 2 Curves of τ/T and $|f|$ with different damping ratios

The curves with the damping ratio ξ = 0.02, 0.05 and 0.08 are given in Fig. 2, within the commonly used range of structural damping ratios. According to Chinese code GB50011 [36], the damping ratio for structures is adopted as 0.05 without special instructions. Typically, 0.03~0.08 is often adopted for reinforced concrete structures, and 0.02~0.05 is often employed for steel structures. The period τ from Eq. (25) is very small, leading to the time ratio τ/T very close to zero. As clearly seen in Fig. 2, the values of $|f|$ under different damping ratios are less than 1, indicating the spectral radius of $\boldsymbol{\Phi}$ satisfying the spectral requirement. Thus, the unconditional spectral stability of the RPIM is demonstrated theoretically.

5.2. Accuracy analysis

During the derivation of recursion formula for equation of motion, the only approximation exists in the integration of inhomogeneous terms Kx. Considering from the beginning of the derivation, the recursion formulation of Eq. (13) can be written as

$$\boldsymbol{u}_{k+1}=\boldsymbol{\Phi}\boldsymbol{u}_k+\eta(\bar{\boldsymbol{\Phi}}_0\mathbf{F}_k+\bar{\boldsymbol{\Phi}}_1\mathbf{F}_{k-1}+\bar{\boldsymbol{\Phi}}_2\mathbf{F}_{k-2}+\bar{\boldsymbol{\Phi}}_3\mathbf{F}_{k-3}) \tag{53}$$

Expanding the $\mathbf{F}_{k-1}$, $\mathbf{F}_{k-2}$ and $\mathbf{F}_{k-3}$ at $\mathbf{F}_k$ with Taylor series, then Eq.(53) can be written as,

$$\begin{aligned}\boldsymbol{u}_{k+1}=\boldsymbol{\Phi}\boldsymbol{u}_k+\eta\bar{\boldsymbol{\Phi}}_0\left(\boldsymbol{u}_k^{(1)}-\boldsymbol{u}_k\right)\\ +\sum_{j=0}^{\infty}\left(\frac{(-\eta)^j}{j!}\bar{\boldsymbol{\Phi}}_1+\frac{(-2\eta)^j}{j!}\bar{\boldsymbol{\Phi}}_2\right.\\ \left.+\frac{(-3\eta)^j}{j!}\bar{\boldsymbol{\Phi}}_3\right)\left(\boldsymbol{u}_k^{(j+1)}-\boldsymbol{u}_k^{(j)}\right)\end{aligned} \tag{54}$$

Combining the addition theorem in Eq. (28) ~ (29) and the coefficients in Eq. (33),

$$\begin{aligned}\boldsymbol{u}_{k+1}=\boldsymbol{u}_k+\eta\boldsymbol{u}_k^{(1)}+\frac{\eta^2}{2}\boldsymbol{v}_k^{(2)}+\frac{\eta^3}{6}\boldsymbol{u}_k^{(3)}+\frac{\eta^4}{24}\boldsymbol{u}_k^{(4)}\\ +\frac{\eta^5}{24}\left(-\frac{15}{2}\boldsymbol{u}_k^{(5)}-\frac{77}{10}\mathbf{H}\boldsymbol{u}_k^{(4)}+O(\eta)\right)+\cdots\end{aligned} \tag{55}$$

Thus, the RPIM with three-point Lagrange interpolation method has the precision of $O(\Delta t^5)$. From Eq.(54), it can be seen that the accuracy of the RPIM is closely related to the time increment Δt.

6. Verification examples

Several examples are analyzed to assess the accuracy and efficiency of the proposed RPIM in dealing with linear and nonlinear dynamic analysis of structures. Two linear elastic analysis cases with specific matrices, free vibration and forced vibration with constant and varied external forces, are given to provide better understanding and easier duplication of the RPIM, as well as a demonstration of application in linear dynamic analysis. In linear dynamic analysis, results from the six different methods, namely ODE45(MATLAB), APIM, CDM, RPIM, MPIM, and PPIM, are provided and discussed. The results from function ode45 in MATLAB are set as references, in which the fourth-order and fifth-order Runge-Kutta algorithm is adopted with varied time increments, most commonly used for nonstiff problems [37]. In nonlinear dynamic analysis, only results from the last four methods are provided due to the inapplicability of the first two methods for nonlinear problems.

6.1. Free vibration with damping

A damped system with initial displacement at the top mass 3 is employed in this example, as shown in Fig. 3, to verify the accuracy and efficiency of the RPIM. The mass matrix M and stiffness matrix K are given directly as follows, with the damping matrix proportional to mass matrix with the relationship C=0.2M. The initial displacement vector is given as $x_0=[0;0;5]$ and the initial velocity vector $\dot{x}_0=[0;\ 0;0]$ is adopted.

$$\mathbf{M}=\begin{bmatrix}100 & 0 & 0\\ 0 & 100 & 0\\ 0 & 0 & 100\end{bmatrix}$$

$$\mathbf{K}=10^2\begin{bmatrix}200 & -100 & 0\\ -100 & 200 & -100\\ 0 & -100 & 200\end{bmatrix}$$

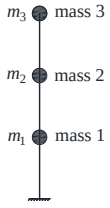

Fig. 3 Configuration of a 3-DOF system with free vibration

The displacement of mass 3 is monitored, and time-displacement curves obtained from the six methods are figured with two different time increments Δt=0.005s (Fig. 4(a), (b)) and Δt=0.02s (Fig. 4(c), (d)). The MPIM and PPIM

provide exactly the same results as RPIM, because they are essentially the same method with the only difference in introduced vector p as discussed in section 3. Thus, results from MPIM and PPIM are figured only when Δt=0.005s, and are also omitted in the following verification examples to display results more clearly and intuitively.

As shown in Fig. 4(a) and (b), both the CDM and RPIM predict very accurate results at time increment Δt=0.005s. As the time increment increases to 0.02s, the APIM method can still provide accurate results, the same as those from MATLAB, since there is no approximation in the APIM. Results from the RPIM are acceptable with the same variation tendency, while results from the CDM is quite unsatisfying with either too high or too low value as well as wrong variation tendency, as illustrated in Fig. 4(c) and (d).

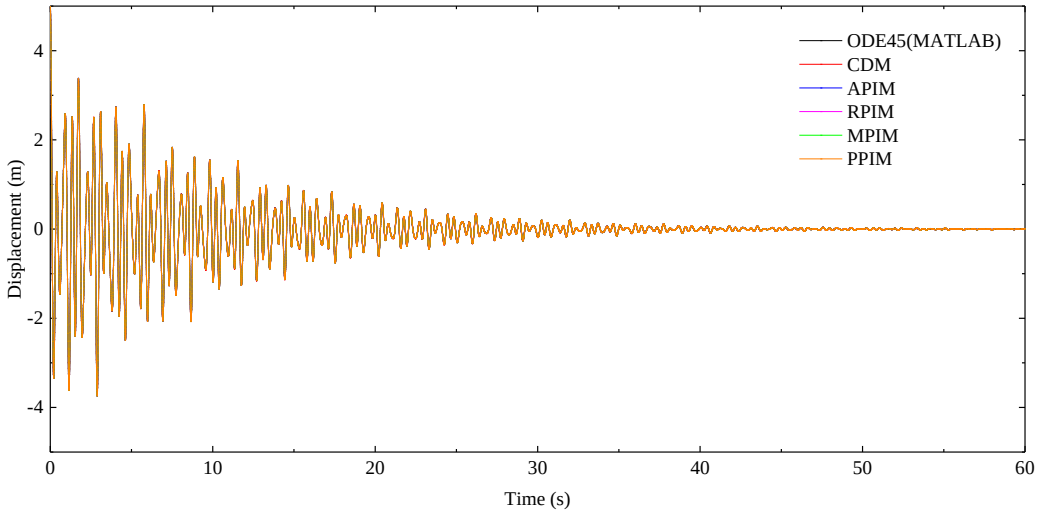

(a) Displacements in one minute with time increment Δt =0.005s

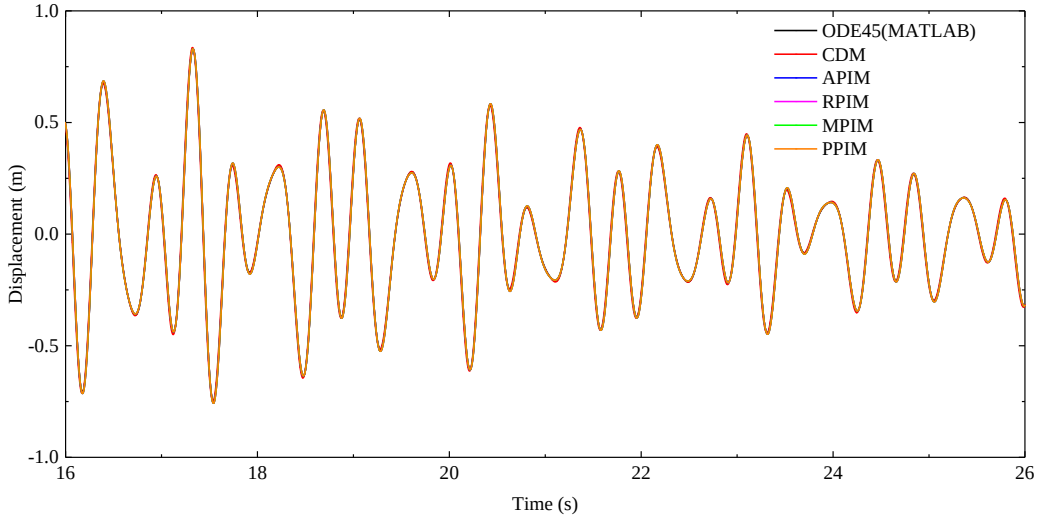

(b) Displacements from 16s to 26s with time increment Δt = 0.005s

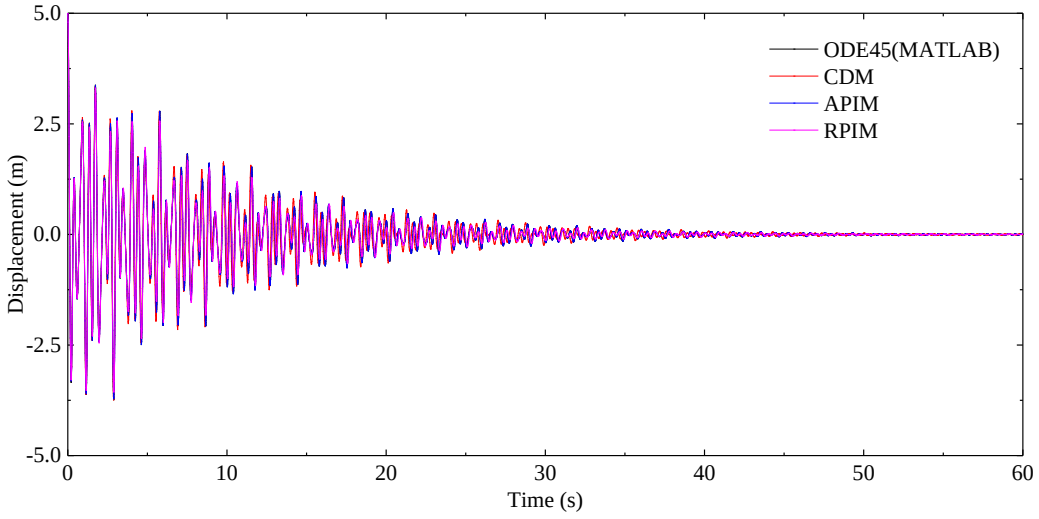

(c) Displacements in one minute with time increment Δt = 0.02s

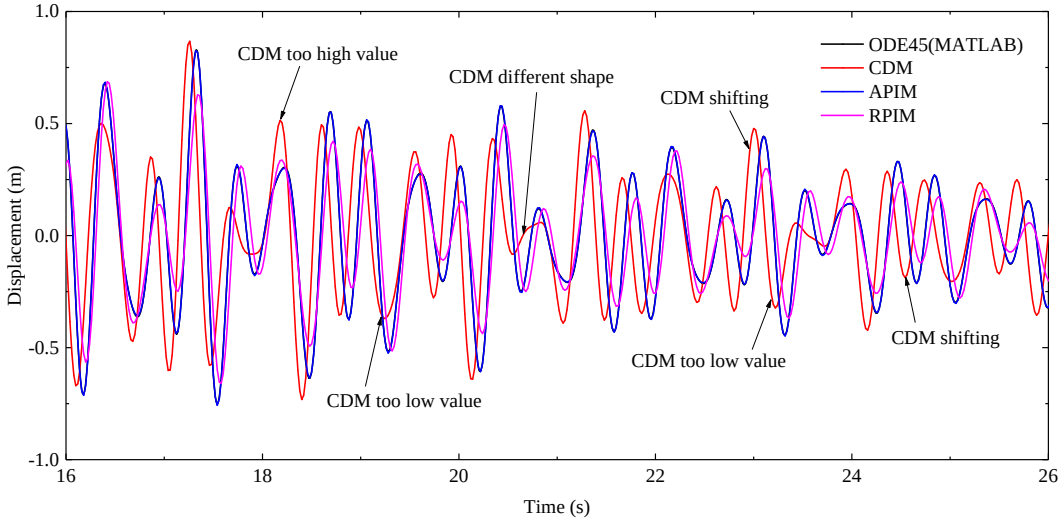

(d) Displacements from 16s to 26s with time increment Δt = 0.02s

Fig. 4 Time-displacement curves of mass 3 during free vibration

The computational time of the RPIM, MPIM, and PPIM with different time increments are illustrated in Fig. 5, and the time reduction percentages of the RPIM compared with the PPIM are also figured. The time consumed by the MPIM is a little lower than the PPIM, but both cost more time than the RPIM. On average, about 65% computational time is reduced with the RPIM, demonstrating extraordinary efficiency of the proposed RPIM. The efficiency of RPIM is largely contributed by the reduced exponential matrix with the introduction of velocity vector.

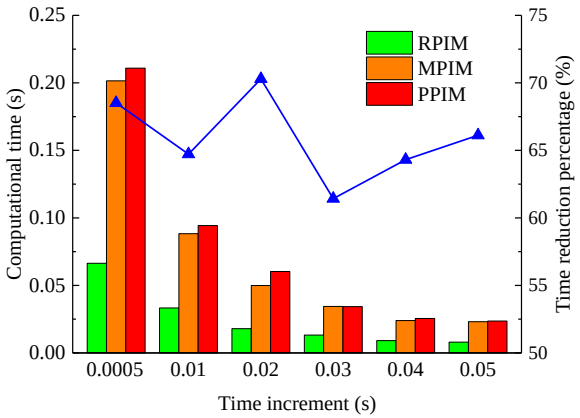

Fig. 5 Computational time and time reduction percentage during free vibration

6.2. Forced vibration with damping

This example is an extension of the free vibration case in section 6.1 with the same M, K and C matrices. However, the different initial displacement $x_0 = [0;\ 0;\ 0]$ and constant force vector defined as follow are adopted in this case.

$$\boldsymbol{F}(t) = [0;\ 0;\ 100]$$

Similarly, the time-displacement curves of mass 3 obtained from the six different methods are given in Fig. 6. Exact results are provided by both the CDM and RPIM at time increment Δt=0.005s, as shown in Fig. 6(a) and (b). As clearly seen from Fig. 6(c) and (d), results from the CDM are unsatisfying with inaccurate peak values and wrong tendency prediction at time increment Δt=0.02s, in shape contrast to satisfying solutions provided by the proposed RPIM. Meanwhile, 35% computational time on average is economized with the RPIM when comparing with the PPIM, as illustrated in Fig. 7. It should be noted that the MPIM consumes a little fewer time than the PPIM, benefiting from simpler H matrix. Thus, superior accuracy and efficiency of RPIM are demonstrated with the ability of providing accurate results compared with the CDM and computational effort saving compared with the PPIM and MPIM.

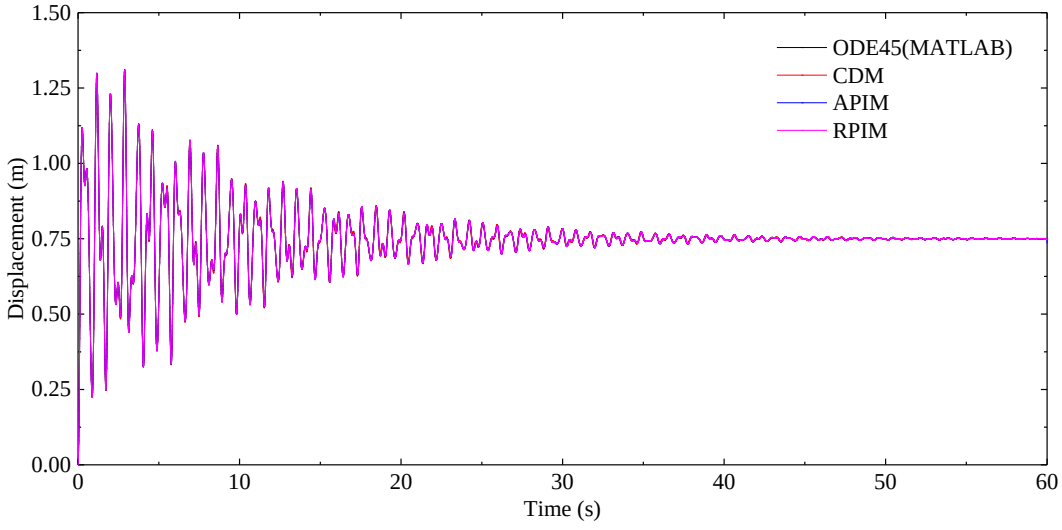

(a) Displacements in one minute with time increment Δt = 0.005s

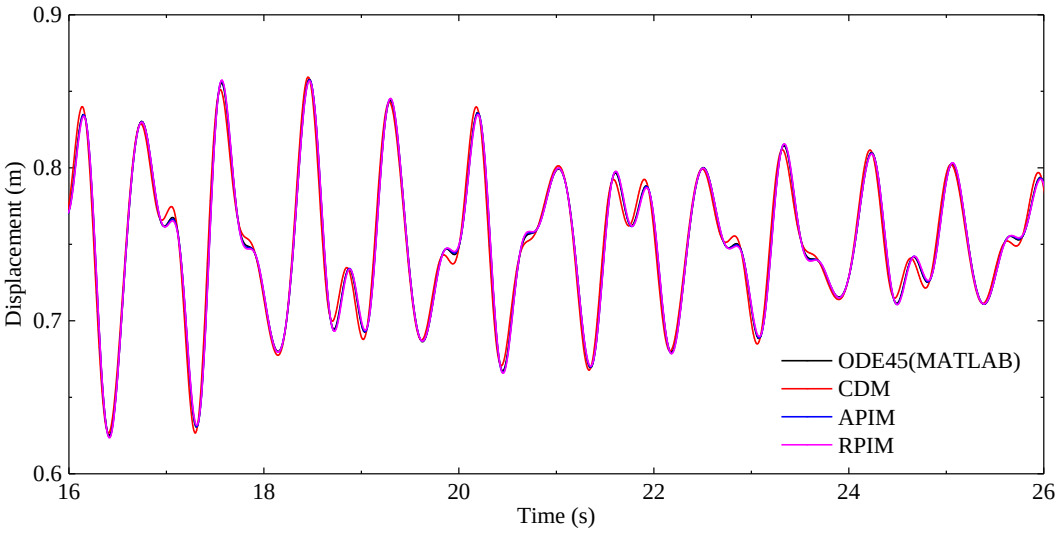

(b) Displacements from 16s to 26s with time increment Δt = 0.005s

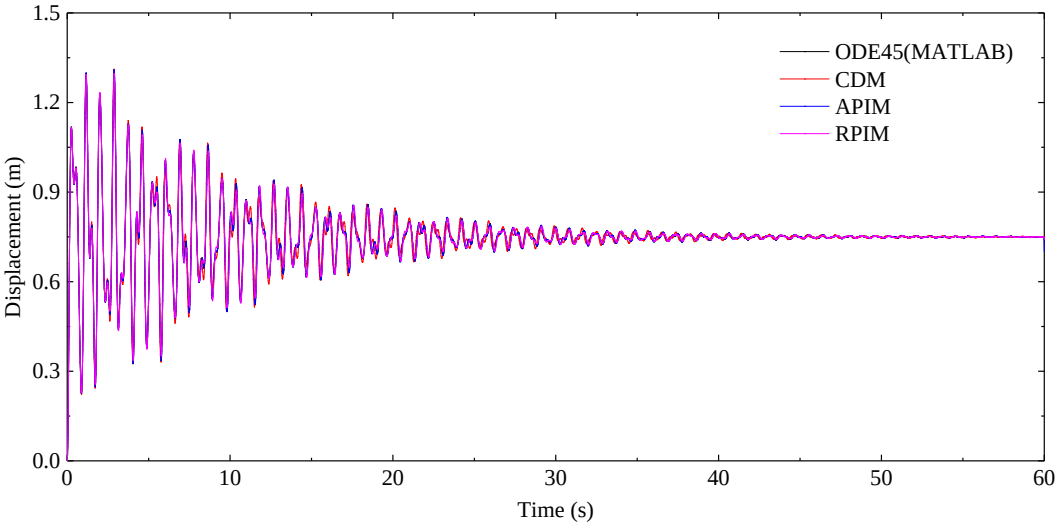

(c) Displacements in one minute with time increment Δt = 0.02s

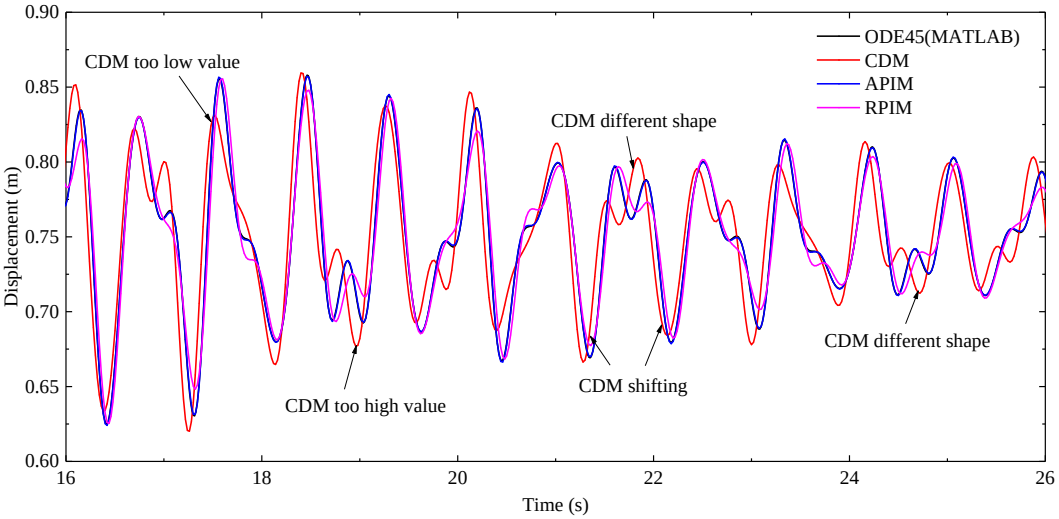

(d) Displacements from 16s to 26s with time increment Δt = 0.02s

Fig. 6 Time-displacement curves of mass 3 during forced vibration with constant force

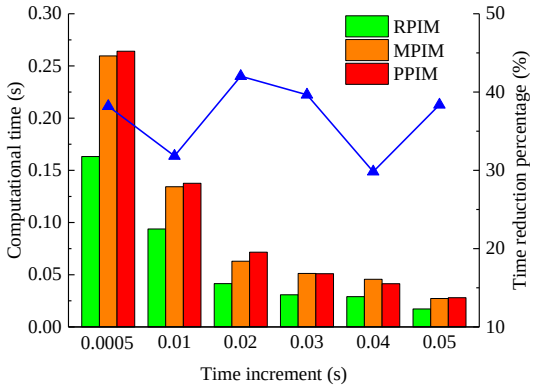

Fig. 7 Computational time and time reduction percentage during forced vibration with constant force

To assess the accuracy and efficiency of the RPIM in dealing with different forms of external loads, a varied external force with sine function is adopted written as,

$$\boldsymbol{F}(t) = [0;\ 0;\ 100]\sin(4\pi t)$$

For simplicity, only results at time increment 0.02s from different methods are given in Fig 8, Results provided by the CDM are unstable with either too high or too low values, oscillating from the accurate solutions. Nevertheless, the RPIM provides much more accurate results, as shown in Fig. 8. In addition, as shown in Fig. 9, about 35% computational time is saved with the RPIM, similar to the percentage in the case with constant external force while less than the 65% in free vibration case. Reason for the decline of efficiency in forced vibration is that multiply operation of inversed mass matrix, and the external force is involved in each step for the RPIM, which occupying larger percentage of computational time than the calculation of exponential matrix. Nevertheless, more computational time will be saved if the external force is in the form of nodal acceleration, for example the seismic problems, since no multiply operation is required as in this case with concentrated nodal force.

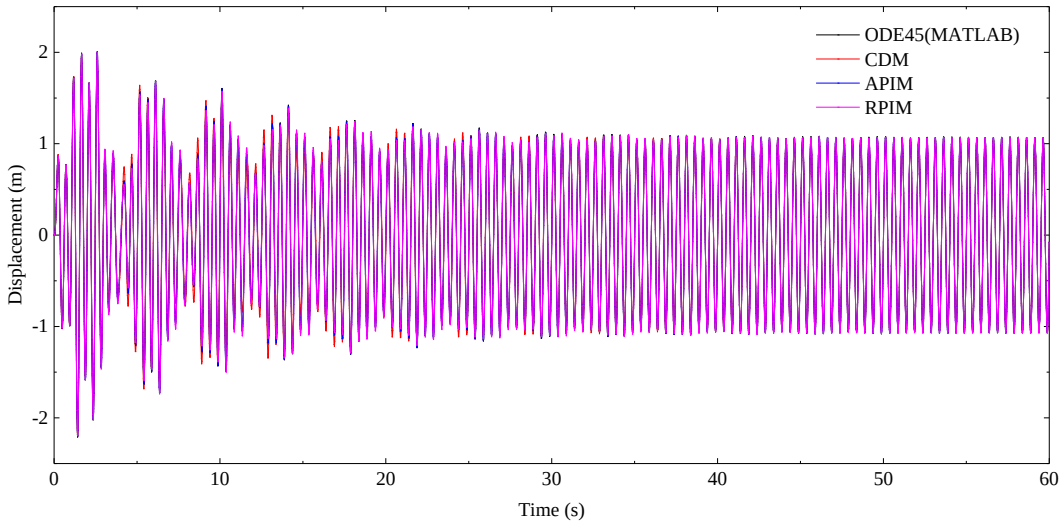

(a) Displacements in one minute with time increment Δt = 0.02s

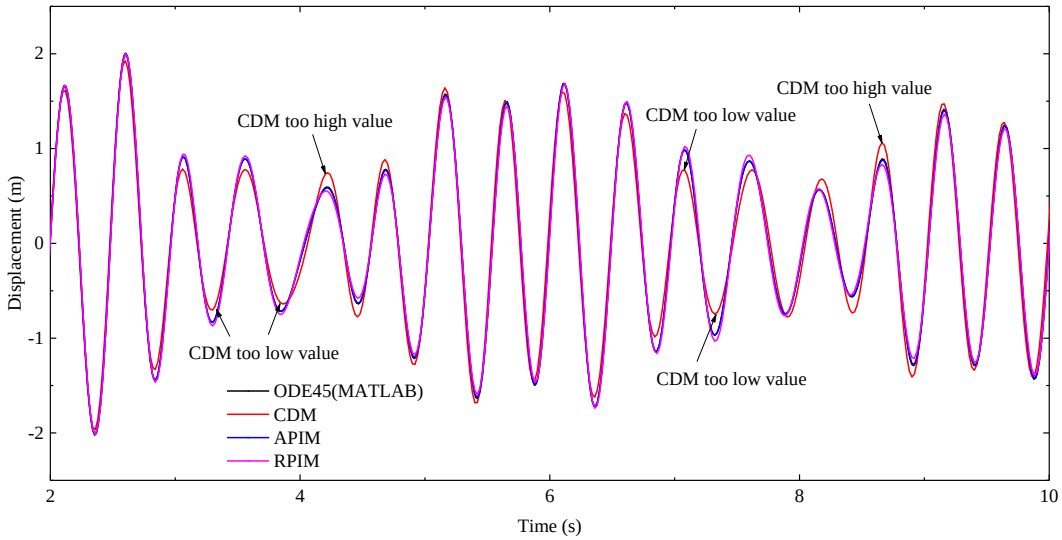

(b) Displacements from 2s to 10s with time increment Δt = 0.02s

Fig. 8 Time-displacement curves of mass 3 during forced vibration with varied force

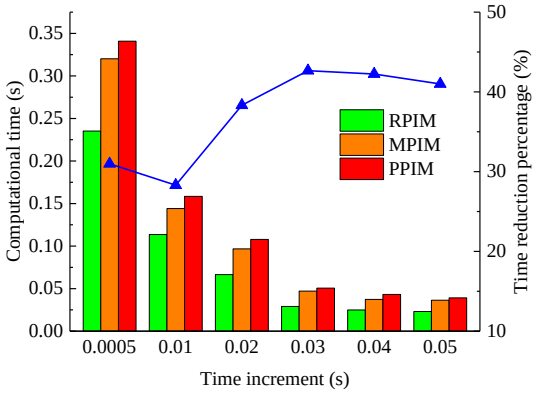

Fig. 9 Computational time and time reduction percentage during forced vibration with varied force

6.3. Nonlinear dynamic analysis of truss

In this example, two-dimensional Pratt truss with two DOFs (i.e., horizontal and vertical displacements) each node is adopted [38-39]. Though the RPIM has the advantage of dealing with consistent mass matrix, the lumped mass matrix is chosen for the simplicity of inverse computation, as required in ABAQUS [7] and OpenSees [8]. Only large displacement and large rotation are considered in the truss element with perfectly elastic material, ignoring material nonlinearity. There is no difference between both geometric and material nonlinearity problem, and geometric nonlinearity only problem, during the nonlinear analysis with the RPIM, since the stiffness matrix varies with time in both scenarios. Constant load P=1000kN is applied at node 1, 2 and 3 simultaneously in ten seconds and fixed boundary condition is employed at four nodes, as illustrated in Fig. 10. Consistent section area A=0.008m2, elastic material with elastic modulus E=2.06×109N/m2 and density ρ=7870kg/m3 are adopted in this case. The geometric information is detailed in Fig. 10.

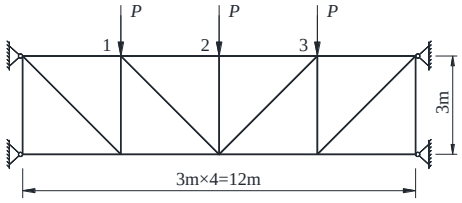

Fig. 10 Loading and boundary conditions of truss

The displacement at node 2 is monitored and curved at time increment 0.004s in Fig. 11. The reference result is calculated with the CDM at a small enough time increment 0.001s. Results from the CDM at time increment Δt =0.004s normally shift from the accurate results as time goes by, while the RPIM provides reasonable solutions with satisfying accuracy, as shown in Fig. 11(a)(b). The accumulated error in the CDM is demonstrated well by shifting in a time-displacement curve, in great contrast to the persistent precise prediction by the RPIM. The discrepancies of the CDM and RPIM in terms of results from Reference are illustrated in Fig. 11(c). It is clearly shown that the error of the CDM is much higher than the RPIM, up to 45% at some time points. The discrepancy of results from the CDM and RPIM both decline with increasing time, with maximum error within 5% with the RPIM and 15% with the CDM from time 5s, demonstrating three times the accuracy of the RPIM as traditional CDM. Computational time is reduced by more than 15% on average with the RPIM by comparison with the PPIM, demonstrating the efficiency of the RPIM, as illustrated in Fig. 12. Time reduction percentage in this example is less than that in linear cases with forced vibration (35%) and in free vibration case (65%), and this is led by the updating of stiffness matrix in each step for nonlinear analysis. Nevertheless, the RPIM exhibits satisfying efficiency in nonlinear analysis. This example demonstrates the applicability of the RPIM for the analysis of steel structures like truss.

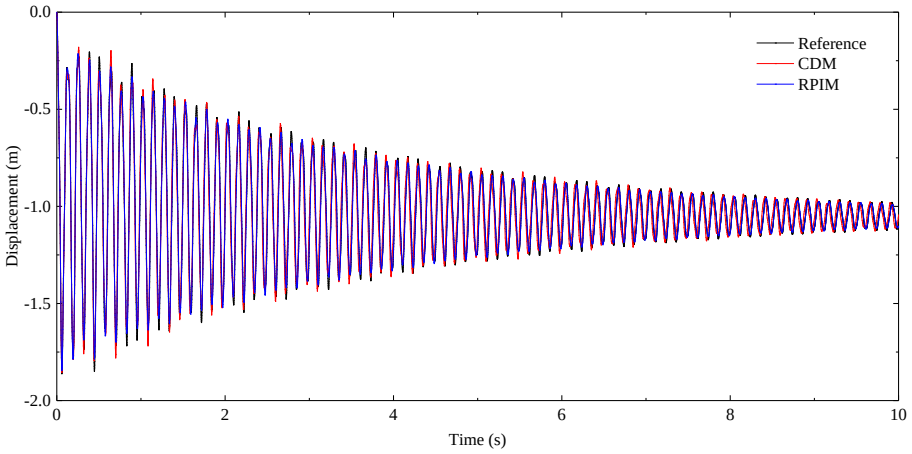

(a) Displacements in ten seconds with time increment Δt = 0.004s

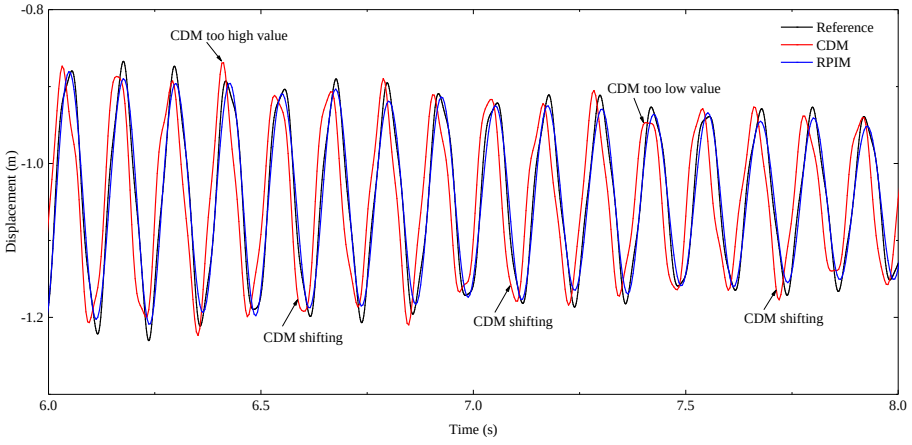

(b) Displacements from 6s to 8s with time increment Δt = 0.004s

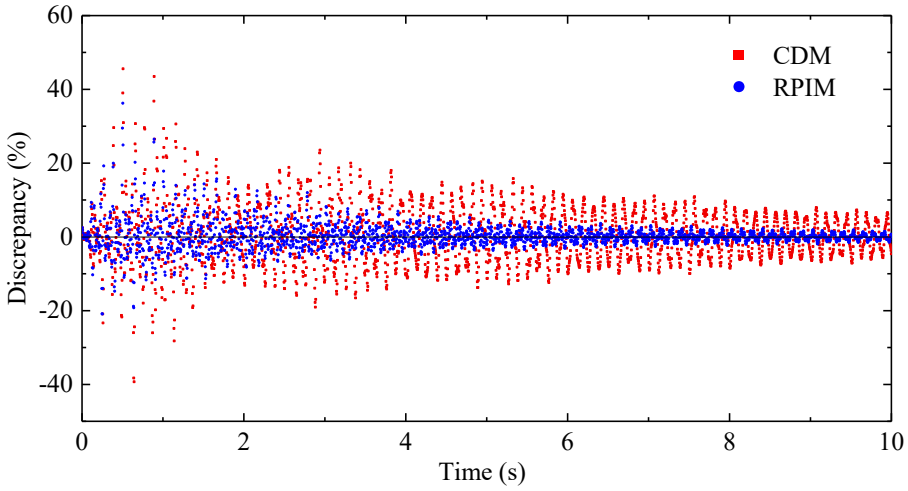

(c) Relative error of CDM and RPIM with time increment Δt = 0.004s

Fig. 11 Time-displacement curves and relative error in nonlinear truss

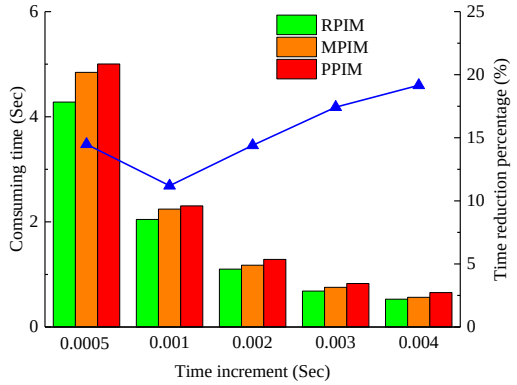

Fig. 12 Computational time and time reduction percentage in nonlinear truss

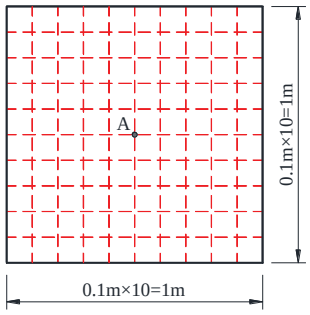

Fig. 13 Configuration of membrane

6.4. Nonlinear analysis of membrane

Membrane element with geometric nonlinearity only is considered in this verification example. A four-node element with two-point Gauss integration and three translation DOFs (e.g., two in-plane translation, one out-plane translation) for each node [38-39] is adopted. A 1m×1m square membrane with ten by ten mesh configuration is analyzed with uniform pressure P=100N/m2 for dynamic analysis, as illustrated in Fig. 13. The clamped boundary condition is adopted at the four sides of the membrane. Elastic material with E=2.06×105N/m2, Poisson's ratio ν=0.3, and density ρ=7870kg/m3 are employed. The thickness of the membrane is consistent with t=0.005m.

The displacements at the center point A are curved with time as illustrated in Fig. 14 with time increment 0.004s, and the result from the CDM with time increment 0.001s is provided as reference. The overall variation tendencies of time-displacement curves obtained from both the CDM and RPIM are consistent with that from reference, as shown in Fig. 14(a). Nevertheless, different shapes and unreasonable values at the peaks are observed in the CDM from Fig. 14(b), while satisfying displacements are provided by the RPIM. The discrepancies of the CDM and RPIM with regard to reference are illustrated in Fig. 14(c). A higher error in the results by the CDM is observed with the largest error near 40% and high error remaining from time 10s to 35s. The accuracy of the RPIM is demonstrated with the largest error near 10% in a small part of the analysis. The computational time of the RPIM is averagely 23% lower than that of the PPIM at different time increments, as illustrated in Fig. 15, and the efficiency of the RPIM is proved. Similar as in other verification examples, the computational time of the MPIM is slightly lower than that of the PPIM due to the simplicity of the introduced vector.

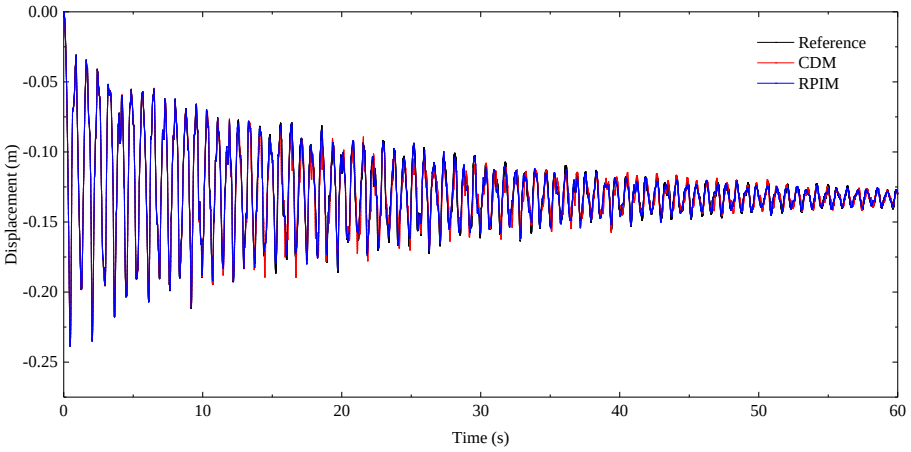

(a) Displacements in one minute with time increment Δt = 0.004s

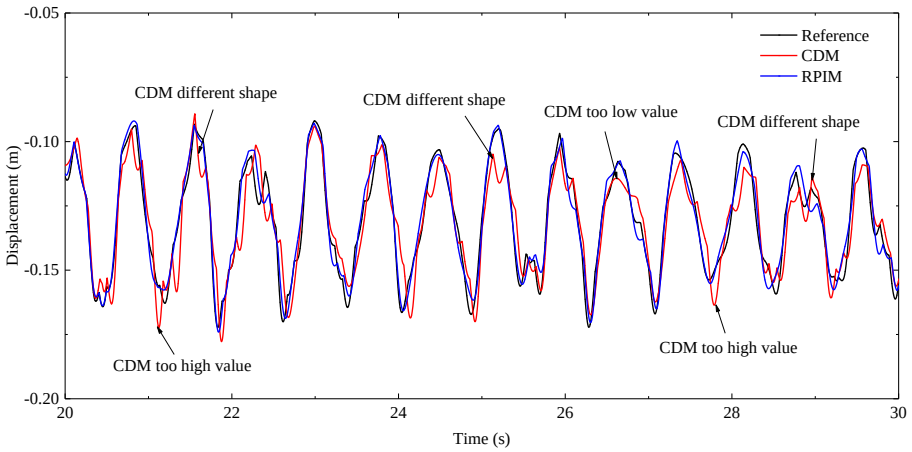

(b) Displacements from 20s to 30s with time increment Δt = 0.004s

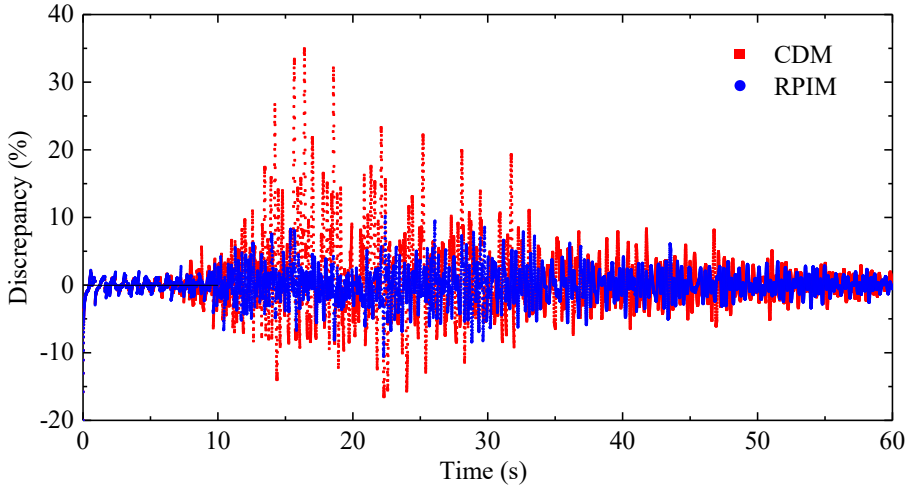

(c) Relative error of CDM and RPIM with time increment Δt = 0.004s

Fig. 14 Time-displacement curves and relative error in nonlinear membrane

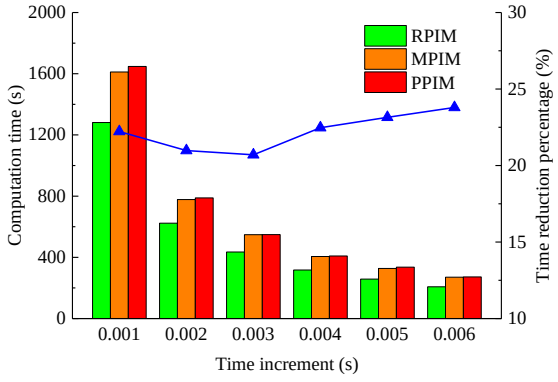

Fig. 15 Computational time and time reduction percentage in nonlinear membrane

7. Conclusions

In this paper, a refined precise integration method (RPIM) is proposed based on the existing precise integration method (PIM) and Duhamel integration method. It has the advantage of unconditional stability, high precision, excellent efficiency. In addition, with the transformation of equation of motion, the stiffness matrix is considered as an unknown variable which can be updated during the analysis, extending the application to nonlinear analysis. By introducing the velocity vector, the calculation of the exponential matrix is much simplified to the operation of a 2×2 matrix. Four typical examples containing linear and nonlinear dynamic analysis are selected to demonstrate the accuracy and efficiency of the RPIM. Several conclusions can be drawn as follows.

(1) The RPIM is unconditionally stable with fifth-order accuracy as illustrated in the stability and accuracy analysis.
(2) The calculation of the exponential matrix is much simplified with the operation of a 2×2 matrix, due to the introduction of velocity vector, and such that the efficiency of the RPIM is largely improved.
(3) The stiffness matrix is considered as a dependent variable and updated during the nonlinear analysis. Thus, the proposed RPIM is applicable to both linear and nonlinear dynamic analysis.
(4) The accuracy of the RPIM is superior to that of the CDM, since the only approximation in the RPIM exists in the internal force described with Lagrange interpolation, demonstrated well by the verification examples.
(5) No inverse of matrices is involved in the RPIM, making it applicable and efficient to deal with nonlinear dynamic analysis of large structures with adequate accuracy.

Acknowledgements

The authors are grateful for financial support from "Science and Technology Planning Project of Guangdong Province (2016A050502022) " and the Research Grant Council of the Hong Kong SAR Government on the project "Joint-based second order direct analysis for domed structures allowing for finite joint stiffness (PolyU 152039/18E)".

References

[1] He, Y.J., Zhou, X.H. and Wang, H.S., “Wind-induced response analysis of the cylindrical reticulated mega-structures”, Advanced Steel Construction, 12, 66-82, 2016.
[2] Li Z, Ren H, Tong X, and Li H. , “A Precise Computation Method of Transient Free Surface Green Function”, Ocean Engineering, 105, 318-326,2015.
[3] Newmark N.M., A Method of Computation for Structural Dynamics. Am Soc Civ Eng 1962.
[4] Wilson E.L., Farhoomand I. and Bathe K.J., “Nonlinear dynamic analysis of complex structures”, Earthquake Engineering Structural Dynamics, 3, 241-252, 1972.

[5] Wilson E.L., A Computer Program for the Dynamic Stress Analysis of Underground Structure, 1968.
[6] Bathe K.J. and Baig M.M.I., “On a composite implicit time integration procedure for nonlinear dynamics”, Computers and Structures, 83, 2513-2524, 2005.
[7] Abaqus 6.17 Documentation. DS SIMULIA Corp, 2017.
[8] The Open System for Earthquake Engineering Simulation. Univeristy of California, Berkeley, 2000.
[9] Dokainish M.A. and Subbaraj K., “A survey of direct time-integration methods in computational structural dynamics I. Explicit methods”, Computers and Structures, 32, 1371-1386, 1989.
[10] Subbaraj K. and Dokainish M.A., “A survey of direct time-integration methods in computational structural dynamics II. Implicit methods”, Computers and Structures, 32, 1387-1401, 1989.
[11] Zhong W.X., “On precise time integration method for structural dynamics”, Journal of Dalian University of Technology, 34, 131-136, 1994.
[12] Zhong W.X. and Williams F.W., “A precise time step integration method”, Proceedings of the Institution of Mechanical Engineers, Part C: Journal of Mechanical Engineering Science 208, 427-430, 1994.
[13] Zhong W.X., “On precise integration method”, Journal of Computational and Applied Mathematics, 163, 59-78, 2004.
[14] Lin J.H., Shen W.P. and Williams F.W., “A high precision direct integration scheme for sturctures subjected to transient dynamic loading”, Computers and Structures , 56, 113-120, 1995.
[15] Wang M.F. and Au F.T.K., “Assessment and improvement of precise time step integration method”, Computers and Structures, 84, 779-786, 2006.
[16] Gao Q., Wu F., Zhang H.W., Lin J.H. and Zhong W.X., “A fast precise integration method for large-scale dynamic structures”, Chinese Journal of Computational Mechanics, 28, 492-498, 2011.
[17] Huang C. and Fu M.H., “A modified precise integration method for long-time duration dynamic analysis”, Mathematical Problems in Engineering, 2018, 1-12, 2018.
[18] Liu Y. abd Shen W.P., “Adaptive algotithm of transition matrix in precise integration method”, Journal of Vibration and Shock, 2, 82-85, 1995.
[19] Shen W.P., Lin J.H. and Williams F.W., “Parallel computing for the high precision direct integration method”, Computer Methods in Applied Mechanics and Engineering, 126, 315-331, 1995.
[20] Gu Y.X., Chen B.S., Zhang H.W. and Guan Z.Q., “Precise time-integration method with dimensional expanding for structural dynamic equations”, AIAA Journal, 39, 2394-2399, 2012.
[21] Gao Q., Wu F., Zhang H.W., Zhong W.X., Howson W.P. and Williams F.W., “A fast precise integration method for structural dynamics problems”, Structural Engineering and Mechanics, 43, 1-13, 2012.
[22] Wang M.F. and Au F.T.K., “Precise integration methods based on Lagrange piecewise interpolation polynomials”, International Journal for Numerical Methods in Engineering, 77, 998-1014, 2009.
[23] Gao Q., Tan S.J. and Zhong W.X., “A survey of the precise integration method”, Scientia Sinica Technologica, 46, 1207-1218, 2016.
[24] Zhong W.X., Zhu J.N. and Zhong X.X., “On a new time integration method for solving time dependent partial differential equations”, Computer Methods in Applied Mechanics and Engineering, 130, 163-178, 1996.
[25] Wu F., Gao Q. and Zhong W.X., “Subdomain Precise Integration Method for Periodic Structures”, Shock and Vibration, 2014.
[26] Gao Q., Zhang H.W., Zhong W.X., Howson W.P. and Williams F.W., “An accurate and efficient method for dynamic analysis of two-dimensional periodic structures”, International Journal of Applied Mechanics, 8, 2016.
[27] Gao Q. and Cui H.C. ,“Efficient and accurate method for 2D periodic structures based on the physical features of the transient heat conduction”, International Journal of Thermal Sciences, 127, 213-231, 2018.
[28] Gao Q., Yao W., Wu F., Zhang H.W., Lin J.H. and Zhong W.X., “An efficient algorithm for dynamic response of periodic structures”, Chinese Journal of Theoretical and Applied Mechanics, 2011.
[29] He D.D., Gao Q. and Zhong W.X., “An efficient method for simulating the dynamic behavior of periodic structures with piecewise linearity”, Nonlinear Dynamics, 94, 2018.
[30] Fung T.C. and Chen Z.L., “Krylov precise time-step integration method”. International Journal for Numerical Methods in Engineering, 68, 1115-1136, 2006.
[31] Su X.X., Wang Y.S. and Zhang C.Z., “A matrix-exponential decomposition based time-domain method for calculating the defect states of scalar waves in two-dimensional periodic structures”, Journal of Computational Physics, 337, 403-420, 2017.
[32] Tan S.J., Gao Q. and Zhong W.X., “Applications of Duhamel term’s precise integration method in solving nonlinear differential equations”, Chinese Journal of Computational Mechanics, 25, 752-758, 2010.
[33] Alipour A. and Zareian F., “Study Rayleigh Damping in Structures; Unceratinties and Treatments”, The 14th World Conference on Earthquake Engineering, Beijing, China, 2008.
[34] Bathe K.J. and Wilson E.L., “Stability and accuracy analysis of direct integration methods”, Earthquake Engineering and Structural Dynamics,1, 3-6, 1983.
[35] Noh G. and Bathe K.J., “Further insights into an implicit time integration scheme for structural dynamics”, Computers and Structures, 202, 15-24, 2018.
[36] Code for seismic design of buildings (GB50011-2010), Ministry of Housing and Urban-rural Construction of the People’s Republic of China, Beijing, China, 2010.
[37] MATLAB Documentation, MathWorks, 2000.
[38] Bathe K.J., Finite element procedures in engineering analysis, Prentice-Hall, Inc, New Jersey, 1982.
[39] Ferreira A.J.M., MATLAB codes for finite element analysis: solids and structures, Springer, 2008.

Advanced Steel Construction – Vol. 16 No. 2 (2020) 137–145
DOI:10.18057/IJASC.2020.16.2.5

DESIGN AND ANALYSIS OF STEEL STRUCTURES CONSIDERING THE 3D BEHAVIOUR OF THE JOINTS

Luís Simões da Silva *, Sara Oliveira, Ricardo Costa and Filippo Gentili

ISISE, Department of Civil Engineering, University of Coimbra, Portugal
** (Corresponding author: E-mail: luisss@dec.uc.pt)*

ABSTRACT

This paper discusses the analysis and design of steel structures using 3D structural models and incorporating the 3D behaviour of the joints. Firstly, the implications of the 3D behaviour of the joints are discussed at the joint level, leading to the need to develop 3D component models. Subsequently, at the frame level, a 3D joint macro-element is presented that encapsulates the behaviour of the joints at each node while maintaining compatibility with the global degrees of freedom of beam elements. Finally, an example is shown for a simple 3D framed structure.

ARTICLE HISTORY

Received: 18 March 2020
Revised: 18 March 2020
Accepted: 18 March 2020

KEYWORDS

Steel;
Stability;
3D joints;
Eurocode 3;
Macro-elements;
OpenSees

1. Introduction

Most structures are tri-dimensional, i.e. develop along three directions, because of their basic function of providing a protected enclosure for people and goods. Many structural schemes and materials exist to address the challenge of choosing the best option for a given building meet this requirement with proper safety levels. Among these, it is the art of the designer to select and optimise the options that maximise sustainability.

The choice of structural schemes is naturally linked to the characteristics of the various structural materials and products (e.g. the large difference between the tensile and compressive resistances of concrete or the susceptibility of steel members to instability phenomena), but it is also intrinsically linked to the knowledge and calculation capabilities that are available throughout the design process and the availability of construction technologies that allow to materialise the design concepts.

Steel structures provide competitive structural solutions, particularly in combination with other materials such as concrete and timber. Multi-storey buildings are often supported by a steel or a steel-concrete composite framed structure, a concrete core and concrete or composite floor systems. Low-rise single storey buildings covering medium to large spans are often supported by steel framed structures and lightweight roofs made from steel panels. In these both cases, steel columns are connected to steel beams that intersect the columns at the various floor levels with an orthogonal grid in the case of regular structures but not necessarily so in an irregularly shaped building. Iconic examples of a highly irregular grids and structures are the Guggenheim Museum in Bilbao or the Beijing National Stadium in Beijing.

Historically, because of limited calculation resources, framed structures were calculated and designed as a set of 2D frames. The theoretical background of this procedure relied in the assumption that the behaviour of this type of structures was not significantly affected by torsional effects and, consequently, their structural response could be adequately represented by independent orthogonal frames. Pitched-roof portal framed buildings are typical examples of a structure that can be modelled and calculated as independent structures in two perpendicular directions.

Nowadays, the available computational resources have eliminated those limitations. Hence, today's standard practice corresponds to the development of 3D framed models of the structure that, besides representing its behaviour with much higher accuracy, present the added advantage of speeding up the design process, given the user-friendliness of most structural analysis and design software packages.

The consideration of 3D structural models of framed structures requires that the stiffness of the various beam-to-column joints is appropriately modelled. Fig. 1 illustrates beam-to-column joints resulting from the intersection of four orthogonal beams, common in 3D framed structures.

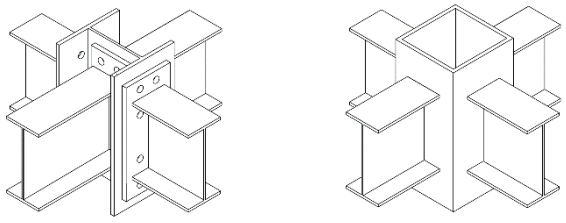

a) I-shaped column b) tubular column

Fig. 1 Detail of beam-to-column joints where 4 beams intersect the column.

Fig. 1a represents two usual joint typologies: end-plate major-axis joints, whereby the beam connects to the flange of the column and end-plate minor-axis joints, whereby the beam connects to the web of the column. End-plate major axis joints are usually moment-resistant joints, either full-strength or partial-strength. In contrast, end-plate minor axis joints directly connected to the column web are either nominally pinned or partial-strength. Although the four joints comprise several components that are independent [1], they all share some common components (in particular the column web panel components) that need to be designed considering the 3D interactions that may control their behaviour.

Fig. 2b represents a typical joint typology to connect I-section beams to a SHS column. In this case, because of symmetry, the 4 joint typologies are similar and correspond to end-plate beam-to-column joints. Because of the slenderness of the column faces, it is well known that the local behaviour of the column depends on the stiffness of each individual beam-to-column joint and it may be assessed using a modified ring model [2, 3].

Obviously, more complex joint details may be adopted that allow to disregard the 3D interactions in the nodal zones of a column or even allow to neglect the flexibility of the joints by considering fully rigid and fully pinned joints as it is illustrated in Fig. 2 [3, 4]. However, these solutions usually lead to increased cost.

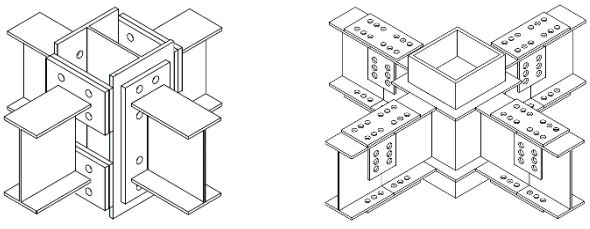

a) I-shaped column b) tubular column

Fig. 2 Detail of complex beam-to-column joint where 4 beams intersect the column.

Hence, as the trend to optimization having in view the increase of the competitivity of steel structures seems irreversible, even from a resource-efficiency point of view [5], it is necessary to capture the 3D interactions that occur at each column node and to consider their implications for the global analysis of the structure as well as the local design of each joint [6].

This paper presents a framework and a design-oriented methodology for the analysis and design of steel structures incorporating the 3D behaviour of the joints. It addresses the local level, i.e. joint level, and the global level, i.e. frame level, followed by the presentation of the development and application example of a 3D joint macro-element suitable for rigorous analysis and design of 3D framed structures implemented in OpenSees [7].

2. Joint level

2.1. Introduction

The behaviour of a steel joint is complex. Its characterization may therefore be addressed with different levels of sophistication. The most common ways to characterize the behaviour of steel joints are:

- Experimental tests, that constitute the most accurate procedure but require specialized human resources and equipment, a high cost and long timespan. Experimental tests are obviously essential whenever new or unproven joint configurations are developed, either to help to identify the relevant failure modes and/or to provide validation of the design procedures. Additionally, in design, experimental tests may be required in other cases, e.g. (i) whenever there is not sufficient consolidated knowledge for the application of some designs options such as, for instance, the use of dissipative steel joints in seismic conditions [8] or (ii) in case of an infrastructure of high importance, whereby any structural problem might lead to expensive consequences and important delays to the use of that infrastructure, as for example, the joints in the large scale cryostat for the DUNE experiment [9].
- Advanced finite element models, that constitute the most accurate and versatile theoretical procedure but require model calibration, qualified and experienced users and are time consuming. Numerical finite element models are nowadays extensively used to (i) enlarge the range of validity of design solutions through parametric studies, (ii) validate design assumptions and (iii) get detailed insight into local behaviours in complex cases that lack simpler design guidance.
- Mechanical models, that provide an accurate representation of the moment-rotation behaviour of the joint typologies that are covered by their application field and are easily incorporated in design codes but, because they require the calibration of the behaviour of the components and the adequacy of the underlying component model, are not available for all joint typologies that may be used in practice.

This third option is of course favoured for practical application because it is the only option that is compatible with the design deadlines and design fees that cover 90% of the cases. This approach will be further detailed in the following section, although it is worth mentioning that some hybrid FEM – mechanical model approaches are starting to appear in the engineering community.

2.2. Component method approach

The component method is the usual designation of a methodology for the assessment of the behaviour of steel joints based on simplified mechanical models. In order to achieve a user-efficient solution, the component method identifies the stress paths that are generated in a joint subject to a given loading. After that, the portions of the joints that have a contribution for the joint behaviour are identified, characterized and condensed in tensile or compressive stress resultants.

The joint is represented by a discrete rigid link-spring model, whereby each spring represents the behaviour of a physical part of the joint subject to a specific loading, henceforth called joint component. It is further noted that the component model may be used with various levels of sophistication, depending on what is desired: whenever only the initial stiffness of the joint is of interest, it is only required to define the behaviour of each component by their linear elastic stiffness. Similarly, if only the resistance of the joint is of interest, it is only necessary to define the resistance of each component. Finally, to obtain the full moment-rotation response of the joint, it is necessary to define the nonlinear force-deformation behaviour of each component that may be represented in a simplified way by bilinear curves.

Although most of the mechanical models developed in the scope of the component method correspond to statically indeterminate structures, simplified generic solutions were developed for the initial stiffness and the resistance that were implemented in design codes [10], providing a practical and speedy way to assess the properties of a joint. Furthermore, most structural design software packages already provide modules to assess the properties of steel joints making use of the component method [11-14].

As becomes clear from the above, the component method relies on the mechanical characterization of the components. Much research effort was dedicated to the development of design models of the key components of a steel joint. Nowadays, a reasonable number of components covering a wide range of joint typologies are well characterized and design expressions/models for their mechanical properties are available in design codes. Fig. 3 illustrates several beam-to-column joint mechanical models developed in the scope of the component philosophy that are appropriate for specific joint typologies.

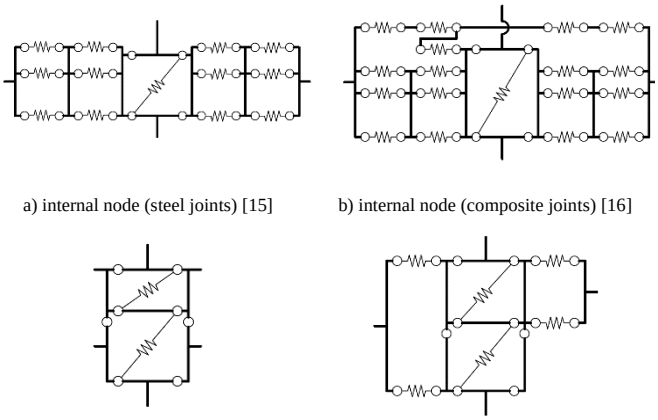

a) internal node (steel joints) [15] b) internal node (composite joints) [16]

c) Internal node (composite joints) [17] d) internal node (steel joints, beams of unequal depth) [18]

Fig. 3 Component method mechanical models for beam-to-column major axis joints.

However, design creativity combined with powerful advances in manufacturing and processing technologies (e.g. 3D printing, just to mention a disruptive technology) are continuously pushing to expand the frontiers of knowledge. The need to consider the 3D behaviour of the joints is one of the consequences.

At present, the component method was basically developed to address uniplanar joints (covering both external and internal nodes), see Fig. 3. Concerning 3D component models, apart from the work developed at the University of Coimbra [19], little work exists in this field. The difficulty starts with the lack of experimental evidence to characterize the components that are relevant for 3D behaviour and the crucial issue of the interactions that need to be considered. This issue will be tackled in section 2.4.

2.3. Detailed FEM approach

Among designers there is a growing wish of addressing the design of the joints by means of advanced nonlinear structural models that detail the nodal zones using shell and solid finite elements. This is of course the desirable future but it is not realistic at the present moment because, besides all the other reasons already mentioned above, (i) the required computing processing resources are not available for a normal design company and (ii) there are not available yet clear and objective numerical "failure" criterion that allows to establish a "component resistance". Besides all the complex phenomena that are present in a steel joint (complex geometry, contact and separation, plasticity and strain hardening, local instabilities, large local deformations, etc.), it is also necessary to adequately interpret peak strains that may occur and that are purely numerical effects that do not correspond to reality but may mask the true results.

Hence, a more realistic approach is to try to interpret and condense the detailed local FEM results (stresses and deformations) into equivalent joint components that follow the principles of the component method. Augusto et al. [20, 21] have developed a methodology to extract the component behaviour from advanced nonlinear numerical models for the column web panel components, both under static monotonic conditions and cyclic conditions. Fig. 4 illustrates the extraction methodology for the component's column web in transverse tension and compression (Fig. 4a and Eq. (1)) and the component column web panel in shear (Fig. 4b and Eq. (2)).

$$F_c = \left(\int^{h_c} \sigma_{33} dy\right) \cdot t_{wc} \ , \quad F_{t,i} = \left(\int^{h_{t,i}} \sigma_{33} dy\right) \cdot t_{wc} \tag{1}$$

$$V_n = \left(\int^{(2t_{fc}/3+r)}_{back} \tau_{23} dz\right) \cdot t_1 + \left(\int^{h_{wc}} \tau_{23} dz\right) \cdot t_{wc} + \left(\int^{(2t_{fc}/3+r)}_{front} \tau_{23} dz\right) \cdot t_1 \quad (2)$$

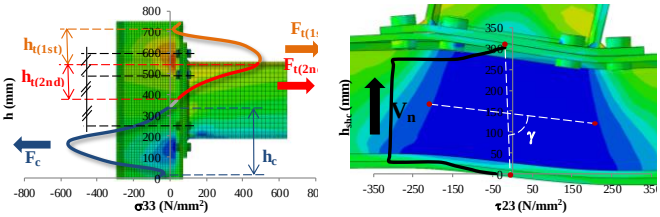

a) Computation of normal force of the column web in transverse tension and compression components.

b) Computation of the shear force of the column web panel in shear component.

Fig. 4 Computation of internal forces in components from detailed FEM models [20].

2.4. 3D component characterization

Focussing on an internal node of a I-shaped column as shown in Fig. 1a, it is clear that the key 3D effects and interactions are concentrated in the column web panel. In order to assess and understand the underlying 3D behaviour of the joints converging to a 3D node, five full scale experimental tests over 5 distinct specimens were carried out at the University of Coimbra [22, 23]. The tested specimens are sub-frames from a representative unbraced regular frame acted by horizontal loads extracted between points of contra-flexure – bolted extended end-plate joints were considered in both minor and major axis directions. Fig. 5 shows the schematic layouts of the five beam-to-column joints tested.

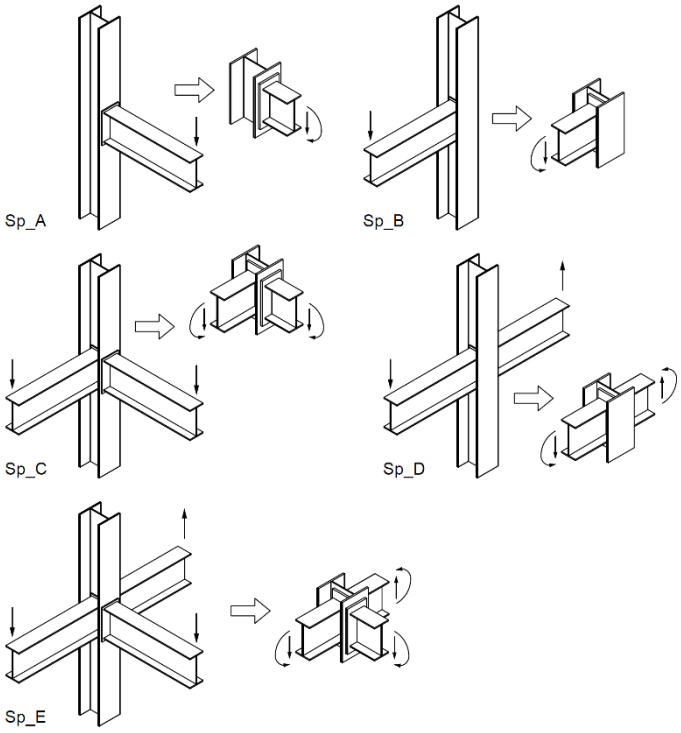

Fig. 5 Schematic representation of the experimental tests.

Fig. 6 shows the behaviour of the major axis joints and the minor axis joints [24]. It was found that, for the column web slenderness tested, the minor axis joint may lead to a reduction of the major axis joint initial stiffness due to the interaction of the minor axis joints with the load introduction components (in plane) of the major axis joint, i.e. the column web in tension (CWT) and the column web in compression (CWC).

It was also found that the post-elastic stiffness of the column web in shear (CWS) is enhanced due to the interaction with the minor axis joints and that the enhancement is larger in beam-to-column joints with double minor axis joints than in beam-to-column joints with a single minor axis joint. No major differences in the plastic moment of major axis joints were found due to the interaction with the minor axis joints [24].

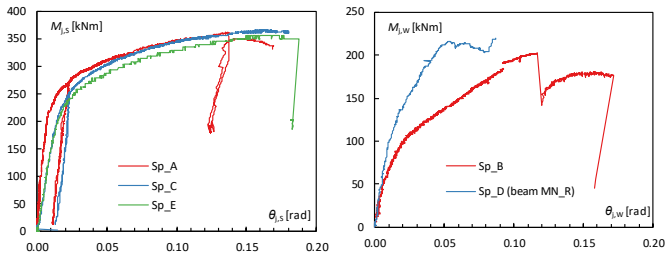

Fig. 6 Behaviour of major axis joints (left) and minor axis joints (right) [24].

Additionally, it was also found that the behaviour of minor axis joints in beam-to-column joints with double minor axis joints has a major enhancement in terms of initial stiffness, post-elastic stiffness and plastic moment when compared with the behaviour of beam-to-column joints with a single minor axis joint. Moreover, it was found that the initial stiffness of minor axis joints in beam-to-column joints with double minor axis joints is of the same order of magnitude of the initial stiffness of the major axis joints in 3D joints, showing that the pinned assumption usually considered for minor axis joint may be too conservative [24].

Having identified the key factors in the 3D behaviour of these joints, it is clear that a 3D beam-to-column joint model must consider the following components and interactions in the column web region of the beam-to-column joint:

- column web panel in transverse tension and compression (load introduction components in the major axis joints);
- column web panel in shear and the interaction between the major axis joints;
- column web panel in out-of-plane bending and the interaction between the minor axis joints;
- the interaction between major and minor axis joints in all these components.

3. Frame level

The accurate assessment of the internal forces and displacements of a 3D steel structure requires the consideration of the flexibility of the various beam-to-column joints. As it was explained in the previous section, this implies that all the relevant sources of deformation of the joints are accounted for and the interactions between the relevant components from the same beam-to-column joints are appropriately considered using 3D component models. Obviously, at the frame level, this means that at each floor level all column nodes of the structural model must be detailed according to the 3D component model that is representative of each nodal zone.

The implementation of such an approach, although theoretically possible, is not feasible in practice for the following reasons:

- time consuming in the definition of the structural model (although this might be mitigated with a clever pre-processor);
- not robust from a calculation point of view due to the susceptibility to numerical instability associated to the large differences of the stiffness of the components and the rigid elements when compared with the stiffness of the beam elements; in case of a nonlinear analysis, this would inevitably lead to the program stopping short of the target load level;
- time-consuming at the post-processing stage.

Hence, following a previous contribution by one of the authors [25], the incorporation of the rigorous behaviour of the beam-to-column joints in the structural model (Fig. 7a) can only be achieved in a practical way with the implementation of a generalized joint element (GJ). This element should be assigned to all beam-to-column joints. However, given the actual detailing of the joints, a standard six degrees-of-freedom (3 translations and 3 rotations) GJ element is not sufficient. The fact that several members converge to the same region but connected to different parts of the column cross-section (flanges or web), e.g. Fig. 1a, means that the GJ element must be composed of several generalized connections (GC) and a generalized column web panel (GCWP), with appropriate eccentricities, as illustrated in Fig. 7b.

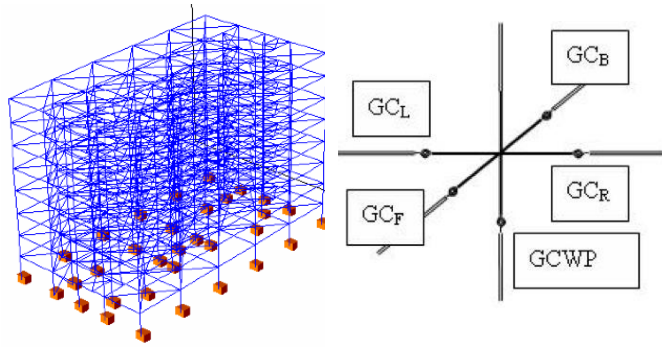

a) Structural model. b) Generalized macro-element.

Fig. 7 Conceptual definition of a generalized joint element [25].

In the next section (section 4) the development, implementation and validation of a 3D joint macro-element suitable for analysis of 3D steel frames is presented.

4. 3D joint macro element

4.1. Requirements for the joint macro-element

The definition of a general beam-to-column joint macro-element, 2D or 3D, must be fully mechanically consistent with the actual behaviour of the beam-to-column joint. Accordingly, the arrangement of the components in the mechanical model must account for:

(i) the number of 1D elements (beam or column) connected to the beam-to-column joint from where the demand for the components (modelled as 0D elements, i.e. springs) comes from;

(ii) the number of elements whose internal forces influence the constitutive relation 0D components.

Combining these two criteria, the following classification of components can be set:

— Type A: in these components the demand comes only from one 1D element connected to the beam-to-column joint and their constitutive behaviour can be assumed constant throughout any load history; the components in the connection (according to EC3-1-8) – except the column web load introduction components – meet these criteria because their demand comes only from one beam and their behaviour is not influenced by the internal forces transmitted to the beam-to-column joint by any other1D element; these components may be considered explicitly in the mechanical model but they may also be assembled in a standard 6 DOF spring;

— Type B: in these components the demand also comes only from one 1D element connected to the beam-to-column joint but their constitutive relations depends on the internal forces transmitted to the beam-to-column joint by one or more 1D elements, e.g. according to EC3-1-8, the strength of the column web load introduction components (CWT and CWC) is influenced by the internal forces in the columns and, according to [24] the behaviour of the CWT and CWC is also influenced by the minor axis joints; these components must be explicitly considered in the macro-element in order to be possible to account the interaction of internal forces coming from the 1D elements at any step of the load history, e.g. an increase in the column axial load due to the collapse of another column next to it may increase the CWC strength and stiffness.

— Type C: in these components the demand comes from several 1D elements connected to the beam-to-column joint and their constitutive relations depend on the internal forces transmitted to the beam-to-column joint by one or more 1D elements (just like in Type B components); the column web in shear and the out-of-plane components in minor axis beam-to-column joints meet these criteria; these components must be explicitly considered in the mechanical model in order to be possible to account the internal forces interaction and thus update the components constitutive relations throughout the load history; furthermore, their arrangement in the mechanical model must also be carefully chosen so that the internal force and the deformation of the corresponding 0D element are directly related to the actual internal force and deformation mode, respectively.

The 3D beam-to-column joint macro-element was developed considering this strategy and the following requirements:

(i) in order to make the model fully compatible with ordinary 1D elements in 3D frame analysis:
   a. 6 external nodes were required – in the more complex scenario four beams and two columns will be connected to the beam-to-column joint;
   b. 6 degrees of freedom (DOFs) per external node were required, leading to 36 external DOFs;

(ii) in order to make the implementation of the 3D beam-to-column joint model in standard programs based in the Finite Element Method (FEM), all the external DOFs were made linearly independent – this required the consideration of components that, for standard deformation modes are considered irrelevant (e.g. beam major axis bending deformation in connections) but that actually can be seen a sleeping components (to which a high stiffness and strength is usually assigned) but that can also be used when nonstandard analysis with nonstandard deformation modes are required (e.g. torsion, shear deformation modes in connections, beam minor axis bending in connections, etc.); when these sleeping 0D elements (the ones underlined in the following figures) are not being considered, their stiffness must be large enough to lead to almost null deformations (however small enough the avoid numerical instability issues).

(iii) to make use of the lowest number of 0D element and internal DOFs to get 36 linearly independent external DOFs – in order to make the beam-to-column joint as simple as possible, the lowest number of 0D elements (required by the strategy already described) were used.

The need for uncouple the column web load introduction components from the rest of the connection components and the need for independent external DOFs led to 0D elements placed in series. This required the consideration of internal degrees of freedom in order to be able to get kinematically defined elements, i.e. elements where any arbitrary deformation can be defined through one, and only one, appropriate choice of displacements along the nodal degrees of freedom.

The 2D beam-to-column macro-elements, being particular cases of the 3D element, may follow the same strategy and satisfy the same requirements with the obvious adaptations of only 4 external nodes and 3 DOFs per external node.

4.2. Description of the joint macro-element

Fig. 8 to 13 represent the DOFs of the 3D joint macro-element model and 0D elements that simulate the components and the connections, where d_{bX} and d_{bY} are the lever arm of the major (along X) and minor (along Y) axis beams, respectively, and d_{cX} is the lever arm of the column.

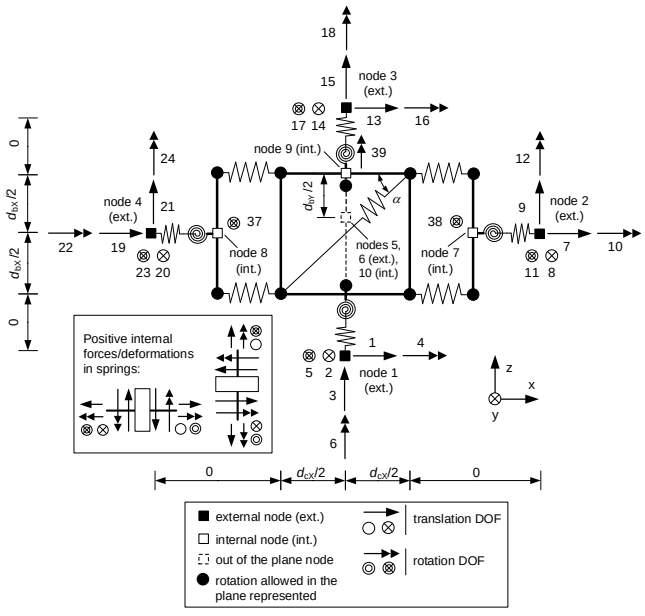

Fig. 8 Degrees of freedom and dimensions (plane XZ).

The following constraints were also considered (not represented Fig. 8 to 13):

(i) the 2D panels are orthogonal to each other and no relative rotation in z axis direction between them is allowed;

(ii) only the deformations allowed by each 0D element are represented where:

— T stands for linear deformation; e.g. TX stands for linear deformation in the X axis direction;
— R stands for angular deformation; e.g. RX stands for angular deformation in the X axis direction.

Table 1 identifies the components/connections of the 3D joint macro-element as well as references were the mechanical behaviour of the components may be gathered from. It should also be mentioned that the 3D model incorporates the special cases of 2D major axis and 2D minor axis macro-elements also developed by the authors [26, 27] but will be omitted for the sake of briefness.

Table 1
Summary of the 0D elements.

0D element	description – reference
01(TX), 02(TX), 04(TX), 05(TX)	load introduction components in the column web (tension or compression) – major axis joints [10]
03(RY), 06(RY)	connections [10]
07(TD)	column web in shear in plane yx – major axis [10]
08(TZ), 10(TZ)	column axial deformation, usually sleeping components
09(RY), 11(RY)	column bending deformation, usually sleeping components
12(TY), 13(RX), 14(RZ), 15(TY), 16(RX), 17(RZ), 18(RX), 19(RZ), 20(RX), 21(RZ), 26(TX), 27(TZ), 28(RY), 29(RZ), 30(TX), 31(TZ), 32(RY), 33(RZ), 34(TY), 35(TY)	sleeping components
22(RX), 23(RX)	connections – minor axis [10]
24(TY), 25(TY)	column web panel in transverse tension/compression [28, 29]

As stated in Table 1, spring 07(TD) in Fig. 11 represents the column web panel in shear and its behaviour can be computed according to section 6 of EN 1993-1-8 [10]. However, due to the differences in the topological configuration of the component column web panel in shear between the EN 1993-1-8 standard model and the model represented in the previous figures, an adjustment is required for the stiffness and the strength of this component. Let S^{EC3} be the stiffness of column web panel in shear from EN 1993-1-8 and S^{EC3} the stiffness of the spring 07(TD). For the sake of consistency, the stiffness coefficient S^{EC3} in EN 1993-1-8 was derived in order to account the column web panel in shear component using the same procedures developed for the rest of the components in the connections, i.e. aligned with the bottom part of the panel. Accordingly, considering a shear deformation γ of the column web caused by a shear force V, the deformation of the corresponding component will be $\Delta = \gamma d_{bX}$ when the associated spring is assumed aligned with the bottom part of the panel (Case I) but will correspond to $\gamma d_{bX} \cos\alpha = \Delta \cos\alpha$ when the associated spring is assumed along the diagonal of the column web in shear (Case II). Consequently, the forces in the spring will be $S^{\mathrm{EC3}}\Delta$ in Case I and $S^{07(TD)}\Delta\cos\alpha$ in Case II. Since the horizontal components of both springs must equal the shear force in the column web, it follows that

$$S^{\mathrm{EC3}}\Delta = S^{07(TD)}\Delta(\cos\alpha)(\cos\alpha) \rightarrow S^{07(TD)} = \frac{S^{\mathrm{EC3}}}{(\cos\alpha)^2} \tag{3}$$

Concerning the resistance f^{max} of component 7, using the same reasoning leads to

$$f_7^{max,07(TD)} = \frac{f^{\max,\mathrm{EC3}}}{\cos\alpha} \tag{4}$$

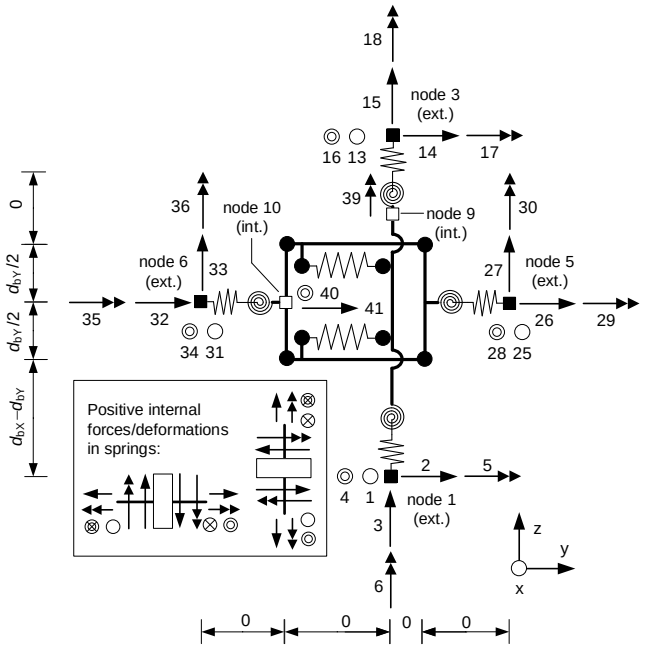

Fig. 9 Degrees of freedom and dimensions (plane YZ).

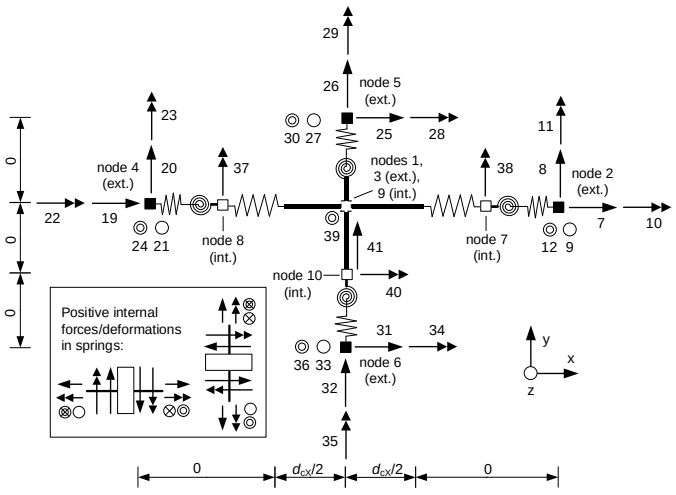

Fig. 10 Degrees of freedom and dimensions (plane YZ).

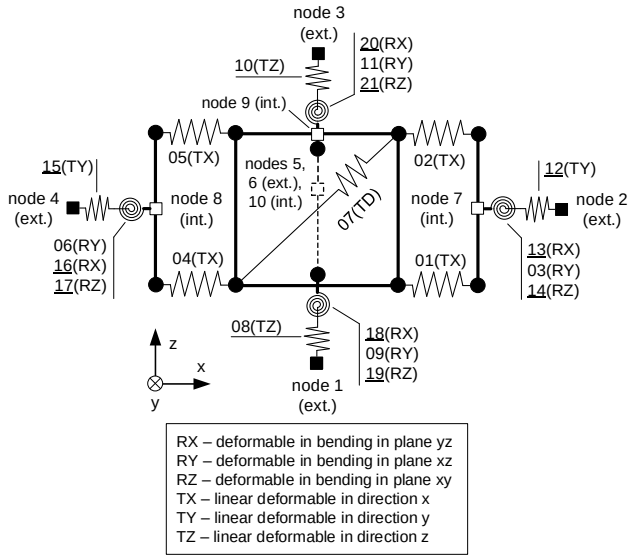

Fig. 11 Components/connections (plane XZ).

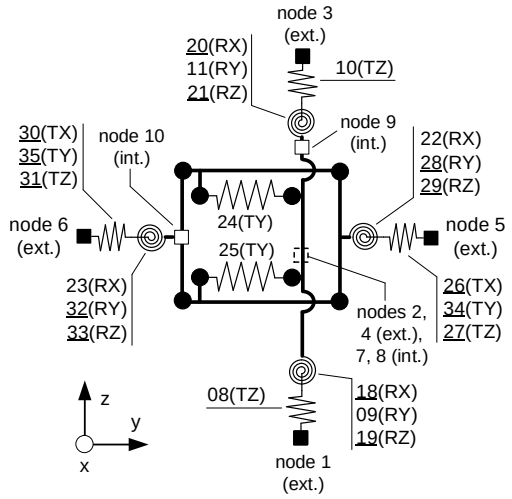

Fig. 12 Components/connections (plane YZ).

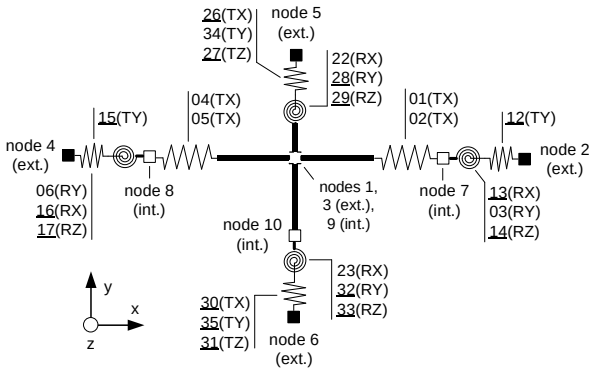

Fig. 13 Components/connections (plane XY).

In the column weak axis direction, a different strategy was considered. One of the possible strategies to account for the interaction of the bending moments coming from the beams in the weak axis directions could be a simple scissors model (see Fig. 14a) where a rotational spring allowing for rotation between the column and the beams accounts for the column web components and two additional rotational springs account for the connections. However, a more general strategy was adopted whereby two linear springs are used instead to account for the column web components (see Fig. 14b).

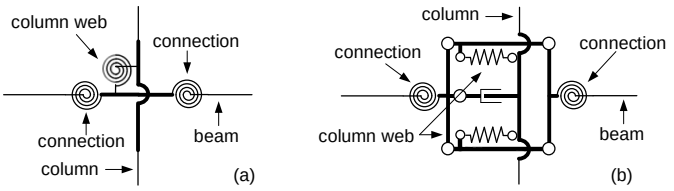

Fig. 14 Minor axis model to account for the beams interaction: (a) scissors model, (b) two springs' model.

The model represented in Fig. 14b was adopted because:

(i) it allows to account for axial forces in the beams, Fig. 15;
(ii) it allows to account for the beam "elongation/shortening" due to the different stiffness of the components;
(iii) in order to get independent external degrees of freedom in the 3D beam-to-column joint model, at least one axial component along the weak axis direction must be provided.

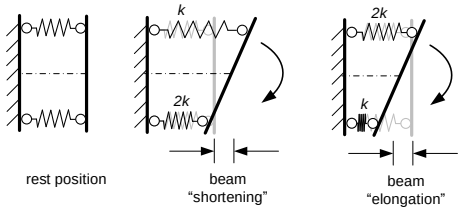

Fig. 15 Beams elongation/shortening due to the differences in stiffness of the transversal components in the web of the column.

4.3. Mathematical formulation

The linearized relation between the deformations in the springs of the model and the nodal displacements (compatibility relations) can be expressed by

$$\Delta = A \cdot u \tag{5}$$

where A is the compatibility matrix, u is the vector o nodal displacements and Δ is the vector of deformations in the springs. According to Fig. 8 to 13

$$\begin{aligned} &\Delta = [\Delta_1 \quad \cdots \quad \Delta_n \quad \cdots \quad \Delta_{35}]^T \text{ and} \\ &u = [u_1 \quad \cdots \quad u_m \quad \cdots \quad u_{41}]^T \end{aligned} \tag{6}$$

where Δ_n is the deformation in spring n and u_m is the nodal displacement according to the DOF m. The compatibility matrix is sparse and thus only the nonzero elements are shown in Table 2 – $A_{i,j}$ is the deformation in spring j caused by a unit displacement in DOF assigned to the row i when all the other DOFs are null.

Table 2
Nonzero elements of the compatibility matrix.

value	element
1	[4,1]; –[1,1]; –[8,3]; [18,4]; –[9,5]; –[19,6]; [1,7]; [2,7]; –[12,8]; [13,10]; –[3,11]; [14,12]; –[2,13]; [5,13]; [24,14]; [10,15]; –[20,16]; [11,17]; [21,18]; –[4,19]; –[5,19]; [15,20]; –[16,22]; [6,23]; –[17,24]; –[26,25]; [34,26]; –[27,27]; [22,28]; [28,29]; –[29,30]; [30,31]; –[35,32]; [31,33]; –[23,34]; –[32,35]; [33,36]; –[6,37]; [3,38]; –[14,39]; [17,39]; [29,39]; –[33,39]; –[22,40]; –[23,40]; –[24,41]; –[25,41]; –[34,41]; [35,41]
0.5	[12,2]; –[13,2]; [8,9]; –[10,9]; [27,9]; –[31,9]; [12,14]; –[15,14]; [8,21]; –[10,21]; [27,21]; –[31,21]
$sin\,\alpha$	[7,9]; –[7,21]
$cos\,\alpha$	–[7,1]; [7,13]
$\frac{d_{bY}}{(2d_{bX})}$	[26,1]; –[30,1]
$\frac{1}{d_{bX}}$	[28,1]; –[32,1]; –[13,2]; [16,2]; –[18,2]; [20,2]; –[28,13]; [32,13]; [13,14]; –[16,14]; –[18,14]; –[20,14]
$\frac{1}{d_{cX}}$	–[9,9]; [11,9]; [9,21]; –[11,21]
$\frac{d_{bY}}{d_{bX}}$	[25,2]
$\frac{(2d_{bX} - d_{bY})}{(2d_{bX})}$	[26,13]; –[30,13]
$\frac{(d_{bX} - d_{bY})}{d_{bX}}$	[25,14]
$\frac{d_{bX}}{2}$	[4,37]; –[5,37]; –[1,38]; [2,38]
$\frac{d_{cX}}{2}$	–[12,39]; [15,39]
$\frac{d_{bY}}{2}$	–[24,40]; –[25,40]

The extended stiffness matrix of the beam-to-column joint can be computed according to equation

$$K = A^T \cdot k \cdot A \tag{7}$$

where k is a 35×35 diagonal matrix where $k_{i,i} = k_i$, and $i = 1, \ldots, 35$ is the stiffness of spring i.

The stiffness matrix computed from (7) requires static condensation in order to become only explicit in terms of the external nodes displacements. Making

$$u = \begin{bmatrix} u_{ext} \\ u_{int} \end{bmatrix} \text{ with } u_{ext} = \begin{bmatrix} u_1 \\ \vdots \\ u_{36} \end{bmatrix} \text{ and } u_{int} = \begin{bmatrix} u_{37} \\ \vdots \\ u_{41} \end{bmatrix} \tag{8}$$

$$F = \begin{bmatrix} F_{ext} \\ F_{int} \end{bmatrix} \text{with } F_{ext} = \begin{bmatrix} F_1 \\ \vdots \\ F_{36} \end{bmatrix} \text{ and } F_{int} = \begin{bmatrix} 0 \\ \vdots \\ 0 \end{bmatrix} \tag{9}$$

yields

$$F = K \cdot u \rightarrow \begin{bmatrix} F_{ext} \\ F_{int} \end{bmatrix} = \begin{bmatrix} K_{ext} & K_{ie} \\ K_{ie} & K_{int} \end{bmatrix} \cdot \begin{bmatrix} u_{ext} \\ u_{int} \end{bmatrix} \tag{10}$$

so that the condensed stiffness matrix may be computed from

$$K_c = K_{ext} - K_{ie}(K_{int})^{-1} K_{ie} \tag{11}$$

4.4. Non-linear analysis procedure

Due to the internal DOFs in the models represented in Fig. 8 to 13, if a nonlinear analysis is required, the proposed beam-column joint elements require a procedure to determine the internal nodal displacements that satisfy internal equilibrium of the element for each iteration of the global solution algorithm. The approach developed by Lowes and Altoontash [30] for reinforced concrete beam-column joints was followed in the implementation of the 3D joint macro element presented in the former section in OpenSees [7].

The solution for the internal nodal displacements, and thus the material state of the beam-to-column joint element, developed by Lowes and Altoontash [30] is a classical Newton-Raphson iteration scheme. According to this scheme, the internal node displacements $u_{int,t}$ at iteration t associated to the imposed external node displacements $u_{ext,t}$ are computed starting from the node internal displacements at iteration $t-1$ and the material responses of the components/connections according to the following procedure:

(i) computation of a first estimate of the deformations of the components/connections

$$\Delta = A.\begin{bmatrix} u_{\text{ext}} \\ u_{int,t-1} \end{bmatrix} \tag{12}$$

where u_{ext} stands for the vectors of displacements assigned to external nodes, u_{int} stands for the vectors of displacements assigned to internal nodes, Δ stands for the vectors of deformations of the components/connections;

(ii) computation of the internal forces (f_i) and the tangent stiffness (k_i) of the components/connections for Δ;

(iii) computation of the unbalanced nodal forces in the internal nodes (F_{int})

$$F_{int} = \tilde{A}^T.f \tag{13}$$

where f stands for the vectors of internal forces in the components/connections, F_{int} stands for the vectors of unbalanced forces in the internal nodes and $\tilde{A}$ stands for the last columns of the compatibility matrixes (related with the internal DOFs);

(iv) iterative internal cycles until the unbalanced forces are small enough (i-th cycle)

a. check for convergence

$$F_{int}^{i}\left(F_{int}^{i}\right)^{T} < \text{tolerance} \rightarrow \text{convergence} \rightarrow \text{STOP} \tag{14}$$

b. computation of the internal node displacements making use of the Newton-Raphson iteration formula

$$u_{int}^{i+1} = u_{int}^{i} - \left(\tilde{A}^T k \tilde{A}\right)^{-1} F_{int}^{i} \tag{15}$$

where k stands for diagonal matrix where $k_{j,j} = k_j$ for each component/connection.

c. computation of the deformations of the components/connections

$$\Delta^{i+1} = A.\begin{bmatrix} u_{\text{ext}} \\ u_{int}^{i+1} \end{bmatrix} \tag{16}$$

d. computation of the internal forces and the tangent stiffness of the components/connections for Δ^{i+1};

e. computation of the unbalanced nodal forces in the internal nodes

$$F_{int}^{i+1} = \tilde{A}^T.f \tag{17}$$

f. new internal cycle $(i = i+1)$

5. Application example

The 3D frame represented in Fig. 16 to 18 was selected to illustrate the application of the 3D joint macro-element presented in section 4. It consists of pinned column base joints and full-strength and rigid external beam-to-column joints (BCJ1/2/5/6) and deformable internal beam-to-column joints (BCJ2/3). The frame was analysed for the load cases LC_1 and LC_2 presented in Table 3, with the load patterns p_1 to p_4 represented in Fig. 16 and 17, using OpenSees. The lumped plasticity element (beamWithHinges element from OpenSees) was used for simulating material non-linear behaviour in the columns and beams of the frame. An elastic-plastic behaviour for steel was considered with Young's modulus $E = 210\,GPa$, Poisson's ratio $\nu = 0.3$, yield strength $f_y = 275\,MPa$ and 0.25% linear strain hardening (as a percentage of the initial elastic modulus).

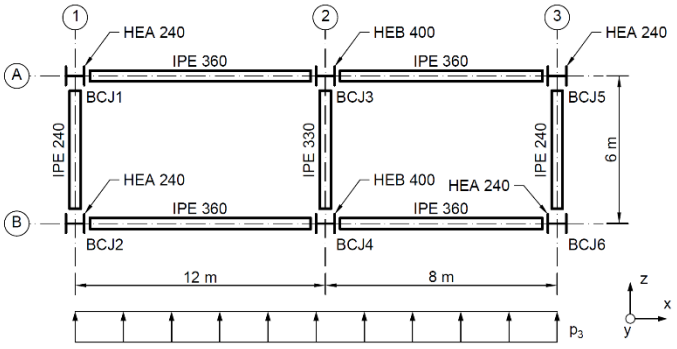

Fig. 16 Plan view of the 3D frame.

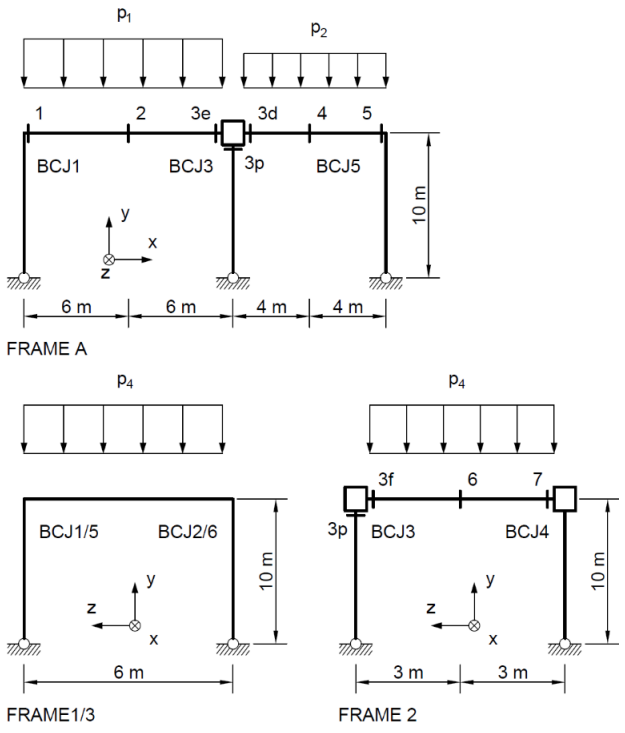

Fig. 17 Schematic representation of the side view of the frames (Frame B is similar to Frame A but no reference cross-sections are considered in Frame B).

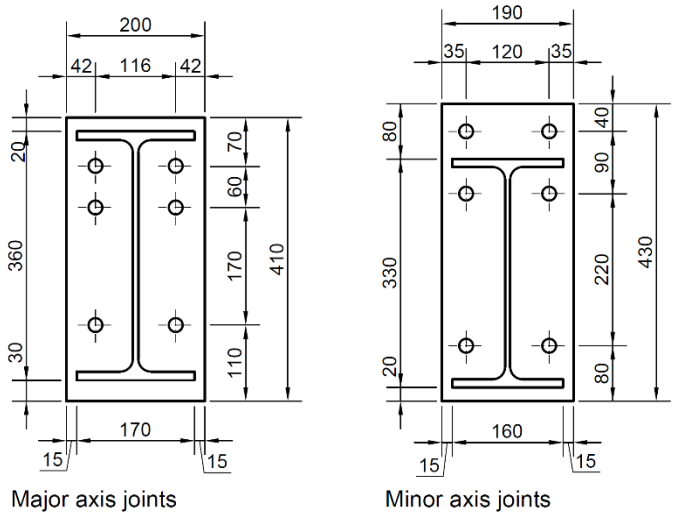

Fig. 18 Detailing of the end plates in major and minor axis joints of BCJ2/3 (in mm).

Table 3
Load cases.

load case	load patterns			
	p_1 (kN/m)	p_2 (kN/m)	p_3 (kN/m)	p_4 (kN/m)
LC_1	20	15	0.4	4
LC_2	26	20	1.0	8

Tables 4 and 5 present the mechanical properties of the components of the major and minor axis joints computed according to EC3-1-8 [10] – the component web panel in transverse tension/compression is assessed according to Neves, Silva and Vellasco [28] and Jaspart, Pietrapertosa, Weynand, Busse and Klinkhammer [29]. The resulting mechanical properties of the 0D elements of the 3D joint macro-element are summarized in Table **6.**

Table 4
Stiffness coefficients and resistance of the major axis joint components.

component	stiffness coefficient (mm)	resistance (kN)
column web panel in shear	10.89	999.9
column web in compression	10.21	934.6
column web in tension, row 1	3.171	639.4
column web in tension, row 2	3.647	767.8
column web in tension, row 3	3.808	767.8
column flange in bending, row 1	50.23	507.1
column flange in bending, row 2	57.76	508.3
column flange in bending, row 3	92.00	508.3
end-plate in bending, row 1	11.99	410.6
end-plate in bending, row 2	7.049	385.9
end-plate in bending, row 3	13.59	393.2
bolts in tension, row 1	8.525	508.4
bolts in tension, row 2	8.525	508.4
bolts in tension, row 3	8.525	508.4

Table 5
Stiffness coefficients and resistance of the minor axis joint components.

component	stiffness coefficient (mm)	resistance (kN)
beam flange in compression	∞	896.5
bolts in tension	9.1	508.4
end-plate in bending, row 1	29.0	386.9
end-plate in bending, row 2	18.2	451.8
end-plate in bending, row 3	17.1	437.9
beam web in tension, row 2	∞	725.4
beam web in tension, row 3	∞	682.6
column web in transverse tension	1.2	115.7
column web in transverse compression	2.1	134.4
column web in transverse tension: punching shear	∞	262.7
column web in transverse compression: punching shear	∞	970.6

Table 6
Mechanical properties of the springs.

0D element		resistance (kN, kNm)	initial stiffness (kN/m, kNm/rad)	post-elastic stiffness (kN/m, kNm/rad)
07(TD)	column web panel in shear	1345.2	4139289	190407
01(TX) 04(TX)	column web in compression	934.6	2144100	49314
02(TX) 05(TX)	column web in tension	2175	1834394	18344
03(RZ) 06(RZ)	external connections (without column web components)	200.2	134462	2689
08(TY)	column axial stiffness	7021	23076666	461533
09(RZ)	column bending stiffness	1147	672933	13458
24(TZ)	top transverse	115.7	252943	5058
25(TZ)	bottom transverse	134.4	435648	8712
22(RX) 23(RX)	external connections (without column web components)	123.5	165127	3302

Two analysis were performed for each load case to assess the influence of a rigorous modelling of the behaviour of beam-to-column joints: (i) three-dimensional analysis considering rigid and full strength beam-to-column joints (case RIG) and (ii) three-dimensional analysis considering the 3D joint macro-element in the internal beam-to-column joints (case 3DJ).

The values of the bending moment for ten reference cross-sections (see Fig. 17) for LC_1 and LC_2 are listed in Tables 7 and 8, respectively. These tables clearly show that the the models with rigid joints (RIG) present significant errors in the bending moment distribution when compared to the component models that account for the deformability of the joints (3DJ).

Table 7
Bending moments for LC_1.

cross-section	RIG				3DJ	
	My (kNm)	error (%)	Mz (kNm)	error (%)	My (kNm)	Mz (kNm)
1	1.2	54.1	90.2	3.3	2.5	93.3
2	3.1	10.2	179.2	8.5	3.4	195.9
3e	6.5	44.5	244.8	17.2	4.5	208.9
3d	3.8	135.2	169.9	22.0	1.6	139.2
3p	41.7	6.4	83.5	6.1	39.1	78.7
3f	2.9	4.9	42.4	6.5	3.0	39.8
4	0.8	37.1	28.0	29.7	1.3	39.9
5	0.6	69.3	2.3	59.2	1.8	5.6
6	0.0	99.8	12.6	27.3	0.0	17.3
7	2.9	5.1	53.3	29.1	3.0	41.3

Table 8
Bending moments for LC_2.

cross-section	RIG				3DJ	
	My (kNm)	error (%)	Mz (kNm)	error (%)	My (kNm)	Mz (kNm)
1	9.0	53.6	144.6	1.8	19.4	147.3
2	8.5	60.3	251.3	2.4	5.3	257.6
3^e	8.7	75.7	255.6	6.1	5.0	240.9
3^d	7.0	19.0	139.7	7.1	8.7	150.4
3^p	125.0	113.7	91.2	28.8	58.5	128.1
3^f	2.0	76.9	94.7	66.1	8.7	57.0
4	3.2	48.3	65.3	1.3	6.1	64.4
5	1.7	86.3	31.1	44.6	12.1	21.5
6	2.0	85.8	94.7	65.4	13.9	57.2
7	2.3	83.7	116.4	96.8	14.1	59.1

This example shows that the 3D macro-element is able to capture the influence of the deformability of the beam-to-column joints in an internal node of a 3D steel frame. It also highlights that with the availability of macro-elements to simulate the nodal regions of a 3D frames in computer software, it is possible to carry out efficiently the global analysis of a 3D steel frame with proper accounting for the influence of the deformability of the joints.

6. Concluding remarks

This paper presented a methodology for the analysis of steel structures using 3D structural models and incorporating the behaviour of the steel joints using 3D component models.

It is shown that the practical way to achieve this goal is the implementation of a node macro-element that encapsulates the deformability of the joints connected to a column. This strategy was implemented in the open source software OpenSeeS and may be easily implemented in commercial software.

Acknowledgments

The research leading to these results has received funding from FEDER funds through the Competitivity Factors Operational Programme - COMPETE and by national funds through FCT – Foundation for Science and Technology within the scope of the project POCI-01-0145-FEDER-007633 and through the Regional Operational Programme CENTRO2020 within the scope of the project CENTRO-01-0145-FEDER-000006.

References

[1] Jaspart, J.-P. and K. Weynand, Design of joints in steel and composite structures. ECCS Eurocode Design Manuals. 2016: ECCS - European Convention for Constructional Steelwork.
[2] Davies, J.M. and K. Morita. Three dimensional cross joints under combined axial branch loading. in Tubular Structures IV. 2001. Delft.
[3] Harada, Y. and L.S.d. Silva. Approach to macro-modeling of 3D tubular column-to-beam joint: an extension of component method for joint modeling. in Connections in Steel Structures VIII. 2016. Boston.
[4] Cabrero, J.M. and E. Bayo, The semi-rigid behaviour of three-dimensional steel beam-to-column joints subjected to proportional loading. Part I. Experimental evaluation. Journal of Constructional Steel Research, 2007. 63: p. 1241–1253.
[5] Gervásio, H., S. Dimova, and A. Pinto, Benchmarking the life-cycle environmental performance of buildings. Sustainability 2018. 10(5).
[6] Silva, L.S.d., R. Simões, and H. Gervásio, Design of steel structures. Eurocode 3: Design of steel structures. parte 1-1: general rules and rules for buildings. ECCS Eurocode Design Manuals. 2013. 456.
[7] McKenna, F., et al., Open System for Earthquake Engineering Simulation (OpenSees). Pacific Earthquake Engineering Research Center, University of California. 2000: Berkeley.
[8] Landolfo, R., et al., Design of steel structures for buildings in seimic areas. Eurocode 8: Design of structures for earthquake resistance. Part 1: general rules, seismic action and rules for buildings, ed. E.E.D. Manuals. 2017: Wiley.
[9] Simões da Silva, L., R. Simões, and H. Gervásio, Deep Underground Neutrino Experiment (DUNE). 2018, University of Coimbra.
[10] CEN, EN 1993-1-8, Eurocode 3: Design of steel structures, Part 1-8: Design of joints, European Committee for Standardisation, Editor. 2005: Brussels. p. 133.
[11] Feldmann + Weynand GmbH, COP - The connection Program. 2018: Aachen.
[12] Borges, L., NASCON - Steel connection analyser 2012: Coimbra.
[13] ISISE, Steel Connections Calculator ECCS EC3 1.8 (iOS and Android). 2018: Coimbra.
[14] Autodesk Inc., Robot Strucctural Analysis Professional. 2012: Providence.
[15] Tschemmernegg, F., D. Rubin, and A. Pavlov. Application of the component method to composite joints. in Control of the semi-rigid behaviour of civil engineering structural connections. 1998. Liège: European Commission.
[16] Huber, G. and F. Tschemmernegg, Modelling of beam-to-column joints: test evaluation and practical application. Journal of Constructional Steel Research, 1998. 45(2): p. 199-216.
[17] Castro, J.M., A.Y. Elghazouli, and B.A. Izzuddin, Modelling of the panel zone in steel and composite moment frames. Engineering Structures, 2005. 27: p. 129–144.
[18] Alves, S.F.S.J., Comportamento de juntas soldadas em nó interno com vigas de diferentes alturas e aço de alta resistência, in Departamento de Engenharia Civil. 2008, Universidade de Coimbra: Coimbra. p. 373.
[19] Costa, R., F. Gentili, and L. Simões da Silva. Development of a three dimensional model for beam-to-column joints under static loading. in X Congresso de Construção Metálica e Mista. 2015. Coimbra.
[20] Augusto, H., et al., Characterization of web panel components in double-extended bolted end-plate steel joints. Journal of Constructional Steel Research, 2016. 116: p. 271–293.
[21] Augusto, H., et al., Cyclic behaviour characterization of web panel components in bolted end-plate steel joints. Journal of Constructional Steel Research, 2016. 133: p. 310-333.
[22] Denis, F., 3DJOINTS - 3D behaviour of steel joints (in Portuguese). 2016, University of Coimbra.
[23] Valdez, J., Numerical and experimental characterization of the interation between major and minor axis joints. 2017, University of Coimbra.
[24] Costa, R., et al., Experimental behaviour of 3D end-plate beam-to-column bolted steel joints. Engineering Structures, 2019. 188: p. 277-289.
[25] Silva, L.S.d., Towards a consistent design approach for steel joints under generalized loading. Journal of Constructional Steel Research, 2008. 64: p. 1059–1075.
[26] Gentili, F., R. Costa, and L. Simões da Silva. Definition and implementation of a simplified model for steel connections in an open source software. in Eighth International Conference on Advances in Steel Structures. 2015. Lisbon.
[27] Costa, R., F. Gentili, and L. Simões da Silva. Simplified model for connections of steel structures in OpenSees. in Nordic Steel Construction Conference. 2015. Tampere.
[28] Neves, L., L.S.d. Silva, and P. Vellasco. A model for predictng the stiffness of beam to concrete filled column and minor axis joints under static monotonic loading. in Eurosteel 2005 – 4th European conference on steel and composite structures - research - Eurocodes - practice. 2005. Aachen.
[29] Jaspart, J.P., et al., Development of a full consistent design approach for bolted and welded joints in buildings frames and trusses between steel members made of hollow and/or open sections. 2005, CIDECT Report 5BP-4/05.
[30] Lowes, L.N. and A. Altoontash, Modeling reinforced-concrete beam-column joints subjected to cyclic loading. Journal of Structural Engineering-ASCE, 2003. 129(12): p. 1686-1697.

Advanced Steel Construction – Vol. 16 No. 2 (2020) 146–155
DOI:10.18057/IJASC.2020.16.2.6

DESIGN METHOD FOR COLD-FORMED STEEL U-SECTION SHORT COLUMNS

Yan-chun Li *, Tian-hua Zhou, Liu-rui Sang and Lei Zhang

Department of Civil Engineering, Chang'an University, Xi'an, China
** (Corresponding author: E-mail: liyanchun@chd.edu.cn)*

ABSTRACT

The axial bearing properties of cold-formed steel U-section short columns are investigated in this paper, including 12 columns with four types of lengths i.e.300 mm, 360 mm, 420 mm, and 450 mm. Then finite element models (FEM) were developed to simulate the experimental specimens and compared with the test results to guarantee the rationality of FEM. Moreover, the width-to-thickness and the height-to-thickness of CFS U-section short columns were examined by FEM. An approach to accurately predict the ultimate capacity of CFS U-section short columns was proposed and certified by a large number of experimental and numerical simulation data, in order to remedy the deficiency that the direct strength method (DSM) has a large error in calculating the ultimate capacity of CFS U-section short columns. Specifically, this paper not only clarified the proposed method depending on the DSM for calculating the ultimate capacity of the CFS U-section columns but also provides reference for practical engineering design and application.

ARTICLE HISTORY

Received: 11 June 2019
Revised: 16 March 2020
Accepted: 29 March 2020

KEYWORDS

Cold-formed steel;
U-section short columns;
Experiment;
Design method

1. Introduction

The cold-formed steel (CFS) structure and design theory of building structures improved the development of thin-walled and lightweight members. Due to the advantages of the diversity of cross sections, good mechanical properties, light material and material saving, while the CFS offering a satisfactory strength to mass ratio and higher post-buckling strength. The common components of CFS, including channel section, Z-section, hat-section, U-section and other single open sections， had been studied quite mature by many scholars [1-10]. Meanwhile, design methods of these simple sections were recorded in the North American Specification (AISIS100) [11] and Australian/New Zealand Standard (AS/NZS 4600) [12], including the effective width method (EWM) and direct strength method (DSM). Moreover, the bearing capacity of the U-section members according to the design methods [11, 12] has been studied quite mature by many researchers [13-19], while the research results showed that the ultimate capacity of CFS U-section members calculated by these methods [11,12] has large error and is unsafe. Therefore, it is necessary to propose a design method in calculating the ultimate capacity for CFS U-section short columns, as shown in Fig. 1.

In the past few years, ample studies have been devoted to the structural behavior and ultimate capacity of U-section members at home and abroad. Ungermann et al. [13] conducted an experiment on plain channel short columns. The research results demonstrated that short column subjected to local buckling only and an approach for an approximation of effective stiffness for coupled instabilities was proposed based on eurocode 3. Loughlan [14] developed numerical studies for fixed-end plain channel columns to examine them interaction of the local-overall flexural and the influence on behavior of local conditions at the plate ends. The results indicated that different boundary conditions resulted in quite different buckling responses of the U-section columns. An experimental research investigating the buckling and ultimate capacity of the CFS plain and dimpled steel columns was conducted by Nguyen et al. [15]. The studies revealed that the buckling and ultimate capacities of dimpled steel columns were up to 33% and 26% greater than plain steel columns, respectively. Duarte [16] presented the experimental and numerical study of CFS plain channel beams. Based on the slenderness concept, a new slenderness-based approach for the web crippling design was proposed. CFS plain channel members were researched by Young [17-19] according to experiments and numerical analyses. The buckling modes and design method were studied by his team.

In this paper, the buckling modes and ultimate capacities of CFS U-section short columns were investigated by the experiment and numerical simulations. Extensive parameters studies were carried out to study the influence of the width-thickness ratio and the height-thickness ratio of the cross-section on ultimate capacities and buckling modes of CFS U-section short columns. Depending on the experimental results and parametric study, an approach to predict the ultimate capacity of CFS U-section short columns was proposed based on the DSM. Then the results obtained by the modified method compared with the data obtained from experiment, FEM and the DSM [11], in order to verify the accuracy of the modified method.

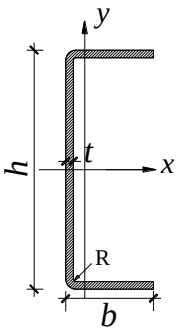

Fig. 1 U-shaped cross-section

2. Experimental design

2.1. Test setup

The POPWILL structure testing machine system and counterforce portal frame were utilized to apply a vertical load in this test. DH3820 static strain testing system was implemented to collect the data of strains and displacements. The loading device was illustrated in Fig. 2. The steel end plates with a thickness of 16 mm were welded to both ends of the members in order to fix the column. In order to eliminate the adverse influence of axial force shifting with the occurrence of local buckling [20], the specimens were placed directly on the testing rig to simulate the fixed-ended boundary condition, as shown in Fig. 2(b).

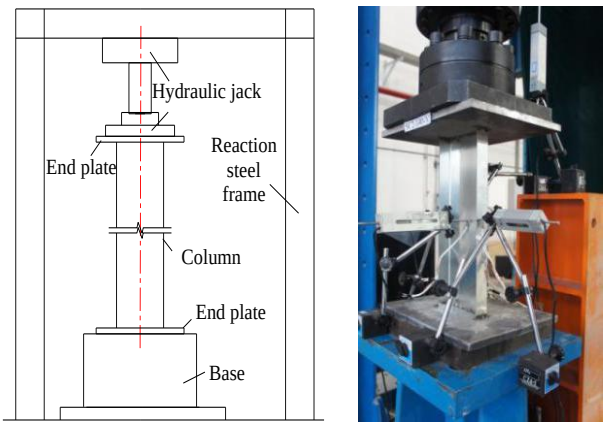

(a) Sketch Map (b) Practicality picture

Fig. 2 Test set-up

2.2. Specimens design

The CFS U-section short columns were shown in Fig. 1. Referring to the technical specification for CFS structure [21], four kinds of cross-sectional dimensions were designed, as listed in Table 1, and the labeling rule of specimens was presented in Fig. 3. Four kinds of lengths, 300mm, 360mm, 420mm, 450mm, were designed in this study. The details of the U-section short column were summarized in Table 1.

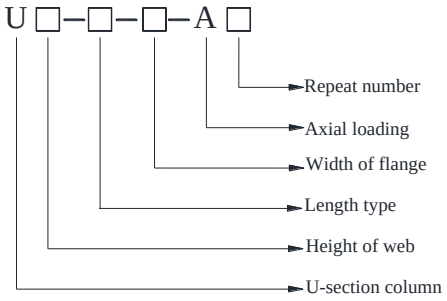

Fig. 3 Labeling rule of specimens

Table 1
Measured dimensions and failure loads of U-section short columns

Specimen	l/mm	Geometric imperfection/mm							Cross-section dimension/mm					Test results	
		Δ_{lfl}	Δ_{rfl}	Δ_{lf}	Δ_{rf}	Δ_w	δ_1	δ_2	h	b_1	b_2	t	A/mm^2	P_u/kN	Mode
U90-300-35-A1	298	1.00	1.50	0.30	0.20	0.35	2.50	0.02	96.00	36.10	35.20	1.19	199.10	36.80	L
U90 -300-35-A2	302	1.55	2.65	0.58	0.15	0.15	1.25	0.04	96.00	37.00	35.80	1.18	199.20	34.80	L
U90-300-35-A3	299	3.50	2.00	0.95	0.27	0.30	4.00	0.06	98.00	35.50	36.80	1.19	202.70	34.00	L
U120-360-50-A1	361	2.70	0.75	0.20	0.55	0.20	3.25	0.55	123.00	53.50	56.50	1.17	276.70	36.81	L
U120-360-50-A2	361	0.50	0.95	0.65	0.85	0.15	1.15	0.85	125.00	55.00	58.00	1.17	282.70	34.86	L
U120-360-50-A3	359	1.95	0.30	1.55	0.60	1.45	1.95	0.60	124.00	54.00	57.00	1.15	279.10	39.28	L
U140-420-50-A1	421	0.95	0.00	0.90	0.30	0.50	0.02	0.30	145.00	43.50	43.00	1.17	307.80	38.20	L
U140-420-50-A2	422	3.30	0.95	0.55	2.50	0.35	2.65	2.50	145.00	43.80	43.30	1.14	298.10	39.59	L
U140-420-50-A3	422	0.80	2.70	0.10	0.80	0.70	0.25	0.80	145.00	43.50	43.00	1.17	307.80	38.80	L
U140-450-35-A1	452	0.02	0.00	0.10	0.25	0.17	0.14	0.20	148.00	37.00	36.00	1.48	327.10	47.70	L
U140-450-35-A2	452	0.60	0.60	0.08	0.18	0.38	0.04	0.17	147.00	35.00	37.00	1.49	326.30	48.10	L
U140-450-35-A3	452	1.65	1.25	0.02	0.10	0.15	1.45	0.38	147.20	36.00	36.10	1.49	326.80	44.00	L

Note: 1. $A_g=(h+b_1+b_1)\times t$; P_u is the ultimate capacity; $P_y=f_y\times A_g$, where f_y is the yield stress. 2. L means local buckling.

2.3. Material characterization

The material properties of basic components adopted in the test were measured according to the codes GB/T228.1-2010 [22]. According to the different thicknesses, two groups of specimens were designed: t_1=1.2 mm, t_2=1.5 mm, as listed in Table 2. T1.2 means that the thickness is 1.2 mm and the second number refers to the repeated number. In addition, the stress-strain curves are presented in Fig. 4.

Table 2
Nominal and measured material properties obtained from tensile coupon tests

Specimen	f_y/MPa	Mean	f_u/MPa	Mean	E/GPa	Mean	Elongation
T1.2-1	332.91		451.65		2.029		32.0
T1.2-2	331.62	334.51	452.42	453.18	2.071	2.065	36.0
T1.2-3	338.99		455.46		2.096		31.0
T1.5-1	293.56		353.91		1.890		40.0
T1.5-2	285.98	289.24	347.33	350.76	1.900	1.898	42.0
T1.5-3	306.70		366.70		2.050		33.9

Note: f_y – the yield stress; f_u – the ultimate stress; E- Elastic modulus

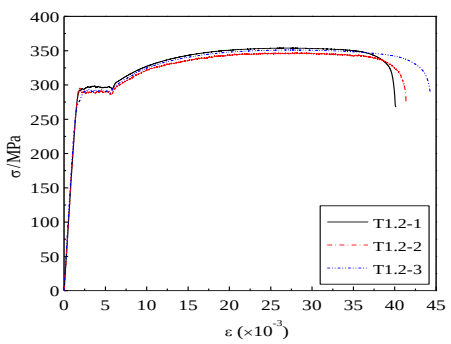

(a)

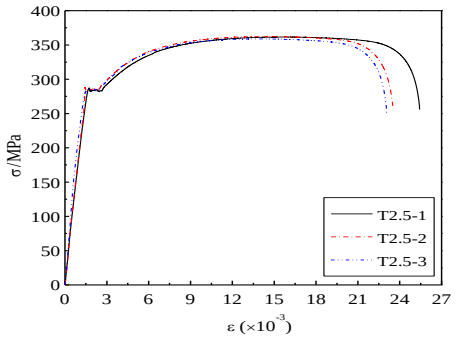

(b)

Fig. 4 Stress vs. strain curve. (a) t=1.2. (b) t=1.5

2.4. Geometric Imperfections

In this study, the initial geometric imperfections of specimens, including local and global imperfections, were measured. Local imperfection refers to the flatness of the plate and the angle between the components, as shown in Fig. 6. The specimens were fixed on the measuring platform and the rigid rod was placed on the selected plate (see Fig. 6), measuring a value with a percentile meter, and then removing the rigid rod to measure a value, finally, subtracting the former value from the latter, that is, the local initial imperfection of the plate, as listed in Table 1.

In addition, the initial geometrical imperfection of overall is the derivation of the vertical degree of the specimen. A dial indicator was used to assess the initial bending of the test members (see Fig. 7). When measuring the initial bending of specimens, specimens were fixed on the measuring platform, and then two values were measured at the two ends of members. Then an average value was measured in the middle of specimens. The latter value was utilized to subtract the average value in front of specimens, that is, the initial bending of specimens (see Table 1).

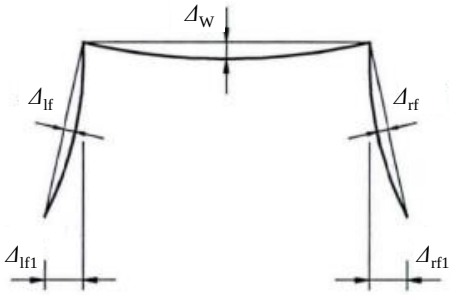

Fig. 5 Local imperfection

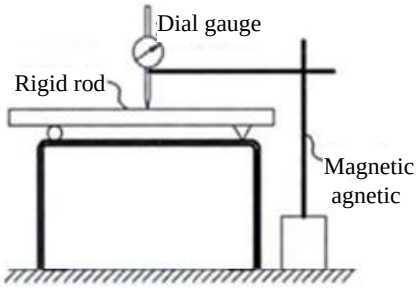

Fig. 6 Device of local imperfection

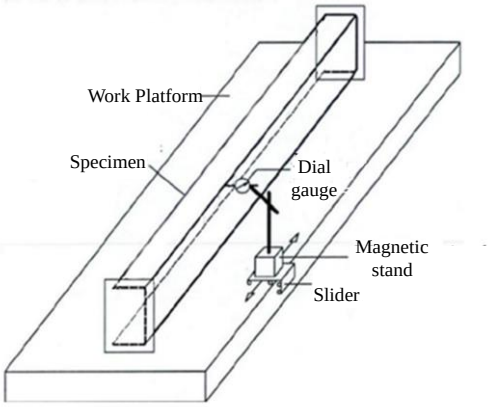

Fig. 7 Device of overall imperfections

3. Experimental results

3.1. Failure modes

3.1.1. U90 series column

The local buckling occurred (Fig. 8) on flanges of the U90-300-35-A1~A3 specimen as load increased to 15.4 kN, while the slight local buckling emerged on flanges of the A2 and A3 specimens when the load reached approximately 18 kN. The failure modes were presented in Table 1.

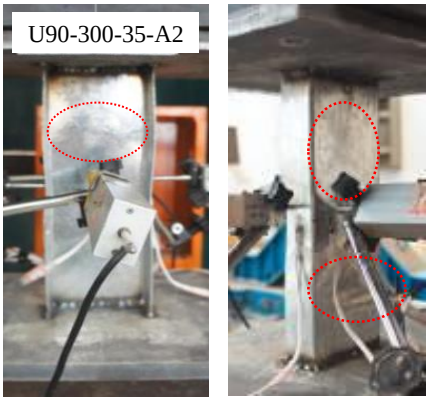

(a) Local buckling

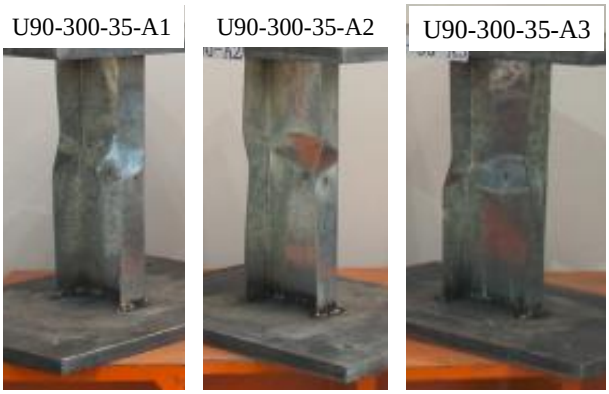

(b) Failure comparison of A1, A2 and A3 specimens

Fig. 8 Experimental phenomena of the U90-300-35-A series specimens

3.1.2. U120 series column

Fig. 9 shows the local buckling failure modes of U120-360-50-A1~A3 specimens subjected to axial pressure. There were no obvious local buckling deformation on the web at the initial stage of loading attributed to the strong welding between the end of the specimen and plates. The failure modes were indicated in Table 1.

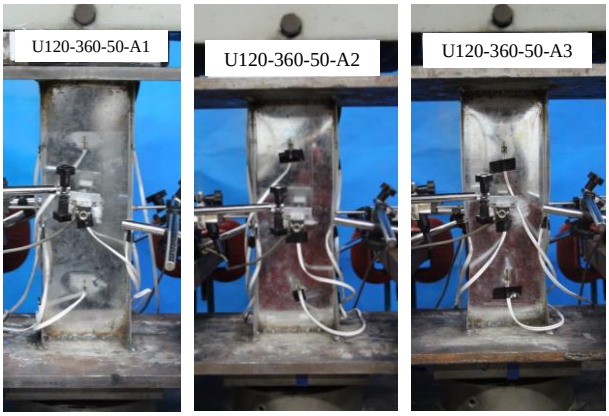

(a) Local buckling of A1, A2 and A3 specimens

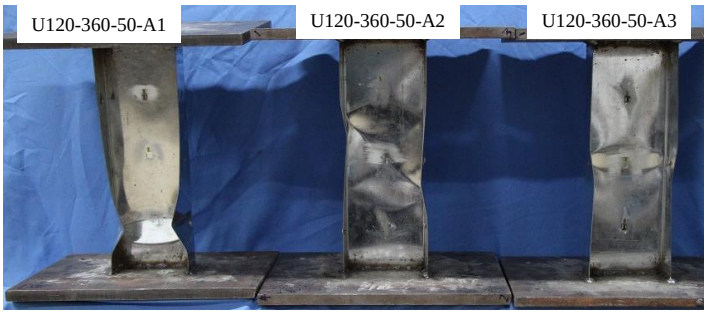

(b) Failure characteristics of A1, A2 and A3 specimens

Fig. 9 Experimental phenomena of the U120-360-50-A series specimens

3.1.3. U140 series column

Failure characteristics of U140-420-50-A1~A3 specimens were as follows: in the process of loading, local buckling occurred on flanges for the three specimens, but no obvious local buckling deformation occurred on the web. Ideally, plastic yielding occurred in the cross-sections of all three specimens when the load reached about 39 kN. Ultimately, all three specimens were damaged due to the local depression of webs and the extension of flanges, as shown in Fig. 10. The failure modes were presented in Table 1.

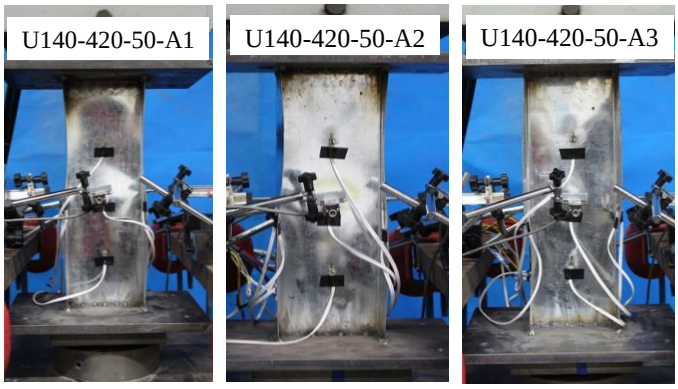

(a) Local buckling of A1, A2 and A3 specimens

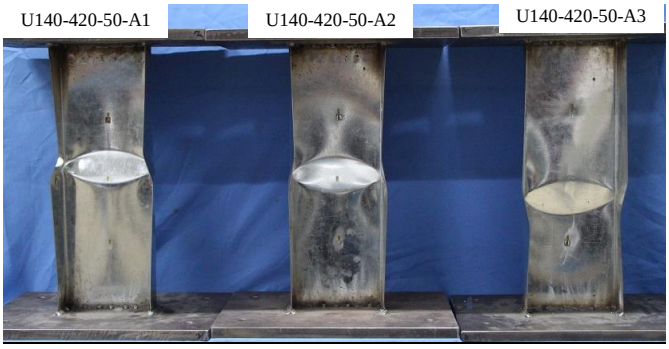

(b) Failure characteristics of A1, A2 and A3 specimens

Fig. 10 Experimental phenomena of the U140-420-50-A series specimens

For U140-450-35-A series columns, due to the specimens were welded strongly on the steel plate, the end of the specimens was not crushed and there was no obvious local buckling deformation on the web at the initial loading stage. Subsequently, with the increase of load, the experimental phenomena of specimens were the same as the U140-450-35-A1~A3 specimens, as shown in Fig. 11. The failure modes were indicated in Table 1.

(a) Local buckling of A1, A2 and A3 specimens

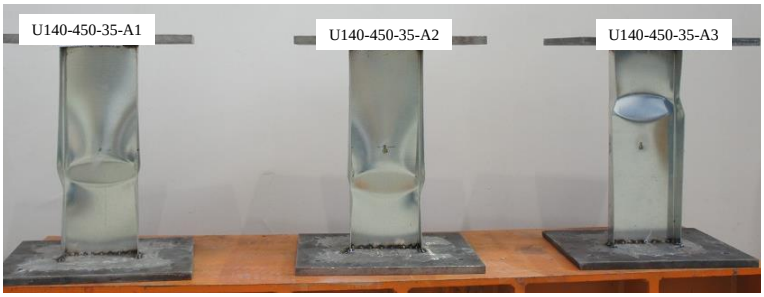

(b) Failure characteristics of A1, A2 and A3 specimens

Fig. 11 Experimental phenomena of the U140-450-35-A series specimens

3.2. Axial load-displacement curve

Fig. 12 exhibits the load-displacement curve of specimens with four types of lengths i.e.300 mm, 360 mm, 420 mm, and 450 mm. In the initial loading period, load-axial displacement curves of all the specimens were basically linear and smooth due to the stable stiffness of the test specimens. When loaded to the ultimate load, the curve showed a downward trend. The stiffness of the specimens decreased significantly, indicating that the test specimens have been damaged. It is obvious that the experimental phenomena, variation trend and ultimate capacity of the three specimens in each group were similar. The phenomenon indicated the accuracy and reliability of the experiment could be guaranteed.

4. The finite element analysis

4.1. Development of finite element model

The finite element software ABAQUS [23] was utilized in this study to establish the finite element model (FEM). The measured geometric dimensions, initial geometric imperfections and material properties (see Table 2) of the test specimens were applied to the FEM.

The column was simulated by shell element, and the element type was the four-node linear reduction integral element S4R. The more accurate results can be obtained when the mesh of specimens was 5 mm × 5 mm. In this paper, the end of the test specimens was attached to the steel plate with a thickness of 16 mm by welding. Because the stiffness of the end plate was larger than that of the specimens, the analytical stiffness was established at the end of the specimen to save the calculation cost. The rigid body displacement was controlled by the reference points on both sides of the model (RP1 and RP2 in Fig. 13). The fixed-ended boundary condition of the short columns was simulated in the FEA by restraining all degree of freedom at both ends of the FEM specimens, except for the translational degree of freedom in the axial loading direction (see Fig. 13). The same as the experiment, the displacement loading control method was employed in the FEA.

Inevitably, there were some imperfections in the fabrication process of cold-formed steel. For the geometric imperfection, the FEM captured the instability deformation modes according to the measured plate irregularity and the initial bending of the specimen. The initial imperfection for local instability and overall instability was advised by Zhang and Young [24].

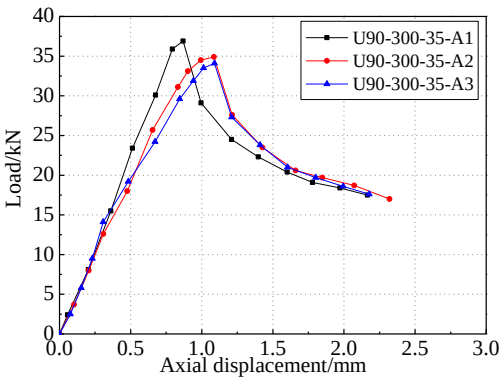

(a)

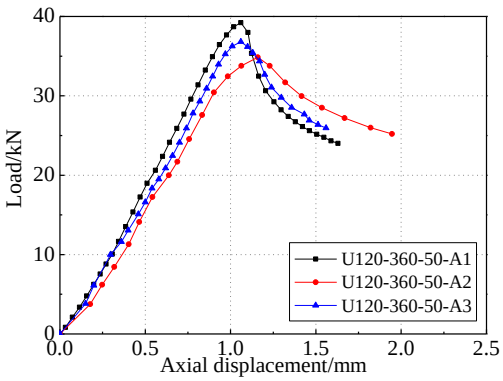

(b)

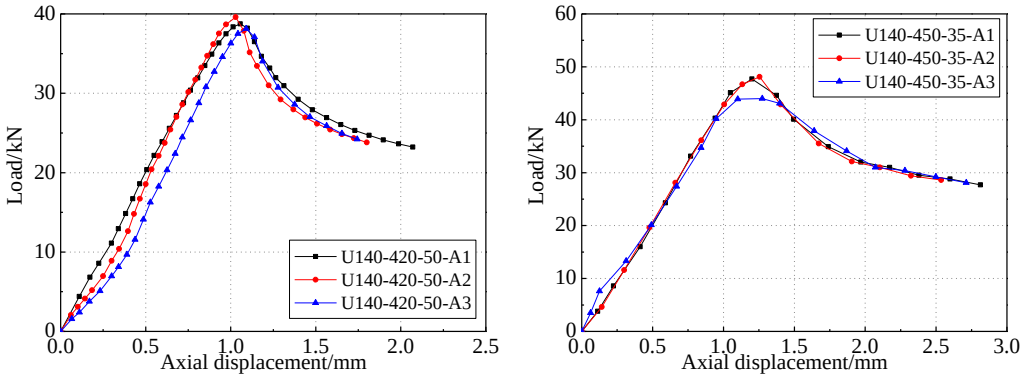

Fig. 12 Load-Axial displacement curves of specimen

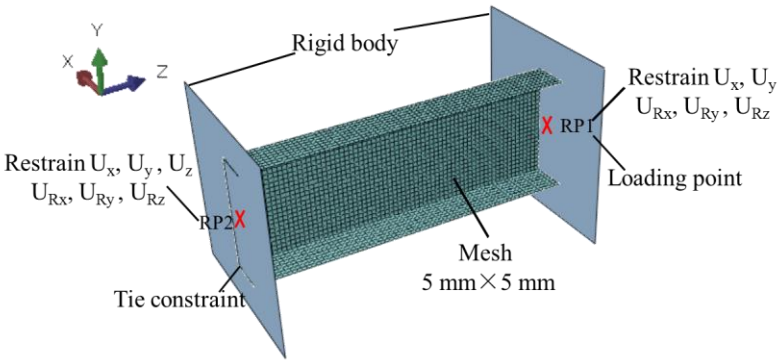

Fig. 13 Finite element mode

4.2. Validated of finite element model

The finite element models were verified by the CFS U-section columns in this study. The results obtained from the FEA (P_{FEA}) were compared with the test results (P_u), as listed in Table 3. The mean value of the P_{FEA}/P_u ratio is 1.05, with the standard deviation (SD) of 0.041. It can be observed that the ultimate capacity and failure mode obtained by the test and FEA is basically the same. What's more, the failure modes and failure position of the experimental specimens are the same as those predicted by FEA, as presented in Fig. 14. As expected, the comparison results clearly indicate that the FEA results are in good agreement with the experimental results. Therefore, the FEM is accurate and reliable in this paper.

Table 3
Comparison of the results of result and finite element analysis

Specimen	FEA results		Test results		P_{FEA}/P_u
	P_{FEA}/kN	Mode	P_u/kN	Mode	
U90-300-35-A1	37.26	L	36.82	L	1.01
U90 -300-35-A2	35.60	L	34.86	L	1.02
U90-300-35-A3	36.23	L	34.23	L	1.06
U120-360-50-A1	37.82	L	36.81	L	1.03
U120-360-50-A2	35.38	L	34.86	L	1.01
U120-360-50-A3	39.62	L	39.28	L	1.01
U140-420-50-A1	40.58	L	38.24	L	1.06
U140-420-50-A2	40.85	L	39.59	L	1.03
U140-420-50-A3	40.98	L	38.82	L	1.06
U140-450-35-A1	51.69	G	47.79	L	1.08
U140-450-35-A2	52.13	G	48.15	L	1.08
U140-450-35-A3	51.43	G	44.36	L	1.16
Mean					1.05
SD					0.041

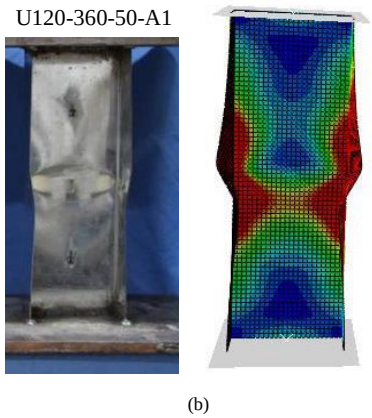

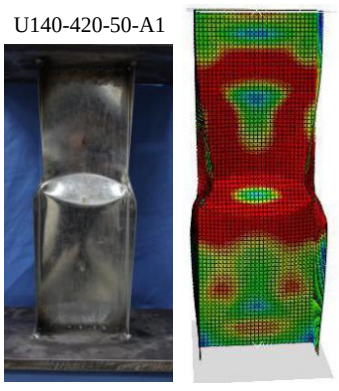

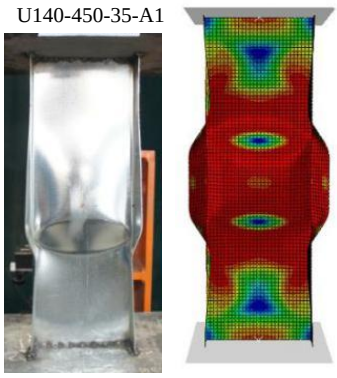

(d)

Fig. 14 Comparisons of failure modes and locations between test and finite element

4.3. Parametric studies

The length of specimens was designed to be about three times the web height (see Table 4) according to American Structural Stability Association. In this paper, a total of 64 FEM are designed by changing the height of webs, the width of flanges, and the thickness of the section. The results obtained by FEA were listed in Table 4, and the following points can be summarized by analysis results:

1. With the height and thickness of webs unchanged, the ultimate capacities of members increased with the increase of the width-thickness ratio of flanges. The phenomenon was mainly attributed to the enhanced constraint of flanges on the web with the increase of the width-thickness ratio of flanges. Therefore, the more difficult the web is to buckle, the higher the ultimate capacities of members will be.

2. The height of webs and the width of flanges remained unchanged, the ultimate capacities of all members were increased by increasing the thickness, and the increase of the ultimate capacity was very significant. This is mainly due to the increase of the thickness, for one thing, the buckling capacity of a single plate was improved, for another, the moment of inertia of member section was increased.

3. With the same flange width and thickness, increasing the height-thickness ratio of webs cannot significantly improve the ultimate capacity of U-section short columns. On one hand, the increase of web height-thickness ratios resulted in the decrease of the critical local buckling load, which led to local buckling more easily, and then affected the ultimate capacity of members. On the other hand, the inertia moment of the section around the weak axis increased slightly with the increase of web height-thickness ratios, which was the reason why simply increasing web height-thickness ratio cannot obviously improve the ultimate capacity of specimens.

Table 4
The parametric analysis of CFS U-section short columns

Specimen	*l*/mm	*b*/*t*	*h*/*t*	P_{FEA}	Specimen	*l*/mm	P_{FEA}	*b*/*t*	*h*/*t*
U140-20-1.0	420	20	140	25.18	U100-20-1.0	300	24.57	20	100
U140-20-1.5	420	13.33	93.33	48.25	U100-20-1.5	300	47.73	13.33	66.67
U140-20-2.0	420	10	70	74.65	U100-20-2.0	300	73.96	10	50
U140-20-2.5	420	8	56	105.39	U100-20-2.5	300	101.45	8	40
U140-40-1.0	420	40	140	30.32	U100-40-1.0	300	28.59	40	100
U140-40-1.5	420	26.67	93.33	58.36	U100-40-1.5	300	57.13	26.67	66.67
U140-40-2.0	420	20	70	93.85	U100-40-2.0	300	91.83	20	50
U140-40-2.5	420	16	56	136.94	U100-40-2.5	300	130.7	16	40
U140-60-1.0	420	60	140	32.11	U100-60-1.0	300	31.07	60	100
U140-60-1.5	420	40	93.33	65.16	U100-60-1.5	300	64.1	40	66.67
U140-60-2.0	420	30	70	104.21	U100-60-2.0	300	103.75	30	50
U140-60-2.5	420	24	56	151.67	U100-60-2.5	300	149.15	24	40
U140-80-1.0	420	80	140	32.69	U100-80-1.0	300	32.89	80	100
U140-80-1.5	420	53.33	93.33	68.1	U100-80-1.5	300	66.8	53.33	66.67
U140-80-2.0	420	40	70	114.38	U100-80-2.0	300	113.63	40	50
U140-80-2.5	420	32	56	166.05	U100-80-2.5	300	163.9	32	40
U120-20-1.0	360	20	120	24.92	U80-20-1.0	240	23.96	20	80
U120-20-1.5	360	13.33	80	47.79	U80-20-1.5	240	46.99	13.33	53.33
U120-20-2.0	360	10	60	74.54	U80-20-2.0	240	71.07	10	40
U120-20-2.5	360	8	48	103.28	U80-20-2.5	240	93.49	8	32
U120-40-1.0	360	40	120	29.48	U80-40-1.0	240	29.03	40	80
U120-40-1.5	360	26.67	80	57.84	U80-40-1.5	240	56.8	26.67	53.33
U120-40-2.0	360	20	60	92.15	U80-40-2.0	240	90.38	20	40
U120-40-2.5	360	16	48	132.71	U80-40-2.5	240	123.92	16	32
U120-60-1.0	360	60	120	31.61	U80-60-1.0	240	31.25	60	80
U120-60-1.5	360	40	80	64.32	U80-60-1.5	240	65.58	40	53.33
U120-60-2.0	360	30	60	104.5	U80-60-2.0	240	103.45	30	40
U120-60-2.5	360	24	48	151.21	U80-60-2.5	240	145.84	24	32
U120-80-1.0	360	80	120	32.42	U80-80-1.0	240	31.56	80	80
U120-80-1.5	360	53.33	80	68.43	U80-80-1.5	240	69	53.33	53.33
U120-80-2.0	360	40	60	114.03	U80-80-2.0	240	110.96	40	40
U120-80-2.5	360	32	48	165.67	U80-80-2.5	240	155.99	32	32

Note: U140-20-1.0, 140-the height of web (*h*); 20-the width of flange (*b*); 1.0-the thickness of section (*t*); P_{FEA}-the ultimate capacity obtained by the finite element analysis.

5. Design methods

The direct strength method (DSM) was proposed by Schafer and Pekoz [25, 26]. The DSM in the current North American Specification [11] and Australian/New Zealand Standard (AS/NZS) [12] applies only to simple single-limb sections, such as C-section, C-section with web stiffened, Z-section, R-section and hat-section. However, it is strongly associated with the geometric parameters and physical parameters of the specimens selected by Schafer in DSM. Therefore, whether the DSM is suitable for CFS U-section short columns remains to be studied.

5.1. Elastic buckling stress

The buckling mode and the corresponding elastic buckling stress are first determined for calculation using the DSM. These buckling modes and elastic buckling stresses are availed from the generalized beam theory software (GBTUL) [27].

5.2. Current direct strength method (CDSM)

The currently available DSM strength expressions, already included in AISI [11] and AS/NZS [12], provided an effective approach to estimate the ultimate capacity of CFS members subjected to columns or beams and failing in local buckling (L), distortional buckling (D), global buckling (G) or local-global buckling (LG) interactive modes. In the case of columns, the nominal strength is given by the expressions:

$$P_n=\min(P_{ne}, P_{nl}, \text{and } P_{nd}) \tag{1}$$

$$P_{ne}=\begin{cases}\left(0.658^{\lambda_c^2}\right)P_y & if \quad \lambda_c \le 1.5\\ \left(\dfrac{0.877}{\lambda_c^2}\right)P_y & if \quad \lambda_c > 1.5\end{cases} \tag{2}$$

$$P_{nel}=\begin{cases}P_{ne} & if \quad \lambda_l \le 0.776\\ \left[1-0.15\left(\dfrac{P_{crl}}{P_{ne}}\right)^{0.4}\right]\left(\dfrac{P_{crl}}{P_{ne}}\right)^{0.4}P_y & if \quad \lambda_l > 0.776\end{cases} \tag{3}$$

$$P_{nd}=\begin{cases}P_y & if \quad \lambda_l \le 0.561\\ \left[1-0.25\left(\dfrac{P_{crd}}{P_y}\right)^{0.6}\right]\left(\dfrac{P_{crd}}{P_y}\right)^{0.6}P_y & if \quad \lambda_l > 0.561\end{cases} \tag{4}$$

where$\lambda_c=(P_y/P_{cre})^{0.5}$, $\lambda_l=(P_y/P_{crl})^{0.5}$, $\lambda_d=(P_y/P_{crd})^{0.5}$, $P_y=A_g*f_y$, $P_{crl}=A_g*f_{crl}$, $P_{crd}=A_g*f_{crd}$; A_g is the gross cross-section area; f_y is the yield strength of steel; P_{cre}, P_{crl}, and P_{crd} are the elastic critical local, distortional and overall buckling load, respectively. P_{ne}, P_{nl}, and P_{nd} are the nominal overall buckling strength, local buckling strength, and distortional buckling strength, respectively.

5.3. Modified direct strength method (MDSM)

Based on experiments, parametric analysis and Mulligan [28], this paper presents a method in calculating the ultimate capacities of CFS U-section short columns, as presented in Table 5. According to the above tests and extensive numerical simulation, only local buckling occurs in short columns, therefore, the formula of DSM designed in this paper only includes local buckling under axial compression, as shown in Eq. (5).

$$P_{nl}=\begin{cases}P_y & if, \lambda_l \le 0.528\\ \left[1-0.24\left(\dfrac{P_{crl}}{P_y}\right)^{0.4}\right]\left(\dfrac{P_{crl}}{P_y}\right)^{0.4}P_y & if, \lambda_l > 0.528\end{cases} \tag{5}$$

where $\lambda_l=(P_y/P_{crl})^{0.5}$, $P_y=A*f_y$, $P_{crl}=A*f_{crl}$, P_{crl} is the elastic critical local buckling load. f_{crl} is the elastic critical local buckling stress. f_y is the yield stress of the material. A is the gross cross-section area.

6. Comparison of experimental and numerical results with design predictions

The results obtained from the experiment (P_{EXP}) and the FEA (P_{FEA}) were compared with the DSM (P_{CDSM}) and the modified DSM (P_{MDSM}) in order to verify the validity of the modified method, as shown in Table 5 and Fig. 15. It is clear that the results P_{CDSM} are generally unsafe with almost all data and the curve, while the results P_{MDSM} are generally conservative and reliable due to the (P_{EXP} and P_{FEA})/ P_{CDSM} ratio mean value of 0.93 with the standard deviation (SD) of 0.059. The mean value of the (P_{EXP} and P_{FEA})/ P_{MDSM} ratio is 1.01 with the SD of 0.056. It is demonstrated that the column strength obtained by the DSM was not safe and unreliable, which are compared with the results of the experimental and the FEA. Furthermore, it can be seen that the modified method agree well with the experiment and FEA results, as shown in Fig. 15. Hence, the proposed method can be used to predict the ultimate capacity of CFS U-section short columns and provides more reasonable design curves for CFS U-section short columns.

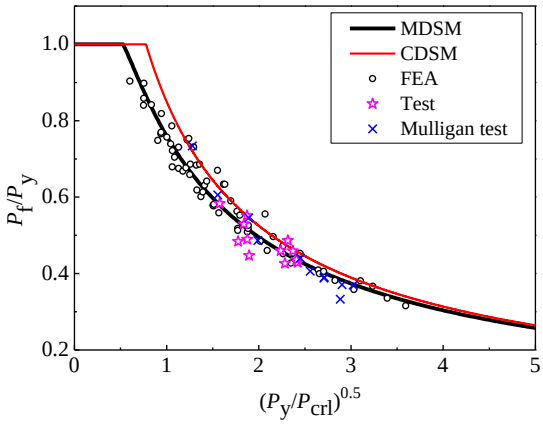

Fig. 15 Modification of the direct strength method

Table5
Comparison of numerical and experimental results with design strengths

Source	Specimen	Test and FEA (kN)	P_{CDSM}	P_{MDSM}	Comparison	
		P_{EXP} and P_{FEA}	(kN)	(kN)	P_{EXP} and P_{FEA} / P_{CDSM}	P_{EXP} and P_{FEA} / P_{MDSM}
This paper	U90-300-35-A1	36.82	39.27	36.53	0.94	1.01
	U90 -300-35-A2	34.86	34.75	32.66	1.00	1.07
	U90-300-35-A3	34.23	35.82	33.64	0.96	1.02
	U120-360-50-A1	36.81	38.71	36.72	0.95	1.00
	U120-360-50-A2	34.86	38.96	36.99	0.89	0.94
	U120-360-50-A3	39.28	38.09	36.20	1.03	1.09
	U140-420-50-A1	38.24	40.62	38.68	0.94	0.99
	U140-420-50-A2	39.59	39.99	38.04	0.99	1.04
	U140-420-50-A3	38.82	40.80	38.84	0.95	1.00

	U140-450-35-A1	47.79	56.32	52.79	0.85	0.91
	U140-450-35-A2	48.15	54.08	50.84	0.89	0.95
	U140-450-35-A3	44.36	53.71	50.52	0.83	0.88
Mulligan [28]	C1	32.92	32.31	29.58	1.02	1.11
	C2	32.69	33.91	31.52	0.96	1.04
	C3	34.69	34.75	32.68	1.00	1.06
	C4	31.58	34.21	32.26	0.92	0.98
	C5	35.06	37.72	36.08	0.93	0.97
	C6	35.09	38.01	36.36	0.92	0.97
	C7	40.74	43.98	41.97	0.93	0.97
	C8	40.92	49.28	47.25	0.83	0.87
	C9	36.47	37.45	35.67	0.97	1.02
	C10	37.90	40.78	39.11	0.93	0.97
	C11	37.81	39.55	37.99	0.96	1.00
FEA	U140-20-1.0	25.18	26.13	24.99	0.96	1.01
	U140-20-1.5	48.25	53.37	50.01	0.90	0.96
	U140-20-2.0	74.65	85.21	78.47	0.88	0.95
	U140-20-2.5	105.39	126.79	114.10	0.83	0.92
	U140-40-1.0	30.32	32.34	30.91	0.94	0.98
	U140-40-1.5	58.36	65.19	61.09	0.90	0.96
	U140-40-2.0	93.85	106.45	97.78	0.88	0.96
	U140-40-2.5	136.94	154.85	139.37	0.88	0.98
	U140-60-1.0	32.11	34.66	33.29	0.93	0.96
	U140-60-1.5	65.16	70.23	66.28	0.93	0.98
	U140-60-2.0	104.21	115.00	106.67	0.91	0.98
	U140-60-2.5	151.67	167.80	152.91	0.90	0.99
	U140-80-1.0	32.69	35.18	33.98	0.93	0.96
	U140-80-1.5	68.10	71.50	68.04	0.95	1.00
	U140-80-2.0	114.38	117.51	110.19	0.97	1.04
	U140-80-2.5	166.05	172.03	158.96	0.97	1.04
	U120-20-1.0	24.92	26.49	25.14	0.94	0.99
	U120-20-1.5	47.79	53.17	49.31	0.90	0.97
	U120-20-2.0	74.54	86.44	78.29	0.86	0.95
	U120-20-2.5	103.28	125.2	110.62	0.82	0.93
	U120-40-1.0	29.48	32.18	30.6	0.92	0.96
	U120-40-1.5	57.84	64.69	60.15	0.89	0.96
	U120-40-2.0	92.15	105.28	95.69	0.88	0.96
	U120-40-2.5	132.71	152.65	135.52	0.87	0.98
	U120-60-1.0	31.61	33.70	32.29	0.94	0.98
	U120-60-1.5	64.32	68.05	63.99	0.95	1.01
	U120-60-2.0	104.50	111.28	102.71	0.94	1.02
	U120-60-2.5	151.21	162.12	146.81	0.93	1.03
	U120-80-1.0	32.42	34.30	33.07	0.95	0.98
	U120-80-1.5	68.43	69.52	65.99	0.98	1.04
	U120-80-2.0	114.03	114.14	106.67	1.00	1.07
	U120-80-2.5	165.67	166.92	153.59	0.99	1.08
	U100-20-1.0	24.57	26.55	24.96	0.93	0.98
	U100-20-1.5	47.73	52.98	48.42	0.90	0.99
	U100-20-2.0	73.96	85.62	75.99	0.86	0.97
	U100-20-2.5	101.45	123.25	106.05	0.82	0.96
	U100-40-1.0	28.59	31.56	29.85	0.91	0.96
	U100-40-1.5	57.13	63.23	58.29	0.90	0.98
	U100-40-2.0	91.83	102.55	92.13	0.90	1.00

U100-40-2.5	130.70	148.17	129.55	0.88	1.01
U100-60-1.0	31.07	32.46	31.02	0.96	1.00
U100-60-1.5	64.10	65.43	61.30	0.98	1.05
U100-60-2.0	103.75	106.84	98.10	0.97	1.06
U100-60-2.5	149.15	155.39	139.78	0.96	1.07
U100-80-1.0	32.89	32.99	31.76	1.00	1.04
U100-80-1.5	66.80	66.85	63.31	1.00	1.06
U100-80-2.0	113.63	109.64	102.16	1.04	1.11
U100-80-2.5	163.90	160.19	146.83	1.02	1.12
U80-20-1.0	23.96	26.63	24.69	0.90	0.97
U80-20-1.5	46.99	52.68	47.12	0.89	1.00
U80-20-2.0	71.07	84.39	72.64	0.84	0.98
U80-20-2.5	93.49	120.38	99.39	0.78	0.94
U80-40-1.0	29.03	30.21	28.42	0.96	1.02
U80-40-1.5	56.80	60.31	55.15	0.94	1.03
U80-40-2.0	90.38	97.48	86.57	0.93	1.04
U80-40-2.5	123.92	140.48	120.96	0.88	1.02
U80-60-1.0	31.25	31.23	29.75	1.00	1.05
U80-60-1.5	65.58	62.84	58.59	1.04	1.12
U80-60-2.0	103.45	102.46	93.46	1.01	1.11
U80-60-2.5	145.84	166.60	150.27	0.88	0.97
U80-80-1.0	31.56	31.44	30.22	1.00	1.04
U80-80-1.5	69.00	63.61	60.12	1.08	1.15
U80-80-2.0	110.96	104.23	96.85	1.06	1.15
U80-80-2.5	155.99	152.16	138.98	1.03	1.12
Mean				0.93	1.01
SD				0.059	0.056

Note: U80-80-2.5; U-short column; 80-the height of web; 80-the width of flange; 2.5-the thickness.

7. Conclusions

The calculation method to predict the ultimate capacity of CFS short columns was proposed in this paper, according to the experiment, the finite element analysis and the current direct strength method. By research of this paper, the following conclusions are summarized:

(1) The calculation results obtained from the current direct strength method have a great error and are unsafe compared with the results obtained by the tests, finite element parameter analysis, and other researchers' test data.

(2) The presented method in this paper provides accurate calculation results for the prediction of the ultimate capacity of CFS U-section short columns, that is, the calculation error and the discreteness is very small. The modified direct strength method is a design method that can be used for engineering design reference.

(3) Due to the lack of accurate and reasonable design method for ultimate capacity of CFS U-section columns in previous researches, therefore, the purpose of this paper is modify the direct strength method to apply to CFS U-section short columns, and lay the foundation for future research on the ultimate capacity of CFS built-up members.

Acknowledgment

The authors are sincerely appreciated to the financial support by the National Natural Science Foundation of China (Grant No. 51878055).

References

[1] Lu, Y., Zhou, T.H., Li, W.C., et al., “Novel local buckling formulae for cold-formed C-section columns considering end condition effect”, Thin-walled structures, 116, 265-276, 2017.

[2] Jun Ye, Iman Hajirasouliha, Jurgen Becque., “Experimental investigation of local-flexural interactive buckling of cold-formed steel channel columns”, Thin-walled structures, 125, 245-258, 2018.

[3] Daniel C.T. Cardoso. and Guilherme C. de Salles., “Explicit equations for distortional buckling of cold-formed steel lipped channel columns”, Thin-walled structures, 119, 925-933, 2017.

[4] Torabian S, Fratamico D C, Schafer B W., “Experimental response of cold-formed steel Zee-section beam-columns”, Thin-walled structures, 98, 496-517, 2016.

[5] Adi Susila. and Jimmy Tan., “Flexural strength performance and buckling mode prediction of cold-formed steel (C section)”, Procedia Engineering, 125, 979-986, 2015.

[6] M. Bock. And E. Real., “Strength curves for web crippling design of cold-formed stainless steel hat sections”, Thin-walled structures, 85, 93-105, 2014.

[7] K.F. Chung, H.C. Ho., “Analysis and design of lapped connections between cold-formed steel Z sections”, Thin-walled structures, 43, 1071-1090, 2005.

[8] Young B. and Rasmussen K.J.R., “Test of fixed-ended plain channel column”, Journey of Structural Engineering, 124 (2), 131-139, 1998.

[9] Fan S.G., Ding R.M., Han Y.L., Chen M.H., Liu C.L., and Tao Y.L., “Experimental study on bearing capacity of austenitic stainless steel lipped channel columns”, Advanced Steel Construction, 16 (1), 65-76, 2020.

[10] Baldassino N., Bernuzzi C. and Simoncelli M., “Experimental vs. theoretical design approaches for thin-walled cold-formed steel beam-columns”, Advanced Steel Construction, 15 (1), 55-65, 2019.

[11] AISI S100-2007., “North American specification for the design of cold-formed steel structural members”, Washington: American Institute of Steel Construction, 2007.

[12] AS/NZS 4600:2005., “Cold-formed steel structures”, Sydney: Australian Institute of Steel Construction, 2005.

[13] Ungermann D., Lübke, Sebastian., Brune B., “Tests and design approach for plain channels in local and coupled local-flexural buckling based on eurocode 3”, Thin-Walled Structures, 81, 108-120, 2014.

[14] Loughlan J. and Yidris N., “The local–overall flexural interaction of fixed-ended plain channel columns and the influence on behavior of local conditions at the constituent plate ends”, Thin-Walled Structures, 81, 132-137, 2014.

[15] Nguyen V B, Wang C J, Mynors D J, et al., “Compression tests of cold-formed plain and dimpled steel columns”, Journal of Constructional Steel Research, 69 (1), 20-29, 2012.

[16] Duarte A P C. and Silvestre N., “A new slenderness-based approach for the web crippling design of plain channel steel beams”, International Journal of Steel Structures, 13 (3), 421-434, 2013.

[17] Young B., “Research on cold-formed steel columns”, Thin-Walled Structures, 46 (7), 731-740, 2008.

[18] Young B., “Bifurcation analysis of thin-walled Plain channel compression members”, Finite Elements in Analysis & Design, 41 (2), 211-225, 2005.

[19] Young B. and Yan J., “Finite element analysis and design of fixed-ended plain channel columns”, Finite Elements in Analysis and Design, 38 (6), 549-566, 2002.

[20] Pedro B. Dinis. and Eduardo M. Batista., “Local–distortional–global interaction in lipped channel columns experimental results, numerical simulations and design considerations”, Thin-walled structures, 61, 2-13, 2012.

[21] GB50018-2002., “Technical Specification for Cold-formed Thin-walled Steel Structures”, Beijing: China Planning Publishing House, 2002, (in Chinese).

[22] GB/T228.1-2010., “Tensile Test of Metal Materials Part 1: Room Temperature Test Methods”, Beijing: China Standard Press, 2010, (in Chinese).

[23] ABAQUS, “Analysis user's manual”, Version 6.9. Dassault systems; 2010.

[24] J. Zhang. and B. Young, “Finite element analysis and design of cold-formed steel built-up closed section columns with web stiffeners”, Thin-Walled Structures, 131, 223-237, 2018.
[25] Schafer B.W. and Pekoz T, “Direct strength prediction of cold-formed steel members using numerical elastic buckling solution”, Proceedings of the fourteenth international specialty conference on cold-formed steel structure, St. Louis, MO: 1998 69-76.
[26] Schafer B.W., “Review: The direct strength method of cold-formed steel member design”, Journal of Constructional Steel Research, 64 (7), 766-778, 2008.
[27] Bebiano R., Pina P., Silvestre N., Camotim D., “GBTUL — buckling and vibration analysis of thin-walled members”, Lisbon, Portugal: DECivil/IST, Technical University of Lisbon, 2008.
[28] Mulligan G.P., “The Influence of local buckling on the structural behavior of singly-symmetric cold-formed steel columns”, Ithaca: Cornell University, 1983.

Advanced Steel Construction – Vol. 16 No. 2 (2020) 156–169
DOI:10.18057/IJASC.2020.16.2.7

BEHAVIOUR OF IMPROVED DIRECT-WELDED CONNECTIONS IN SQUARE CFST COLUMN MOMENT FRAMES UNDER BIDIRECTIONAL LOADING

Helmy Tjahjanto [1, 2, *], Gregory MacRae [2] and Anthony Abu [2]

[1] *Department of Civil Engineering, Parahyangan Catholic University, Jl. Ciumbuleuit 94 Bandung 40141, Indonesia*
[2] *Department of Civil and Natural Resources Engineering, University of Canterbury, Private Bag 4800 Christchurch 8140, New Zealand*
*（*Corresponding author. Ph. +62-22-2033-692, E-mail: helmy.hermawan@unpar.ac.id*）

ABSTRACT

The behaviour of square concrete-filled steel tubular (CFST) column subassemblies with direct-welded connections has been experimentally investigated. The connection strength and stiffness have been improved by utilizing through-rods and washer plates to the column. Bidirectional loading tests have been conducted and indicate that the direct-welded connections with through-rods and washer plates result in better performance compared to the unstiffened connection. Out-of-plane shear fracture in the column tube plates due to the high stress concentration at the beam flange tips is critical and may limit the capacity of the connections. Numerical analyses have been conducted to obtain the relationship between the considered design parameters and the stress concentration in the tube plates, which has subsequently been formulated for design. The elastic rotational stiffness of the CFST joints for moment frame analyses has also been developed.

ARTICLE HISTORY

Received: 29 May 2019
Revised: 15 April 2020
Accepted: 18 April 2020

KEYWORDS

1. Introduction

Concrete-filled steel tubular (CFST) columns have been used in moment frame structures because of their good seismic performance. The concrete core and the steel tube act as a composite member to create higher strength and ductility. The concrete core could delay local buckling of the steel tube while the tube may prevent splitting of the concrete core. During construction stages, the steel tubes can also be used as formworks for the wet concrete, so the needs for temporary formworks can be minimized. The shapes of CFST column sections are commonly circular or square, which is beneficial for two-way frame structures because the columns can be constructed with moment connections in both directions. In particular, the square CFST sections are more desirable for making connections due to their flat surfaces.

Various methods of connecting beams to CFST columns have been proposed and tested. These include the diaphragm-type connections as evaluated by Nishiyama, et al. (2004) and Park, et al. (2011). Li, et al. (2009) and Sheet, et al. (2013) studied the behaviour of CFST column structures with beam-end plate connections combined with through-bolts. Alternatively, blind bolts were used in beam to CFST column connections with flush endplates and with T-stubs as proposed by Wang, et al. (2009) and Yao, et al. (2008), respectively. The advantages and disadvantages of each connection type have been summarized by Chunhaviriyakul, et al. (2015).

Among the developed connection types, the direct-welded type is one of the simplest connections. In direct-welded connections the beams are welded directly to the CFST column tube walls or plates as illustrated in Fig. 1. Since there is no conflicting element inside the CFST joints, this method is suitable for two-way frame connections. However, the joints have low strength and stiffness, because each side of the tube is not interconnected and the plates can deform separately while out-of-plane forces apply. For that reason, Schneider and Alostaz (1998) emphasized that the direct-welded connections are not normally recommended for use in seismic areas, unless the tube plates are stiffened. Improvement can be made to the direct-welded connections, such as utilizing T-stiffeners as proposed by Kang, et al. (2001). Another method to improve the strength and the stiffness of CFST column connections has been proposed by Hoang, et al. (2015) and Xu, et al. (2018) with the recommendation that long bolts should be installed through the CFST sections and fastened at both ends.

Besides the CFST joint strength and stiffness, there are also issues with direct-welded connections that should be considered. Fracture on the CFST walls near the weld was observed in the tests conducted by Li, et al. (2017). In two-way frames, early failures may occur caused by bidirectional loading interactions. The beams in perpendicular directions may reach their ultimate capacity at the same time. This negative impact of bidirectional loading may cause column yielding as found by MacRae and Tagawa (2001) and Dutta and Kunnath (2013). Different results were obtained by Tjahjanto, et al. (2019), which found that the effects of perpendicular lateral loading on two-way beam-to-CFST-column connections with external diaphragms are not significant.

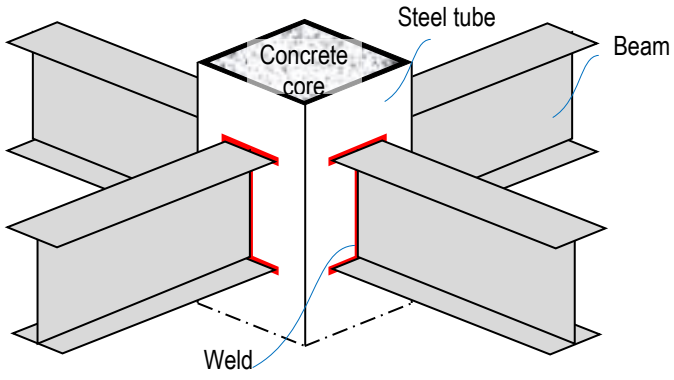

Fig. 1 Illustration of a two-way direct-welded connection in a square CFST column joint

Based on the discussion above, it is obvious that if direct welded connections are to be used, modifications are required to improve their stiffness and strength. Increasing the out-of-plane stiffness of the tube plates can improve the overall performance of the connections. From a practical point of view, it will be beneficial if the modifications do not increase the construction cost significantly. This paper describes experimental and numerical studies on improved direct-welded connections, with an emphasis on the tube-to-beam interfaces. The studies have been conducted to answer the following questions:

1) What is the likely performance of unstiffened direct-welded connections?
2) How can direct-welded connections in moment frame structures with square CFST columns be improved?
3) How does an improved direct-welded connection perform under bidirectional loading?
4) What mechanisms should be considered in design?

2. Conceptual development

A CFST column joint with an unstiffened direct-welded connection on one of its sides is considered. When a beam end moment occurs, a tension force from the connected beam flange is transferred to the joint through the tube plate. The tension force results in out-of-plane deformation of the column tube plate

(Fig. 2 (a)). The maximum out-of-plane displacement normally occurs along the weld line connected to the beam tension flange (Node A). The deformation causes bending of the tube plate in the horizontal and vertical sections. In the horizontal section, the deformation at the corner of the tubes (Node B) is restricted by the side plate or web plate of the tube. While Node C and Node D are considerably far from the beam tension flange, the plate at those nodes is quite undeformed. In most cases, the plate curvature in the horizontal section (AB) is much larger compared to the curvature in the vertical section, AC and AD. This makes the AB line become critical to the beam flange tension.

In Fig 2. (b), two pairs of through-rods are installed above and below the beam tension flange to provide additional out-of-plane restraints for the tube plate. As the curved lines in the vertical section (AC' and AD') become shorter, the plate out-of-plane stiffness increases and the curved line in the horizontal section, AB, becomes less critical. In such a configuration, the effectiveness of the restraining to the tube plate out-of-plane deformation depends on the distance between the rods and the beam flanges. In a joint with beams welded on both directions, vertical offsets between perpendicular through-rods must be provided. Consequently, some rods are placed further from the beam flanges. By way of solution, the flexural stiffness of the tube plate can be increased by inserting washer plates underneath the nuts (Fig. 2(c)). As the nuts are fastened, the washer plates clamp the tube plate and increase its out-of-plane stiffness.

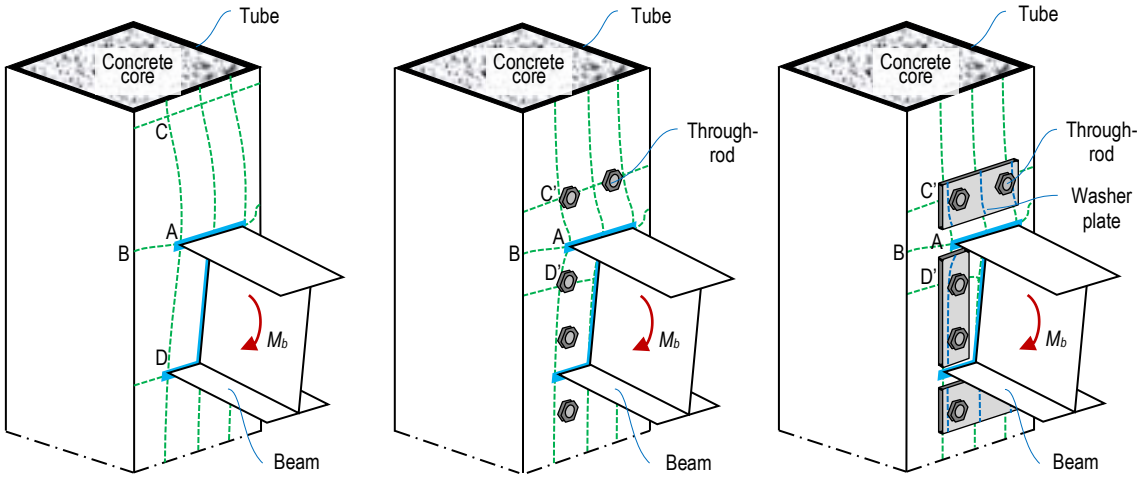

(a) Unstiffened (b) With through-rods (c) With through-rods and washer plates

Fig. 2 Out-of-plane deformation of tube plates due to beam end moments

3. Experimental program

A moment frame subassembly with square CFST column representing an interior joint in a two-way moment frame structure under lateral loading has been tested. The subassembly consists of one CFST column and four beams which are directly welded to the column tube (Fig. 3). A universal (bidirectional) hinge was placed under the column base to allow rotations in both perpendicular horizontal axes. Lateral loadings were applied on top of the column in both directions. No axial load was applied to the column. The subassembly was designed to satisfy the strong-column-weak-beam design criteria. The CFST column was SHS 250x250x9 ($f_{y\text{-}tube}$ = 311 MPa) tube filled with unreinforced concrete core (f_c' = 43.8 MPa). The beams were 200UB29.8 sections $f_{y\text{-}beam}$ = 354 MPa). The beams were welded to the column tube (10 mm fillet weld, E48xx). Threaded M16 rods (Grade 8.8) were used as through-rods for stiffening the tube plates against out-of-plane deformations. Sliding hinge joints (SHJ) with symmetric friction connections in the bottom flange and web of the beams were used as the beam splice connections.

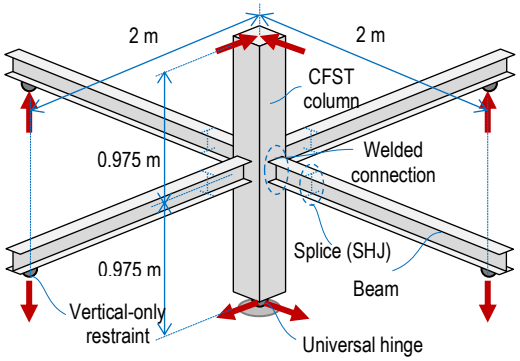

Fig. 3 Structural system and loading application of the tested subassembly

The test setup and instrumentation arrangement are shown Fig. 4 and Fig. 5. Hydraulic actuators were used to generate lateral displacements. In the W-E direction, one hydraulic actuator was attached to the top of the column. In the N-S direction, a pair of hydraulic actuators was used to avoid the possibility of column twisting. Those actuators were parallel and programmed to result in equal displacements. Lateral-torsional buckling failure of the beams was avoided by connecting diagonal braces between adjacent beams. Global rotation of the structure at beam level was controlled by two actuators connected to the end of W-E beams. The displacement of the beam-level-actuators was programmed to be proportional to the displacement of the column-top actuators based on the elevation ratio between the corresponding points to the column base.

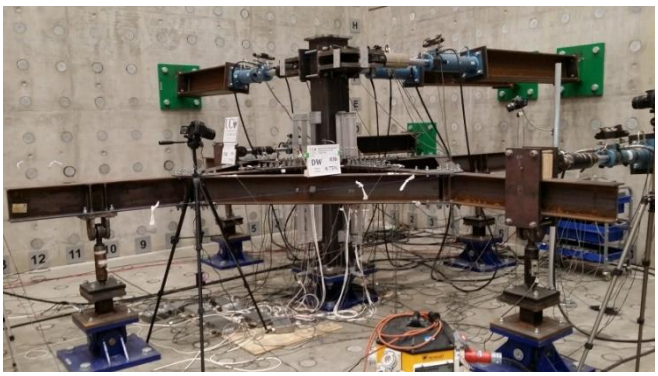

Fig. 4 The specimen and instrumentation during testing

The specimen was tested in three main stages:

1) DW-01: Unstiffened direct-welded connection (Fig. 6(a)). The through-rods had been installed through the column without nuts (unfastened).
2) DW-02: Improved direct-welded connection with through-rods (Fig. 6(b)). The rods were fastened and pretensioned.
3) DW-03: Improved direct-welded connection with through-rods and washer plates (Fig. 6(c)). Washer plates (12-mm-thick plate, Grade 300) were inserted between the tube and the nuts at both sides of the column before

the rods were pretensioned. The connection details are shown in Fig. 7. The vertical distance between the through-rods and the beam flanges, s_r, amounted to 70 mm for the connection in W-E direction and 40 mm for the connection in N-S direction.

The through-rods were pretensioned using the calibrated torque wrench method. The pretension force was estimated at 60% of the nominal proof load as specified in AS/NZS 1252:1996 (1996).

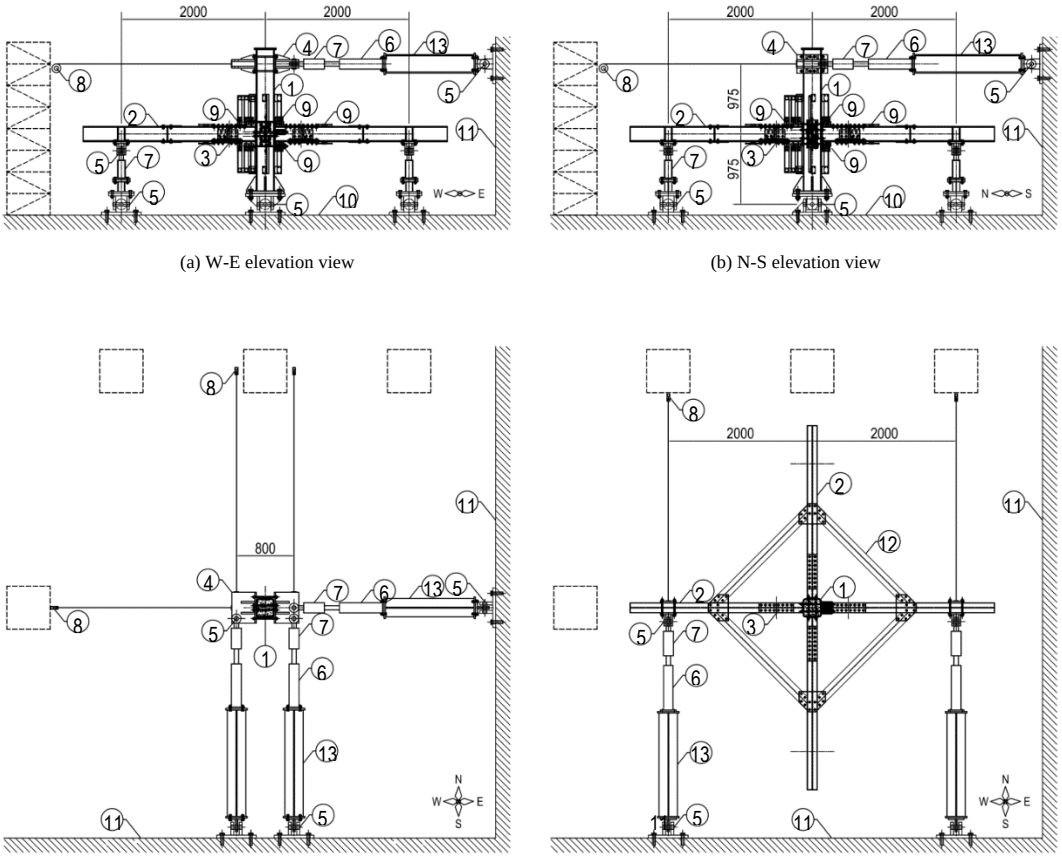

(a) W-E elevation view

(b) N-S elevation view

(c) Plan view at column top level

(d) Plan view at beam level

Legend: 1 – CFST column; 2 – beam; 3 – SHJ; 4 – loading bracket; 5 – universal pin; 6 – actuator; 7 – load cell; 8 – string/rotary potentiometer; 9 – displacement potentiometer/transducer; 10 – strong floor; 11 – strong wall; 12 – bracing beam; 13 – extension beam

Fig. 5 Test setup

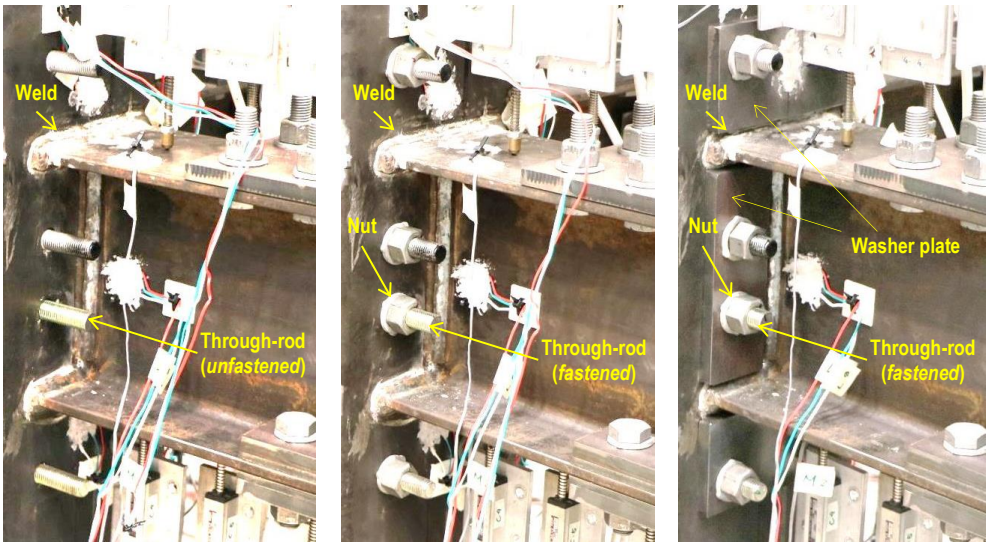

(a) DW-01 (unstiffened)

(b) DW-02 (with nuts)

(c) DW-03 (with nuts and washer plates)

Fig. 6 Variation of the test specimen

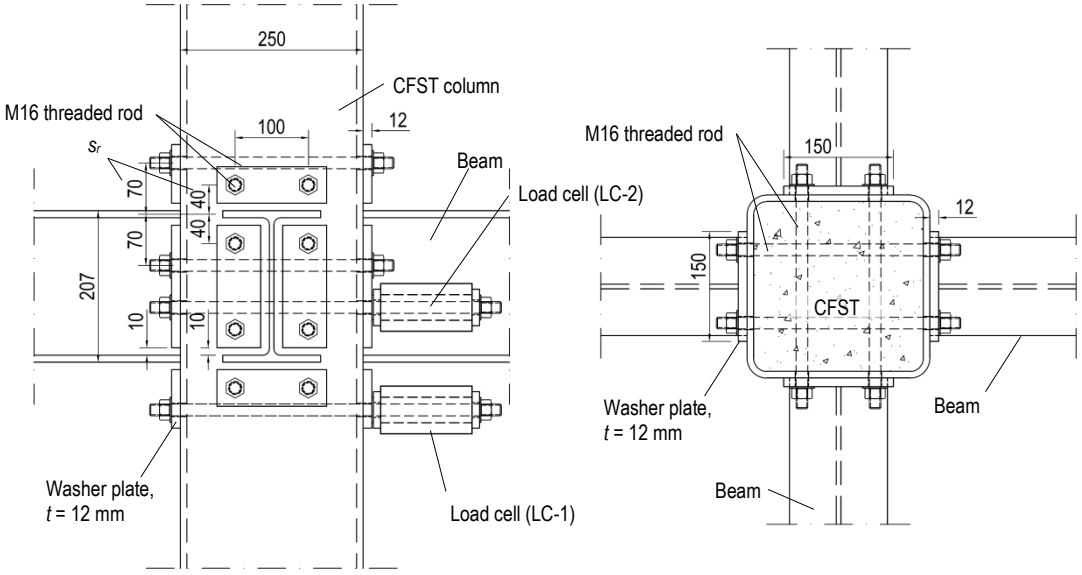

(a) Elevation view (W-E) (b) Plan view

Fig. 7 Details of CFST joint with through-rods and washer plates

An integrated loading protocol was applied to control all actuators to work simultaneously. Three loading phases were conducted in each drift increment (Fig. 8): (1) three cycles in W-E direction; (2) three cycles in N-S direction; and (3) a combination of both directions to follow a cloverleaf path. The first two configurations (DW-01 and DW-02) were tested to obtain their elastic behaviour. The tests were conducted with the drift ratio limited to 0.3% to avoid any inelastic mechanisms. For the DW-03 configuration, the maximum drift ratios for each loading stage were increased gradually: 0.1%, 0.15%, 0.2%, 0.3%, 0.4%, 0.5%, 0.75%, 1%, 1.5%, 2%, 3%, 4%, and 5%. At these phases, inelastic mechanisms (e.g. bolt slipping in SHJ and yielding in beam or tube) were expected to occur.

An additional test (DW-04) was conducted after the test of DW-03. The beam splices were made rigid by welding the plates in the previously tested SHJ in order to generate more damage to the beam-to-column connections. The loading stages for the DW-04 test consist of one cycle in each perpendicular axis and one bidirectional cycle with a maximum drift ratio of 5%.

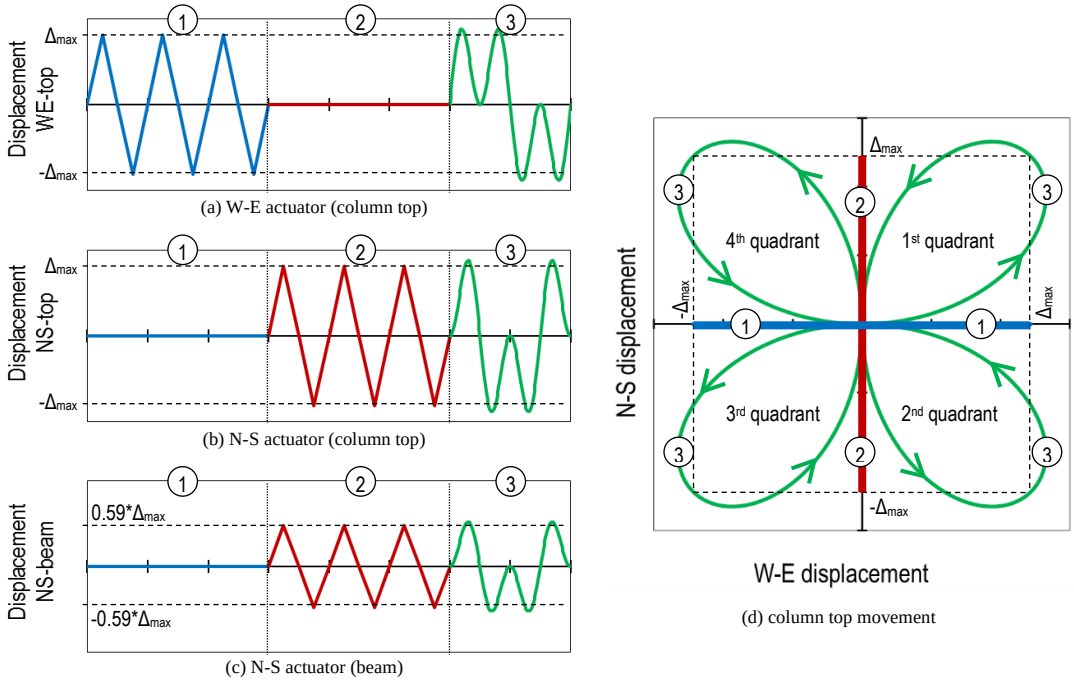

(a) W-E actuator (column top)

(b) N-S actuator (column top)

(c) N-S actuator (beam)

(d) column top movement

Fig. 8 General loading protocols

4. Behaviour

4.1. Elastic stiffness

The connections elastic rotational stiffness is evaluated using the tests of DW-01, DW-02 and DW-03 configurations. The rotational stiffness is computed as beam end moment, M_b, divided by the relative rotation between the beams and the column at the joints as illustrated in Fig. 9. The angle of rotation, θ_B, is calculated as the ratio of vertical displacement at point B, δ_B, to its distance to the column surface (80 mm). The vertical displacement was measured using a displacement transducer, which was attached to an aluminum angle bracket. The bracket was bolted to the column tube at point A, which is assumed to be unaffected by the column tube deformation at the beam-column joint.

Beam end moment, M_b, versus angle of rotation, θ_B, curves are shown in Fig. 10. The curves were plotted from the tests of configurations DW-01, DW-02 and DW-03 with a 0.3% drift ratio. The rotational stiffness of DW-01 is approximately 3500 kNm/rad, or equal to $2.4*E_sI_b/L_b$, in W-E and N-S directions. The beams flexural stiffness parameter, E_sI_b/L_b, is used for

comparison, where E_s is the modulus of elasticity of steel (= 200 GPa), I_b is the second moment of area of the beam section (= 2.91*107 mm^4), and L_b is the span of the beam (= 2000 mm). It is shown that the rotational stiffness is increased after the through-rods were fastened and pretensioned (DW-02) and after the washer plates were inserted (DW-03). In W-E direction, where the rod-to-beam distance is longer (s_r = 70 mm), the rotational stiffness in DW-02 and DW-03 amounts to approximately 7000 kNm/rad (or equal to 4.8*E_sI_b/L_b) and 8500 kNm/rad (or equal to 5.8* E_sI_b/L_b) respectively (Fig. 10 (a)). In N-S direction, where the rod-to-beam distance is shorter (s_r = 40 mm), the rotational stiffness increases in DW-02 and DW-03 to be approximately 10500 kNm/rad (or equal to 7.2* E_sI_b/L_b) and 13000 kNm/rad (or equal to 8.9* E_sI_b/L_b) respectively (Fig. 10 (b)).

For joint rigidity classification purposes, the rotational stiffness of each configuration is compared to the ranges specified in Eurocode EN 1993-1-8 (2005). The dashed lines represent the boundaries of connection rigidity classification. All the curves lie within Zone 2 (between 0.5 E_sI_b/L_b and 25 E_sI_b/L_b) and can thus be classified as 'semi-rigid'.

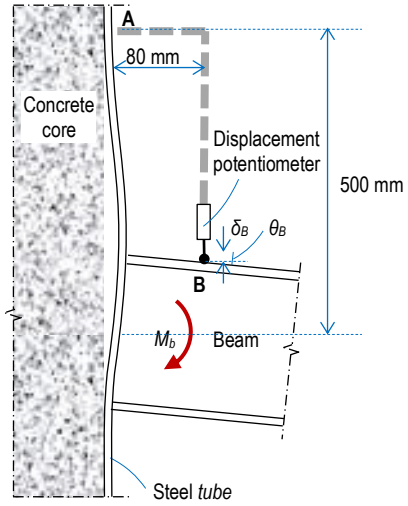

Fig. 9 Illustration of beam-column relative rotation measurement

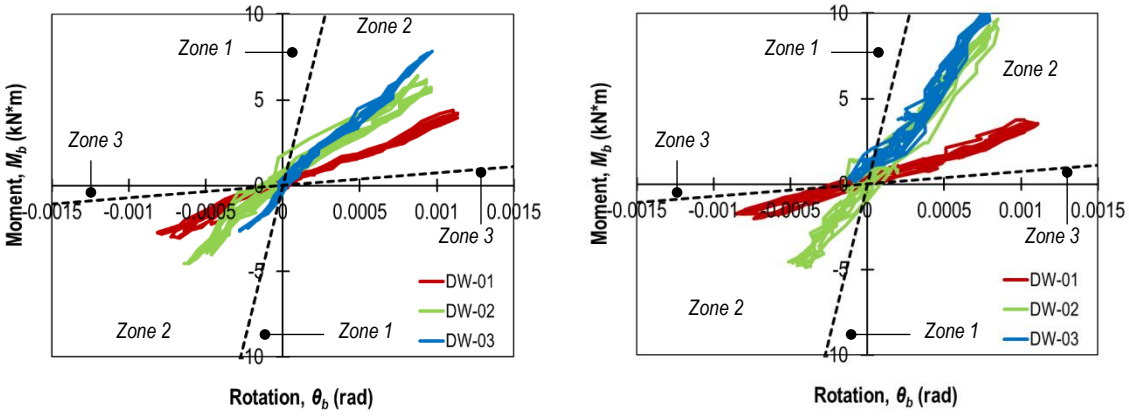

(a) W-E direction

(b) N-S direction

Fig. 10 Beam end moment versus beam-column relative rotation at 0.3% drift ratio

4.2. Stress increment in the tube

The stress increment in the tube is evaluated. The stress is presented in terms of von Mises stress, which is calculated from the measured strain and plotted versus the beam moment up to the 0.3% drift ratio, when the steel remained in the elastic region (Fig. 11). The strain values are obtained using rectangular strain gauge rosettes attached at the corner of the steel tube at the beam flange level. In W-E and N-S directions, with the bolt centres at 70 mm and 40 mm from the beam flange centres respectively, the stress increment in the unstiffened DW connection (DW-01) is estimated at approximately 13 MPa/kNm. The predicted corresponding yielding moment is 24 kNm to reach the yield strength of the tube (F_y = 311 MPa). In W-E direction (Fig. 11(a)), the stress increment of DW-02 and DW-03 is estimated at approximately 7 MPa/kNm (54% of the rate of DW-01) and 6 MPa/kNm (46% of the rate of DW-01), respectively. This implies that stiffening the tube with through-rods and washer plates can delay yielding at the column corner to twice the yielding moment of the unstiffened connection.

More significant improvement is obtained in N-S direction because the rods are closer to the beam flanges and make the tube more effectively restrained for out-ouf-plane deformation (Fig. 11(b)). The von Mises stress rates of DW-02 and DW-03 are 3.5 MPa/kNm (27% of the rate of DW-01) and 2.5 MPa/kNm (19% of the rate of DW-01), respectively. From the results, it can be concluded that reducing the distance between the rods and the beam flange can significantly delay yielding at the column corner.

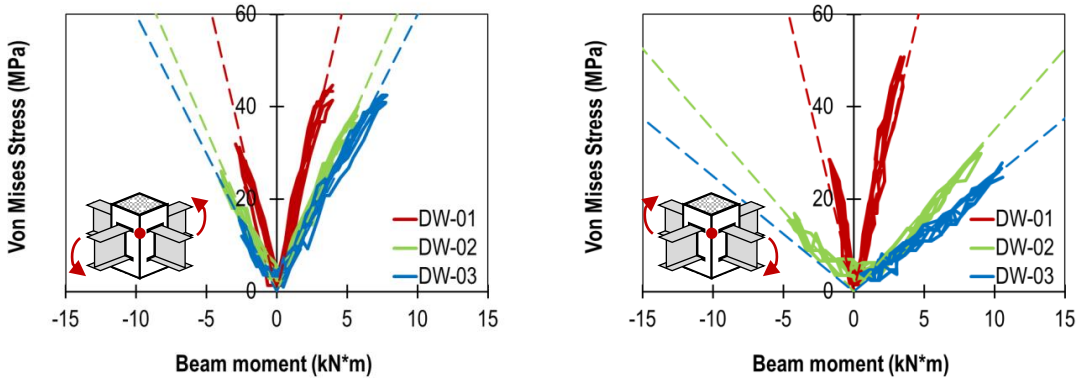

(a) W-E direction

(b) N-S direction

Fig. 11 Von Mises stress (at tube corner) versus beam end moment at 0.3% drift ratio

4.3. Hysteretic behaviour

The hysteretic behaviour of DW-03 (continuous lines) and DW-04 (dashed lines) under one-way and two-way loadings is shown in Fig. 12. The loading stages for DW-03 range from a 0.1% to a 5% drift ratio. The DW-04 configuration, where the beam splices are made rigid after the final loading series of DW-03, has been tested for the 5% drift ratio. The subassembly hysteretic behaviour in W-E direction and the one in N-S direction are plotted in Fig. 12(a) and (c) respectively.

The beam-to-column connection in N-S direction has better energy dissipation which is indicated by the less-pinched shape in hysteretic curves. The lateral force capacities of the subassembly in both directions are less than the predicted corresponding lateral force at the beam yield moment, M_{yb}. Declining of the structure lateral capacity was caused by two factors: (1) different beam flange behaviour under tension and compression forces which causes unsymmetrical stress distribution along the beam depth; and (2) sliding of the friction connections in the SHJs. The first causes early yielding ($\varepsilon \geq 0.0015$) which occurs in the compression flanges, especially if the rods are far from the flanges, as shown in Fig. 13(a). The effect of unsymmetrical stresses in beams is less significant if the rods are close to the beam flanges (Fig. 13(b). Yielding in the middle of the beam compression flange occurs when the strain exceeds the yield strain ($\varepsilon \geq \varepsilon_y = 0.0015$).

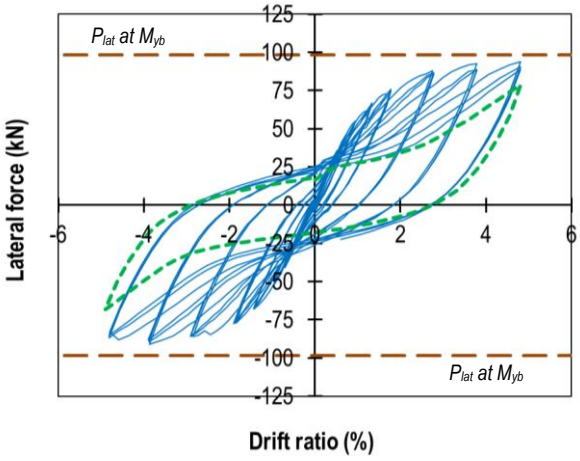

(a) W-E direction (s_r = 70 mm), one-way

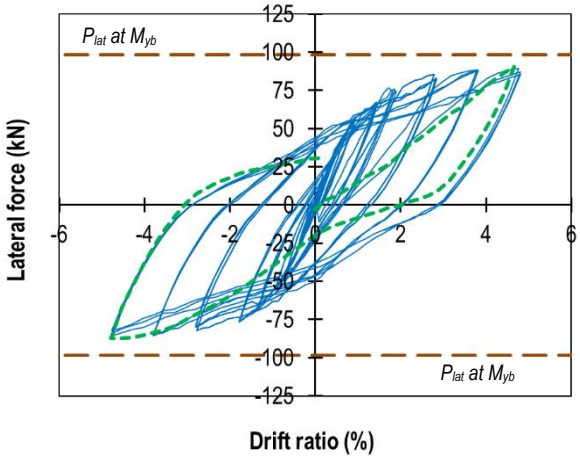

(b) N-S direction (s_r = 40 mm), one-way

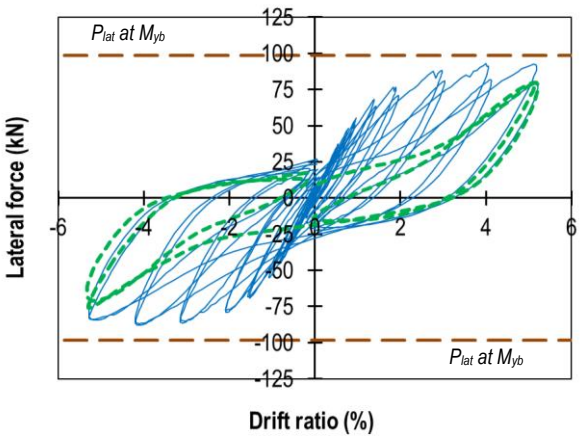

(c) W-E direction (s_r = 70 mm), two-way

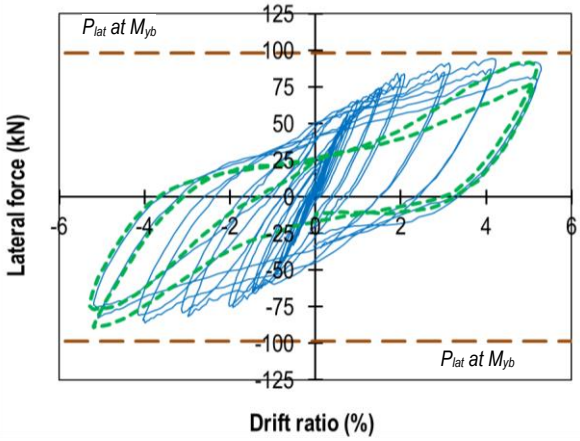

(d) N-S direction (s_r = 40 mm), two-way

Fig. 12 Hysteresis curves of lateral force versus displacement of ED-03

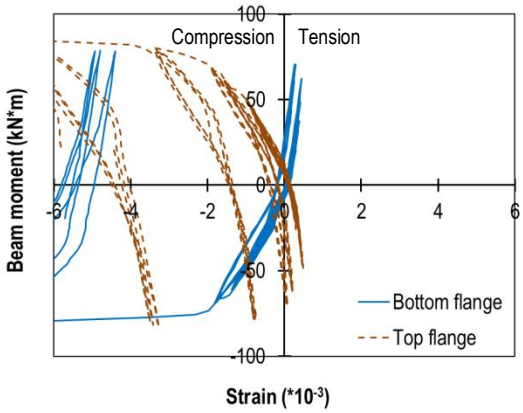

(a) W-E direction

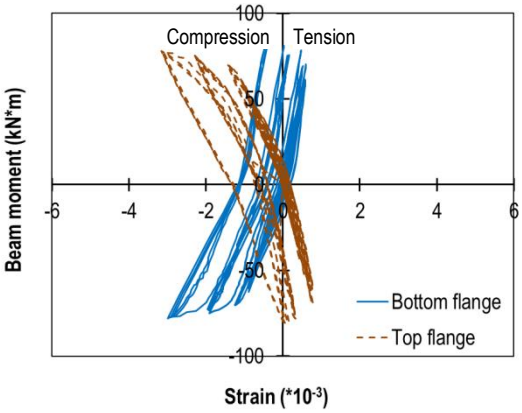

(b) N-S direction

Fig. 13 Strain in beam flanges (midpoint) due to bending moment

4.4. Component deformations

The relative rotation between the beam and the column is computed at the tube and at the beam, as illustrated in Fig. 14. The contribution of the tube, θ_t, is calculated from the out-of-plane displacement of the tube plate (Node C), δ_t, divided by the distance between Node C to the beam compression flange (Fig. 14(a)). The total joint rotation, which is computed at the beam, θ_b, is the relative vertical displacement of the beam near the joint (Node B), δ_b, divided by the distance between Node B to the connection (Fig. 14(b)). The hysteretic curves of the beam end moment versus rotations, θ_b and θ_t, for both W-E and N-S directions are plotted in Fig. 15. There are significant differences between the tube contribution, θ_t, and the total rotation, θ_b, which indicate that large inelastic deformation occurred at the beam-to-tube welded connection.

The effect of the distance of the rods to the beam flanges, s_r, can be found by comparing the curves of W-E and N-S directions. In W-E direction, where s_r is longer (70 mm), the maximum rotation of the tube is 0.009 rad and the beam rotation is 0.036 rad. In N-S direction, the maximum rotation of the tube is 0.004 rad and the beam rotation amounts to 0.029 rad.

The beam end moments, M_b, versus relative rotation at beam splices are plotted in Fig. 16. The W-E direction is depicted in Fig. 16(a) and the N-S direction in Fig. 16(b). The rotations are mostly caused by sliding in the friction connections on bottom flanges. Sliding of the friction connections occurred at approximately M_b = 60 kNm, or equal to an effective friction coefficient, μ_i = 0.34. The sliding resistance increases gradually until the beam end moments reach 80 kNm with the corresponding friction coefficient, μ = 0.45.

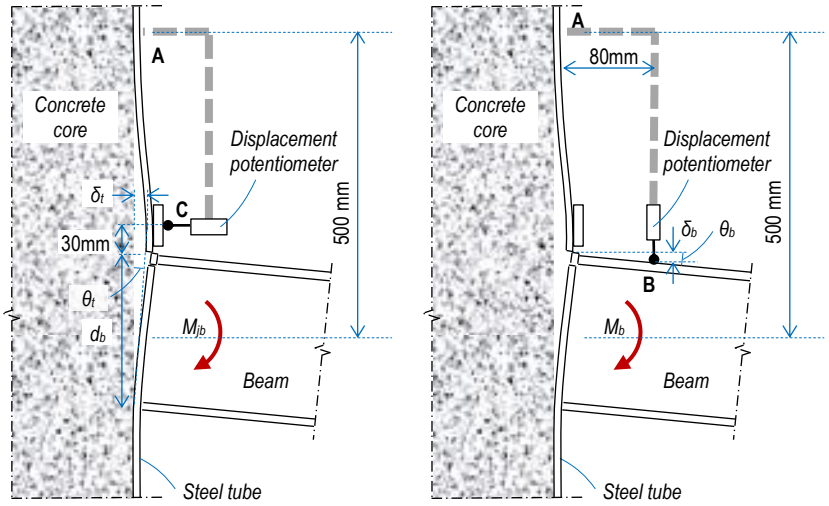

(a) At steel tube (b) At beam

Fig. 14 Illustration of beam-tube deformation discontinuity measurement

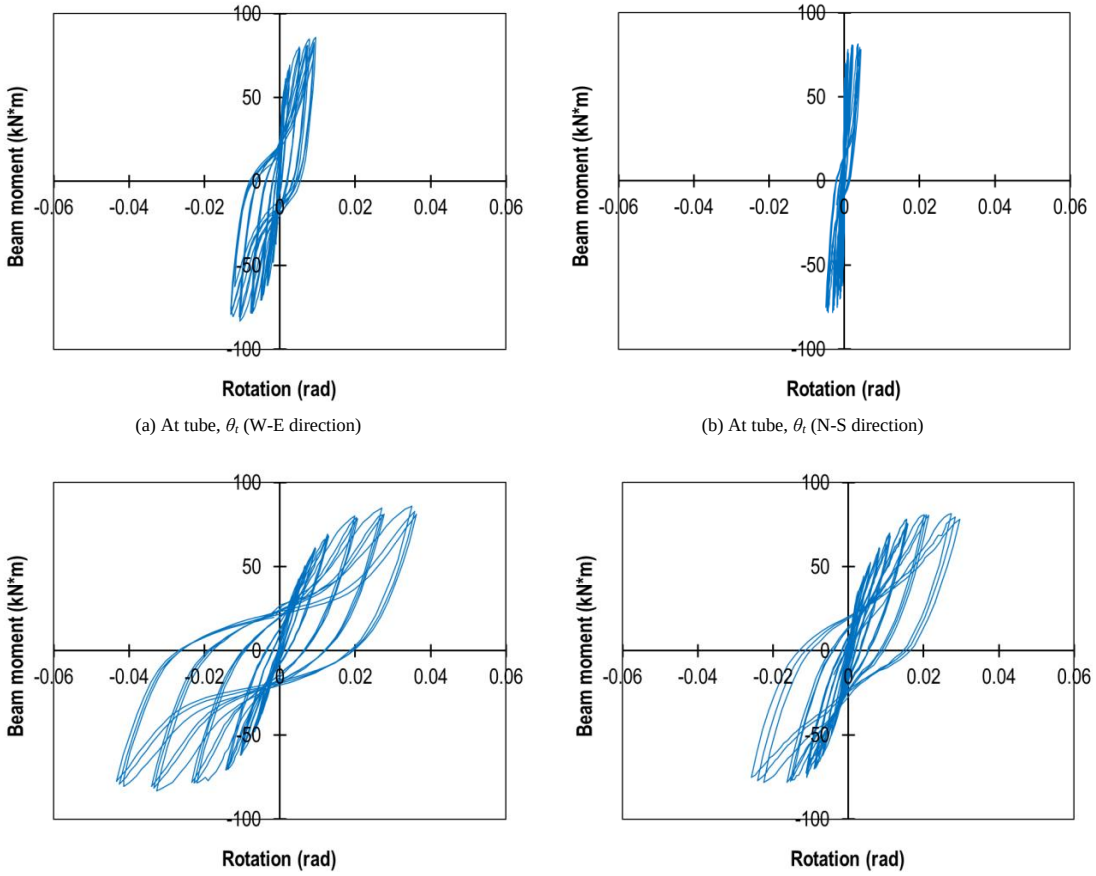

(a) At tube, θ_t (W-E direction) (b) At tube, θ_t (N-S direction)

(c) At beam, θ_b (W-E direction) (d) At beam, θ_b (N-S direction)

Fig. 15 Beam end moment versus rotation of joints (DW-03)

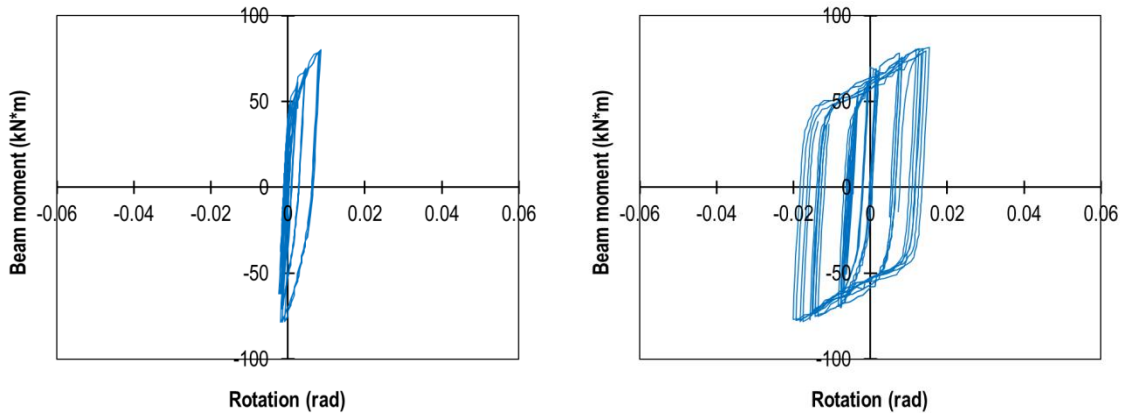

(a) W-E direction (b) N-S direction

Fig. 16 Beam end moment versus rotation at splices (DW-03)

The relative rotation contribution of each component in the subassembly is presented in Fig. 17. For the W-E direction (Fig. 17(a)) and N-S direction (Fig. 17(b)), the inelastic deformations (joint + splice) are the major contributor to the total rotations, especially when the total rotation is larger than 0.015 rad (1.5% drift ratio). In both directions, the contributions of inelastic deformations (joint + splice) are about 94% of the total rotations at the 5% drift ratio.

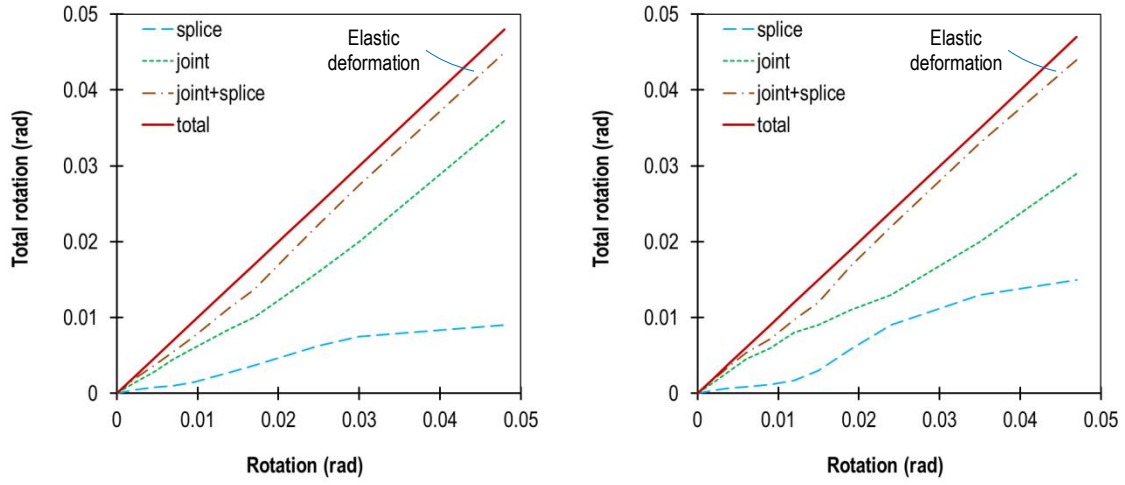

(a) W-E direction (b) N-S direction

Fig. 17 Component rotations of DW-03

4.5. Failure modes

Large inelastic deformations at the joints are indicated in the discontinuity between the deformations measured at the tube and the beams. Observation shows that local deformations at the welded connections are mainly caused by fractures in the tube due to tension forces from the beam flanges. Fracture of the tube plates was initiated from the tip of the beam flanges and propagated to the middle of the tube as the loading increased. The visible cracks in the tube were first observed at the 2% drift ratio loading stage in W-E direction and at the 4% drift ratio loading stage in N-S direction. The fractured tube at the peak of bidirectional loading phase (5% drift ratio) is shown in Fig. 18. By comparing the crack width of the adjacent beam flanges, it can be implied that the tube plate damage in W-E direction is larger than the one in N-S direction.

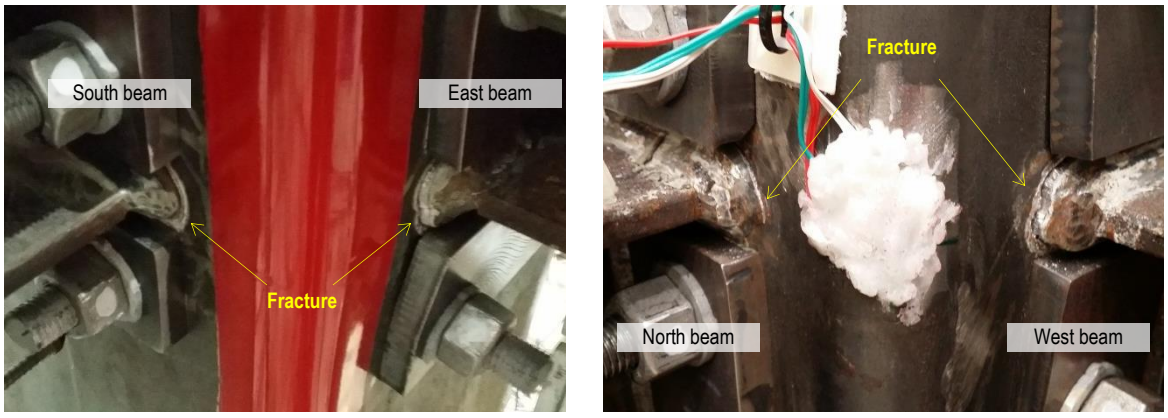

(a) Bottom flanges (b) Top flanges

Fig. 18 Fracture of steel tube at 5% drift ratio (two-way loading)

The through-rods tension forces were measured in the W-E direction using hollow cylindrical load cells that were inserted between the nuts and washer plates on an outer rod (LC-1) and an inner rod (LC-2), as arranged in Fig. 7. The pretension forces applied to the rods were approximately 60% of the nominal proof load, N_{tf}, whose value is 95 kN for M16 Grade 8.8 bolt/rod (AS 1252). The tension forces versus beam end moment hysteretic curves are plotted in Fig. 19. It is shown that the incremental rate of tension forces in the outer rods is approximately 80% of the inner rods under positive beam end moments. The rod tension forces are relatively constant under the negative moments, indicating the rods are in the compression zones.

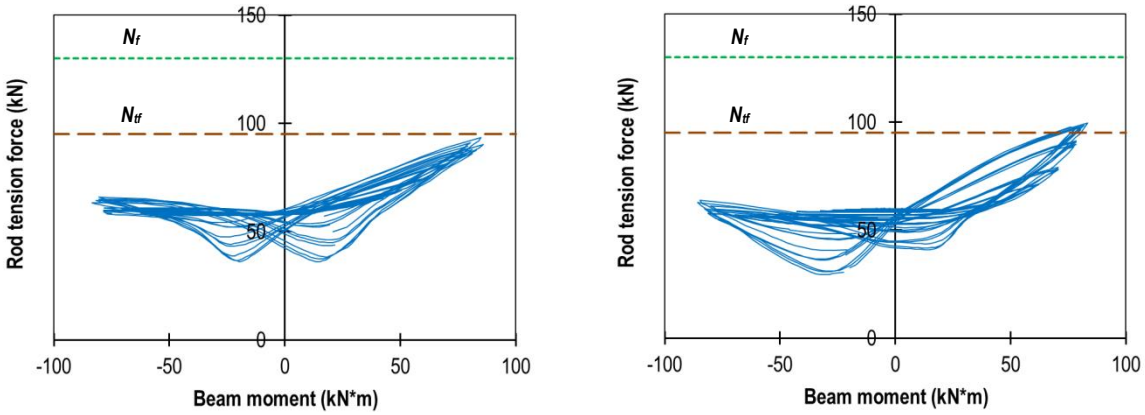

(a) Outer rod (LC-1)

(b) Inner rod (LC-2)

Fig. 19 Rod tension forces versus beam end moment (W-E direction)

As the concrete core damage cannot be observed during the tests, some parts of the column tube plates are removed after the ultimate test of the DW-04 configuration. Fig. 20 shows the indication of cone pull-out failure of the concrete around the through-rods in the N-S direction. However, there is no visible crack or concrete failure indication in the W-E direction.

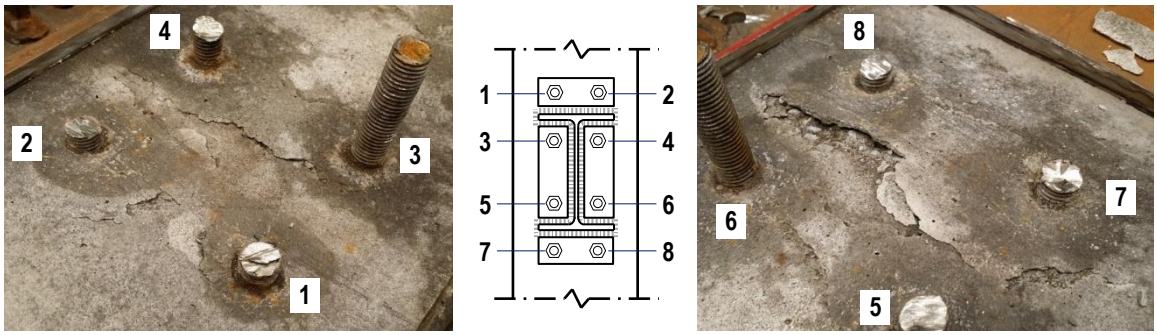

Fig. 20 Concrete cone pull-out failure in N-S direction after testing of DW-04

5. Numerical Analysis

5.1. Finite element model

Finite element analyses (FEA) have been conducted to evaluate the local behaviour of the beam-to-column interface, especially the tube fracture mechanism. The analyses were carried out using ABAQUS (SIMULIA 2012), simulating the behaviour of the connection in one considered direction, as shown in Fig. 21. The model consisted of one beam and a half-modeled CFST column. All steel plates were modeled as homogenous shell elements (S4R) with elasto-plastic materials ($f_{y\text{-}beam}$ = 354 MPa, $f_{y\text{-}tube}$ = 311 MPa). The concrete core in the CFST column was modeled as solid or brick elements (C3D8R) with a linearly elastic material. Interactions of concrete-to-steel and steel-to-steel surfaces are defined to have normal-hard-contact behaviour. Welded connection between the beam and the tube was defined as the 'tie' constraint between the paired nodes.

Three direct-welded connection configurations were evaluated, namely: (1) unstiffened; (2) stiffened with through-rods; and (3) stiffened with through-rods and washer plates, as described in Fig. 21. In the stiffened connections, through-rods were modeled as one-dimensional beam elements. The embedded parts of the rods were constrained to the concrete core to imply fully bonded interactions. The nuts were modeled as rigid shell element, linked to the end of the rods. Pretension forces in the rods were applied using a method similar to what had been conducted by Cipitioglu et al. (2002). The typical modelling stages are: (1) in the initial step, the length of the rod was made shorter than the total thickness of the connected parts; (2) longitudinal displacement was applied to the nut until the rod length exceeded the total thickness of the connected parts; (3) the nut displacement was deactivated and the contact interaction between the nut and the tube surfaces was activated.

Variations were made for the stiffened connections: the vertical distance between the rods and beam flanges (s_r = 40 mm and s_r = 70 mm); the rods pretension forces (10% N_{tf} and 90% N_{tf}); and washer plates thicknesses (t_{wp} = 12 mm and t_{wp} = 25 mm). The models with 10%N_{tf} were analyzed to represent a joint with snug tightened rods and the models with 90%N_{tf} were analyzed to represent a joint with proof-loaded rods considering long-term loss of the rods pretension forces. By way of comparison, derived from an indicative study which was conducted separately, the average of the pretension losses of the rods is 5%, measured at 8 months after pretensioning.

The nomenclature for each configuration describes: the connection type (U for unstiffened; R for with rods; RW for with rods and washer plates) – vertical distance of the rods to beam flange (in mm) – pretensioning force of the rods (in % to nominal proof load, N_{tf}) – washer plate thickness (in mm). For example: the model of RW-70-10-12 represents the configuration with rods (70 mm distance to flange, 10% N_{tf} pretension) and washer plates (t_{wp} = 12 mm).

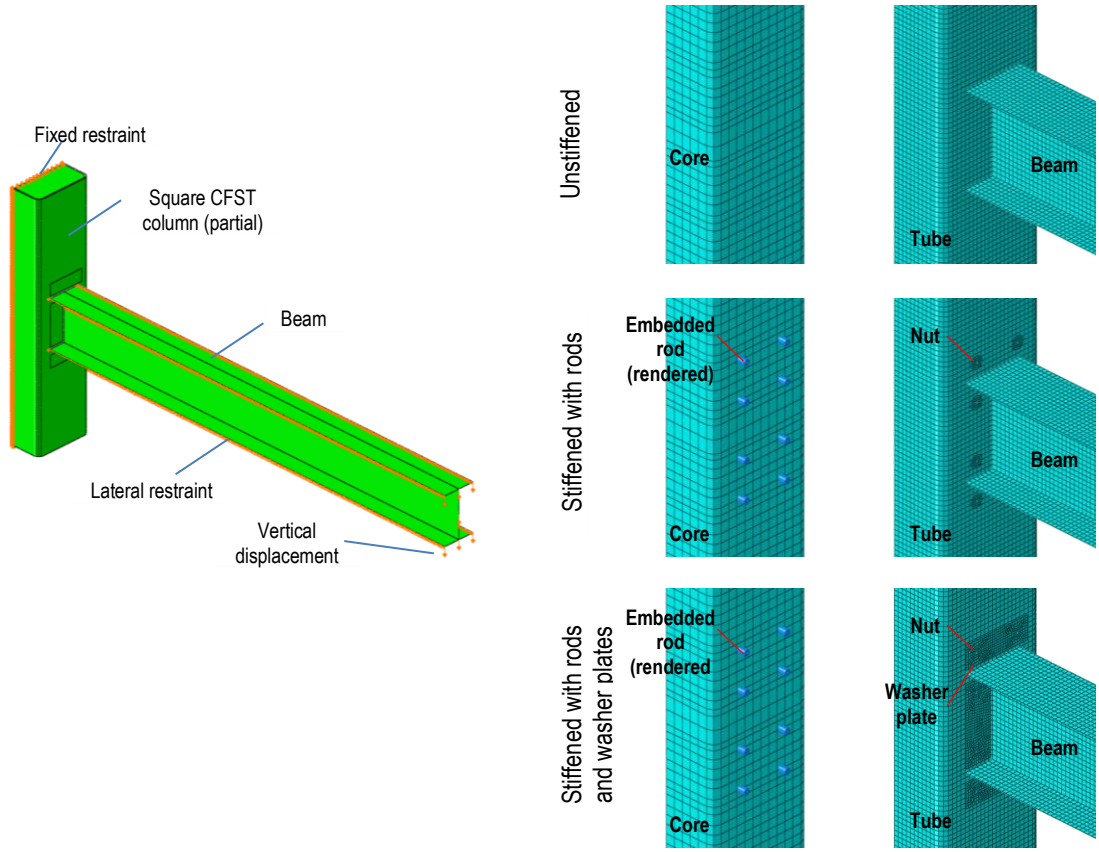

Fig. 21 Finite element modeling

5.2. Numerical results

The distributions of tension stress in beam flange due to beam moment are plotted in Fig. 22, in terms of ratio of nodal stress, σ, to estimated flange tension stress, σ_{est}, and the relative distance to the beam flange middle point (as the ratio to beam flange width, b_f). The estimated flange tension stresses are calculated with Eq. (1). The equation takes the assumption that the beams remain elastic as the fracture of the tube is expected to occur earlier than the beam yielding.

$$\sigma_{est}=\frac{M_b}{Z_{xb}} \quad (1)$$

where:
M_b is the beam end moment;
Z_{xb} is the beam elastic section modulus

It can be seen that in all configurations, the tension stresses in beam flanges are not uniformly distributed. The maximum stresses, σ_{max}, are sharply located at the tip of the beam flange which can initiate out-of-plane shear failure mechanisms in the tube plates. Table 1 summarizes the stress concentration factors, f_σ, which are computed as $\sigma_{max}/\sigma_{est}$ for all considered configurations. The lower stress concentration factors in configurations with through-rods and washer plates imply that stiffening the tube plates can reduce the possibility of pull-out fracture in the tube plates.

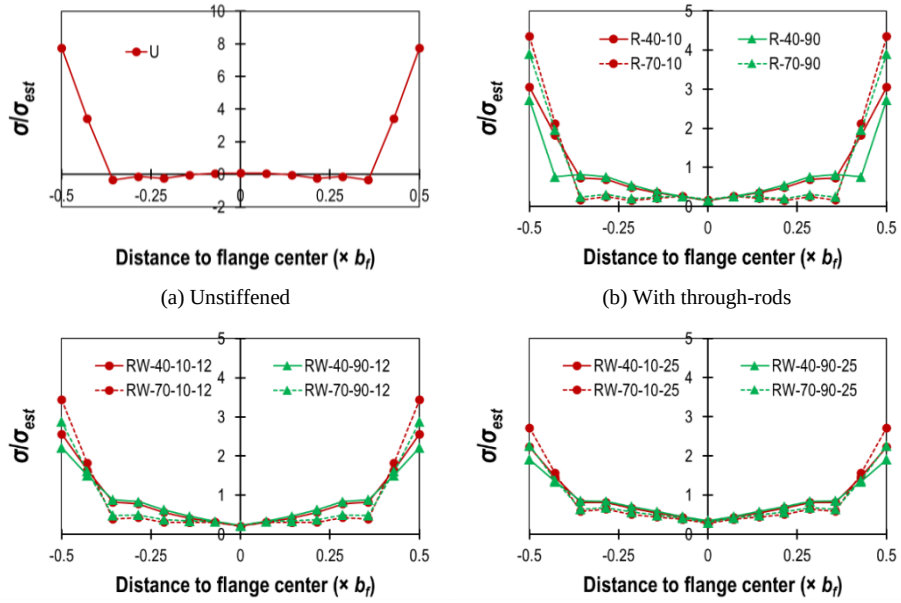

(a) Unstiffened

(b) With through-rods

(c) With through-rods and washer plates, t_{wp} = 12 mm

(d) With through-rods and washer plates, t_{wp} = 25 mm

Fig. 22 Tension stress distribution along beam flange from FE results

Table 1
Tension stress concentration factor along beam flange

Rod distance, s_{rod}	Rod pretension force	Washer plate thickness, t_w	Stress concentration factor ($f_\sigma = \sigma_{max}/\sigma_{est}$)
Unstiffened			7.76
70 mm	10% N_{tf}	No washer plate	4.35
70 mm	90% N_{tf}	No washer plate	3.90
40 mm	10% N_{tf}	No washer plate	3.81
40 mm	90% N_{tf}	No washer plate	2.73
70 mm	10% N_{tf}	12 mm	3.44
70 mm	90% N_{tf}	12 mm	2.72
40 mm	10% N_{tf}	12 mm	2.56
40 mm	90% N_{tf}	12 mm	2.23
70 mm	10% N_{tf}	25 mm	2.88
70 mm	90% N_{tf}	25 mm	2.26
40 mm	10% N_{tf}	25 mm	2.22
40 mm	90% N_{tf}	25 mm	1.91

6. Design formulation

6.1. Stress concentration factor

In order to avoid early failure, the column tubes and the welded connections along the beam flanges should have sufficient capacity to resist out-of-plane shear induced by tension forces from the beam flanges. The demand can be expressed in term of shear force per unit length, V_t*, which can be calculated as the beam flange tension stress multiplied by the flange thickness, t_f. A stress concentration factor, f_σ, must be taken into account to compensate the sharply distributed stresses near the beam flange tips, as follows:

$$V_t^{'} = f_\sigma \sigma_{est} t_f \tag{2}$$

From FE results, it is found that f_σ is influenced by the rod arrangement, rod pretension forces, and washer plate thickness. In Fig. 23, the relationship between f_σ and a non-dimensional geometrical parameter is plotted for different rod pretension levels, 10%N_{tf} and 90% N_{tf}. The stress concentration factor, f_σ, can be calculated with the following equations:

For snug-tightened rods (10%N_{tf}):

$$f_\sigma = 4.5 \times \left[\frac{L_e^{\,2} b_{wp} \left(t_{wp}^{\,3} + t_t^{\,3} \right)}{L_{wp}^{\,3} t_t^{\,3}} \right]^{-0.15} \tag{3a}$$

For proof loaded rods (90%N_{tf}):

$$f_\sigma = 4.9 \times \left[\frac{L_e^{\,2} b_{wp} \left(t_{wp}^{\,3} + t_t^{\,3} \right)}{L_{wp}^{\,3} t_t^{\,3}} \right]^{-0.13} \tag{3b}$$

where:

L_e is the clearance between the beam flange tips to the column edges;
b_{wp} is the outer washer plate width ($\geq b_f$);
t_{wp} is the washer plate thickness;
t_t is the tube plate thickness;
L_{wp} is the washer plate outstand length which contributes to transferring the force to the rods.

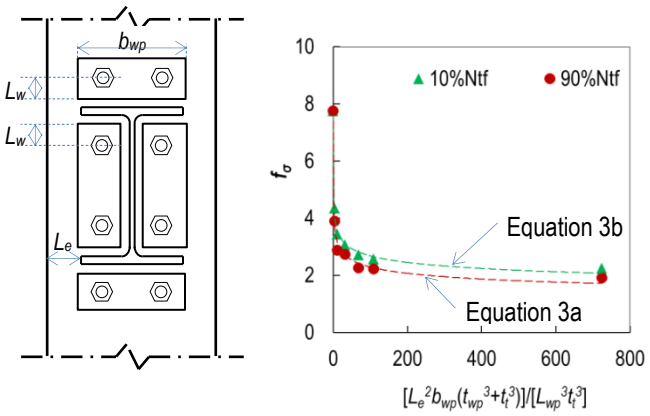

Fig. 23 Stress concentration factor, f_σ, formulation

6.2. Rotational stiffness of the joints

In the unstiffened direct-welded connection, the tube out-of-plane deformation is restrained at the corner of the column. The force transfer mechanism in the tube can be simplified by analyzing the horizontal plate strip as a one-way plate as shown in Fig. 24. The elastic rotational stiffness of the beam-to-column connection due to tube out-of-plane deformation, k_θ, can be calculated with Eq. (4):

$$k_\theta = \frac{2 E_s b_{eff} t_t^{\,3} h_b^{\,2}}{L_e^{\,3}} \tag{4}$$

where:

E_s is the modulus of elasticity of steel material;
b_{eff} is the average width of the flexible segment of the horizontal strip (= L_e, assuming 45° yield lines and thin flanges);
t_t is the tube plate thickness;
h_b is the distance between beam flange centres; and
L_e is the clearance between beam flange tips to column edges.

The connection elastic rotational stiffness, which is estimated with Eq. (4), is indicated as the slope of the dotted line in Fig. 25. The beam end moment versus connection rotation curves which are obtained from the experiments and from FE analyses are also compared with the proposed equation. It is shown that the proposed equation can accurately estimate the elastic rotational stiffness of unstiffened direct-welded connections.

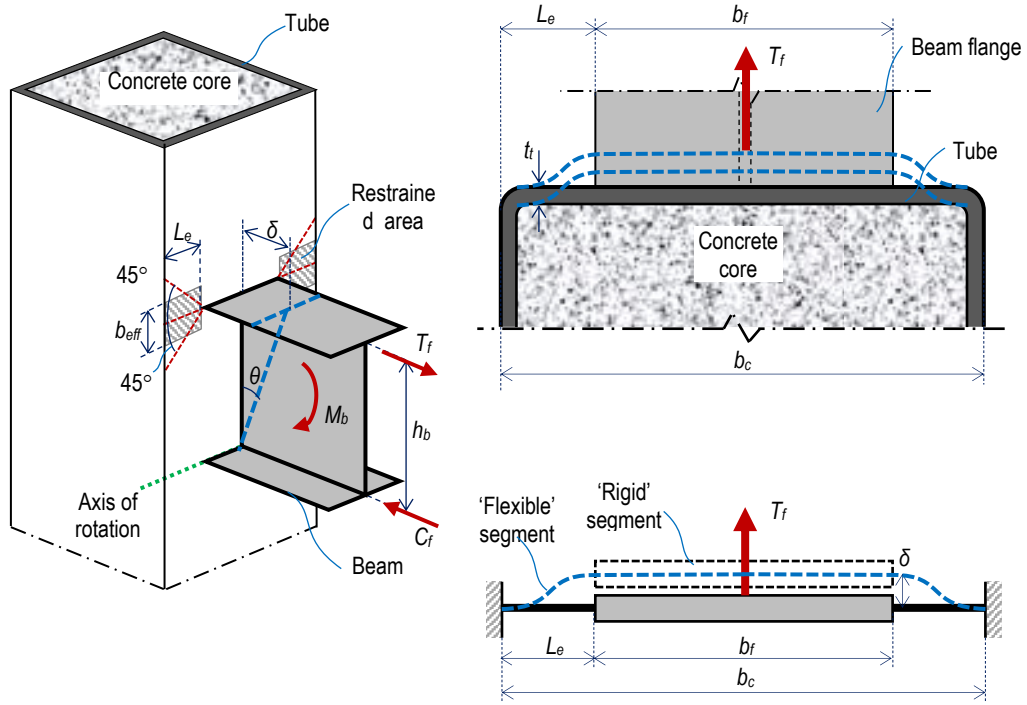

Fig. 24 One-way plate analogy for unstiffened direct-welded connection

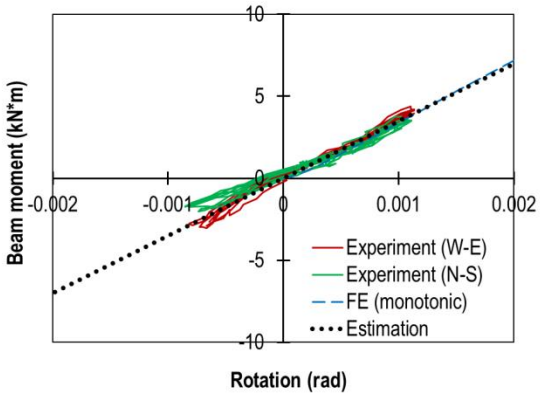

Fig. 25 Beam moment versus rotation of unstiffened direct-welded connections

In the direct-welded connections with through-rods, both with and without washer plates, the stiffness of the tube plates and washer plates in vertical direction also contributes to the tube out-of-plane stiffness. However, the clamping effect of the rods is not continuously provided along the column width, as illustrated in Fig. 26. For connections stiffened with through-rods, the rotational stiffness, k_θ, can be approximated using the following equation:

$$k_\theta = \frac{2E_s b_{eff} t_t^{\,3} h_b^{\,2}}{L_e^{\,3}} + \beta_r \times \frac{2E_s b_c t_t^{\,3} h_b^{\,2}}{s_r^{\,3}} \tag{5}$$

The fixity factor, β_r, is taken into account to consider the clamping effect of the rods (Fig. 27(a)).

For snug-tightened rods (10%N_{tf}):

$$\beta_r = min\left[1.1 - 3.2\left(\frac{t_t}{s_r}\right), 1.0\right] \tag{6a}$$

For proofloaded rods (90%N_{tf}):

$$\beta_r = min\left[1.6 - 4.5\left(\frac{t_t}{s_r}\right), 1.0\right] \tag{6b}$$

where:

E_s is is the modulus of elasticity of steel material;
b_{eff} is average width of the flexible segment of the horizontal strip (= L_e, assuming 45° yield lines and thin flanges);
t_t is the tube plate thickness;
h_b is the distance between the beam flange centres;
L_e is the clearance between the beam flange tips to the column edges;
b_c is the column width; and
s_r is the rod distance to the beam flange.

Similarly, for connections stiffened with through-rods and washer plates, the rotational stiffness, k_θ, can be calculated with the following equation:

$$k_\theta = \frac{2E_s b_{eff} t_t^{\,3} h_b^{\,2}}{L_e^{\,3}} + \beta_{rw} \times \frac{2E_s b_{wp}\left(t_t^{\,3} + t_{wp}^{\,3}\right) h_b^{\,2}}{s_r^{\,3}} \tag{7}$$

The fixity factor, β_{rw}, is taken into account to consider the rods clamping effect (Fig. 27(b)).

For snug-tightened rods (10%N_{tf}):

$$\beta_{rw} = min\left[0.05\left(\frac{t_{wp}}{s_r}\right)^{-1.6}, 1.0\right] \tag{8a}$$

For proofloaded rods (90%N_{tf}):

$$\beta_{rw} = min\left[0.07\left(\frac{t_{wp}}{s_r}\right)^{-1.6}, 1.0\right] \tag{8b}$$

where:

t_{wp} is the washer plate thickness and
b_{wp} is the outer washer plate width ($\geq b_f$)

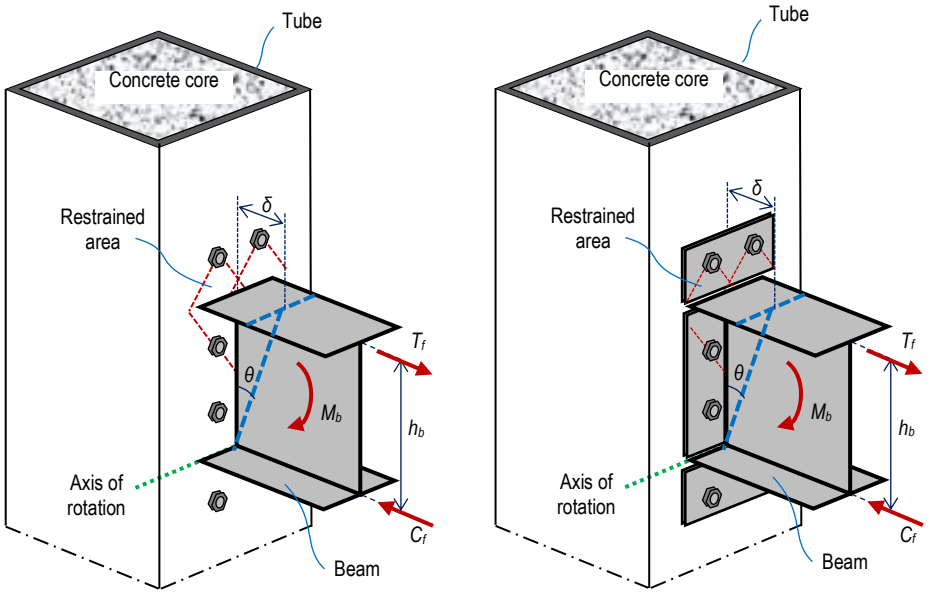

(a) With through-rods (b) With through-rods and washer plates

Fig. 26 Illustration of restrain provided by through-rods in improved direct-welded connections

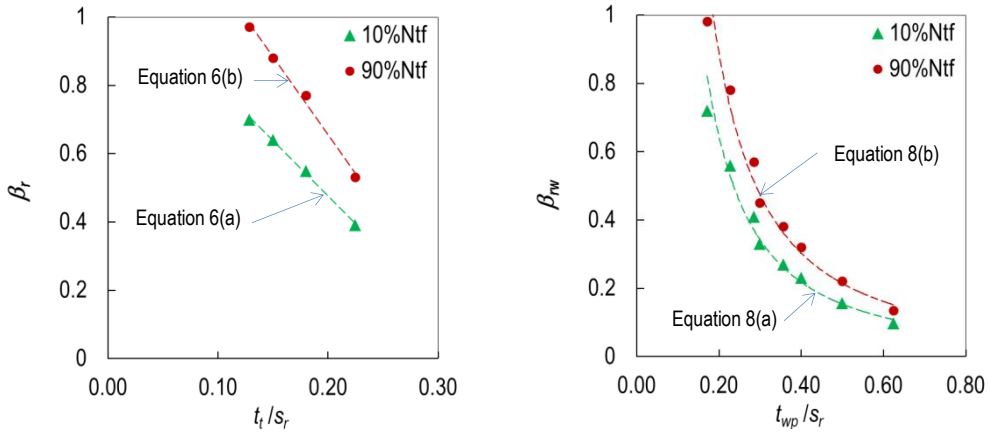

(a) With through-rods (b) With through-rods and washer plates

Fig. 27 Fixity factors for improved direct-welded connections

7. Conclusions

Bidirectional loading tests have been conducted on a CFST column subassembly with improved direct-welded beam-to-column connections. Finite element analyses were conducted to further evaluate the potential of the steel tube fracture which was observed during the tests. In addition, equations were developed to estimate the stress concentration from beam tension forces and the rotational stiffness of the connections. The following conclusions may be drawn from these tests, analyses, and equations:

1) The unstiffened direct-welded connections have low rotational stiffness due to flexibility of the tube plates in resisting out-of-plane deformations. Early yielding is likely to occur, which is indicated by the high stress increment rate at the tube.
2) The out-of-plane stiffness of the tube plates in joints with direct-welded connections can be improved by fastening and pretensioning threaded rods passing through the column. The stiffness can be further increased by inserting thick washer plates underneath the nuts of the through-rods. The stiffness increases up to 2.4 times and 3.7 times that of the unstiffened connections in connections with through-rods only and with through-rods and washer plates, respectively.
3) The proposed improvement methods also reduce stress concentration in the column tube plates due to beam flange tension forces. The effectiveness of the methods is influenced by the configuration of the rods, their pretension forces, and the thickness of the washer plates. The effect of bidirectional loading on the behaviour of the connections is not significant.
4) Design formulations are developed to estimate the out-of-plane shear demand in the column tube plates. A stress concentration factor should be taken into account to consider the critical stress in the tube plates under beam flange tension forces. Formulations to estimate the elastic rotational stiffness of improved direct-welded connections are also proposed for moment frame analyses.

References

[1] AS/NZS 1252:1996. 1996. High-strength steel bolts with associated nuts and washers for structural engineering. Standards New Zealand.
[2] Chunhaviriyakul, P., G.A. MacRae, D. Anderson, G.C. Clifton, and R.T. Leon. 2015. "Suitability of CFT columns for New Zealand Moment Frames." Bulletin of the New Zealand Society for Earthquake Engineering 48 (1).
[3] Citipitioglu, A.M., R.M. Haj-Ali, and D.W. White. 2002. "Refined 3D finite element modeling of partially-restrained connections including slip." Journal of Constructional Steel Research 58: 995-1013.
[4] Dutta, S.C., and S.K. Kunnath. 2013. "Effect of bidirectional interaction on seismic demand of structures." Soil Dynamics and Earthquake Engineering 52: 27-39.
[5] EN 1993-1-8. 2005. Design of steel structures, Part 1.8: Design of joints. Brussels: European Committee for Standardization.
[6] Hoang, V-L., J-P. Jaspart, and J-F. Demonceau. 2015. "Extended end-plate to concrete-filled rectangular column joint using long bolts." Journal of Constructional Steel Research 113: 156-168.

[7] Kang, C.H., K.J. Shin, Y.S. Oh, and T.S. Moon. 2001. “Hysteresis behavior of CFT column to H-beam connections with external T-stiffeners and penetrated elements.” Engineering Structures 23: 1194-1201.
[8] Li, L., W. Wang, Y. Chen, and L.H. Teh. 2017. “Column-wall failure mode of steel moment connection with inner diaphragm and catenary mechanism.” Engineering Structures 131: 553–563.
[9] Li, X., Y. Xiao, and Y.T. Wu. 2009. “Seismic behavior of exterior connections with steel beams bolted to CFT columns.” Journal of Constructional Steel Research 65: 1438-1446.
[10] MacRae, G.A., and H.T. Tagawa. 2001. “Seismic Behavior of 3D Steel Moment Frame with Biaxial Columns.” Journal of Structural Engineering 127 (5): 490-497.
[11] Nishiyama, I., T. Fujimoto, T. Fukumoto, and K. Yoshioka. 2004. “Inelastic force-deformation response of joint shear panels in beam-column moment connections to concrete-filled tubes.” Journal of Structural Engineering 130: 244-252.
[12] Park, T., W-S. Hwang, R. T. Leon, and J. W. Hu. 2011. “Damage Evaluation of Composite-Special Moment Frames with Concrete-filled Tube Columns under Strong Seismic Loads.” KSCE Journal of Civil Engineering 15 (8): 1381-1394.
[13] Schneider, S.P., and Y.M. Alostaz. 1998. “Experimental behavior of connections to concrete-filled steel tubes.” Journal of Constructional Steel Research 45 (3): 321-352.
[14] Sheet, I.S., U. Gunasekaran, and G.A. MacRae. 2013. “Experimental investigation of CFT column to steel beam connections under cyclic loading.” Journal of Constructional Steel Research 86: 167–182.
[15] SIMULIA. 2012. Abaqus/CAE User’s Manual.
[16] Tjahjato, H., G. MacRae, A. Abu, C. Clifton, T. Beetham, and N. Mago. 2019. “Diaphragm Axial Capacity for External Diaphragm Connections (EDCS) in Square CFST Column Structures.” Bulletin of the New Zealand Society for Earthquake Engineering 52 (3).
[17] Wang, J-F., L-H. Han, and B. Uy. 2009. “Behaviour of flush end plate joints to concrete-filled steel tubular columns.” Journal of Constructional Steel Research 65: 925-939.
[18] Xu, M., S. Gao, S. Zhang, and H. Li. 2018. “Experimental study on bolted CFST-column joints with different configurations in accommodating column-loss.” Journal of Constructional Steel Research 151: 122–131.
[19] Yao, H., H. Goldsworthy, and E. Gad. 2008. “Experimental and Numerical Investigation of the Tensile Behavior of Blind-Bolted T-Stub Connections to Concrete-Filled Circular Columns.” Journal of Structural Engineering 134: 198-208.

Advanced Steel Construction – Vol. 16 No. 2 (2020) 170–180
DOI:10.18057/IJASC.2020.16.2.8

IMPROVED FORCE ITERATION METHOD BASED ON RATIONAL SHAPE DESIGN SOLVING SELF-STRESS MODES OF CABLE-TRUSS TENSILE STRUCTURE

Su-duo Xue [1], Jian Lu [1, *], Xiong-yan Li [1] and Ren-jie Liu [2]

[1]*College of Civil and Architecture Engineering, Beijing University of Technology*
100 Ping Le Yuan, Chaoyang District, Beijing 100124, China
[2]*Civil Engineering College Institute, Yantai University, Yantai, Shandong 264000, China*
[*] (*Corresponding author: E-mail: lujian2020@126.com*)

ABSTRACT

Cable-truss tensile structure is one of the most competitive spatial structures. The shape determination and solving self-stress modes are two key problems in design. Although equilibrium matrix theory can solve the two problems, it need good programming and matrix operation capacity, which is difficult to be mastered by engineers and designers. Other methods are mainly used to solve self-stress modes, but how to design rational shape of structure is not introduced and these methods cannot be directly used in finite element (FEM) software. For these problems, based on existed FEM software, the improved force iteration method based on rational shape is proposed. The new method is based on the topological relation of cable-truss tensile structure, and a simple formula for shape determination was deduced from the rational shape. By studying force iteration method, improved force iteration method is proposed to solve self-stress mode of cable-truss tensile structures. The new method is based on the idea that is shape determination first and then solving self-stress modes, which can rapidly determine rational shape and self-stress mode. And then the feasible prestress can be solved. The new method can be used in FEM software and consider material properties and nonlinearity. Numerical examples show that the new method has a systematic solution flow and high convergence accuracy.

ARTICLE HISTORY

Received: 15 August 2019
Revised: 19 April 2020
Accepted: 29 April 2020

KEYWORDS

Cable-truss tensile structure;
Shape determination;
Self-stress modes;
FEM;
Improved force iteration method

1. Introduction

Tensegrity structures, which always consist of continuous tension struts and discontinuous compression struts, were proposed by Fuller [1]. The first tensegrity structure was designed by Snelson in 1948 [2], but it was only a structure model [3]. According to the basis of tensegrity concept, Geiger[4] first created the practical meaningful tensegrity which was called cable dome which includes a compression ring in the boundary of a tensegrity structure, the so-called Geiger form dome. The most important features of cable dome are its innovative configuration, lightness and high structural efficiency, which have attracted attention from engineers and designers. Meanwhile, the first cable dome was designed by Geiger for the Olympics in Seoul (1986) [4]. After that, many kinds of cable dome structures were built all over the world, such as the Redbrid Arena in Illinois (1988), the Florida Suncoast Dome in ST. Petersburg (1988), the Taoyuan Arena in Taiwan (1993), and the oval plan Levy form cable dome for the Olympics in Georgia (1996) [5]. In addition, the recent cable dome was the National Fitness center in Ejin Horo Banner, Inner Mongolia (2012) [6].

Meanwhile, there are many novel types of tensile structures at home and abroad and the typical type is cable-truss tensile structure (CTTS), such as spoke cable-truss structure [7] and annular crossed cable-truss structure (ACCTS) [8,9], shown in Fig. 1. Cable dome structure is also a kind of CTTS, shown in Fig. 1. CTTS refers to the tension integral structure formed by a series of the same type of planar cable-truss frames according to certain layout principles. The common point of this type structure is that integral structure can be divided into the same type planar cable-truss frame which has the same characteristics including light weight, large stiffness, strong spanning capacity and simple construction. There are some engineering cases of spoke cable-truss structure, such as Foshan Stadium in China, Shenzhen Bao'an Stadium in China, Yueqing Stadium in China [10]，Busan Stadium in South Korea [11]. But ACCTS [8,9] is in the stages of theoretical and experimental research and there are no engineering cases.

In the state of zero stress, CTTS is a kind of mechanism without specific shape and bearing capacity. In the state of prestress, it has specific shape and certain stiffness. So, two problems of the paper are proposed: rational shape determination and solving self-stress modes.

As early as 1864, stability judgment method for traditional rigid structures proposed by Maxwell is not suitable [12]. By studying Maxwell criteria and topological relations of tensile structure, the matrix decomposition method was proposed by Pellegrino and Calladine in 1986 [13-15]. Now matrix decomposition method is widely used in shape determination, but matrix decomposition method needs programming and matrix operation to judge whether the shape of structure is rational, which is not easy to be mastered by engineers and designers. So, it is urgent to find a simple method for determining the rational shape of CTTS. Based on the research of CTTS, the paper divides CTTS into planar cable-truss frame, and deduces the simple judgment equation of rational shape from the rational shape of planar cable-truss frame.

For how to solve self-stress modes, based on the flexibility method, Hanaor [16] proposed a unified method for the analysis and prestress design of tensile structures. Pellegrino and Calladine [13-15] proposed the singular value decomposition (SVD) technique to solve the independent self-stress modes. Considering the inherent geometric symmetry of cable domes and based on SVD, Yuan et al. [17,18] proposed the concept of integral feasible prestress modes and proposed a general method that referred to DSVD for solving the problems of shape determination and the initial prestress distribution of various forms of cable dome [19]. Based on the linear adjustment theory, a new numerical algorithm was presented for the initial prestress finding procedure of assemblying cable-strut [20]. Later, Wang et al. [21] proposed a simple method to design the prestress for cable dome with self-weight based on the nodal equilibrium equation after changing the structural self-weight into the nodal force. Tian et al. [22] proposed constrains removed method to solve the self-stress mode of spoke cable-truss structures based on FEM software. Guo et al. [23] innovated a Newton iteration method to update the prestress and a simple method for updating the structural geometry shape under different states. Guo et al. [24] developed a pretension simulation algorithm to find the feasible prestress and based on the fuzzy relationship between prestress and internal force. The existing methods mostly based on equilibrium matrix theory or nodal equilibrium method to solve the self-stress modes of structures. But those methods cannot consider structural deformation and material properties, and cannot use the existing FEM software to solve these problems.

Based on the existed FEM software, rational shape and the basic principle of force iteration method, an improved force iteration method is proposed to solve the self-stress mode of CTTS. The new method first divides CTTS into planar cable-truss frame for simple design, and then according to the unique topological relation of planar cable-truss frame, the internal relationship to maintain its balance is deduced from its rational shape. Secondly, planar cable-truss frame with rational shape can be obtained by using the internal relationship. Finally, the CTTS can be obtained by assembling planar cable-truss frames in reverse.

The layout of the paper is as follows. How to design the rational shape of CTTS is studied in section 2. Based on the basic principle of force iteration method and the features of the existed FEM software, an improved force iteration method is proposed in section 3. In section 4, three examples are given to verify the feasibility of the new method. In section 5, the way to solve the feasible prestress under self-weight and external loads is proposed

and cable dome is taken as an example. Some conclusions are drawn at the end of the paper.

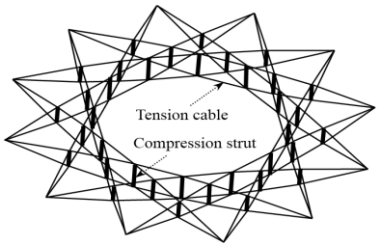

(a) Annular crossed cable-truss structure (ACCTS)

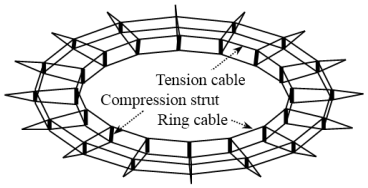

(b) Spoke cable-truss structure

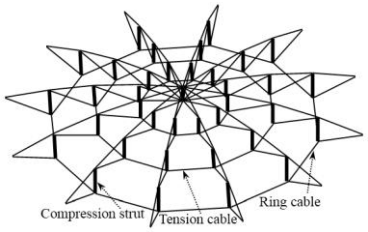

(c) Cable dome structure

Fig. 1 Schematic diagrams of three types of cable-truss tensile structures

2. The criteria of rational shape design

2.1. Annular crossed cable-truss structure (ACCTS)

ACCTS [8,9] can be simplified into planar cable-truss frame, shown in Fig. 2. Assume that all nodes of the planar cable-truss frame are in equilibrium state, and the derivation process is described in detail. The vertical components are strut, and the others are cable.

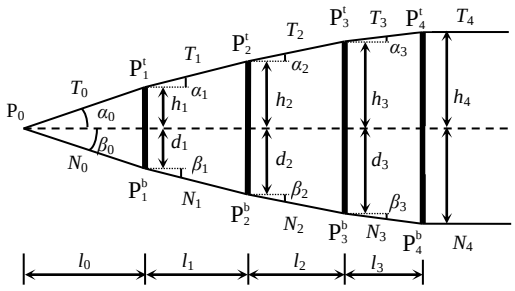

Fig. 2 Diagram of half planar cable-truss frame

Taking the whole structure as the research object, the moment of node P_0 can be obtained:

$$T_4 \cdot h_4 - N_4 \cdot d_4 = 0 \tag{1}$$

Taking all upper nodes as the research object, equilibrium equation in horizontal direction of each node is obtained. After simplification, the general equation is obtained:

$$T_4 = T_i \cdot \cos\alpha_i \tag{2}$$

Similarly, the general equation of each lower node in horizontal direction is obtained:

$$N_4 = N_i \cdot \cos\beta_i \tag{3}$$

Taking all the struts as the research object, and the equilibrium equation of each strut in vertical direction is obtained:

$$T_i \cdot \sin\alpha_i = N_i \cdot \sin\beta_i \tag{4}$$

Substitute Eq. (2) and (3) into Eq. (4), and then obtain Eq. (5):

$$T_4 \cdot \tan\alpha_i = N_4 \cdot \tan\beta_i \tag{5}$$

Eq. (5) shows that the horizontal force components of the upper and lower chord cables are equal for any planar cable-truss frame with rational shape. Furthermore, the vertical force of each node also keeps the struts in equilibrium state. The horizontal and vertical equilibrium forces keep planar cable-truss frame in integral equilibrium state.

According to geometric relationship, then obtain Eq. (6) and Eq. (7):

$$\begin{cases} \tan\alpha_0 = h_1 / l_0 \\ \tan\beta_0 = d_1 / l_0 \end{cases} \tag{6}$$

$$\begin{cases} \tan\alpha_1 = (h_1 - h_2) / l_1 \\ \tan\beta_1 = (d_1 - d_2) / l_1 \end{cases} \tag{7}$$

From Eq. (5), (6) and (7), then obtain Eq. (8) and (9):

$$\frac{\tan\alpha_0}{\tan\beta_0} = \frac{h_1}{d_1} = \frac{N_4}{T_4} \tag{8}$$

$$\frac{\tan\alpha_1}{\tan\beta_1} = \frac{h_2 - h_1}{d_2 - d_1} = \frac{N_4}{T_4} \tag{9}$$

Based on Difference Ratio Theorem, and Eq. (10) from Eq. (8) and (9) is obtain:

$$\frac{\tan\alpha_1}{\tan\beta_1} = \frac{h_2 - h_1}{d_2 - d_1} = \frac{h_1}{d_1} = \frac{h_2}{d_2} = \frac{\tan\alpha_0}{\tan\beta_0} = c \tag{10}$$

Similarly, the general equation can be written as:

$$\frac{h_1}{d_1} = \frac{h_2}{d_2} = \frac{h_3}{d_3} = \frac{h_4}{d_4} = \cdots = \frac{h_i}{d_i} = c \tag{11}$$

Eq. (11) shows that the ratio of the upper part and lower part of all struts of planar cable-truss frame in a rational shape is a constant *C*. In total, when the ratio of the upper part and lower part of all struts of the planar cable-truss frame is constant *C*, the horizontal force components of the upper and lower chord cables are equal, and planar cable-truss frame is in equilibrium state and has an independent self-stress mode.

Reference [25] can be used to select the rise-span ratio of upper and lower chord cables, and then rational constant *C* can be obtained.

Meanwhile, the contour of planar cable-truss frame should follow the three curves:

$$\begin{cases} y + ax^2 + bx + c = 0 \\ ax^2 + by^2 + c = 0 \\ y + a\cosh(x / a) = 0 \end{cases} \tag{12}$$

The three curves not only can meet the requirements of drainage slope, but can provide the geometric shapes which can stiffen planar cable-truss frame under prestress.

2.2. Cable dome structure and spoke cable-truss structure

As cable dome structure and spoke cable-truss structure cannot enhance the overall stability and anti-lateral stiffness of the structure by the form of crossed connection like ACCTS, cable dome structure and spoke cable-truss structure enhance the overall stability and anti-lateral stiffness of the structure by adding ring cables (shown in Fig. 1b and Fig. 1c). Cable dome structure and spoke cable-truss structure can be divided into a series of planar cable-truss frames, so their design criteria of rational shape are similar to those of ACCTS. However, when cable dome structure and spoke cable-truss structure are simplified and calculated, it is necessary to replace the ring cable by the equivalent lower chord cables according to the equivalent stiffness principle. The difference between ring cable and equivalent lower chord cable is that the sectional size of cable is different.

Because the calculation process of equivalent lower chord cable of cable dome structure is the same as that of spoke cable-truss structure, the outermost ring cable of cable dome (shown in fig. 1c) can be taken as the research object, and the simplified calculation model of cable dome structure is shown in Fig. 3. The calculation model can be considered as a composite cable-truss structure consisting of three planar cable-truss frames extending along the resultant force lines, including cable-truss frame 212’5, cable-truss frame 322’3’6’6, cable-truss frame 433’4’7’7, respectively. Its contour design can still refer to the shape design criteria of ACCTS.

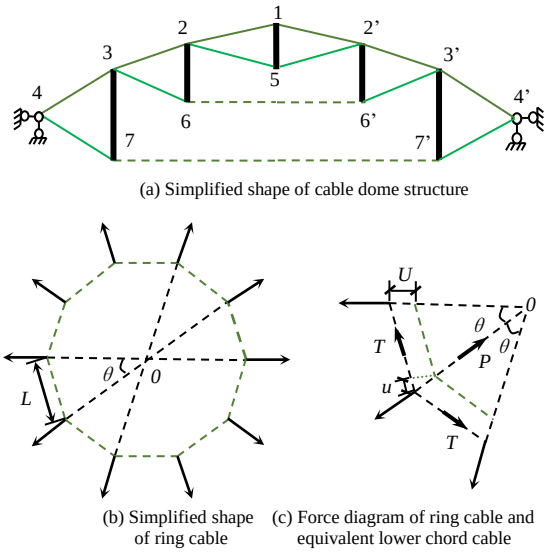

(a) Simplified shape of cable dome structure

(b) Simplified shape of ring cable (c) Force diagram of ring cable and equivalent lower chord cable

Fig. 3 Simplified calculation diagram of equivalent lower chord cable of cable dome

Assuming elastic modulus, cross-sectional area and length of cable is E, Ar, and L, respectively. The radius of polygon consisting of ring cable is R and the internal force of ring cable is T. The cross-sectional area, cable force and tensile stiffness of equivalent lower chord able is Aeq, P and EAeq, respectively. The cross-sectional area of equivalent lower chord cable is calculated as follows.

It can be seen from the Fig. 3c that the relationship between tensile force of ring cable and internal force of equivalent lower chord cable is obtained:

$$P = 2T\sin\frac{\theta}{2} \tag{13}$$

The length of ring cable:

$$L = 2R\sin\frac{\theta}{2} \tag{14}$$

The elongation of each ring cable is obtained:

$$u = \frac{T}{EA_r}L = \frac{T}{EA_r}2R\sin\frac{\theta}{2} = \frac{PR}{EA_r} \tag{15}$$

According geometric relationship, radial displacement of equivalent lower chord cable can be obtained from the elongation of each cable:

$$U = \frac{u}{2\sin(\theta/2)} = \frac{PR}{2EA_r\sin(\theta/2)} \tag{16}$$

So, the internal force of equivalent lower chord cable can be obtained:

$$P = \frac{2EA_r}{R}U\sin\frac{\theta}{2} \tag{17}$$

From the relationship between force and displacement, P can also simplify into the form of equivalent area Aeq:

$$P = EA_{eq}\cdot\frac{U}{R} \tag{18}$$

By comparing Eq. (17) with Eq. (18), the equivalent area can be obtained:

$$A_{eq} = 2A_r\sin\frac{\theta}{2} \tag{19}$$

3. Solving self-stress modes

3.1. The theoretical basis of solving self-stress modes

Equilibrium theory [13-16] is a common method to solve self-stress of cable-strut tensile structures, and the basic equation is as follows:

$$\boldsymbol{A}\times\boldsymbol{T}=\boldsymbol{F} \tag{20}$$

A is equilibrium matrix. ***T*** is internal forces of struts. ***F*** is the equivalent nodal force vector generated by external loads. Essentially, Eq. (20) is an equilibrium process of internal forces and external loads at each node. By singular value decomposition of the equilibrium matrix ***A***, the number of structural self-stress modes can be determined and the self-stress modes of each order can be obtained. However, equilibrium matrix cannot be obtained by the existed FEM software. Generally, equilibrium matrix ***A*** needs to be obtained by means of computer programming, which is not convenient to use and not easy to be mastered by designers and engineers. Meanwhile, equilibrium matrix theory cannot consider structural deformation and material properties, and cannot reflect real self-stress modes.

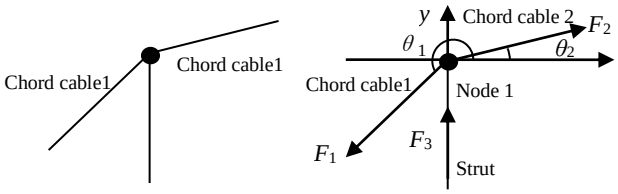

(a) Basic force unit (b) Force condition of node 1

Fig. 4 Basic force unit modal and its force state

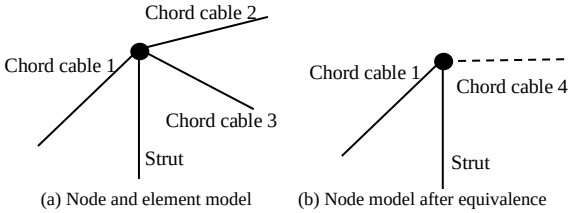

(a) Node and element model (b) Node model after equivalence

Fig. 5 Basic force modal of and its force state cable dome

Taking basic force unit in Fig. 4 as an example, and its force condition is shown in Fig. 4b. For cable dome structure, the internal forces of chord cable 2 and cable 3 can be equivalent to chord cable 4, shown in Fig. 5, which is similar to basic force unit in Fig. 4. The node equilibrium equation are established by the coordinate system shown in Fig. 4b, which can be written as the Eq. (21).

As solving self-stress modes, the condition under external loads cannot be considered. Namely, Eq. (21) can be written as Eq. (22).

$$\begin{bmatrix} \cos\theta_1 & \cos\theta_2 & 0 \\ \sin\theta_1 & \sin\theta_2 & 1 \end{bmatrix} \begin{bmatrix} F_1 \\ F_2 \\ F_3 \end{bmatrix} = \begin{bmatrix} P_1 \\ P_2 \end{bmatrix} \tag{21}$$

$$\begin{bmatrix} \cos\theta_1 & \cos\theta_2 & 0 \\ \sin\theta_1 & \sin\theta_2 & 1 \end{bmatrix} \begin{bmatrix} F_1 \\ F_2 \\ F_3 \end{bmatrix} = \begin{bmatrix} 0 \\ 0 \end{bmatrix} \tag{22}$$

$$\boldsymbol{A} = \begin{bmatrix} \cos\theta_1 & \cos\theta_2 & 0 \\ \sin\theta_1 & \sin\theta_2 & 1 \end{bmatrix} \tag{23}$$

$$\{\overline{F_1}, \overline{F_2}, \overline{F_3}\}^T = \{\frac{\cos_2}{\sin(\theta_2 - \theta_1)}, \frac{\cos_1}{\sin(\theta_1 - \theta_2)}, 1\}^{\mathrm{T}} \tag{24}$$

F_1 and F_2 represent internal forces of two chord cables, and F_3 represents a strut (or linked cable). θ_1 and θ_2 are the angles between the two chords and the positive direction of the x axis respectively, and $\cos\theta_1$, $\sin\theta_1$, $\cos\theta_2$ and $\sin\theta_2$ are not zero. Eq. (23) is the coefficient matrix of Eq. (24), and $\boldsymbol{A}$ is a matrix of order 2×3, and its rank is equal to 2. So, the basic solution set of Eq. (23) has only one free vector basis, which can be written as Eq. (24). Eq. (22) can be satisfied if F_1, F_2 and F_3 are set by ratio of Eq. (24). That is, node 1 can keep balance and be in the design shape. The group of proportional relations is called the self-stress mode of basic force unit [22].

When each basic force unit can be in equilibrium state of the design shape under external load and then when the internal forces of all elements are integrated into the vector $\boldsymbol{T}$ of Eq. (20), Eq. (20) can be naturally satisfied. At this point, for the planar cable-truss frame, $\boldsymbol{T}$ is a group of prestress values that can meet the force balance and be in a rational shape. When the external force is zero, the group of prestress values is self-stress mode of planar cable-truss frame. For basic force unit, the internal force of element can be obtained by solving two linear independent equations. But for the integral cable-truss frame, it is difficult to obtain the internal force of each element by solving system of simultaneous equations due to a huge number of nodes.

ANSYS FEM software not only solve basic force unit, but solve integral planar cable-truss frame directly. When solving the basic force unit or planar cable-truss frame, ANSYS software cannot solve equilibrium matrix $\boldsymbol{A}$ in Eq. (20), and cannot directly solve Eq. (21) and (22), but can solve Eq. (25). In FEM software, the element stiffness matrix is obtained first, and then the integral stiffness matrix is assembled (the assembly process of the stiffness matrix is hidden in the background of software). Therefore, the internal forces of the planar cable-truss frame can be obtained through basic force unit.

$$(\boldsymbol{K}_E + \boldsymbol{K}_G)\ \boldsymbol{U} = \boldsymbol{F} + \boldsymbol{P} + \boldsymbol{R} \tag{25}$$

For Eq. (25), $\boldsymbol{K}_E$ is elastic stiffness matrix. $\boldsymbol{K}_G$ is geometry stiffness matrix. $\boldsymbol{U}$ is nodal displacement vector. $\boldsymbol{P}$ is prestress vector of component. $\boldsymbol{R}$ is the unbalanced force vector generated by the higher order terms of $\boldsymbol{U}$ in the solving process. The geometric stiffness matrix $\boldsymbol{K}_G$ is related to nodal coordinates and the prestress of members.

When solve the Eq. (25), force iteration method or displacement iteration method can be used [26], and the solution obtained is the solution of Eq. (21) and Eq. (22). For the basic force unit shown in Fig. 4, the convergence speed of force iteration method or displacement iteration method is very fast [26]. Generally, only 3~4 times iterations are needed to achieve high accuracy. According to the simplicity degree of the existed FEM software, the force iteration method is recommended.

3.2. Improved force iteration method

According to the force iteration method in section 3.1, it is necessary to improve the force iteration method when solving the self-stress mode of planar cable-truss frame. Taking basic force unit as an example, the specific process is as follows:

(1) First, a group of initial prestress values of $\boldsymbol{F}_0$=[F_1, F_2, F_3] is assigned to the basic force unit, shown in Fig. 6a;

(2) By using force iteration method to solve the basic force unit in Fig. 6a, the prestress value of basic force unit can be obtained as $\boldsymbol{F}_1$=[$F_{1,1}$, $F_{2,1}$, $F_{3,1}$]. The unbalanced displacement of node 1 is u_1, iteration process shown in Fig. 6b. (the 1st subscript represents element number, and the 2nd subscript represents the number of iteration, the same below.)

(3) In the 2nd iteration, rather than substituting $\boldsymbol{F}_1$=[$F_{1,1}$, $F_{2,1}$, $F_{3,1}$] into the original basic force unit to calculate (iteration process shown in Fig. 6c), but taking one of initial cable force as the basic value (choose F_1 or F_2). Then updating the prestress of rest elements, the group of updated cable values are $\boldsymbol{F}_1^1$=[$F_{1,1}^1$, $F_{2,1}^1$, $F_{3,1}^1$], which can be written as $\boldsymbol{F}_1^1$=[1, $F_{2,1}/F_{1,1}$, $F_{3,1}/F_{1,1}$] *F_1. The unbalanced displacement of node 1 is u_2 ($u_2 < u_1$), iteration process shown in 6d. The unbalanced displacement value u_2^0 is equal to u_2 when nonlinear, dead weight and external load are not considered. After the cable forces are updated, the improved force iteration method can approach the target value gradually and obtain the unbalanced displacement of structure under target prestress. (The superscript represents the result after each iteration and cable forces update, the same below)

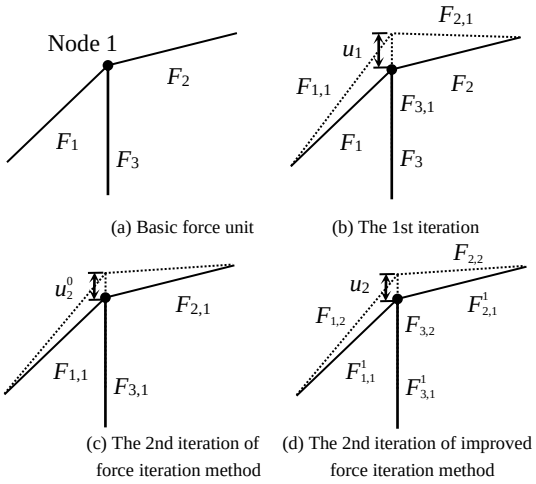

Fig. 6 Schematic diagram of solving process of force iteration method

(4) The convergence criteria of cable force and structural displacement , which is $|\boldsymbol{F}_j - \boldsymbol{F}_{j-1}| < \delta_1$, $|u_j - u_{j-1}| < \delta_2$ respectively, are used to judge whether the results meet the requirements. (δ_1 and δ_2 is convergence accuracy which is equal to 0.001.) When the last two calculation results satisfy the convergence accuracy requirements, the calculation stops. Otherwise, the calculation continues until the calculation results meet requirements.

3.3. Improved force iteration method based on rational shape to solve self-stress mode of CTTS

Based on FEM software and improved force iteration method, improved force iteration method based on rational shape to solve self-stress mode of CTTS is proposed. The theoretical basis of this method is equilibrium matrix theory, which reflects in the solution process of force iteration method and extends to solve the self-stress mode of planar cable-truss frame.

Because planar cable-truss frame has many nodes and is symmetrical structure, the below several points should be paid more attentions when improved force iteration method is used to update cable force: (a) The element of planar cable-truss structure should be grouped; (b) Assuming that the ith group cable forces (F_i) are the basic values, the ratio values of updating cable forces are according to the ratio of each group cable forces F_k (k is not equal to i) being relative to the ith group cable F_i obtained by each iteration calculation; (c) When updating the ith group cable force, directly update the ith group cable force according to the baisc values; (d) After all groups of prestress values are updated and compensated, they can be used as the initial prestress values of the next iteration.

Solving process is as follow:

(1) The simplified model of CTTS is designed by the design criteria of rational shape in section 2, and planar cable-truss frame with rational shape is obtained;

(2) The cable and strut elements of planar cable-truss frame are grouped into n groups, and the initial prestress value is $\boldsymbol{F}_0 = [F_{1,0}, F_{2,0}, ..., F_{i,0}, ..., F_{n,0}]$;

(3) Taking $\boldsymbol{F}_0$ as the initial prestress condition of the 1st nonlinear iteration, the result of the 1st iteration is $\boldsymbol{F}_1 = [F_{1,1}, F_{2,1}, ..., F_{i,1}, ..., F_{n,1}]$. The displacement of each control node is $\boldsymbol{U}_1 = [u_{1,1}, u_{2,1}, ..., u_{i,1}, ..., u_{n,1}]$. By the convergence criteria of force and displacement to judge whether the results meet the Eq. (26), if the results meet Eq. (26), then $\boldsymbol{F}_1$ is the self-stress mode, otherwise continue to iterate.

$$\begin{cases} \left| \boldsymbol{F}_j - \boldsymbol{F}_{j-1} \right| \le \delta_1 \\ \left| \boldsymbol{U}_j - \boldsymbol{U}_{j-1} \right| \le \delta_2 \end{cases} \tag{26}$$

$\boldsymbol{F}_j$ and $\boldsymbol{F}_{j-1}$ are the jth and j-1th iteration calculation prestress values. $\boldsymbol{U}_j$ and $\boldsymbol{U}_{j-1}$ are the jth and j-1th iteration calculation displacement values, the same below.

(4) Update cable force (or prestress compensation) on the basis of $\boldsymbol{F}_1$. When updating cable force, any group of cable elements in $\boldsymbol{F}_1$ can be selected as the reference. If take the ith group cable force as reference, the updating jth group cable force is $F_{j,1}^1 = F_{i,0} \dfrac{F_{j,1}}{F_{i,1}}$, and the updating cable force is $\boldsymbol{F}_1^1 = [F_{1,1}^1, F_{2,1}^1, ..., F_{i,1}^1, ..., F_{n,1}^1]$. $\boldsymbol{F}_1^1$ can be further written as Eq. (27) and (28):

$$\boldsymbol{F}_1^1 = [\frac{F_{1,1}}{F_{i,1}} F_{i,0}, \frac{F_{2,1}}{F_{i,1}} F_{i,0}, ..., \frac{F_{i,1}}{F_{i,1}} F_{i,0}, ..., \frac{F_{n,1}}{F_{i,1}} F_{i,0}] \tag{27}$$

$$\boldsymbol{F}_1^1 = [\frac{F_{1,1}}{F_{i,1}}, \frac{F_{2,1}}{F_{i,1}}, ..., 1, ..., \frac{F_{n,1}}{F_{i,1}}] F_{i,0} \tag{28}$$

Taking $\boldsymbol{F}_1^1$ as the initial prestress condition of the 2nd nonlinear iteration, the result of the 2nd iteration is $\boldsymbol{F}_2 = [F_{1,2}, F_{2,2}, ..., F_{i,2}, ..., F_{n,2}]$. The displacement of each control node is $\boldsymbol{U}_2 = [u_{1,2}, u_{2,2}, ..., u_{i,2}, ..., u_{n,2}]$. According to the convergence criteria of force and displacement to judge whether the results meet the Eq. (26), if the results meet Eq. (26), then $\boldsymbol{F}_2$ is the self-stress mode, otherwise continue to iterate.

(5) Update cable force on the basis of $\boldsymbol{F}_2$. The updating jth group cable force is $F_{j,2}^2 = F_{i,0} \dfrac{F_{j,2}}{F_{i,2}}$, and the updating cable force is $\boldsymbol{F}_2^2 = [F_{1,2}^2, F_{2,2}^2, ..., F_{i,2}^2, ..., F_{n,2}^2]$. $\boldsymbol{F}_2^2$ can be further written as Eq. (29) and (30):

$$\boldsymbol{F}_2^2 = [\frac{F_{1,2}}{F_{i,2}} F_{i,0}, \frac{F_{2,2}}{F_{i,2}} F_{i,0}, ..., \frac{F_{i,2}}{F_{i,2}} F_{i,0}, ..., \frac{F_{n,2}}{F_{i,2}} F_{i,0}] \tag{29}$$

$$\boldsymbol{F}_2^2 = [\frac{F_{1,2}}{F_{i,2}}, \frac{F_{2,2}}{F_{i,2}}, ..., 1, ..., \frac{F_{n,2}}{F_{i,2}}] F_{i,0} \tag{30}$$

Taking $\boldsymbol{F}_2^2$ as the initial prestress condition of the 3rd nonlinear iteration, the result of the 3rd iteration is $\boldsymbol{F}_3 = [F_{1,3}, F_{2,3}, ..., F_{i,3}, ..., F_{n,3}]$. The displacement of each control node is $\boldsymbol{U}_3 = [u_{1,3}, u_{2,3}, ..., u_{i,3}, ..., u_{n,3}]$. According to the convergence criteria of force and displacement to judge whether the results meet the Eq. (26), if the results meet Eq. (26), then $\boldsymbol{F}_3$ is the self-stress mode, otherwise continue to iterate.

(6) ……

(7) Similarly, Update cable force on the basis of $\boldsymbol{F}_k$. The updating jth group cable force is $F_{j,k}^k = F_{i,0} \dfrac{F_{j,k}}{F_{i,k}}$, and the updating cable force is $\boldsymbol{F}_k^k = [F_{1,k}^k, F_{2,k}^k, ..., F_{i,k}^k, ..., F_{n,k}^k]$. $\boldsymbol{F}_k^k$ can be further written as Eq. (31) and (32):

$$\boldsymbol{F}_k^k = [\frac{F_{1,k}}{F_{i,k}} F_{i,0}, \frac{F_{2,k}}{F_{i,k}} F_{i,0}, ..., \frac{F_{i,k}}{F_{i,k}} F_{i,0}, ..., \frac{F_{n,k}}{F_{i,k}} F_{i,0}] \tag{31}$$

$$\boldsymbol{F}_k^k = [\frac{F_{1,k}}{F_{i,k}}, \frac{F_{2,k}}{F_{i,k}}, ..., 1, ..., \frac{F_{n,k}}{F_{i,k}}] F_{i,0} \tag{32}$$

Taking $\boldsymbol{F}_k^k$ as the initial prestress condition of the k+1th nonlinear iteration, the result of the k+1th iteration is $\boldsymbol{F}_{k+1} = [F_{1,k+1}, F_{2,k+1}, ..., F_{i,k+1}, ..., F_{n,K+1}]$. The displacement of each node is $\boldsymbol{U}_{k+1} = [u_{1,k+1}, u_{2,k+1}, ..., u_{i,k+1}, ..., u_{n,k+1}]$. According to the convergence criteria of force and displacement to judge whether the results meet the Eq. (26), if the results meet Eq. (26), then $\boldsymbol{F}_{k+1}$ is the self-stress mode, otherwise continue to iterate.

(8) Finally, substitute the self-stress mode obtained from planar cable-truss frame into the general FEM model, and further verify whether the self-stress modes obtained from planar cable-truss frame is correct. The self-stress mode is correct if the convergence accuracy is satisfied. Otherwise go back to step (2), and recalculate.

The solving flow chart of improved force iteration method based on rational shape, shown in Fig. 7.

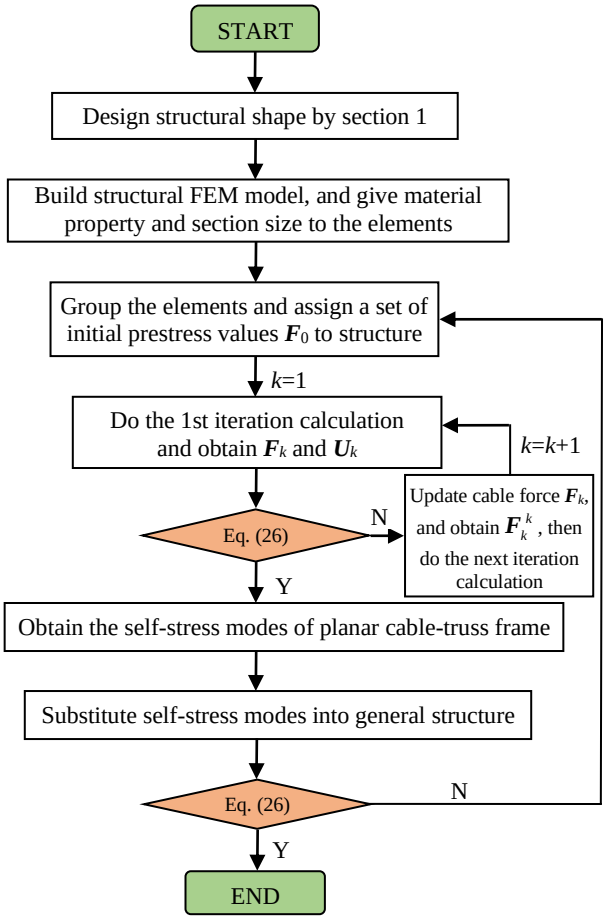

Fig. 7 Flow chart of form-finding of new method

4. Examples

4.1. Annular crossed cable-truss structure

By the design criteria in section 2, design a ACCTS with a diameter with 100m (Radius R_1=50m). According to the daylighting requirements and seating requirements of stadium, the radius R_2 of the open-air part is 25.08m. The ring equivalent components are 12, and a single planar cable-truss frame spans 4 ring equivalent components, whose span is 86.60m. Firstly, assuming the vector heights of the upper and lower chord cables are 3.662m and 5.413m, respectively. Secondly, assuming the contour of planar cable-truss frame is a certain parabola, and obtain the coordinates of all nodes by numerical calculation. The perspective diagram of ACCTS is shown in Fig. 8. The size of planar cable-truss frame is shown in Fig. 9. Elastic modulus of cable is 1.3×10^5Mpa. Elastic modulus of strut is 2.06×10^5Mpa. Poisson's ratio of cable and strut is 0.3, and cross-sections of cable and strut are shown in Table 1.

The self-stress mode of ACCTS is solved by improved force iteration method based on rational shape. As the stiffness of structural outer ring beam is very large, the constraint between structure and outer ring beam can be considered as rigid constraints. Taking cable force of element 2-4 as the updating basis value, assume that target prestress of element 2-4 is 240kN and the prestresses of other cables are 240kN. The results obtained by using the new method are compared with the theoretical values, shown in Table 1. The theoretical values are obtained by "node equilibrium method" in reference [21]. The iteration processes are shown in Fig. 10.

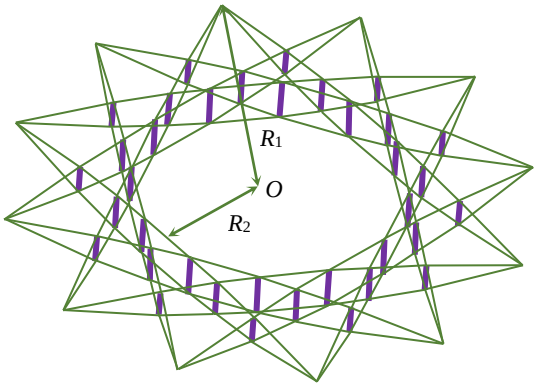

Fig. 8 Annular crossed cable truss structure

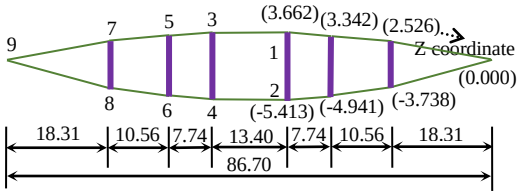

Fig. 9 Geometry size of single planar cable-truss frame

Table 1
Prestress distribution of ACCTS Unit: kN

Element number	Cross-section (mm^2)	Theoretical values	Iteration process of the new method					error (%)
			Initial values	1st	2nd	3rd	4th	
1-3	1495.93	354.00	240.00	266.92	348.2	354.28	354.64	0.18
3-5	1495.93	354.30	240.00	267.14	348.49	354.56	354.91	0.17
5-7	1495.93	355.66	240.00	267.74	349.27	355.35	355.71	0.01
7-9	1495.93	357.96	240.00	269.53	351.56	357.69	358.04	0.02
2-4	1930.57	**240.00**	**240.00**	**185.04**	**235.9**	**239.58**	**239.8**	0.08
4-6	1930.57	240.45	240.00	185.38	236.33	240.03	240.25	0.08
6-8	1930.57	241.54	240.00	186.25	237.44	241.16	241.38	0.06
8-9	1930.57	244.94	240.00	188.84	240.79	244.56	244.78	0.06
3-4	2578.76	-29.30	240.00	-22.375	-28.791	-29.262	-29.289	0.03
5-6	2578.76	-25.36	240.00	-19.393	-24.957	-25.366	-25.39	0.11
7-8	2578.76	-43.35	240.00	-33.033	-42.51	-43.206	-43.246	0.23

Error=abs([new method]-[theoretical values]/[theoretical values])×100

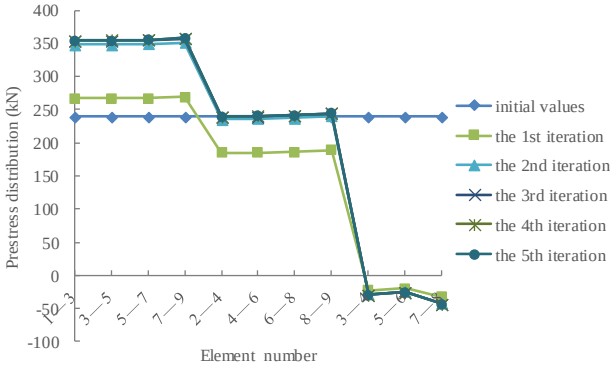

Fig. 10 Trend chart of prestress distribution in iterative process

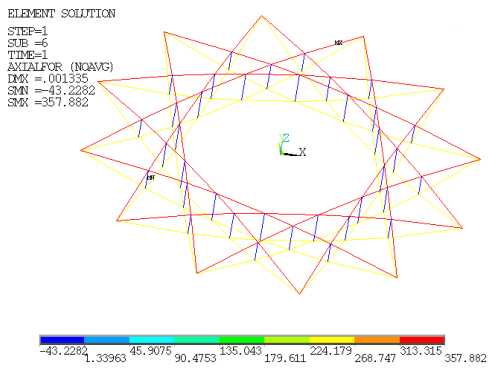

Fig. 11 Calculation results of integral FEM model

Table 2
The change of displacement convergence value in the iteration process

Number of iteration	1st	2nd	3rd	4th
Maximum displacement/m	0.0541	0.004	0.0014	0.0012

It can be seen from Fig.10 that the cable force distribution tends to be stable when the 3rd iteration is carried out, and the cable forces change very slightly when the iteration continues. Meanwhile, it can be seen from Table 1 that the 3rd iteration results are basically equal to the 4th iteration's and the cable force tends to be stable. The maximum error of prestress is 0.23%, which meets engineering accuracy requirement. Displacement convergence values in iteration process are shown in Table 2. Table 2 shows that the errors between the calculation results of the 3rd and 4th displacement and design coordinates are 0.0014m and 0.0012m, respectively. The difference is 0.0002m. The calculation results of integral FEM model show in Fig. 11 by substituting the self-stress modes obtained from planar cable-truss frame into the integral FEM model, and internal forces and displacement of elements are basically equal to the results obtained from planar cable-truss frame. The example shows that new method has the advantages of fast convergence, high accuracy, stable calculation. The new method can accurately and quickly determine the prestress distribution that meets the design shape requirements.

4.2. Spoke cable-truss structure

Taking reference [22] as an example. Spoke cable-truss structure consists of 16 planar cable-truss frames, shown in Fig. 12. The schematic diagram of planar cable-truss structure is shown in Fig. 13. Element 3-4 and 5-6 are compression struts, and others are tension cables. Element 1-3 and 2-4 are equivalent lower chord. The cross-section of cable and strut are 7.069mm^2 and 143.728mm^2. Elastic modulus of cable and strut are 1.8×10^5Mpa and 2.06×10^5Mpa. Poisson's ratio of cable and strut is 0.3.

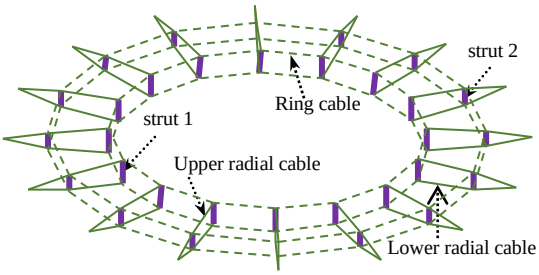

Fig. 12 Spoke Cable-truss Structure

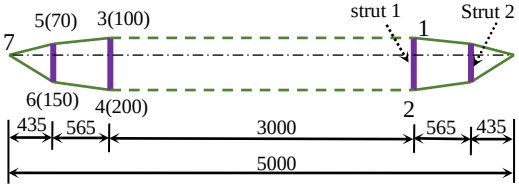

Fig. 13 Size of original cable-truss frame Unit: mm

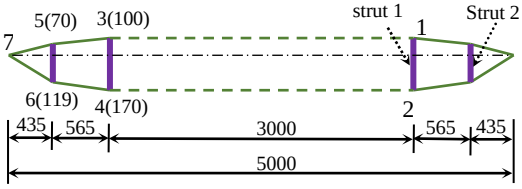

Fig. 14 Size of modified cable-truss frame Unit: mm

By the new method, first judge whether the structural shape is rational, and then solve the self-stress modes. It can be known that the ratio of upper and lower part of strut 1 is C_1=100/200=0.5, and the ratio of upper and lower part of strut 2 is C_2=70/150=0.47. Because C_1 is not equal to C_2, structural shape is not rational, which shows that the independent self-stress mode does not exist. The reference [22] judged whether the structure had a self-stress mode by comparing the internal force of strut obtaining from solving the upper chord node 1, 3, 5 with the internal force of strut obtaining from solving the lower chord node 2, 4, 6. If the internal forces of struts obtained from solving the upper and lower nodes are equal, the structure exists a self-stress mode. Otherwise, the self-stress mode does not exist. Compared with the method in reference [22], the new method simplifies the judgment process.

It needs to redesign the structural shape because the original structure does not have self-stress mode. Modified criteria: Generally, the coordinate values of the upper chord nodes are not changed to meet the drainage slope requirements of structure. Meanwhile, the coordinate values of lower chord nodes are generally not allowed to move downward to meet the audience's view and daylighting requirements.

To be the same as the modified geometrical shape of reference [22], the coordinates of upper chord nodes is unchanged, and modified coordinate of node 6 is 119mm. According to section 2, in order to ensure the original structure has the self-stress mode, the ratio of upper and lower chord lengths of all struts must be guaranteed to be equal. Namely, there exists an x value to make the equation 70/119=100/x exist and x is the modified coordinate of node 4, which is equal to 170mm. Reference [22] uesed the method of "modify the structural coordinate first – then solve the internal forces of components – finally judge whether the shape is rational", and determined that the coordinate of node 4 is equal to 170mm through 8 iterations. Compared with the method in reference [22], the new method improves calculation efficiency. The modified geometrical shape is shown in Fig. 14.

The self-stress mode of spoke cable-truss structure is solved by using improved force iteration method based on rational shape. As the stiffness of structural outer ring beam is very large, the constraint between structure and outer ring beam can be considered as rigid constraints. According to Eq. (19) $A_{eq}=2A_r\sin(\theta/2)$ (θ=22.5^0), the equivalent cross-sections of equivalent lower chord cables are shown in Table 3.

Table 3
Cross-section equivalent lower chord

Element number	Element 1-3	Element 2-4
Original areas/ mm^2	7.069	7.069
Equivalent areas/ mm^2	2.758	2.758

Taking cable force of element 4-6 as the updating basis, assume that target prestress of element 4-6 is 11.144kN and others' are 11.144kN. The results obtaining by using the new method are compared with the theoretical values. The comparative results are shown in Table 4. The theoretical values are obtained by "node equilibrium method" in reference [22]. The iteration processes are shown in Fig. 15.

Table 4
Prestress distribution of Spoke cable-truss Structure Unit: kN

Element number	Reference [22]	Initial value	Iteration process of the new method							Error (%)
			1st	2nd	3rd	4th	5th	6th	7th	
4-6	**11.1440**	**11.114**	**9.385**	**10.193**	**10.668**	**10.912**	**11.048**	**11.091**	**11.115**	0.26
6-7	11.5050	11.114	9.664	10.512	11.007	11.265	11.408	11.451	11.476	0.25
5-7	19.0760	11.114	12.454	15.349	17.720	18.920	18.683	18.878	18.984	0.48
3-5	18.8599	11.114	12.295	15.165	16.873	17.886	18.472	18.663	18.769	0.48
1-3	**48.2680**	**11.114**	**31.472**	**38.815**	**43.185**	**45.776**	**47.278**	**47.765**	**48.034**	0.48
2-4	**28.4460**	**11.114**	**23.949**	**26.013**	**27.228**	**27.848**	**28.197**	**28.310**	**28.371**	0.26
3-4	-1.0000	11.114	-0.761	-0.871	-0.934	-0.969	-0.988	-0.994	-0.998	0.20
5-6	-2.0308	11.114	-1.542	-1.767	-1.896	-1.967	-2.007	-2.019	-2.026	0.24

Error=abs([the 7th iteration results]-reference [22])/ reference [22]×100, tensile force of ring cable and internal force of equivalent lower chord cable are converted according to Eq. (13): $P=2T\sin(\theta/2)$. P stands for internal force of equivalent lower chord cable, T stands for tensile force of ring cable, θ=22.5^0. The internal forces of ring cable in Table 4 are equivalent calculated internal forces.

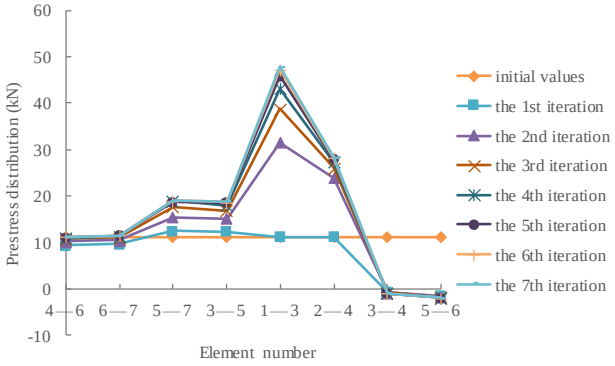

Fig. 15 Trend chart of pretress distribution in iterative process

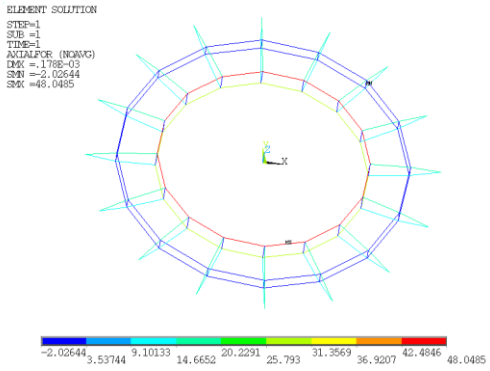

Fig. 16 Calculation results of integral FEM model

Table 5
The change of displacement convergence values in iteration process

Number of iteration	1st	2nd	3rd	4th	5th	6th	7th
Maximum displacement/m	0.0168	0.0086	0.0044	0.0022	0.0009	0.00048	0.00026

It can be seen from Fig. 15 and Table 4 that the distribution of cable forces tends to be stable when the 4th iteration is accomplished, and the cable force changes very slightly when the iteration continues. According to the comparison between the results of the 7th iteration and reference [22], the maximum error of prestress force is 0.48%. The displacement convergence values in iteration process are shown in Table 5. Table 5 shows that the errors between the calculation results of the 6th and 7th iterations and the design coordinates are 0.00048m and 0.00026m, respectively. The difference of both is 0.00022m. The calculation results of integral FEM model show in Fig. 16 by substituting the self-stress modes obtained from planar cable-truss frame into the integral FEM model, and internal forces and displacements of element are basically equal to the results obtained from planar cable-truss frame. From the calculation results of force and displacement, it can meet the requirements of engineering accuracy. The example shows that new method has fast design, reasonable shape determination and stable solving self-stress mode.

4.3. Cable dome structure

Taking cable dome structure without inner ring as an example, shown in Fig. 17. The structure exists a single self-stress mode, and its span and vector height are 100m and 10m, respectively. The ring equivalent components are 12. Namely, the structure consists of 12 planar cable-truss frames, shown in Fig. 18. Elastic modulus of cable and strut is 1.9×10^8kN/m^2 and 2.06×10^8kN/m^2, respectively, and its Poisson's ratio is 0.3. The density of cable and strut is 7.85×10^3kg/m^3. Structural size and element number are shown in Fig. 18. The cable dome structure in Fig. 17 conforms to the design criteria in section 2, so geometric shape is rational. Namely, the structure has a self-stress mode and makes the structure rigidized.

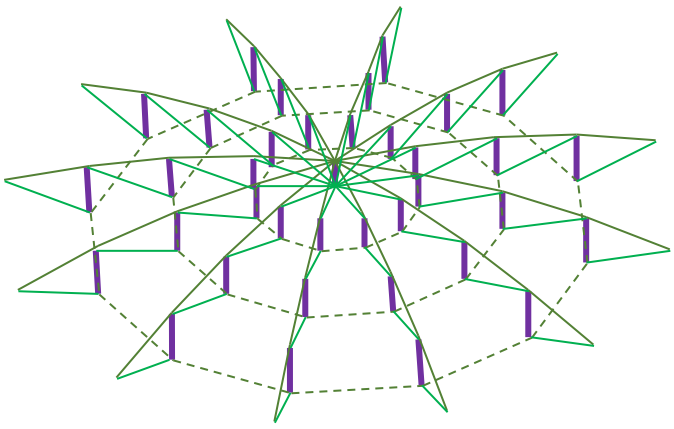

Fig. 17 Three dimensional diagram of cable dome structure without inner ring

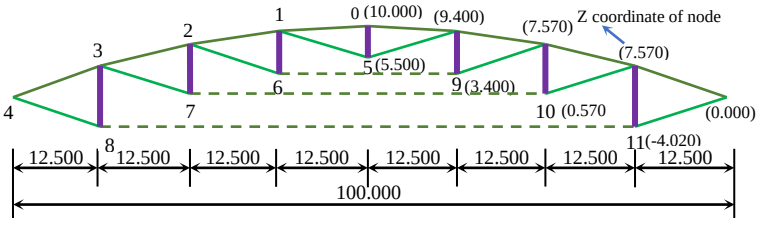

Fig. 18 Element number and geometry size of composited planar cable-truss frame

The self-stress mode of cable dome structure is solved by using improved force iteration method based on rational shape. As the stiffness of structural outer ring beam is very large, the constraints between structure and outer ring beam can be considered as rigid constraints. According to Eq. (19) $A_{eq}=2A_r\sin(\theta/2)$ (θ=22.5^0), the equivalent cross-section of equivalent lower chord cable is shown in Table 6. Taking cable force of element 3-4 as the updating basis, assume that target prestress of element 3-4 is 2734.18kN and others' are 2734.184kN. The results obtained by using the new method are compared with the theoretical values. The comparative results are shown in Table 7. The theoretical values are obtained by "nodal equilibrium method" in reference [23]. The iteration results of new method are shown in Fig. 19.

Table 6
Cross-section of equivalent lower chord

Element number	6-9	7-10	8-11
Original area/ mm^2	6273.00	7658.40	19473.20
Equivalent area/ mm^2	3247.14	3964.28	10080.07

Table 7
Prestress distribution of cable dome structure Unit: kN

Element number	Sectional area /mm^2	Ref. [23] SVD	Iteration process of the new method							Error /%
			Initial	1st	2nd	3rd	4th	5th	6th	
0-1	2116.6	865.675	2734.18	945.910	779.194	864.159	866.033	866.154	866.144	0.054
1-2	3271.2	1008.881	2734.18	1118.900	914.313	1007.055	1009.060	1009.202	1009.192	0.031
2-3	5349.3	1477.825	2734.18	1646.400	1338.940	1474.829	1477.563	1477.765	1477.765	0.004
3-4	7658.4	**2734.18**	**2734.18**	**3042.100**	**2480.223**	**2728.711**	**2733.876**	**2734.281**	**2734.179**	0.000
1-5	1193.0	139.987	2734.18	170.300	132.719	139.706	139.8277	139.848	139.838	0.106
2-6	1193.0	459.785	2734.18	517.860	416.668	458.650	459.3486	459.399	459.389	0.086
3-7	3271.2	1194.105	2734.18	1326.900	1084.882	1191.710	1194.039	1194.241	1194.242	0.012
4-8	7658.4	3005.301	2734.18	3351.200	2822.578	3000.286	3006.666	3007.071	3007.071	0.059
6-9	6273.0	842.445	2734.18	948.686	763.194	840.468	841.740	841.818	841.818	0.075
7-10	7658.4	2202.098	2734.18	2446.677	2000.323	2197.910	2202.409	2202.605	2202.605	0.023
8-11	19473.2	5526.226	2734.18	6162.867	5190.862	5517.761	5529.499	5530.281	5530.086	0.070
0-5	6672.7	**-500.000**	**2734.18**	**-599.736**	**-470.116**	**-499.018**	**-499.564**	**-499.613**	**-499.607**	0.079
1-6	1306.9	-145.676	2734.18	-163.170	-131.798	-145.286	-145.518	-145.539	-145.539	0.094
2-7	3543.7	-355.683	2734.18	-395.470	-322.407	-354.809	-355.488	-355.538	-355.538	0.041
3-8	8262.4	-921.348	2734.18	-1025.30	-849.264	-919.183	-921.036	-921.158	-921.148	0.022

Error=abs([the 6th iteration results]-reference [23])/ reference [23]×100, tensile force of ring cable and internal force of equivalent lower chord are converted according to Eq. (13): $P = 2T\sin(\theta/2)$. P stands for internal force of equivalent lower chord, T stands for tensile force of ring cable, θ=30^0. The internal forces of ring cable in Table 7 are equivalent calculated internal forces.

Table 8
The real calculation results of element 0-5 in the original structure

Iteration number	1st	2nd	3rd	4th	5th	6th
New method/kN	-99.956	-78.353	-83.170	-83.261	-83.269	-83.268
6 times/kN	**-599.736**	**-470.116**	**-499.018**	**-499.564**	**-499.613**	**-499.607**

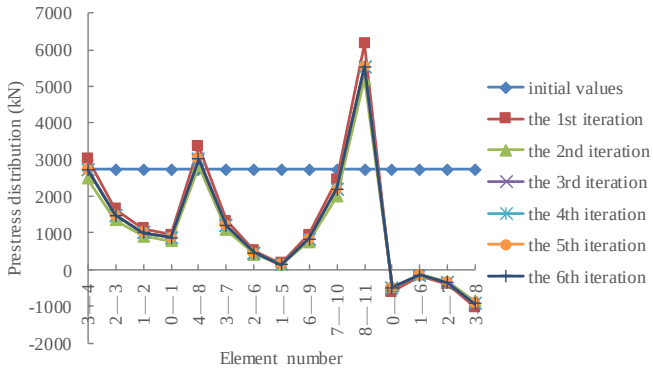

Fig. 19 Trend chart of pretress distribution in iterative process

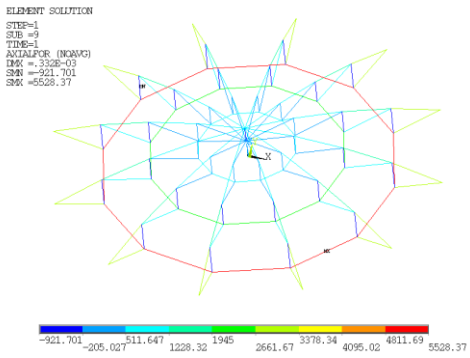

Fig. 20 Calculation results of integral FEM model

Table 9
The change of displacement convergence values in iteration process

Iteration number	1st	2nd	3rd	4th	5th	6th
Maximum displacement/m	0.2985	0.0159	0.0051	0.0057	0.0058	0.0058

It can be seen from Table 7 and Fig. 19 that the cable force distribution tends to be stable when the 4th iteration is accomplished, and the cable force changes very slightly when the iteration continues. According to the comparison between the results of the 6th iteration and SVD, the maximum error of prestress force is 0.106%. The displacement convergence values in iteration process are shown in Table 9. Table 9 shows that the errors between the calculation results of the 5th and 6th and the design coordinates are 0.0058m and 0.0058m, respectively. The difference is zero. The calculation results of integral FEM model show in Fig. 20 by substituting the self-stress modes obtained from planar cable-truss frame into the integral FEM model, and internal forces and displacements of elements are basically equal to the results obtained from planar cable-truss frame. From the calculation results of forces and displacements, it can meet the requirements of engineering accuracy. The example shows that new method has fast design, reasonable shape determination and stable solving self-stress mode. The new method proposes a new approach to solve the self-stress mode of cable dome structure.

5. The method of solving feasible prestress

Reference [21-23] can be referred to solve the feasible prestress under self-weight and external loads. Self-weight and external loads can be equivalent to concentrated forces on each node, shown in Fig. 21.

Solving process of equivalent concentrated force [27]:

(1) Firstly, based on SHELL 154 element in ANSYS, the virtual surface units are built on the grid composed of upper chord cable section of cable-truss frame (the virtual unit only transfers load and does not participate in calculation).

(2) Secondly, the load value of membrane surface is obtained according to the literature or specifications.

(3) Finally, all the lower joints of cable-truss frame are constrained along the z-axis, and the constrained reaction forces are the vertical equivalent nodal load of each node. In fact, the method is an approximate method.

Taking reference [23] as an example. To compare with the calculation results in reference [23], the membrane load is 0.6kN/m^2 being the same as reference [23], and the equivalent nodal load of each type of node under self-weight and external loads are shown in Table 10. The compared results of feasible prestress and self-stress mode under self-weight and external loads are shown in Table 11.

Table 10
Equivalent nodal loads under self-weight and external loads

Node number	0	1	2	3	4
Self-weight/kN	-8.274	-45.826	-16.104	-7.479	-23.071
External loads/kN	-111.700	-46.818	-96.854	-139.520	-98.025

Table 11 shows that the structural feasible prestress under self-weight changes slightly comparing with its self-stress mode, so the influence of self-weight can be ignored in design. But under the external loads of 0.6kN/m^2, the structural feasible prestress changes dramatically, so the influence of external loads on the structure should be considered in the actual design.

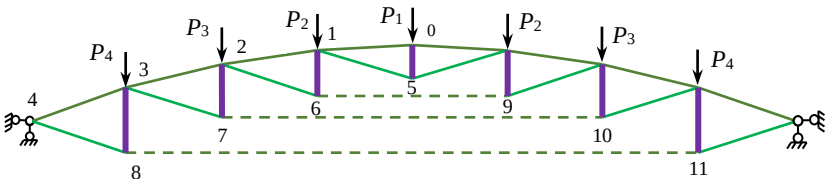

Fig. 21 Applying method of equivalent nodal loads

Table 11
The feasible Prestess under self-weight and external loads Unit: kN

Element	0-1	1-2	2-3	3-4	1-5	2-6	3-7	4-8	6-9	7-10	8-11	0-5	1-6	2-7	3-8
no self-weight	866.14	1009.19	1477.76	2734.17	139.83	459.38	1194.24	3007.07	841.81	2202.60	5530.08	-499.60	-145.54	-355.54	-921.15
Self-weight	697.64	810.60	1320.00	2639.00	110.40	505.32	1260.90	3115.10	925.47	2325.00	5727.70	-949.42	-361.38	-115.29	-396.09
External loads	528.59	607.77	1020.90	2339.20	76.98	410.91	1270.30	3455.90	752.42	2340.80	6353.20	-925.60	-286.64	-84.57	-286.31

6. Conclusions

The paper proposes “Improved force iteration method based on rational shape design solving self-stress mode of cable-truss tensile structure”. The conclusions are as follows. According to the topology of CTTS, the internal relation of maintaining the structural balance is obtained based on the rational shape of planar cable-truss frame. This special relation can be used to complete the fast design of planar cable-truss frame (the designed structure has an independent self-stress mode) or to determine whether the geometric shape of the existing cable-truss structure is rational or not. And then assemble the planar cable-truss frame to form the spatial CTTS. Finally, the way to solve feasible prestress is proposed. The examples show that the new method has the advantages of systematic design and solution flow, high accuracy, fast convergence and stable calculation. Meanwhile, the new method can be used in FEM software, which is easy to learn for engineers and designers. The new method offers a new approach for form-finding and design of CTTS.

Acknowledgements

The authors would like to acknowledge the financial support of the National Natural Science Foundation of China (51778017), the financial support of the National Natural Science Foundation of China (51878014), the Natural Science Foundation of Beijing Municipality (8172011).

References

[1] Fuller R.B. “Synergetics explorations in the geometry of thinking”. London: Macmillan Pbulishing Co., Inc, 1975.
[2] Snelson K. “The art of tensegrity. International Journal Space Structure”, 27(2 and 3), 71−80, 2012.
[3] Motro R., “Tensegrity: Structural Systems for the Future”, London: Krogan Page Science, 2003.
[4] Geiger D.H., Stefaniuk A., and Chen D., “The design and construction of two cable domes for the Korean Olympics”, Shells, membrane and space frames, proceedings IASS symposium, Japan, 1986, Vol. 2, pp. 265−272.
[5] Levy M.P., “The Georgia Dome and beyond: Achieving light weight-long span structures”, Spatial, lattice and tension structures, proceedings IASS-ASCE international symposium, New York, 1994, pp. 560−562.
[6] Ge J.Q., Zhang A.L., Liu X.G., Zhang G.J., Ye X.B., Wang S., and Liu X.C., “Analysis of tension form-finding and whole loading process simulation of cable dome structure”, Journal of Building Structures, 33(4), 1−11, 2012.
[7] Deng H., Jiang Q.F., and Kwan A.S.K., “Shape finding of incomplete cable-strut assembles containing slack and prestressed elements”, Computers and Structures, 83, 1767−79, 2005.
[8] Liu R.J., Li X.Y., Xue S.D., Marijke M., and Ye J.H., “Experimental and numerical research on Annular Crossed Cable-Truss Structure under cable rupture”, Earthquake Engineering and Engineering Vibration, 16(3), 557−569, 2017.
[9] Xue S.D., Liu R.J., Li X.Y., and Marijke M., “Concept proposal and feasibility verification of the annular crossed cable-truss structure”, International Journal of Steel Structures, 17(4), 1549−60, 2017.
[10] Deng H., Zhang M.R., Liu H.C., Dong S.L., Zhang Z.H., and Chen L.Q., “Numerical analysis of the pretension deviations of novel Crescent-shaped tensile canopy structural system”, Engineering Structures, 119, 24−33, 2016.
[11] Jeon B.S., and Lee J.H., “Cable membrane roof structure with oval opening of stadium for 2002 FIFA world Cup in Busan”. In: Proceedings of sixth Asian-Pacific conference on shell and spatial structures, South Korea; 2000, Vol. 2, pp.1037−1042.
[12] Maxwell, J.C., “On the calculation of the equilibrium and stiffness of frames”, Phil. Mag, 27, 294−299, 1864.
[13] Pellegrino S., “Structural computations with the singular value decomposition of the equilibrium matrix”, International Journal of Solids and Strutures, 30(21), 3025−35, 1993.

[14] Pellegrino S., and Calladine C.R., "Matrix analysis of statically and kinematically indeterminate frameworks", International Journal of Solids and Strutures, 22(4), 409−428, 1986.
[15] Calladine C.R., and Pellegrino S., "First-order infinitesimal mechanisms", International Journal of Solids and Strutures, 27(4), 505−15, 1991.
[16] Hanaor A., "Prestressed pin-jointed structures with the singular value decomposition of the equilibrium matrix", International Journal of Solids & Strutures, 30(21), 3025−3035, 1993.
[17] Yuan X.F., and Dong S.L., "Nonlinear analysis and optimum design of cable domes", Engineering Structures, 24(7), 965−977, 2002.
[18] Yuan X.F., and Dong S.L., "Integral feasible prestress of cable domes", Computers and Structures, 81(21), 211−219, 2003.
[19] Yuan X.F., Chen L.M., and Dong S.L., "Prestress design of cable domes with new forms", International Journal of Solids and Strutures, 44(9), 2773−2782, 2007.
[20] Zhang L.M., Chen W.J., and Dong S.L., "Initial prestress finding procedure and structural performance research for Levy cable dome based on linear adjustment theory", Journal of Zhejiang University Science A, 8(9), 1366−72, 2007.
[21] Wang Z.H., Yuan X.F., and Dong S.L., "Simple approach for force finding analysis of circular Geiger domes with consideration of self-weight", Journal of Construtional Steel Research, 66(2), 317−322, 2010.
[22] Tian G.Y., Guo Y.L., Wang Y.H., Wang X.A., and Jiang L.X., "Constraints removed method for self-stress mode problem of spokestructures", Spatial Structure, 15(04), 38−43+16, 2009.
[23] Guo J.M., and Jiang J.Q., "An algorithm for calculating the feasible pre-stress of cable-struts structure", Engineering Structures, 118(1), 228−39, 2016.
[24] Guo J.M., and Zhou D., "Pretension simulation and experiment of a negative Gaussian curvature cable dome", Engineering Structures, 127, 737−747, 2016.
[25] Shen S.Z., Xu C.B., and Zhao C., "Suspension structure design", Beijing, China Architecture & Building Press, 17−19, 2006.
[26] Guo Y.L., and Tian G.Y., "Cable structure system, design theory and construction control", Beijing, Science Press, 2014.
[27] Chen Z.H., Liu H.B., Zhou T., and Qu X.Z., "Parametric calculation and analysis of spatial structure APDL", Beijing, China Water and Power Press, 2009.

Advanced Steel Construction – Vol. 16 No. 2 (2020) 181–190
DOI:10.18057/IJASC.2020.16.2.9

EFFECT OF DIFFERENT ROLL FORMING PROCESSES ON MATERIAL PROPERTIES OF SQUARE TUBES

Fei Han *, Yun Wang, Tao Zhang, Qian Li and Yu Song

School of Mechancial and Materials Engineeing, North China University of Technology, Beijing, 100144, China
** (Corresponding author: E-mail: hanfei@ncut.edu.cn)*

ABSTRACT

Different roll forming processes result in parts with different properties. This study compared the behavior of square tubes manufactured using two different processes, namely continuous and direct forming process, and then examined the yield strength, ultimate strength, residual stress, and metallography in different regions. Furthermore, finite element models of direct and continuous forming were developed, and the results obtained using these models agreed well with the experimental results. The yield and ultimate strengths of each part of the continuously formed square tube were higher than those of the directly formed square tube. The residual stress showed that different processes considerably affected the longitudinal residual stress but had a less significant effect on the horizontal residual stress. The residual stress due to continuous forming was higher than that due to direct forming. Microscopic tests showed that the weld seam of the continuously formed square tube exhibited greater plasticity and anti-impact toughness than that of the directly formed square tube. This study can serve as a guide to practical production and suitable process selection.

ARTICLE HISTORY

Received: 13 January 2020
Revised: 26 April 2020
Accepted: 30 April 2020

KEYWORDS

Roll forming;
Material property;
Residual stress;
Metallography

1. Introduction

Square tubes are widely used, especially in the construction industry, because they use less base material and have low energy consumption, high production efficiency, and high quality. Two manufacturing methods are commonly used for square tubes: direct and continuous forming. In direct forming, the sheet is directly roll-formed into an open rectangular part, and the edges are then welded to form the final closed rectangular tube. In continuous forming, the sheet is first roll-formed into a round tube, the edges are then welded to form a closed round profile, and the round tube is flattened to form the final closed rectangular tube.

The behavior of square and rectangular tubes is different from that of base materials. Cold forming of steel sheets produces work-hardening effects. Thus, the material properties such as yield and ultimate strengths are all locally affected by a degree that depends on the bending situation. Different forming processes have different effects on the material properties, metallography, and residual stresses in the flat, corner, and welding seam regions, which can have a significant effect on the quality. For safe use and accurate predictions, many researchers have studied the material properties and residual stress of the complete cross section and in each region. Huang [1] conducted a large number of tensile tests on several groups of carbon steel, stainless steel, and alloy steel after cold roll forming. Using quasi-static tensile and dynamic tensile tests, the static and dynamic tensile stress–strain curves were obtained at different rates. In addition, the specific steps of the tensile experiment were summarized to provide a reference for other similar experiments. Kohar et al. [2] studied the influence of the elastic–plastic behavior of a square tube material on steady crushing force, peak crush force, energy absorption, and crushing effect of square tube axial crushing. Different processes result in different material properties, and different deformation histories can cause different work hardening in each part of the tube. Hu et al. [3] tested the material properties of various parts of the same type of a processed square tube. Sun and Packer [4] found that the effects of cold forming indicated that no clear yield point could be obtained. Li et al. [5] found that the yield strength of flat coupons had a greater effect on local buckling than that of the corner coupons. Li and Young [6] conducted tensile tests on roll-formed high-strength steel. In their study, the material properties were studied under high-temperature conditions, and a new curve for the material properties was proposed.

Davani et al. [7] demonstrated that the microstructure significantly affected the mechanical properties, and it could be confirmed using the material properties. Pham and Kim [8] found that the grain size, shape, and orientation had significant effect on the hardness of the phases. Luo et al. [9] investigated the evolution of microstructures and mechanical properties and discussed the formation mechanism of titanium oxides. Miura et al. [10] found that the increased hardness was caused by grain refinement and the formation of martensite.

Manufacturing processes lead to residual stresses in the specimens. These residual stresses usually exert a negative effect on their performance [11]. The roll-forming process is well known to possibly result in a high residual stress in its products, and this residual stress is one of the main factors affecting the bearing capacity of steel members [12]. In addition, residual stress can also affect the rate of crack propagation, which can lead to a shorter fatigue life [13]. Ma et al. [14] studied cold roll forming of high-strength hollow steel sections. Li et al. [15] studied the longitudinal residual stresses of annealed and non-annealed steel tubes with square and rectangular hollow sections which are cold-formed and thick-walled. The effects of process parameters such as thickness, depth-to-thickness ratio, and the yield strength of a flat plate on the residual stress are analyzed. Using extensive tensile tests, the effect of cold roll forming was studied, the residual stress in three regions was measured, and a new type of high-strength steel-structure model, which correlated well with the experimental results, was proposed. Liu and Chung [16] proposed a finite element model that could effectively predict the residual stress distribution after welding. Yao et al. [17] proposed a finite element-based method to predict the equivalent plastic strain and residual stress in the square, rectangular, and elliptical hollow sections of cold-formed steel, which include normal-grade and high-strength steel.

In addition to the experiments, the different behavior, material properties, and residual stresses in different regions have been explored using finite element analysis (FEA). Wen and Pick [18] investigated the edge buckling of ERW pipes using FEA. Their results showed that edge buckling could be prevented by setting the machine parameters, such as the roll gaps. Li et al. [19] set up a FEA model to simulate different processes and found different residual stress distributions and magnitudes. Some researchers have ignored the differences in the material behavior in corner and flat regions when establishing the FEA models [20]. However, Yuan et al. [21] built a more detailed model that considered the effects of geometric imperfections and residual welding stress. Thus, details from various parts of the model were required. In addition, Yang et al. [22] proposed an analytical model to determine the effect of friction on the tube forming process and final thickness distribution along the tube section.

Most of these investigations were mainly concerned with the material properties and residual stress of complete cross sections and each region. These methods ensured reliability in the engineering perspective but did not consider the forming effect or combine the results with microstructure analysis to explain the deformation mechanism. Square tubes formed using different processes have different plastic strain histories. This can lead to differences in the material properties, microstructure, and residual stress, which can affect the performance of the product.

In this study, the aim is to improve the understanding of the material properties, microstructure and residual stress of the two square tube forming processes. Macro and micro experiments were conducted to investigate the material properties observed. A quasi-static tensile test, experiments concerning the metallography, and residual stress tests were performed. Finally, FEA was carried out and then verified using the experimental data. The results of the

experiments and simulations were compared, and the mechanism underlying the changes in the material properties of square and rectangular tubes under different processes was investigated.

2. Experiment and FEA

2.1. Tensile Test

Fig. 1 shows that the strain value was obtained using an optical measurement system (ARAMIS, GOM). The specimens were prepared and tested according to the Chinese Metallic Materials-Tensile Testing standard (GB/T228–2002) using an MTS displacement sensor. The chemical composition of Q235 steel is listed in Table 1.

Fig. 1 Experimental test

Table 1
Chemical composition of Q235 steel (wt%)

C	Si	Mn	S	P	Cr	Ni	Cu
0.16	0.21	0.5	0.034	0.027	0.18	0.26	0.19

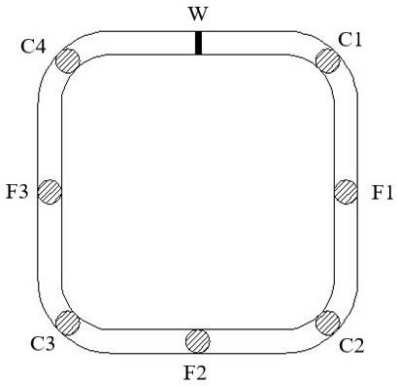

Fig. 2 Sampling positions and labeling

Fig. 2 shows that two tensile specimens were taken from the corners, i.e., flat and welding seam regions in each square tube. The schematic diagram of the flat specimen is shown in Fig. 3(a) in which gauge length of the specimen L_0 was 55 mm and length of the parallel segment *Lc* was 95 mm. Fig. 3(b) shows the schematic diagram of the round-corner specimen where the gauge section length of the specimen was 40 mm, the length of the parallel segment was 80 mm, and total length *Lt* of both specimens was 200 mm. Fig. 3(c) shows the position of the rounded specimen end in the square tube section, where *B1* denotes the linear distance between the tangent points of the outer surface of the round corner of the square tube. Fig. 3(d) shows the position of the rounded specimen gauge section in the square tube section, where *B2* is the width of the gauge section, which represented the linear distance between the tangent points of the inner surface of the round corner of the square tube.

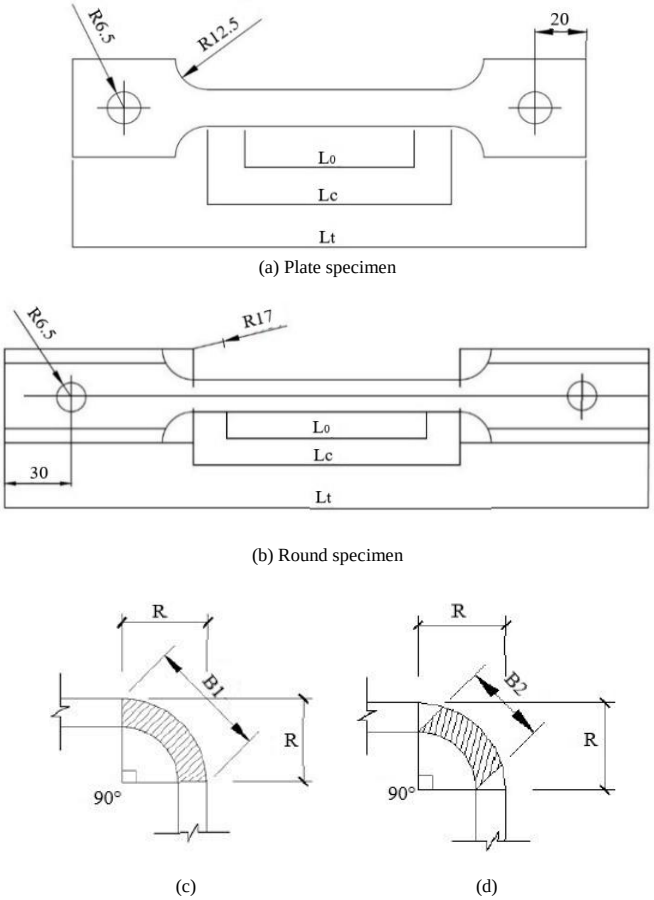

(a) Plate specimen

(b) Round specimen

(c) (d)

Fig. 3 Specimen size and sampling position

2.2. Design of the Flower Diagram and Finite element Simulation

The flowers for the direct and continuous forming are shown in Fig. 4. In the direct forming process, the bending corner was formed from the outside to the inside, and finally, welding was performed. In the continuous forming process, a round tube was formed, welded, and then shaped into a square tube.

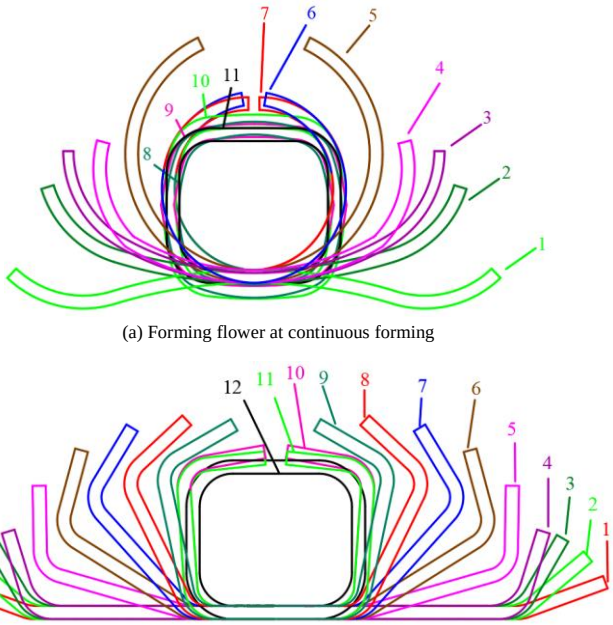

(a) Forming flower at continuous forming

(b) Forming flower at direct forming

Fig. 4 Forming flowers for direct and continuous forming

A typical component with the final shape of a square rectangular tube is shown in Fig. 5. The components used in this study were made from Q235 steel, and its material properties are shown in Fig. 6.

The finite element model of the direct and continuous forming were established in ABAQUS/Explicit, and the mesh type of the component was S4R. The two assembly processes are shown in Fig. 7.

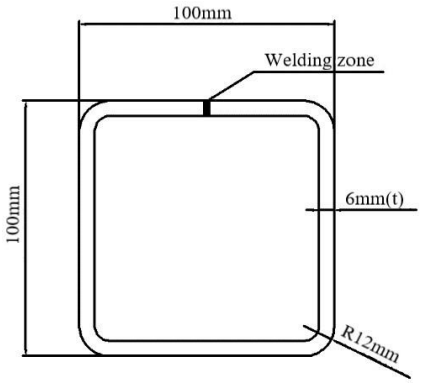

Fig. 5 Geometric dimensions of the specimen

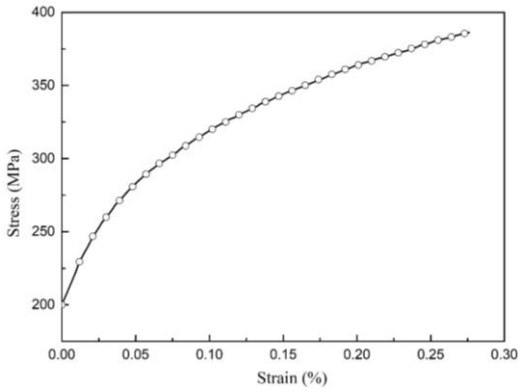

Fig. 6 True stress-plastic strain diagram for Q235 steel

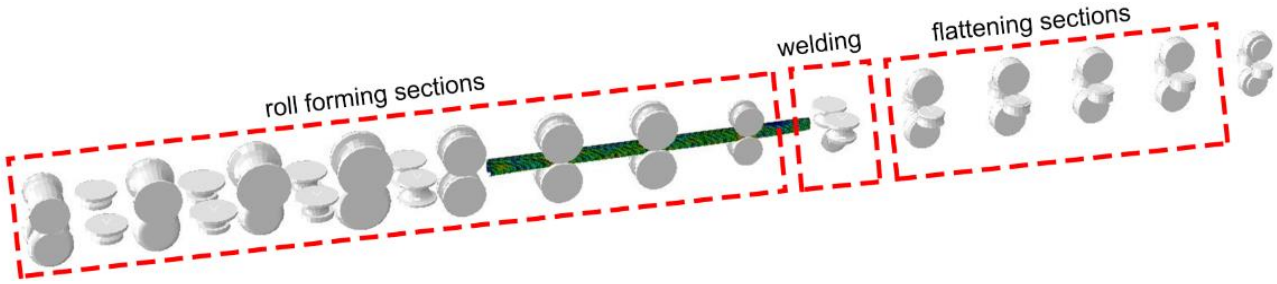

(a) Continuous forming

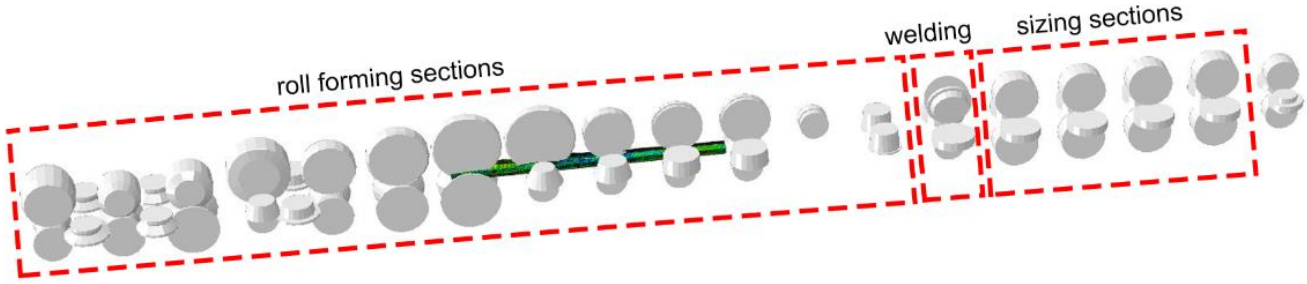

(b) Direct forming

Fig. 7 FEA model of the different roll forming processes

3. Results and discussion

3.1. Differences in Material Properties Between the Two Processes

A summary of the obtained material properties is listed in Table 2. $RP_{0.2}$ indicates the average yield strength, and *Rm* is the average ultimate strength. Coefficients *ρ1* and *ρ2* are the ratios of the yield strength of the flat and corner regions to that of the base material, respectively, whereas *ρ3* and *ρ4* denote the ratios of the ultimate strength of the flat and corner regions to that of the base material, respectively.

According to the previously designed dimensions of the flat and corner tensile test specimens, the position and shape of the specimens after the tensile fracture are shown in Fig. 8. The material properties significantly vary throughout the square tube. In the same tube, the corner material has a higher degree of work hardening than the flat material. Li [5] found that the strain could reach or exceed the yield strain of the flat specimens, which means that the sections become plastic when local buckling occurs. Different forming processes result in different material properties, and different deformation histories cause different work hardening in each part of the square tube. Shengde Hu tested the material properties of various parts of square tubes processed using the same method and found that the material properties in the flat and corner regions were different [3]. To investigate the effects of different forming processes on the material properties, a tensile test was performed on various parts of the square tubes that were processed using different techniques.

Stress–strain curves in the different regions of the square tube are obtained, and some of these curves are shown in Fig. 9. The repeated experiments demonstrate a high degree of data coincidence, which validate the reliability of the experiment. For each type of square tube, two base materials are considered for comparative experiments.

Fig. 8 Tensile test specimens of flat and corner

Table 2
Material properties

Process	Position	$RP_{0.2}$	Rm	*ρ1*	*ρ2*	*ρ3*	*ρ4*
Continuous forming	Flat	375	430	1.16	1.34	1.11	1.27
	Welding	524	548				
	Corner	503	543				
Derect forming	Flat	312	395	1.03	1.52	1.07	1.29
	Welding	466	519				
	Corner	474	512				

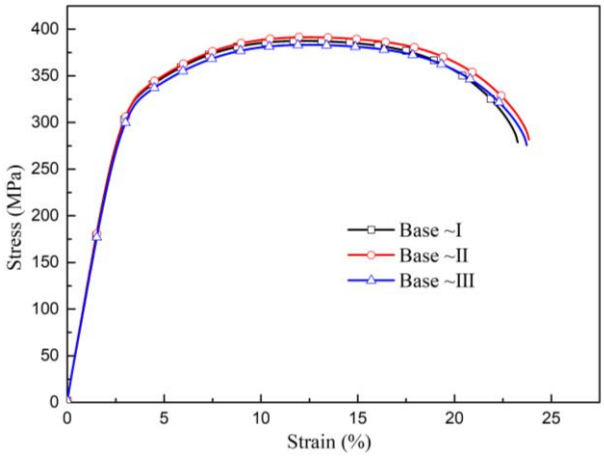

(a) Base material

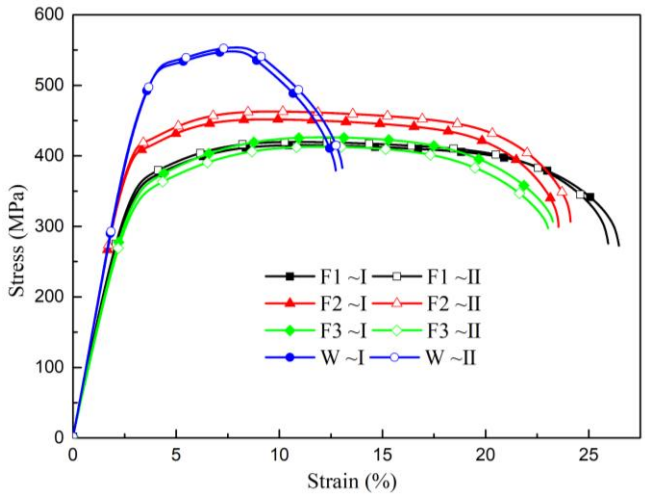

(b) Flat and weld of continuous forming

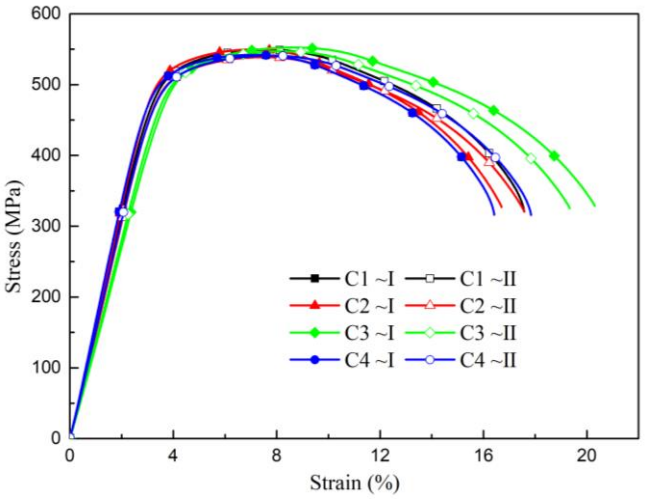

(c) Corner of continuous forming

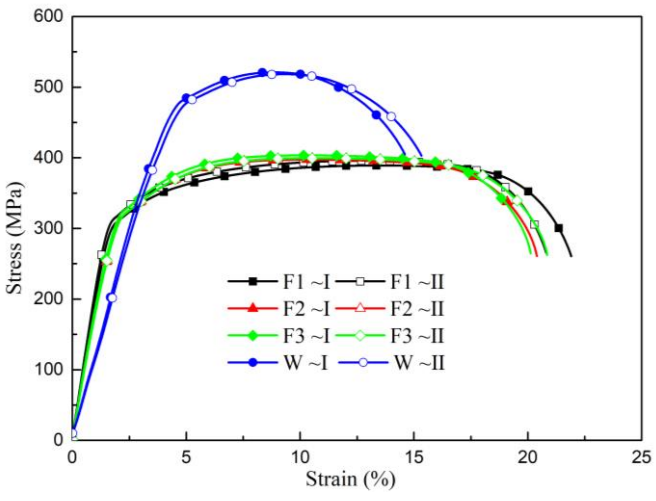

(d) Flat and weld of direct forming

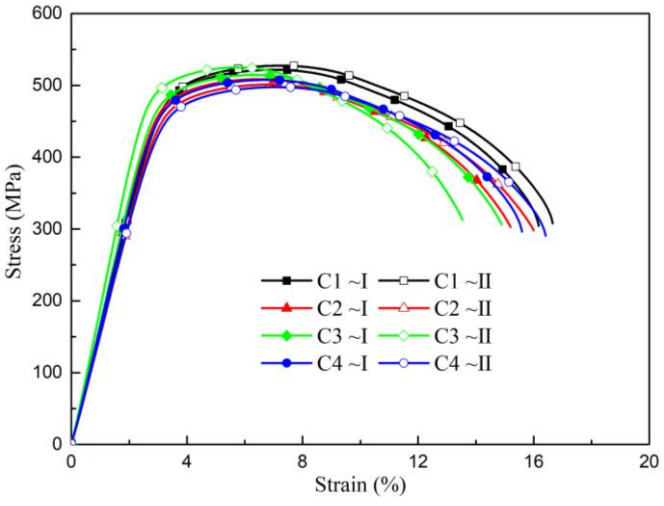

(e) Corner of direct forming

Fig. 9 Stress–strain curve in the different regions of the square tube

The trends of the curves obtained from direct and continuous forming are similar. Comparing the curves shown in Figs. 9(a) and (d), we can see that the

mechanical properties of the base material and the flat part of direct forming are basically the same, which is similar to the curve in Fig. 9(b), although with a slight difference. The reason is that in the continuous forming process, the flat part is first bent and then reshaped, which is different from direct forming, resulting in a change in the mechanical properties of the plate. Comparing the flat region and the corner region of the two forming processes, it is observed that the deformation in the corner region is larger than that in the flat region during the forming process, which results in a large difference in the yield and ultimate strengths of the material. The yield and ultimate strengths obtained by continuous forming are slightly larger than those obtained by direct forming. The yield and ultimate strengths of the four corner regions of the square tube in the same forming process exhibit small fluctuations, which is closely related to the deformation of the four corner regions during the forming process.

However, in the roll formed square tube, the yielding platform of the material from the flat region becomes shorter or disappears, whereas no yielding platform is present in the material collected from the corner region. This result shows that the crystal structure of the base material is destroyed during the forming process, which then recombines into a new crystal structure. In addition, it changes the mechanical properties of the material. The yield strength of the flat plate opposite the weld seam is higher than that on either side, indicating that the different forming processes exert a certain influence on the material-performance parameters. The deformation is larger on the side opposite the weld seam; hence, it exhibits the largest yield strength. Because of the joint action of the solder and high temperatures at the weld, the yield and ultimate strengths increase significantly.

As shown by the lists in Tables 3 and 4, the yield and ultimate strengths in each region are higher in the continuously formed square tube than in the directly formed square tube. The relative increase in the yield strength is largest at F2 in the continuously formed tube because it has the largest relative deformation. The increase in the yield strength at the welding seam in the continuously formed tube is higher than that in the directly formed tube.

Table 3
Yield strength following the different processes

Position	F1	F2	F3	W	C1	C2	C3	C4
Continuous forming / MPa	358	411	356	524	500	496	514	503
Direct forming / MPa	309	321	305	466	480	469	485	460
Coefficient	1.16	1.28	1.17	1.12	1.04	1.06	1.06	1.09

Table 4
Ultimate strength following the different processes

Position	F1	F2	F3	W	C1	C2	C3	C4
Continuous forming / MPa	416	455	418	548	544	543	546	540
Direct forming / MPa	391	394	399	519	524	504	519	502
Coefficient	1.06	1.15	1.05	1.06	1.04	1.08	1.05	1.08

*"Coefficient" refers to the ultimate strength ratio of the continuous to the direct forming.

Table 5
Specimen elongation after fracture

Process	Position	S_A (%)	S_B (%)	$\overline{S}$ (%)	$\overline{S}_S$ (%)
Continuous forming	Base material	31.72	32.20	31.96	31.96
	Flat F1	25.81	24.18	24.99	
	Flat F2	20.87	22.53	21.70	23.96
	Flat F3	25.45	24.90	25.18	
	Flat W	15.45	12.90	14.18	14.18
	Corner C1	15.76	16.25	16.01	
	Corner C2	17.88	19.67	18.78	16.91
	Corner C3	15.76	15.44	15.60	
	CornerC4	16.57	17.89	17.23	
Direct forming	Base material	32.39	35.63	34.01	34.01
	Flat F1	21.99	22.43	22.21	
	Flat F2	23.87	20.56	22.22	21.96
	Flat F3	21.18	21.71	21.45	
	Flat W	14.19	12.77	13.48	13.48
	Corner C1	14.91	15.51	15.21	
	Corner C2	17.89	14.31	16.1	15.25
	Corner C3	14.49	14.35	14.42	
	Corner C4	13.26	17.25	15.26	

Elongation is an important index for measuring the material plasticity. In this experiment, the gauge section length before and after the fracture of all the specimens are measured, and the elongation after fracture of each specimen is then obtained according to the elongation formula. The experimental data are listed in Table 5. S_A and S_B are the measured values of the elongation of test specimens A and B (repeated test specimens), respectively. $\overline{S}$ is the average elongation of the repeated specimens. $\overline{S}_S$ is the average elongation at the same sampling position (flat or round corner) of the cross section.

The base material exhibits the highest elongation than the other parts of the square tube. The elongation of the flat specimen is close to that of the base material because the compressive deformation of the flat specimen is small during the forming process of the square tube and the effect of the roll forming is not obvious. However, because the rounded corners are greatly affected by the roll forming effect and the flat plates at the welds are subjected to high temperature, their elongation is relatively lower than that of the base material.

The plastic strain causes improvements in the yield and ultimate strengths. The strain history obtained from the FEA model confirms the above-described behavior. Fig. 10(a) shows that at the corner of the square tube, i.e., C2, the

different deformation histories indicate that the tubes manufactured using the two processes exhibit significantly different plastic-strain histories. The continuously formed square tube experiences plastic strain during the forming of the round tube in the first station, and the strain change is more evenly distributed throughout the entire process. Conversely, during the direct forming, only certain stations experience deformation; thus, the curve suddenly increases. However, the final strains are similar, resulting in similar improvements in the material performance, which is consistent with the results of the tensile test.

Fig. 10(b) shows that at the flat part of square tube F2, the strain history shows that almost no plastic behavior can be observed at position F1 during the direct forming. However, obvious plastic behavior appears in the flat region because the flat material also participates in the deformation during the continuous forming but does not participate during the direct forming. The different strain values explain the differences in the behavior of the material properties of the specimens manufactured using the two processes.

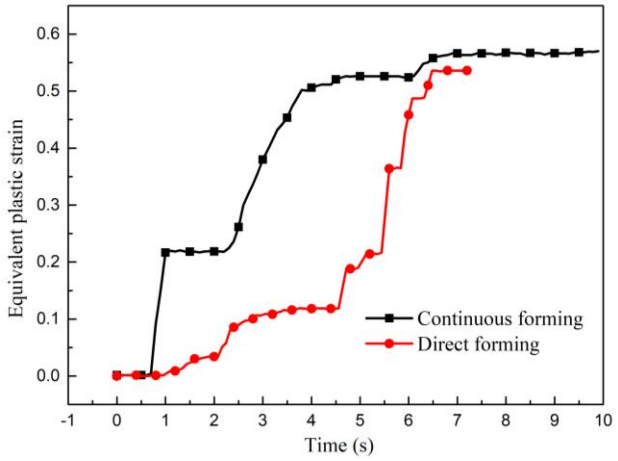

(a) At the corner of the tubes

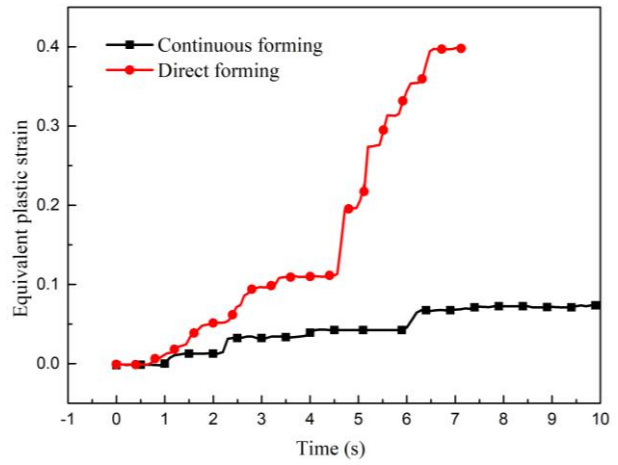

(b) At the flat region of the tubes

Fig. 10 Comparison of the equivalent plastic strain of the tubes manufactured using direct and continuous forming

The material properties can also be explained by the metallographic distribution [23]. For the characterization, the microstructure specimens are taken from the flat, corner, and welded-joint regions. The specimens are ground using abrasive paper, polished, and then etched using 4% nitric-acid alcohol solution. An OLYMPUS OLES4100 light microscope is used to extract the morphological parameters. Fig. 11 shows the microstructure (200× magnification) of the flat and corner regions in the tubes manufactured using different techniques. (a) shows the flat regions of the continuously formed tube, (b) shows the flat regions of the directly formed tube, (c) shows the corner regions of the continuously formed tube, and (d) shows the corner regions of the directly formed tube. The crystal structure is observed using the microscope and shows that the continuously formed tube illustrates the behavior of smaller grains and little austenite.

Fig. 11 shows that the metallographic structures of the two forming processes are similar, and the distribution of ferrite and pearlite is relatively uniform. The average ferrite diameter in the flat regions is measured, and the average grain diameter of the two processed square tubes is shown in Fig. 12. The ferrite diameters are denoted as D1 in the directly formed tube and D2 in the continuously formed tube. The continuously formed square tube has a smaller crystal grain size, and the macroscopic aspect shows that the yield and ultimate strengths in the flat region of the continuously formed square tube are larger.

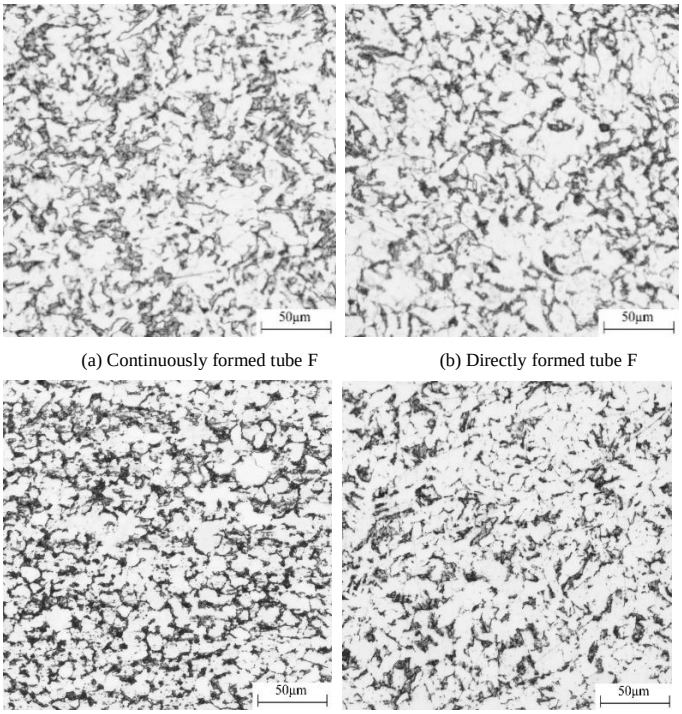

(a) Continuously formed tube F (b) Directly formed tube F

(c) Continuously formed tube C1 (d) Directly formed tube C1

Fig. 11 Microstructure of the flat and corner regions of the tubes manufactured using different techniques

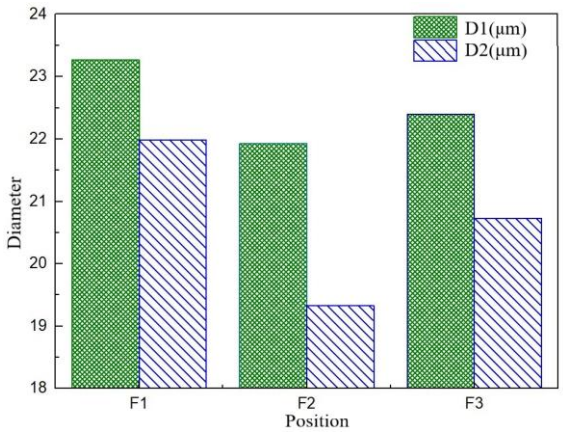

Fig. 12 Ferrite diameter under the two processes

In the metallurgical structure of the corner regions, the average grain diameters of the directly formed square tube are 19.61, 20.09, 20.49, and 20.01 μm, whereas those of the continuously formed tube are 19.63, 18.81, 18.49, and 19.26 μm. Compared with the directly formed tube, the grain size of the continuously formed tube is smaller because in the continuous forming process, the sheet material is first formed into a round tube and then shaped into a square tube. Thus, the corner region undergoes two rounds of external tension and internal pressure. The grains produce a subtle difference, the massive ferrite becomes smaller, and the number of pearlite grains increases during the extrusion process. This result confirms that in the tensile test, the continuously formed tubes have larger yield and ultimate strengths than the directly formed tubes.

3.2. Difference in the residual stress from the two processes

The continuously and directly formed specimens are measured using the hole-drilling method to find the transverse, longitudinal, and equivalent residual stresses. The positions where the measurements are recorded are shown in Fig. 13. The experimental setup used to test the square tube specimens is shown in

Fig. 14.

The deformation during the direct forming is concentrated at the corners. However, the flat region is also involved in the deformation during the continuous forming, which causes further residual stress in this region. Fig. 15 shows the distribution of the equivalent residual stress. The residual stress distribution has a large stress gradient due to the cold forming and welding effects. The residual stress at the weld seam is significantly higher than at other locations, and the equivalent residual stress near the weld seam exhibits a decreasing gradient because the heat from welding causes localized expansion, which is taken up by either of the molten metals. Because of the constraints from the far part of the weld zone, when the weld cools, some areas cool and contract more than the others, leaving residual stresses.

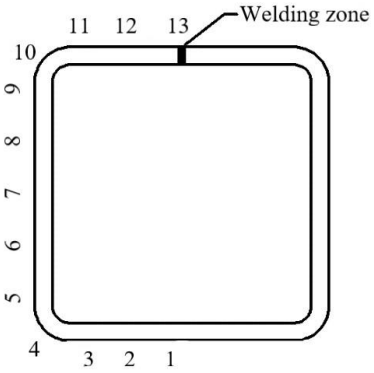

Fig. 13 Positions of the residual stress measurements

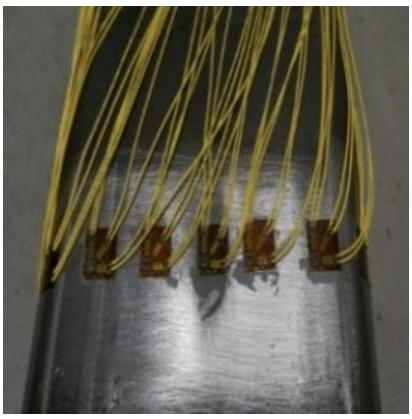

Fig. 14 Experimental setup for the residual-stress measurements

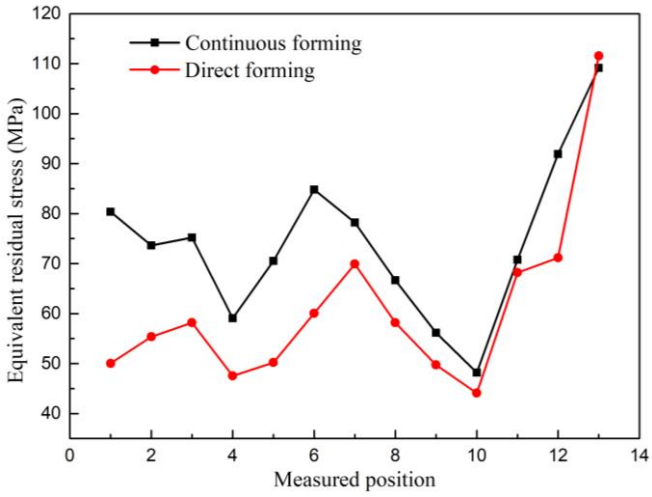

Fig. 15 Residual stress from continuous and direct forming

The distribution of the horizontal residual stress is shown in Fig. 16. Under different processing techniques, the stress distribution trend is the same. At the same position, the stress from continuous forming is higher than that from direct forming. The stress is lower in the corner region than that in the flat region, and all the values are small, indicating that both processing techniques exert only a small effect on the horizontal residual stress.

The distribution of the longitudinal residual stress is shown in Fig. 17. The trend that describes the longitudinal residual stress distribution is not obvious. In general, the longitudinal residual stress from the continuous forming is higher than that from the direct forming, which indicates that roll forming causes both longitudinal and horizontal deformation. The longitudinal strain is affected by more factors, and the processing is more complicated. The differences in the deformation process indicate that the longitudinal residual stress is more complicated in the flat region of the continuously formed tube than that in the directly formed tube. The mean horizontal residual stress is similar in both cases, indicating that the forming process has a significant effect on the longitudinal residual stress and less influence on the horizontal residual stress. The residual stress from the continuous forming is also higher than that from the direct forming.

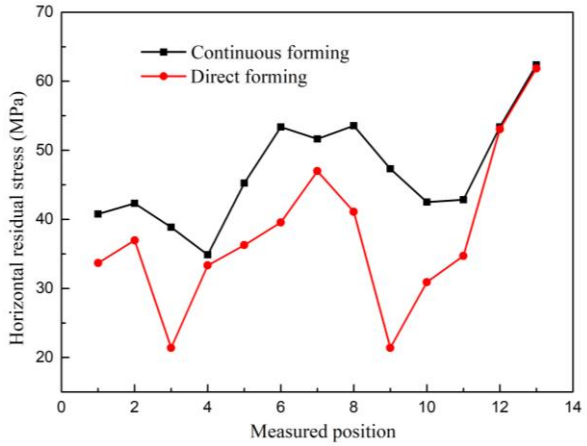

Fig. 16 Horizontal residual stress from continuous and direct forming

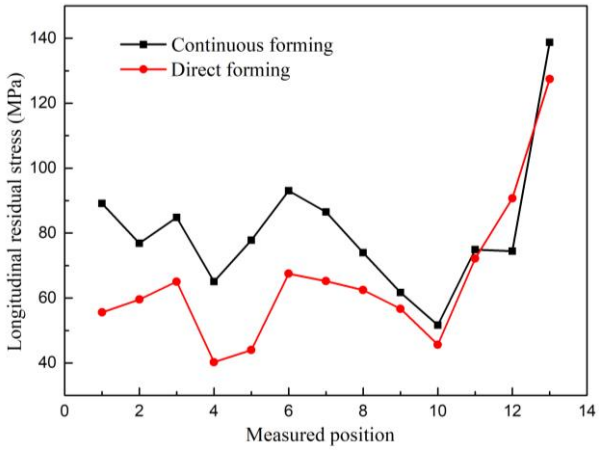

Fig. 17 Longitudinal residual stress from continuous and direct forming

3.3. Differences in the microstructure of the welding seam between two processes

The two processes result in welds with different material properties. The quality of the weld after the continuous forming is better than that after the direct forming. The main reason for this is that when the round tube is welded, a large pressing force is applied above the recrystallization temperature, which is equivalent to hot working in the weld zone. This force promotes recrystallization and refining of the grains in this region. Fig. 18 shows a stress cloud diagram of the FEA. The continuous forming welding pressure is greater than the direct forming welding pressure.

In addition to a larger press force being applied using the squeeze rolls, a large horizontal press force is produced by flattening the sections to make the welding edge fully pressed. Therefore, the range width of the continuously formed welding zones (50×magnification), which is shown in Fig. 19, is smaller than that in the direct forming. Fig. 19 shows the microstructure of the decarburized layer, which represents the overheated and recrystallized zone of the square tube weld of the two forming processes. Through the evolution of the cube elements in three zones, they represent the microstructure and change in the weld zone.

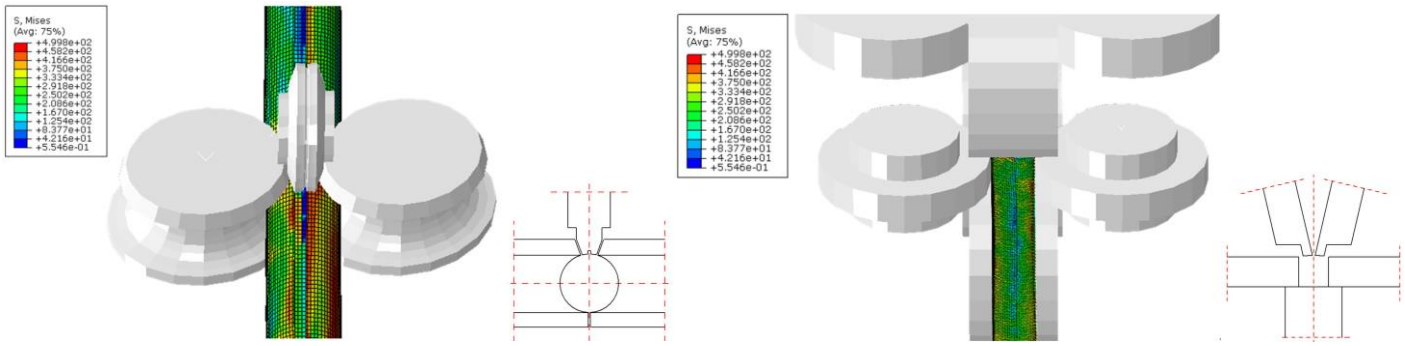

(a) Continuous forming (b) Direct forming

Fig. 18 Stress contour and 2D roll profile of the squeeze rolls

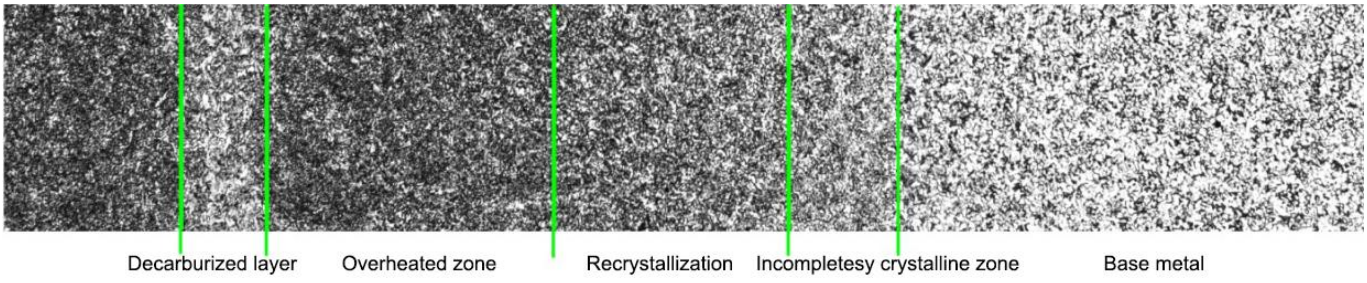

(a) Welding seam from continuous forming

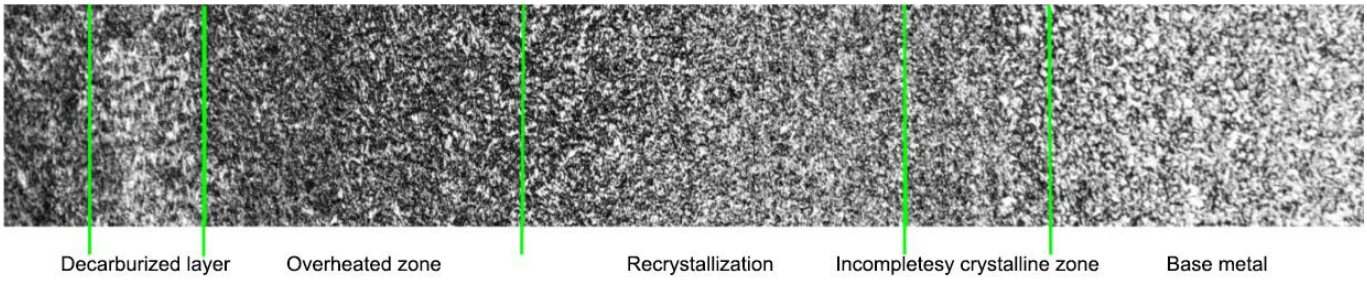

(b) Welding seam from direct forming

Fig. 19 Microstructure for each zone

Fig. 20 shows that that the Widmanstatten structure of the decarburized layer of the directly formed square tube is obviously more than that of the continuously formed square tube, and the grains are larger. Continuous forming uses round-tube welding, and large welding pressure is applied during the welding process. The tube welding end can be fully contacted, in contrast to that in the direct forming, which can effectively inhibit the growth of austenite grains. The existence of ferrite in the Widmanstatten forms a weak surface, which greatly reduces the plasticity and impact toughness of the material. In the microstructure analysis, fewer Widmanstatten structures are observed in the decarburized layer of the continuously formed specimen, and its plasticity and anti-impact toughness were better than those in the directly formed specimen.

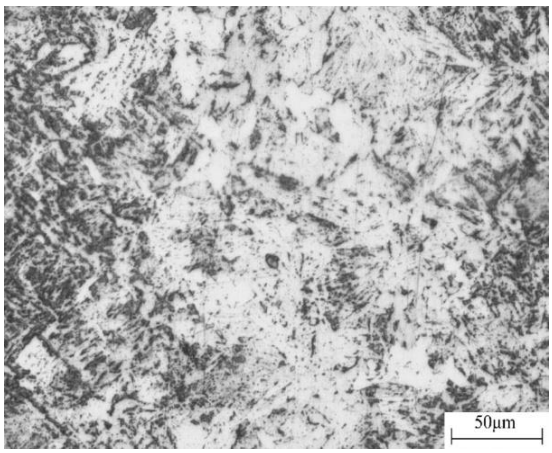

(a) Direct forming

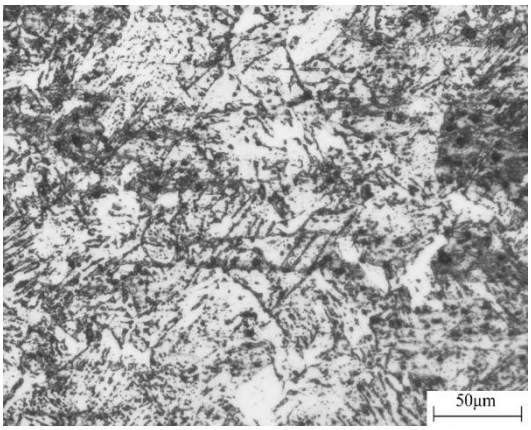

(b) Continuous forming

Fig. 20 Microstructure of the 200-times decarburized layer

When the overheating zone is welded, the temperature is in the range from below the solidus to 1200 ℃. Fig. 21 shows the metallographic structure of the superheated zone of the square tube in the two forming processes under a 200× light-magnification microscope. We can observe that the structure of the directly formed square-tube overheating zone contains more Widmanstatten structures and larger grains. There exist several Widmanstatten structures that contain ferrite in the decarburized layer and superheated zone, which directly lead to the low strength and poor toughness in the welding zone.

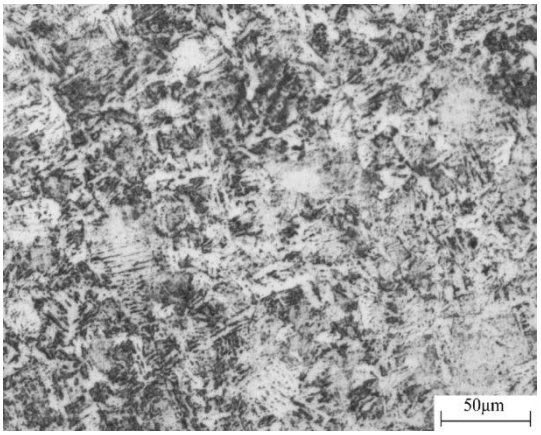

(a) Direct forming

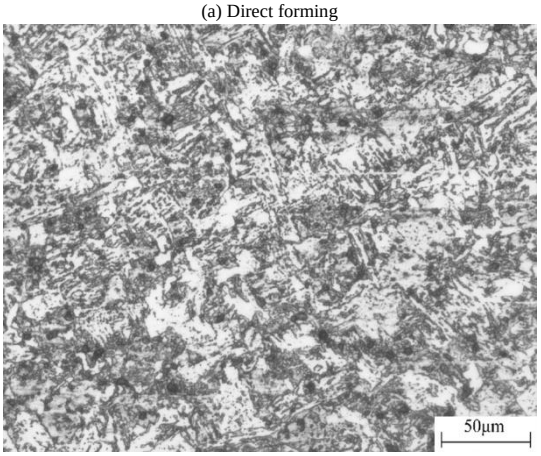

(b) Continuous forming

Fig. 21 Metallographic structure in the 200-times overheated zone

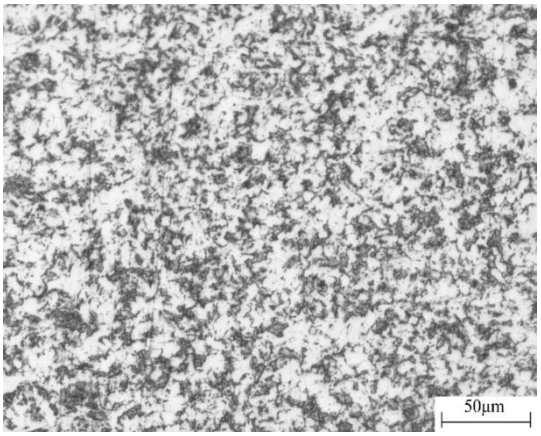

(a) Direct forming

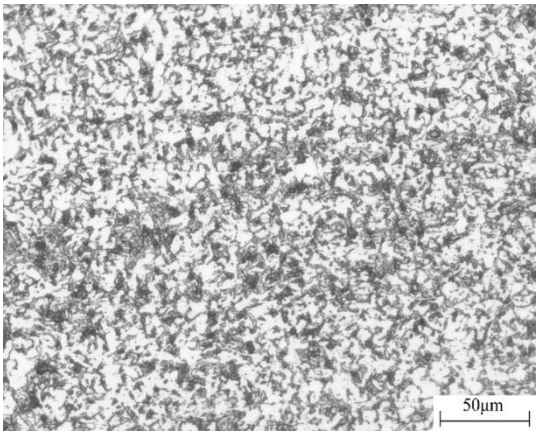

(b) Continuous forming

Fig. 22 Microstructure of the 200-times recrystallized zone

Fig. 22 shows the metallographic structure of the recrystallization zone in the direct and continuous forming square tube welding. We can observe the presence of a small amount of bainite grains besides the uniform and fine pearlite and ferrite in the structure. Thus, the strength and toughness of the materials in the recrystallization zone are better. Compared with those shown in Figs. 22(a) and (b), the pearlite and ferrite in the recrystallization zone in the continuously formed specimen are obviously more uniform and finer, and more pearlite grains are present. The overall performance of the continuously formed square tube in this area is better. It has not only a higher yield strength but also better toughness. Because of the effect of recrystallization, the strength and toughness of this zone in the square tube in both forming processes are better than those of the base material.

4. Conclusions

In this study, tensile tests, metallography, and residual stress measurements were performed on square tubes made by two forming processes. Furthermore, finite element models were set up using ABAQUS. The behavior of the directly and continuously formed tubes was described. The main research findings and conclusions are as follows.

(1) Compared with that in the base material, the strength of the flat and corner regions in both tubes had improved, and the strength in the corner regions was greater than that in the flat regions. The yield and ultimate strengths of each part of the continuously formed square tube were higher than those of the directly formed square tube. However, the roll forming effect produced by the two forming processes reduced the elongation of the square tube. The greater the roll forming effect, more obvious was the reduction in elongation.

(2) FEA demonstrated that the largest difference in plastic strain occurred in the flat regions. The strain histories were different at the corners, but the final strains were similar. The residual stress showed that different processes had an obvious effect on the longitudinal residual stress and lesser effect on the horizontal residual stress. The residual stress from continuous forming was higher than that from direct forming.

(3) The microstructure in the corner regions of both tubes were similar, and more differences occurred in the flat regions. The grains in the flat and corners regions of the continuously formed square tube were more uniform and finer than those of the directly formed square tube, and the mechanical properties were better.

(4) Weld-seam metallographic experiments were implemented. The microscopic tests indicated that the weld seam of the continuously formed square tube had greater plasticity and anti-impact toughness than the directly formed square tube.

Acknowledgements

The authors are grateful to the National Natural Science Foundation of China (No.51074204), Beijing Municipal Education Commission Project of "Great Wall Scholar"Program (No. CIT&TCD20190306), and the Project of Beijing Municipal Natural Science and Beijing Municipal Education Commission Jointly Fundation (No. KZ201910009011) for their financial supports. Also, thanks are given to the High-level Featured Disciplines Development Project of North China University of Technology (2020-2025) and Yujie Talent Support Program of North China University of Technology (No. 18XN154-005).

References

[1] Huang Y. and Young B., "The art of coupon tests", Journal of Constructional Steel Research, 96(6), 159-175, 2014.
[2] Kohar C.P., Mohammadi M., Mishra R.K. and Inal K., "Effects of elastic–plastic behaviour on the axial crush response of square tubes", Thin-Walled Structures, 93, 64-87, 2015.
[3] Hu S.D., Ye B. and Li L.X., "Materials properties of thick-wall cold-rolled welded tube with a rectangular or square hollow section", Construction and Building Materials, 25, 2683-2689, 2011.
[4] Sun M. and Packer J.A., "Direct-formed and continuous-formed rectangular hollow sections-comparison of static properties", Journal of Constructional Steel Research, 92, 67-78, 2014.
[5] Li G.W. and Li Y.Q., "Overall stability behavior of axially compressed cold-formed thick-walled steel tubes", Thin-Walled Structures, 125, 234-244, 2018.
[6] Li H.T. and Young B., "Material properties of cold-formed high strength steel at elevated temperatures", Thin-Walled Structures, 115, 289-299, 2017.
[7] Davani R.K.Z., Miresmaeili R. and Soltanmohammadi M., "Effect of thermomechanical parameters on mechanical properties of base metal and heat affected zone of X65 pipeline steel weld in the presence of hydrogen", Materials Science and Engineering: A, 718, 135-146, 2018.
[8] Pham T.H. and Kim S.E., "Nanoindentation for investigation of microstructural compositions in SM490 steel weld zone", Journal of Constructional Steel Research, 110, 40-47, 2015.
[9] Luo X., Niu Y.W., Chen X.H., Tang H. and Wang Z.D., "High performance in base metal and CGHAZ for ferrite-pearlite steels", Journal of Materials Processing Technology, 242, 101-109, 2017.
[10] Miura T., Ueji R., Fujii H., Komine H. and Yanagimoto J., "Stabilization of austenite in low carbon Cr–Mo steel by high speed deformation during friction stir welding", Materials &

Design, 90, 915-921, 2016.
[11] Shokrieh M.M., Jalili S.M. and Kamangar M.A., "An eigen-strain approach on the estimation of non-uniform residual stress distribution using incremental hole-drilling and slitting techniques", International Journal of Mechanical Sciences, 148, 383-392, 2018.
[12] Li G.W., Li Y.Q., Xu J. and Cao X., "Experimental investigation on the longitudinal residual stress of cold-formed thick-walled SHS and RHS steel tubes", Thin-Walled Structures, 138, 473-484, 2019.
[13] Acevedo C., Nussbaumer A. and Drezet J.M., "Evaluation of residual welding stresses and fatigue crack behavior in tubular K-joints in compression", Stahlbau, 80(7), 483-491, 2011.
[14] Ma J.L., Chan T.M. and Young B., "Material properties and residual stresses of cold-formed high strength steel hollow sections" Journal of Constructional Steel Research, 109, 152-165, 2015.
[15] Li G.W., Li Y.Q., Xi J. and Cao X., "Experimental investigation on the longitudinal residual stress of cold-formed thick-walled SHS and RHS steel tubes", Thin-Walled Structures, 138, 473-483, 2015.
[16] Liu X. and Chung K.F., "Experimental and numerical investigation into temperature histories and residual stress distributions of high strength steel S690 welded H-sections", Engineering Structures, 165, 396-411, 2018.
[17] Yao Y., Quach W.M. and Young B., "Finite element-based method for residual stresses and plastic strains in cold-formed steel hollow sections", Engineering Structures, 188, 24-42, 2019.
[18] Wen B.C. and Pick R.J., "Modelling of skelp edge instabilities in the roll forming of ERW pipe", Journal of Materials Processing Technology, 41(4), 425-446, 1994.
[19] Li S.H., Zeng G., Ma Y.F., Guo Y.J. and Lai X.M., "Residual stresses in roll-formed square hollow sections", Thin-Walled Structures, 47(5), 505-513, 2009.
[20] Ye Y., Zhang S.J., Han L.H. and Liu Y., "Square concrete-filled stainless steel/carbon steel bimetallic tubular stub columns under axial compression", Journal of Constructional Steel Research, 146, 49-62, 2018.
[21] Yuan F., Huang H. and Chen M.C., "Effect of stiffeners on the eccentric compression behaviour of square concrete-filled steel tubular columns", Thin-Walled Structures, 135, 196-209, 2019.
[22] Yang Z.Y., Zhao C.C., Dong G.J., Du B. and Zhang L., "Analytical model of corner filling with granular media to investigate the friction effect between tube and media", International Journal of Advanced Manufacturing Technology, 99, 211–224, 2018.
[23] Amraei M., Jiao H., Zhao X.L. and Tong L.W., "Fatigue testing of butt-welded high strength square hollow sections strengthened with CFRP", Thin-Walled Structures, 120, 260-268, 2017.